UNIVERSITAT
POLITÈCNICA
DE VALÈNCIA

Departamento de Máquinas y Motores Térmicos

TESIS DOCTORAL:

"On the Aerothermal Flow Field in a Transonic HP Turbine Stage with a Multi-Profile LP Stator Vane"

Autor: D. Sergio Lavagnoli
Director: Dr. D. José María Desantes
Dr. D. Guillermo Paniagua

Valencia, October 2012

TESIS DOCTORAL

“On the Aerothermal Flow Field in a Transonic HP Turbine Stage with a Multi-Profile LP Stator Vane”

AUTORES

Realizada por:	D. Sergio Lavagnoli
Dirigida por:	Dr. D. José María Desantes
	Dr. D. Guillermo Paniagua

TRIBUNAL CALIFICADOR

Presidente:	Dr. D. Antonio José Torregrosa Huguet
Secretario:	Dr. D. José Galindo Lucas
Vocales:	Dr. D. Remy Dénos
	Dr. D. Thomas Povey
	Dr. D. Jesús Manuel Fernández Oro

VOCALES SUPLENTES

Dr. D. Stefano Bianchi
Dr. D. Tolga Yasa

To my readers

Abstract

The quest for higher performances and durability of modern aero-engines requires the understanding of the complex aero-thermal flow experienced in a multi-row environment. In particular, the high and low pressure turbine components have a great impact into the engine overall performance, and improvements in the turbine efficiencies can only be achieved through detailed research on the three-dimensional unsteady aerodynamics and heat transfer. The present thesis presents an experimental study of the aerothermodynamics in one and a half turbine stage, focusing on: the aero-thermal flow in the overtip region of a transonic highly loaded high pressure (HP) rotor, and the aerodynamics and heat transfer of an innovative low pressure (LP) stator with a multi-profile configuration placed downstream of the high pressure turbine, within an s-shaped duct.

Advanced instrumentation and measurement techniques were used and developed to perform the experimental investigation in a short-duration turbine test rig where both high spatial and time accuracy is indispensable. The flow field at the rotor shroud was investigated with simultaneous measurements of heat transfer, static pressure and blade tip clearance by using fast response pressure, wall temperature and capacitance probes. Through repeat experiments at the same turbine operating point, the time-averaged and time-resolved adiabatic wall temperature and convective heat transfer coefficient were evaluated.

In the frame of new engine architectures, a novel stator for a LP turbine is proposed with a multi-splitter layout that represents a new design solution towards compact, lighter and performing aero-engine turbomachinery. It contains small aero-vanes and large structural aerodynamic airfoils which are used to support the engine shaft and house service devices. The research focuses on the experimental investigation of the global performance, aerodynamics and thermodynamics of this novel HP-LP vane layout. The turbine was tested at three operating regimes depending on the pressure ratio and the rotational speed. Time-averaged and time-resolved surface pressure and heat flux measurements at the mid-section of the multi-splitter stator were used to characterize the steady and unsteady aero-thermal flow field. State-of-art CFD simulations were used to support the analysis and the understanding of the complex phenomena that characterize the flow physics and assess the efficiency of the structural LP vane at design and off-design conditions.

The goals of the research were to provide guidelines to design future aero-engines and promote the understanding of the flow physics in transonic turbine multi-row environments through analysis of the experimental data and comparison with the numerical models. The study provides an extensive experimental database to improve and validate turbomachinery CFD simulations.

Resumen

El incremento de la eficiencia y la fiabilidad de los actuales aeromotores requiere comprender el complejo flujo aero-termodinámico en presencia de varias cascadas de álabes. En particular, las turbinas de alta y baja presión tienen un gran impacto en las prestaciones globales del motor, y la mejora de las eficiencias tan sólo es posible mediante una detallada investigación aerodinámica del flujo tridimensional no estacionario y de la transferencia de calor en la turbina. La presente tesis muestra un estudio experimental de la aero-termodinámica del flujo a través de una etapa y media de turbina, concentrándose en: el flujo aero-termodinámico en la región sobre la punta del álabe de un rotor transónico de alta presión muy cargado y la aerodinámica y la transferencia de calor en un innovador estator de baja presión con una configuración multi-perfil situado aguas abajo de la turbina de alta presión, dentro de un conducto en ”S”.

Instrumentación y técnicas de medida avanzadas fueron desarrolladas y utilizadas para la investigación experimental en un banco de ensayos de corta duración para turbinas donde las resoluciones espacial y temporal son ambas indispensables. El campo fluido sobre el cárter del rotor fue investigado con medidas simultáneas de transferencia de calor, presión estática y holgura de la punta del álabe usando sondas de alta velocidad para medir presión, temperatura de pared y capacitancia. La evolución temporal de temperatura adiabática de pared y coeficiente de convección fue evaluada y promediada repitiendo los experimentos para el mismo punto de operación de la turbina.

Se propone un nuevo estátor para una turbina de baja presión con perfiles múltiples que, en el marco de la arquitectura de aeromotores de vanguardia, representa un diseño innovador para una turbomaquinaria compacta, más ligera y con más prestaciones. Está compuesto de álabes de reducido tamaño y otros más grandes con finalidad estructural que sirven para soportar el eje y alojar dispositivos auxiliares. La investigación se centra en el estudio experimental de las prestaciones globales y de las características aero-termodinámicas de la nueva configuración, teniendo en cuenta la interacción con el rotor de la turbina de alta presión. Los ensayos de la turbina se realizaron a tres regímenes de operación distintos en función de la relación de expansión y la velocidad de giro. La evolución temporal de la presión en la pared y del flujo de calor en la zona media radial del estátor multi-perfil y sus promedios temporales se utilizaron para caracterizar el flujo aero-termodinámico estacionario y no estacionario. Simulaciones CFD de vanguardia se utilizaron para fundamentar el análisis y el entendimiento de los complejos fenómenos que caracterizan el flujo y evaluar la eficiencia del estátor en condiciones tanto de diseño como fuera de diseño.

El objetivo de la investigación fue proporcionar pautas para el diseño de futuros aeromotores y fomentar la comprensión de la física del flujo transónico en turbinas con varias cascadas de álabes a través del análisis

de los datos experimentales y la comparación con los modelos computacionales. El estudio proporciona una extensiva base de datos experimental para mejorar y validar simulaciones CFD en turbomaquinaria.

Resum

El increment de l'eficiència i la fiabilitat dels actuals aeromotors requereix comprendre el complex flux aero-termodinàmic en presencia de varies cascades d'àleps. En partícula, les turbines d'alta y baixa pressió tenen un gran impacte en les prestacions globals del motor, i la millora de les eficiències tan sols es possible mitjançant una detallada investigació aerodinàmica del flux tridimensional no estacionari i de la transferència de calor en la turbina. La present tesis mostra un estudi experimental de la aero-termodinàmica del flux a través d'una etapa i mitja de turbina, concentrant-se en: el flux aero-termodinàmic en la regió sobre la punta del àlep d'un rotor transsònic d'alta pressió i molt carregat i la aerodinàmica i la transferència de calor en un innovador estator de baixa pressió amb una configuració multi-perfil situat aigües baix de la turbina d'alta pressió, dins d'un conducte en "S".

Instrumentació i tècniques de mesura avançades foren desenvolupades i utilitzades per la investigació experimental en un banc d'assajos de curta duració per turbines on les resolucions espacials i temporals son ambdós indispensables. El camp fluït sota el càrter del rotor fou investigat amb mesures simultànies de transferència de calor, pressió estàtica i folgança de la punta del àlep utilitzant sondes d'alta velocitat per mesurar pressió, temperatura de paret i capacitància. L'evolució temporal de temperatura adiabàtica de paret i coeficient de convecció fou avaluat i amitjanat repetint els experiments per al mateix punt d'operació de la turbina.

Es proposa un nou estator per una turbina de baixa pressió amb perfils múltiples que, en el marc de l'arquitectura d'aeromotors d'avantguarda, representa un disseny innovador per una turbomaquinaria compacta, més lleugera i amb més prestacions. Està compost d'àleps de reduïda grandària i altres més grans amb finalitat estructural que serveix per suportar l'eix i allotjar dispositius auxiliars. La investigació es centra en el estudi experimental de les prestacions globals i de les característiques aero-termodinàmiques de la nova configuració, tenint en conter la interacció amb el rotor de la turbina d'alta pressió. Els assajos de la turbina en van realitzar a tres règims d'operació diferents en funció de la relació d'expansió i la velocitat de gir. L'evolució temporal de la pressió en la paret i del flux de calor en la zona mitja radial del estator multi-perfil i les seues mitjanes temporals s'utilitzaren per caracteritzar el flux aero-termodinàmic estacionari i no estacionari. Simulacions CFD d'avantguarda s'utilitzaren per fonamentar l'anàlisi i l'enteniment del complexes fenòmens que caracteritzen el flux i avaluar l'eficiència del estator en condicions tant de disseny com fora de disseny. L'objectiu de la investigació fou proporcionar pautes per al disseny de futurs aeromotors i fomentar la comprensió de la física del flux transsònic en turbines amb varies cascades d'àleps a través de l'anàlisi de les dades experimentals i la comparació amb els models computacionals. El estudi proporciona una extensiva base de dades experimental per millorar i validar

simulacions CFD en turbomaquinaria.

Acknowledgements

Here comes the part of this thesis where I can thank the people who have helped and supported me during all my PhD and made it a unique great life experience.

My deepest gratitude goes to my supervisor Prof. Guillermo Paniagua. He first provided me with the opportunity to start my PhD research. He dragged me into a very exciting project and introduced me to the art of research. Over the last four years he has been to me a continuous source of motivation, advices, and inspiration. His ideas and his constant presence have guided my efforts towards the PhD goal.

Thanks are due to my promoter Prof. José María Desantes and Prof. Francisco Payri of UPV for accepting me as a doctoral student at the UPV and for their support during the PhD. I am also obliged to Prof. Tony Arts for letting me join the Turbomachinery and Propulsion Department and supporting my doctoral studies at the VKI.

A special thanks to the members of the Doctoral Jury, Prof. Antonio Torregrosa, Prof. José Galindo and, in particular, Dr. Remy Dénos, Prof. Thomas Povey and Prof. Jesús Fernández Oro for the review of this manuscript and their valuable suggestions.

I own more than a thanks to Dr. Tolga Yasa, he was the one who introduced me to the lab for the first time and had the patience to teach me all I know about experimental research. It has been a pleasure to work with him, together we carried out more than 200 turbine experiments and we shared the thrill of manually operating a rotating turbine stage.

I would also like to express my gratitude to all the TU staff, especially Pierre Londers for his help and work in the turbine lab, I have really enjoyed working with him. A very special thanks goes to Terence Boeyen and Walter Sgalbiero of the VKI workshop for the successful realization of every kind of instrumentation I needed during my experimental research. I am grateful to Julien Desset and Gérard Goossens for their technical support on the design and drawings of many of the experimental setup components. I would like to thank Ing. Johan Prinsier for his assistance and help in the use of the CFD tools and Lionel Castillon of ONERA for providing a large part of the numerical simulations used in this doctoral research.

During the four years of my PhD I have had the chance to work with many students who were enrolled in some of the VKI educational programs. While I was supposed to be an advisor for them, I truly believe it was

them who were actually supervising my work. Thanks Leticia, Jorge, Nuno, Jurij, Glauco, Simone, Francesco, Peter, Victor, and Cis. From them I have learned while receiving essential help for my research studies. Thanks to them I understand better the importance of team-work to achieve ambitious goals.

My PhD studies would have not been so great without all the friends I had the chance to meet and who made the past four years of my life cheerful and light-hearted in a unique way. A very special thanks to Pane, Pimpinotto, Don Matteo, Mick, Victor F., Bayindir, Beni, Ceyhun, Mike, Bacco, Juan Pedro, Stefano, Maxime, Jayson, Jason, Bernd, Anny, my past and actual office-mates Laura, MarcoPau, Sebastian, my right-arm in Valencia Pablo.

I am obliged to thank my family for the daily dose of love and care on which they fed their beloved grandson, son and brother in the last years far away from home.

An infinite thanks to my dear Silvia, for her passionate warm love, endless patience and genuine support during all my intense studies.

The work presented in this thesis was realized in the frame of the European Research Project TATEF-2 (”Turbine Aero-Thermal External Flows”), contract AST3-CT-2004-502924 funded by the European Community and this financial support is gratefully acknowledged.

Sergio Lavagnoli
July 2012

Contents

List of Figures

List of Tables

Nomenclature

Roman Symbols

A	area	[m^2]
C	chord	[m]
C	capacitance	[F]
c_p,c	isobaric specific heat	[Jkg^{-1}K^{-1}]
d	distance	[m]
e	airfoil thickness	[m]
f_s	sampling frequency	[Hz]
g	pitch	[m]
h	tip clearance	[m]
h_{aw}	adiabatic convective heat transfer coefficient	[Wm^{-2}K^{-1}]
H	blade height	[m]
k	thermal conductivity	[Wm^{-1}K^{-1}]
$\dot{m}$	mass flow	[kgs^{-1}]
L	length	[m]
M	Mach number	[-]
N	rotational speed	[rpm]
Nu	Nusselt number	[-]
P	pressure	[Pa]
$\dot{Q}$	heat flux	[Wm^{-2}]
R	radius	[m]
Re	Reynolds number	[-]
S	area (capacitance sensor)	[m^2]
S	curvilinear abscissa	[m]
t	time	[s]
T	temperature	[K]
Tu	turbulence intensity	[%]
U	peripheral blade speed	[ms^{-1}]
v	absolute flow speed	[ms^{-1}]
w	relative flow speed	[ms^{-1}]
y	radial position	[m]

Greek Symbols

α	yaw angle, absolute flow angle	[degrees]
α	thermal diffusivity	[m^{2}s^{-1}]

β	relative flow angle	[degrees]
γ	specific heat ratio	[-]
δ	relative flow angle (rotor frame)	[degrees]
Δ	variation, difference	[ ]
ε	permittivity	[Fm^{-1}]
ζ	kinetic loss coefficient	[-]
μ	dynamic viscosity	[Pa·s]
Π	pressure ratio	[-]
ρ	density	[kgm^{-3}]
σ	standard deviation	[ ]
Φ	flow coefficient	[-]
ϕ,φ	rotor phase	[-]
Ψ	load coefficient	[-]
ω	rotational speed	[rads^{-1}]
Ω	reduced frequency	[-]

Subscript

amb	ambient conditions
aw	adiabatic wall
ax	axial direction, turbine axis
air	air
$cool$	relative to cooling, coolant stream
f	final
gas	relative to the main flow
ini	initial
is	isentropic
$local$	local value
max	maximum value
m	mean value
$mean$	mean value
out	relative to the outlet
r	relative to the rotor
ref	reference value
s	static quantity, relative to the stator
tip	relative to tip, rotor blade tip
w,$wall$	wall, relative to the surface
0	total quantity, absolute conditions, vacuum
1	turbine stage inlet, first nozzle guide vane inlet
2	first nozzle guide vane outlet, rotor inlet
3	rotor outlet, second stator vane inlet
4	second stator vane outlet, one-and-a-half stage outlet
∞	infinite

Acronyms

AV	Aero-Vane
BPF	Blade Passage Period
CFD	Computational Fluid Dynamics
DC	Direct Current
DoR	Degree of Reaction
FFT	Fast Fourier Transform
IP	Intermediate Pressure
HL	Low Pressure
HP	High Pressure
HPR	High Pressure Rotor
HPT	High Pressure Turbine
HPV	High Pressure Vane
LE	Leading Edge
LPT	Low Pressure Turbine
LPV	Low Pressure Vane
NGV	Nozzle Guide Vane
NISRE	Non-ISentropic Simple Radial Equilibrium
PLA	Phase-Locked Average
PS	Pressure Side
RANS	Reynolds Averaged Navier-Stokes solver
S	Strut airfoil
SS	Suction Side
TC	ThermoCouple
TE	Trailing Edge
TF	Thin-Film
(20:1)	Uncertainty band at 95% confidence level
VKI	von Karman Institute for Fluid Dynamics

Chapter 1

Introduction

1.1 Research for jet engine turbines

Turbomachinery aerothermodynamics is an essential research area for energy production and propulsion. Great efforts and resources have been spent in the last decades to improve reliability and maintainability of aircraft engines with concurrent reduction of the specific fuel consumption and weight. In recent years, the interest of the gas turbine community has significantly grown towards efficient generations of civil aero-engines with limited noise pollution. A key component of modern gas turbine engines is the high-pressure (HP) turbine module, Fig. 1.1. The high-pressure turbine, located downstream of the combustion chamber, is used to power the HP compressor. This component is the most challenging part of the whole engine to be designed because of the large aerodynamic loads, blade speeds and extreme temperatures.

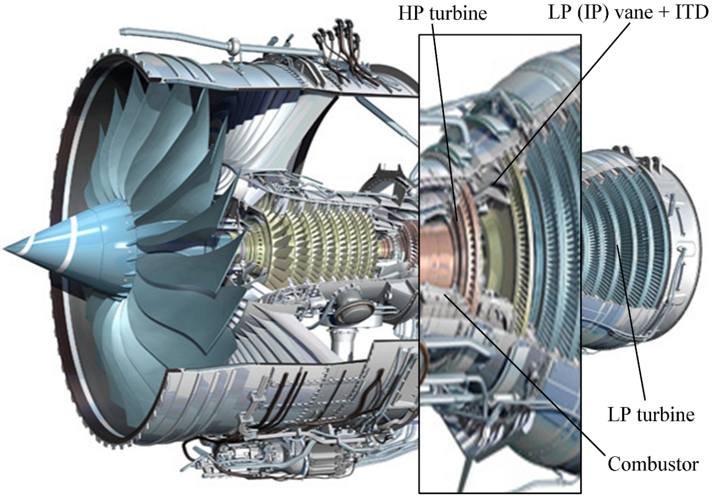

Figure 1.1: *Section view of the Rolls-Royce Trent 1000 engine (Copyright Rolls-Royce).*

The maturity of the turbine technology is illustrated by the efficiency levels in excess of 90% with limited margins for further enhancements. Therefore, improvements in turbine performance compel a thoroughly understanding of the flow in the machine environment.

Since the 1990s, aero-thermal research on HP turbines at engine-like conditions (correct Mach, Reynolds and rotational numbers; temperature ratios) has been conducted by groups in three countries:

- UK: Oxford University [1] and QinetiQ in Farnborough [2]
- USA: MIT [3], Ohio State University [4] and Wright Patterson Air Force Research Laboratory [5]
- Belgium: von Karman Institute [6]

Research on the characterization of the flow field in a single-stage transonic turbine stage may be classified according to which extent the engine environment is reproduced. Uncooled turbine geometries have been investigated in order to measure and identify shock interaction [7–9], stator-rotor potential field interaction [10, 11], viscous phenomena such as secondary flow generation [12, 13] and wake effects [14], heat transfer [15, 16].

Efficient cooling strategies are required to guarantee the airfoil integrity while operating at gas temperatures that exceed the material melting point. Hence, cooling of airfoils and disk cavities, endwalls and shrouds are important research topics. Experimental works have addressed the impact of coolant flows. Airfoil cooling has been the subject of a large number of works where the research focused on the understanding of the coolant-to-mainstream interaction and effects on both the turbine aerodynamics and cooling effectiveness [17, 18]. Cold air is ejected from the hub disk cavity to prevent hot gas ingestion and promote refrigeration of the rotor wheel and blade hub platform [19]. Public literature on this topic is scarce and only few works reported experiments on hub disk purge flows at engine-like conditions [20, 21].

The highest degree of sophistication in turbine research is achieved in a multi-component environment. The unsteady flow interactions between the high-pressure turbine and components downstream (an IP or LP turbine) or upstream (combustor) has only been recently published. Experimental studies were conducted on the effect of flow temperature distortions at the turbine inlet section that simulate the presence of an upstream combustion chamber [22, 23], hot-streaks effects on the aerodynamics and heat transfer [24, 25], hot-streak clocking [26, 27]. As modern engine design philosophy places emphasis on higher blade loading and smaller engine length, the effects of unsteady interactions in a multi-row scenario become of utmost interest for turbine designers. Research focused on the study of the stator-stator clocking effects on both the aerothermal performance of the downstream vane [28–30] and the unsteady rotor flow field [31, 32]. Additionally, a number of publications addressed the interactions within an aggressive s-shaped inter-turbine diffuser [33, 34].

The present survey on turbine aerothermal research has shown the large variety of studies and the inherent complexity of the experiments. The present work explores two different aspects of modern turbines: the unsteady heat transfer and aerodynamics of the casing overtip flow, the experimental analysis of the aerothermodynamics of an innovative low-pressure vane with a multi-airfoil geometry.

1.2 Objectives of the work

The first part of the thesis addresses the unsteady heat transfer and aerodynamics of the casing overtip flow in a high-speed shroudless HP rotor, Fig. 1.2a. The understanding of the complex flow phenomena and heat transfer occurring at the blade tip gap is of crucial importance to develop new transonic turbine designs with enhanced blade lifetime and improved thermal and aerodynamic performances. The control of the aerodynamic and the thermal loads on the rotor blade tip and rotor casing remain an extraordinary challenge. However, little experimental research has been carried out on rotor shroud flows at fully matched engine conditions because of the complexity of the required measurement hardware. The present research targets the experimental characterization of the aerodynamic and work processes in the rotor tip gap. One of the primary scopes of the work is to obtain measurements that are representative of the real engine situation where all the relevant turbine parameters are correctly reproduced. These unique data shall be used to obtain a better insight on the interaction of the tip leakage flow with the rotor blade passage and shroud. An important goal of the research is to identify the individual effects of the flow-field and the gas temperature on the heat transfer generation in the overtip region. The experimental programme also investigates the existence of correlations between the thermal and aerodynamic flow parameters with the rotor geometry, in particular the blade tip clearance size. The measurements of the tip gap flow are performed over a range of very tight tip gaps which has never been previously investigated. This will allow to obtain original observations on the aerothermodynamics of extremely narrow rotating clearances, representative of the working levels to be adopted in future aero-engine generations. The assessment of the rotor casing heat loads can be used to perform reliable thermal analysis that targets improved endwall cooling strategies and support design solutions for enhanced turbine shroud durability. The gathered experimental data should serve to propose and validate flow models for the overtip flow physics that can be used by turbine designer to predict possible scenarios related with the design of high-performance transonic blade tip sections.

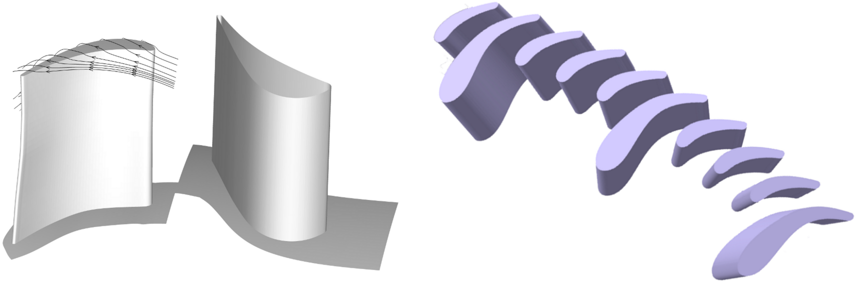

Figure 1.2: *Topics of the research work: a) view of the overtip flow on a unshrouded rotor blade and b) the multi-profile LP vane architecture*

The second part of this doctoral work is dedicated to the experimental analysis of a multi-profile vane through measurements of the steady and unsteady airfoil loads and heat transfer in a multi-row environment, Fig. 1.2b. Experimental investigation into this type of turbine vane row architecture at engine representative conditions is unprecedented, and no public literature is available on the subject. The constant improvement of engine performance must be accelerated by exploring new technologies and novel aerodynamic configurations, such as the one presented here, which must be first tested and understood in experimental facilities before being exposed to CFD research [35]. The research addresses the different aspects involved in the overall performances of the low-pressure vane component. Accurate time-average and time-resolved pressure and heat flux measurements on the stator airfoils are used to gain understanding of the complex flow physics in a one-and-half turbine stage. The main objective is to comprehend the interaction mechanisms between the LP vane and the upstream HP turbine stage and to evaluate the interference effects between the bulky pylon-like strut profile with the small conventional airfoils. The measurement of the unsteady thermal and aerodynamic fields provides valuable information on the periodic vane forces and the heat transfer pulsations in the perspective of improving high-cycle thermal and structural fatigue and noise generation. The heat transfer data also allows for detailed information on the boundary layer status on the vane airfoils. Experiments are carried out at different operating turbine regimes to analyze the behavior of the multi-splitter vane at design and off-design conditions. Additionally, one of the target of the work is to estimate the impact of the multi-airfoil architecture on the aerodynamic performance of a LP stator in comparison to conventional, single-airfoil, geometry. Overall, the present research wants to provide guidelines about the design of multi-airfoil turbine rows and assess the potential benefit of the multi-body stator configuration in a simulated engine scenario. This study is of great interest to the turbomachinery community as the multi-profile design concept could be adopted in the next generation of jet engines to increase the performances of the HP-LP turbine modules while reducing the components' size and weight [36]. Additionally, the work brings a contribution to the technical knowledge required to design compact s-shaped transition ducts with an integrated structural low-pressure vane.

1.3 Research methodology

The present dissertation reports the results of an experimental research which has lasted four years. The aerothermal flow field on a one-and-a-half turbine stage was investigated in a annular rotating short-duration facility able to mimic the real engine conditions. Two distinct test campaigns were carried out for the study of the rotor shroud flow and the aerodynamics and heat transfer of the multi-splitter LP vane.

One design and two off-design turbine operating conditions (in terms of turbine pressure ratio and rotational speed) were selected for the investigation of the LP vane performances, whereas the rotor casing flow measurements were carried out at design conditions only. Once the turbine operation points were determined, the turbine wind tunnel parameters were adjusted such as to reproduce the desired turbine conditions in terms of Reynolds and Mach number, rotational numbers and temperature ratios. The aerodynamic conditions across the turbine stage are constantly monitored during the experiments with detailed measurements of the time-average total pressure, total temperature and static pressure. The actual blade tip clearance is also measured thanks to a novel capacitance sensor located on the rotor shroud.

In the first part of the experimental programme extensive testing is carried out to characterize the aerothermal flow field on the LP vane geometry. Pneumatic transducers, fast-response pressure sensors and thin-film gauges are used to measure the steady and unsteady pressure loads and heat flux around the airfoils mid-span section using interchangeable instrumented vanes. Analysis of the LP stator performances is also supported by steady and unsteady CFD calculations.

The investigation of the rotor shroud flow is performed through simultaneous measurements of static pressure, heat flux and tip clearance at three locations around the turbine annulus. Two novel probes were manufactured and instrumented with thin-film gauges and fast-response kulite gauges to be fit into the rotor casing. The heat transfer probe was equipped with an heat exchanger that allows adjusting the temperature of the thin-film substrate prior to a turbine run. This enabled to measure the adiabatic wall temperature and convective heat transfer coefficient through repeat turbine experiments at locally different wall temperatures. The effect of the tip clearance on the aerodynamics and heat transfer of the overtip flow is also investigated by exploitation of the large blade-to-blade tip gap variations of the current rotor geometry.

The analysis of the large amount of experimental data is supported by evaluation of the measurement uncertainty. Use of CFD predictions is made to support the experimental observations and help the flow understanding.

1.4 Thesis outline

This dissertation consists of six chapters which describe the work and results of the doctoral research activity.

Chapter 1 offers a general overview of the state-of-art research on high-pressure aero-engine turbines that defines the scientific background of the present work. The main objectives of the thesis are presented and the research approach used in the investigation is briefly illustrated.

Chapter 2 describes the turbine wind tunnel and the investigated one-and-a-half turbine stage with details on the design and geometry of the HP turbine and multi-profile LP vane. The definition of the turbine operating conditions is reported here together with the final conditions experimentally measured. A short description of the CFD methodology is also provided.

Chapter 3 presents the development of accurate rotor tip clearance measurements for the transient blow-down test rig. After the description of the measurement system, the sensor calibration procedure and data processing techniques are explained. A methodology for the determination of the tip clearance uncertainty is proposed. Finally, the results of intensive turbine testing is presented and discussed.

Chapter 4 reports the description of the rotor casing flow investigation. The instrumentation elaborated for this turbine experiment is described and extensive explanations are provided on the measurement principles, dedicated data reduction procedures and uncertainty estimations. The measured time-average and time-resolved adiabatic wall temperature, convective coefficient, static pressure and tip clearance are presented and results are extensively discussed.

Chapter 5 details the outcome of the aerothermal research on the multi-body LP vane. The aerodynamic flow field is first described and steady and unsteady pressure loads and vane forces are provided. Then, the time-average and time-resolved heat transfer results are reported and commented. The aerodynamic performances of the multi-splitter LP vane are analyzed by means of CFD calculations in comparison to a conventional "single-airfoil" stator architecture.

Finally, Chapter 6 summarizes the results of this work and outlines the main conclusions.

Chapter 2

Experimental apparatus and numerical resources

2.1 The turbine test rig

The experimental investigation on the turbine stage article presented in this thesis was conducted in the compression tube facility installed at the von Karman Institute for Fluid Dynamics as depicted in Fig. 2.1.

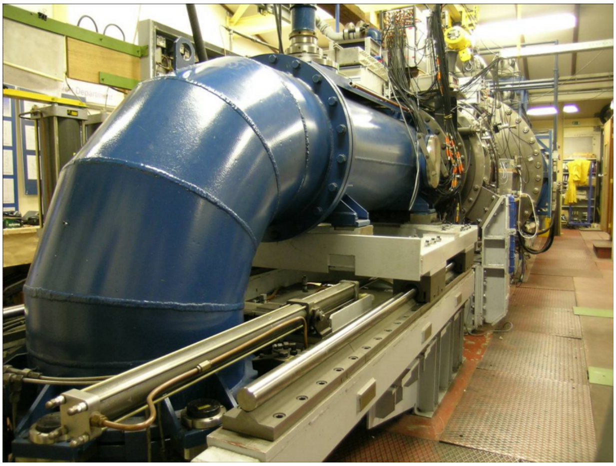

Figure 2.1: *The von Karman Institute compression tube turbine rig*

The compression tube test rig is a short-duration wind tunnel for aero-thermal testing of engine-size annular rotating turbine stages in aero-engine similarity. The turbine facility working principle is based on the concept of the *"Isentropic Light Piston Compression Tube"* which was first developed at University of Oxford in the 1970s [37, 38]. The design and construction of the von Karman Institute compression tube facility started in 1989 [39] and was completed in 1995. A detailed and comprehensive description of the turbine rig is given by Paniagua [40]. The wind tunnel consists of three main elements: the compression tube, the test section and the dump tank (Fig. 2.2). The upstream cylinder (8 m long with a diameter of 1.6 m) contains a free-moving light piston which performs the air compression.

The test section that contains the research turbine is located in between the two reservoirs. A fast opening shutter valve separates the compression cylinder from the test section which is connected to the vacuum tank via an adjustable sonic throat.

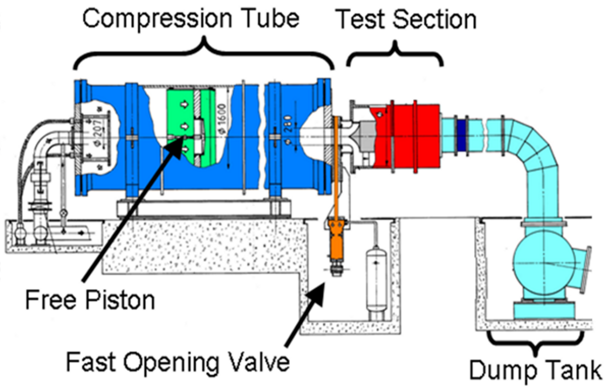

Figure 2.2: *Sketch of the rotating annular turbine facility*

In a typical test cycle, the shutter valve is initially closed and the test section and the dump tank are evacuated to vacuum, about 30 mbar absolute pressure. The piston is at the rear part of the cylinder which is set to an initial pressure P_{ini} at ambient temperature T_{amb}. The turbine rotor is spun up to nearly its design speed by an auxiliary power turbine. In order to start a blow-down, cold high-pressure air is injected in the back of the cylinder through sonic throats that regulate the injected mass flow. The piston starts traveling along the tube driven by the gas entering from the back, and thereby compresses the gas initially in the tube in a quasi-isentropic fashion to the desired final pressure P_f. Adjustment of the initial pressure level in the compression tube (P_{ini}) allows setting the desired turbine inlet total temperature according to:

$$T_f = T_{ini}\left(\frac{P_f}{P_{ini}}\right)^{\frac{\gamma-1}{\gamma}} \tag{2.1}$$

Once the specified tube pressure is reached P_f, the shutter valve quickly opens (~70 ms) and lets the pressurized and heated gas to discharge into the test section.

A blow-down of hot gas takes place over the cold turbine stage initially at ambient temperature. As a consequence of the work exchange with the high enthalpy flow, the rotor accelerates throughout the test since there is no break device that can absorb the delivered net power. The turbine pressure ratio is controlled by a variable sonic throat. The opening of the sonic valve is adjusted prior to a test such that the volumetric flow rate entering at the back of the compression tube matches the volumetric flow rate through the test section. This ensures that the aero-thermal parameters are maintained constant during the blow-down. The degree of reaction of the turbine imposes the nozzle guide vane exit Mach number. Once the piston reaches the end of the cylinder or the throttle valve becomes unchoked due to the filling of the dump tank, the test gas conditions are not anymore constant. This condition corresponds to the end of the test.

Fig. 2.3 shows the evolution of the main turbine parameters during a typical wind tunnel run. After the opening of the shutter valve at time 0 s, the turbine inlet total temperature (T_{01}) and pressure (P_{01}) steeply rise up to their nominal test values in about 100 ms. The pressure losses in the settling chamber mitigate the pressure fluctuations at the turbine inlet (P_{01}) and outlet (P_{s3}), which assume a step-like shape during the wind tunnel blow-down start-up. On the other hand, the sudden release of gas into the test section induces a large temperature peak at the beginning of the transient which is recorded by both the turbine inlet and outlet temperature sensors. Once the inlet turbine flow is stabilized, the correct aerodynamic conditions exist in the test section for about 200-300 ms.

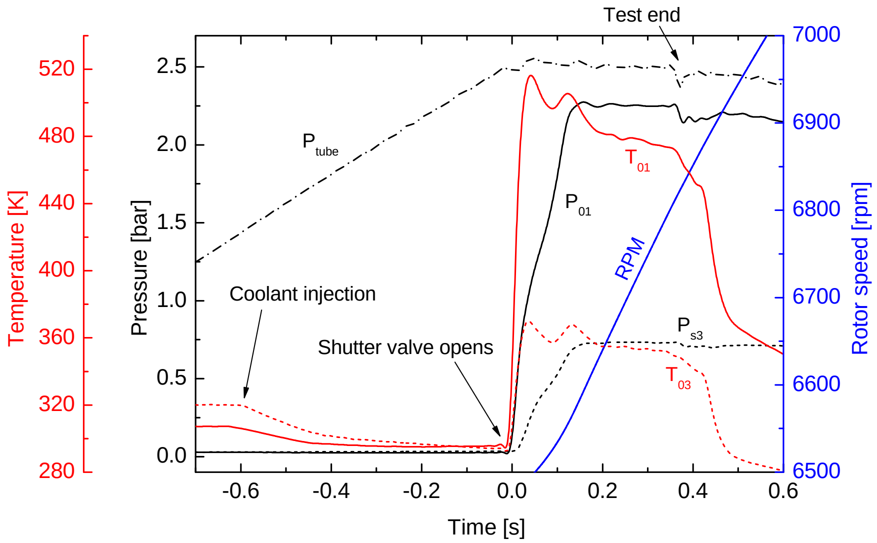

Figure 2.3: *Typical evolution of the turbine parameters during a blow-down test*

A detailed view of the test section is provided in Fig. 2.4. Upstream of the nozzle guide vane an inlet contraction reproduces the outlet geometry of a combustion chamber to simulate the real engine configuration.

The wind tunnel is also equipped with a coolant supply system that provides "cold" air at ambient temperature into the test section. The coolant release starts some time before the blow-down takes place (typically 0.5-0.8 s before the vent hole opening) and its effect is measured by temperature probes downstream of the turbine stage (T_{03}) in Fig. 2.3. In order to halve the rotor acceleration during the "flow-on" phase, an inertia wheel is installed behind the rotor disk to increase the rotating assembly total inertia from 9.7 kgm^2 up to 17.8 kgm^2 [41]. At the test end the rotor starts decelerating because of ventilation losses, and an aero-brake is activated to rapidly decelerate the rotor disk to rest in only 2-3 minutes. The von Karman Institute turbine rig is the world's largest short-duration isentropic light piston facility. The test section is designed to install turbine blade rows with a tip diameter of nearly 800 mm. In the configuration adopted for the present experimental research reported in this thesis the test section was modified to accommodate a novel low-pressure (LP) stator vane component with a maximum outer diameter of about 930 mm, Fig. 2.4.

This wind tunnel provides a fully-scaled environment for testing large-scale turbine components in engine-like conditions. Reynolds and Mach numbers can be adjusted independently. The transient character of the experiments allows reproducing and measuring the convective heat transfer processes of the hot engine operation preserving the gas-to-wall and gas-to-coolant temperature ratios found in modern aero-engines. Table 2.1 lists the main turbine parameters reproduced in the the von Karman Institute turbine test rig compared to the real engine conditions.

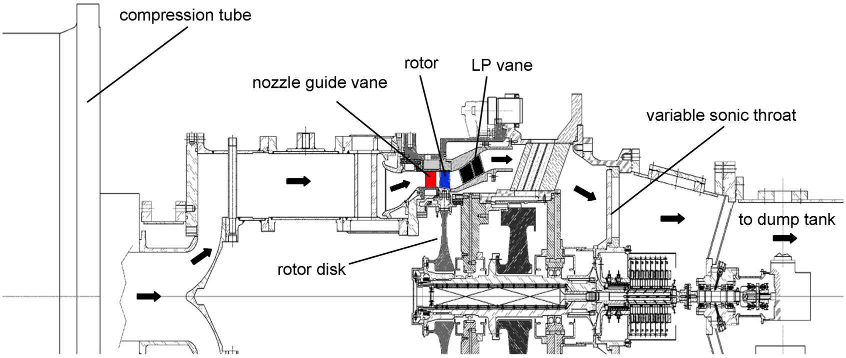

Figure 2.4: *Meridional cut view of the turbine test section*

2.2 The 1.5 turbine stage

The tested turbine module is composed of a high pressure stage and a low pressure vane. The test section was adapted to include a s-shape diffuser which links the HP stage to the downstream second stator. The LP stator

TURBINE PARAMETER	AERO-ENGINE	WIND TUNNEL
Stage pressure ratio	2 – 5	2 – 5
$\mathrm{M}_{\mathrm{vane,exit}}$	transonic	transonic
$\mathrm{Re}_{\mathrm{vane,exit}}$	$1 - 3 \times 10^6$	$1 - 3 \times 10^6$
Inlet total flow temperature	1700 – 2100 K	400 – 500 K
Coolant flow temperature	850 K	285 K
Blade wall temperature	1200 – 1400 K	295 K
$\mathrm{T}_{\mathrm{coolant}}/\mathrm{T}_{\mathrm{gas}}$	0.5 – 0.6	0.6
$\mathrm{T}_{\mathrm{wall}}/\mathrm{T}_{\mathrm{gas}}$	0.6 – 0.7	0.6 – 0.7

Table 2.1: *Aero-thermal scaling in the turbine rig*

was placed within the duct. A meridional view of the test section that contains the one and a half turbine stage is given in Fig. 2.5.

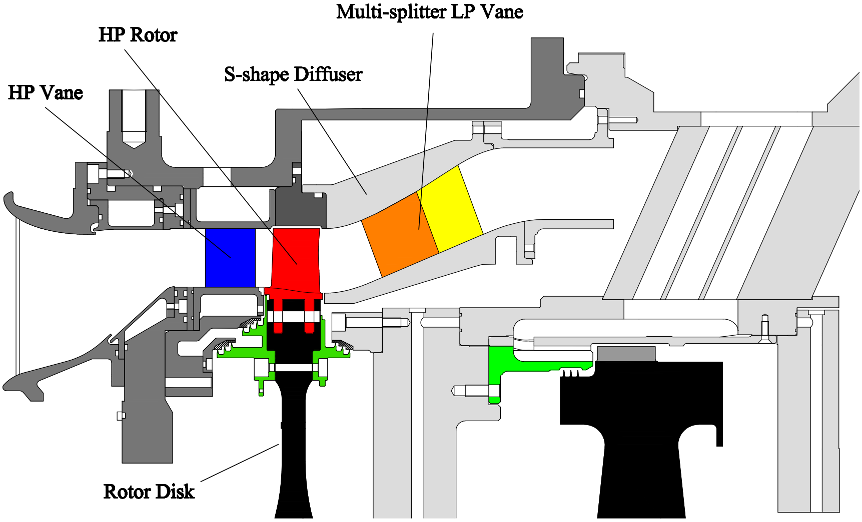

Figure 2.5: *Detailed view of the 1.5 turbine stage*

2.2.1 The high pressure turbine stage

The single-stage HP turbine stage is representative of advanced aero-engines. The nozzle guide vane and the rotor rows were designed in the early 1990s by Fiat Avio. The nozzle guide vane is composed of 43 airfoils. It was designed for an axial inlet flow and a Reynolds number of $1{\times}10^6$ to provide a flow turning of 73 degrees and a transonic outlet flow. The stator has a low aspect ratio (H/C=0.70) that limits the secondary flow generation. For the current experimental work the stator stagger angle was 51.9 degrees. The 3D vane geometry is a cylindrical airfoil resulting from radial stacking of the 2D mid-section profile (Fig. 2.6a). The stacking line of the vane number 01 corresponds to the vertical axis of the machine and is taken as a reference for all the measurements. The vane is equipped with a cooling slot along the airfoil for coolant ejection from the pressure side near the trailing edge. A detail of the cooling slot geometry is given in Fig. 2.6b.

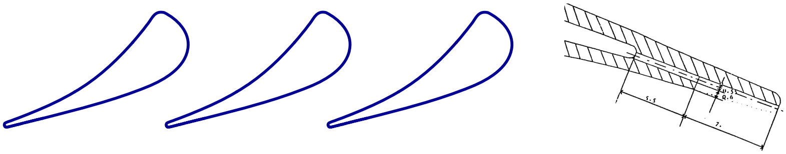

(a) **(b)**

Figure 2.6: *HP nozzle guide vane: a) 2D vane geometry and b) detail of the trailing edge configuration for pressure side coolant ejection*

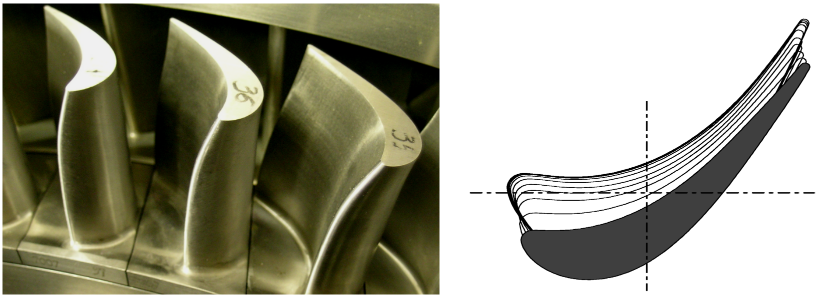

(a) **(b)**

Figure 2.7: *HP rotor row: a) picture of the rotor blades and b) rotor stacking along the blade span*

The rotor row was designed based on the HP vane outlet flow and considering an outlet Reynolds number of 0.5×10^6. The rotor counts 64 twisted unshrouded blades. Fig. 2.7a displays a picture of the rotor blades installed in the turbine rig. The rotor blade count resulted from a trade-off between numerical efforts for the unsteady Navier-Stokes calculations of the turbine stage, minimization of the secondary flows, and an adequate minimum TE thickness. The rotor has a pitch-to-chord ratio of 0.75, an aspect ratio of 1.05 and a TE thickness of 1.02 mm. The blade count ratio is ~2/3. The blade profiles are radially stacked with a negative bowing in order to unload the tip sections (Fig. 2.7b). Endwall contouring is used to reduce the rotor exit speed through an increment of the blade channel height by ~10% in the axial direction as shown in Fig. 2.5. The stator-rotor axial gap is 38% of the HP stator axial chord. The rotor tip clearance was measured by means of wear gauges and a capacitance-based proximity probe during the experimental campaign. An extensive discussion of the tip clearance results is provided in chapter 3. A summary of the HP turbine stage characteristics is reported in Table 2.2.

		HP VANE			HP ROTOR		
Blade count		43			64		
H/C		0.70			1.05		
g/C		0.75			0.75		
R_{tip}/R_{hub}		0.872			0.868		
H (inlet/outlet)	[mm]	50.70 / 50.70			51.97 / 55.81		
		hub	*mid-span*	*tip*	*hub*	*mid-span*	*tip*
Chord	[mm]	72.00	72.00	72.00	50.74	48.23	49.75
Axial chord	[mm]	43.07	43.07	43.07	41.84	39.78	40.04
Pitch	[mm]	50.34	54.04	57.75	33.76	36.28	38.80
Throat	[mm]	13.64	15.36	17.07	13.00	14.54	19.50
Inlet radius	[mm]	344.50	369.85	395.20	343.23	369.50	395.20
Outlet radius	[mm]	344.50	369.85	395.20	339.39	367.30	395.20

Table 2.2: *Design characteristics of the HP turbine stage*

2.2.2 The multi-splitter low pressure vane

In the frame of new engine architectures, an innovative stator for the LP turbine was proposed with a multi-splitter configuration (Fig. 2.8a). The struts were re-designed from an aerodynamic point of view and included in the LP vane together with small aero-vanes. The LP vane was placed inside an S-shaped transition duct similar to those adopted in modern engine designs. Fig. 2.8b shows a 3D view of the LP vane downstream of the HP turbine stage.

The LP vane was designed by Snecma Moteurs in the frame of the European Project TATEF2 (Turbine Aero-Thermal External Flows 2). Details on the design methodology can be found in [42]. The design of the stator row and of the transition duct were optimized iteratively through combined use of mono-dimensional analysis, meridional flow calculations and 3D Navier-Stokes simulations.

The LP vane is composed of 16 large aerodynamic struts (structural vanes) and 48 smaller airfoils (aero-vanes), arranged in a multi-splitter configuration. The aerodynamic design of the stator was based on the HP turbine outlet flow conditions, namely an absolute Mach number of 0.43 and a flow

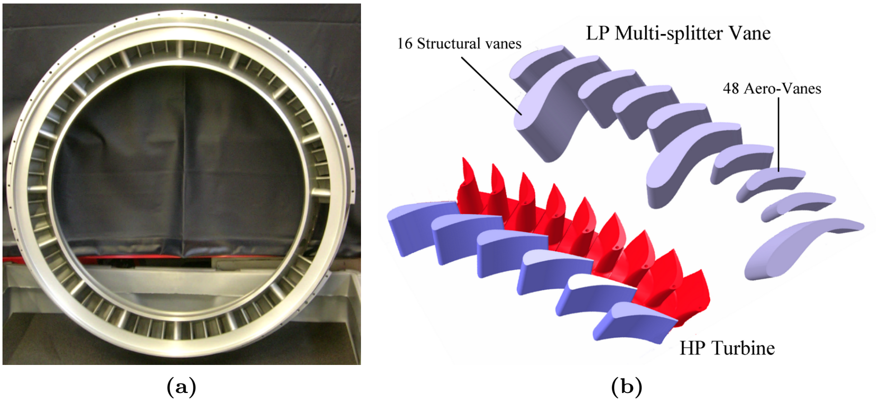

(a) (b)

Figure 2.8: *The multi-splitter LP vane: a) picture of the LP vane module and b) installation downstream of the HP turbine stage*

angle of -13 degrees at mid-span with radial distributions of total temperature, pressure and flow angle available from previous measurements of the rotor outlet flow. The LP vane outlet conditions were chosen such as the exit flow angle is +60 degrees with an exit Mach number of 0.7, representative of typical engine conditions. The selected outlet flow angle corresponded to a co-rotative turbine configuration which provides a flow turning of ~70 degrees. Three small aero-vanes are located in every large structural airfoil pitch. Furthermore, the selected vane count ratio offers the best compromise between costs and measurement efforts. The resulting four vane passages were designed identical in an attempt to maintain the same mass flow distribution at the stator outlet, guarantee uniform flow conditions, and limit the the stator vibrations in a multi-profile configuration. The rear part of each profile was designed identical with the same pitch as shown in Fig. 2.9a. The 3D geometry of the four airfoils was obtained by stacking the same 2D profile along a straight line. The small aero-vanes were designed identical to ease the vane instrumentation and simplify the manufacturing (Fig. 2.9b). The large maximum blade thickness for the strut vanes is imposed by the design objectives. The maximum strut thickness (e_{max}) was selected to be 20 mm, representative of minimum values required by mechanical reasons since these bulky struts are used to support the engine case and to house service devices and lubrication pipes. In order to maintain the profile losses at an acceptable level, the ratio between the maximum thickness and the chord (e_{max}/C) is limited to 0.2 for the structural airfoil. For similar profile loss concerns, the pitch to chord ratio (g/C) of the small aerodynamic airfoil is also limited. The aspect ratio (H/C) results from a compromise between secondary flow minimization and flow diffusion through the vane channels (small vane height). The main geometric characteristics of the low pressure vane are reported in Table 2.3.

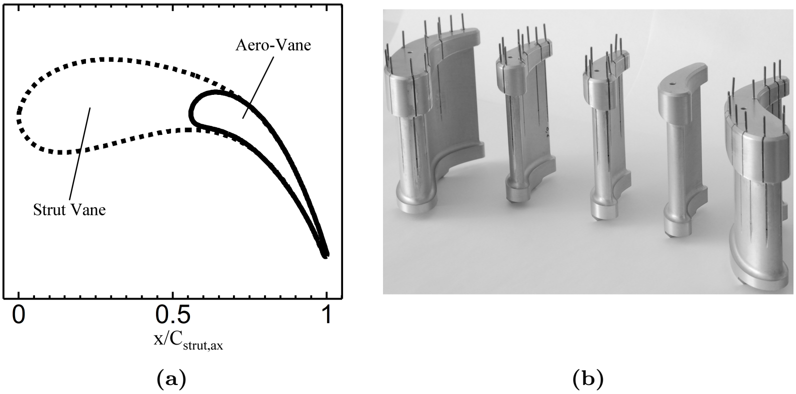

(a) (b)

Figure 2.9: *The airfoils of the multi-profile LP vane: a) Comparison of the strut and aero-vane profiles and b) picture of the four airfoils in multi-splitter vane configuration*

The geometry of the transition diffuser was selected to be representative of modern engine configurations, with a relatively aggressive mean hade angle of 30 degrees. In order to guarantee an optimal diffusion rate in the duct and avoid boundary layer separation, the slope of the tip endwall was reduced to 26 degrees in the front part (where the flow turning is still limited), and increased to 32 degrees in the rear part. The geometric characteristics of the s-shaped transition duct are listed in Table 2.4. The location of the strut leading edge in the duct was selected according to the maximum airfoil thickness to limit the interaction with the upstream turbine rows. The position of the LP stator with respect to the HP turbine is reported in Table 2.5.

2.3 Turbine operating conditions

2.3.1 Design of the turbine operative conditions

The scope of this investigation was to study the interaction phenomena occurring between the three blade rows and assess the aero-thermal performance of the multi-splitter low pressure vane. The initial target was to investigate the one and a half turbine stage at two operating regimes by varying the HP turbine total-to-static pressure ratio, i.e., the flow speed, at

LP MULTI-SPLITTER VANE

		Structural Airfoil			Aero-Vane Airfoil		
Vane count		16			48		
Chord*	[mm]	99.0			51.8		
Axial chord*	[mm]	95.4			41.9		
Stagger angle	[deg]	15.6			36.0		
e_{max}	[mm]	20.00			8.75		
e_{max}/C		0.20			0.17		
H (Inlet/Outlet)	[mm]	52.56 / 63.85			56.76 / 63.85		
H/C (Inlet/Outlet)		0.53 / 0.64			1.10 / 1.23		
		hub	*mid-span*	*tip*	*hub*	*mid-span*	*tip*
Inlet radius	[mm]	353.0	377.7	402.3	373.9	400.5	427.2
Outlet radius	[mm]	390.3	420.2	450.2	390.3	420.2	450.2
Pitch (inlet)	[mm]	138.6	148.3	158.0	36.7	39.3	41.9
g/C (inlet)		1.40	1.50	1.60	0.71	0.76	0.81

*Evaluated along a streamline

Table 2.3: *Geometric characteristics of the multi-splitter LP vane*

S-SHAPE DUCT

Area Ratio (A_{out}/A_{in})		1.3
Axial Length	[mm]	189
L/H		3
Hade angle - tip	[deg]	26 - 32
Hade angle - hub	[deg]	30

Table 2.4: *Inter-turbine diffuser characteristics*

Axial gap TE HPV - LE HPR	$0.38\times C_{st1,ax}$
Axial gap TE HPR - LE strut LPV	$1.15\times C_{r,ax}$
Axial gap TE HPR - LE aero-vane LPV	$1.56\times C_{r,ax}$

Table 2.5: *Blade rows distances at mid-span*

fixed inlet flow and rotor speed. The design pressure ratio was selected such that the HP stator was choked and transonic, while the rotor flow remained highly subsonic with limited excursions into the transonic regime (NOM P/p). Thus, the turbine flow was characterized by both viscous and shock wave interactions. The effect of the flow speed was studied by reducing the stage pressure ratio to a lower value than for the nominal condition, which provided fully subsonic flow across the turbine where the viscous effects and the secondary flow are expected to be predominant (LOW P/p). One of the main target of the present experimental investigation is the measurement of the heat transfer onto the LP vane airfoils. A sufficient temperature difference must exist between the hot flow gas and the cold vane surfaces to accurately determine the wall heat flux, and respect the gas-to-wall temperature ratio found in a real engine environment. Therefore, the turbine inlet total temperature has been set to 480 K to account for the total temperature drop across the rotor due to work extraction, and achieve a total temperature of 350-360 K at the LP stator inlet for the highest pressure ratio. Consequently, the inlet total pressure and the design rotor speed have been set respectively to 2.23 bar and 6790 rpm in order to preserve the correct similarity with engine conditions in terms of Reynolds number and mechanical speed ($N/\sqrt{T_{01}}$). Cooling was adopted during the experiments with coolant mass flow ejection (3% of the overall mass flow) through the HP stator trailing edge.

The design of the test conditions was carried out by means of through-flow calculations of the single stage HP turbine that yielded detailed information on the stage flow characteristics. The design test conditions are summarized in Table 2.6 where the velocities, pressures and temperatures of the stage are presented together with the main turbine working parameters. At off-design condition (LOW P/p - 6790 rpm), the inlet flow angle for the LP vane changes drastically. Such large flow angle variation was expected to have a detrimental effect on the LP vane aerodynamics since the flow approaches the structural vane airfoil with a significant negative incidence. Therefore, a third test condition was selected to correct the rotor outlet flow angle at low pressure ratio by reducing the rotational speed down to 4500 rpm (LOW P/p - LOW speed). Fig. 2.10 illustrates the velocity triangles at mid-span for the three turbine operating regimes.

It is important to note that the design of the experimental test conditions presented above is solely based on the aerodynamics of the HP turbine stage, and the effect of the LP multi-splitter vane and of the transition duct is neglected.

However, as the turbine pressure ratio increases, the flow speed at the turbine outlet and through the downstream stator raises, and once the second stator flow becomes choked, the turbine back pressure cannot be further reduced. Hence, there was a limit to the HP turbine pressure ratio that could be attained in the current experimental setup, which depended on the capacity of the second stator.

		NOM P/p - NOM speed			LOW P/p - NOM speed			LOW P/p - LOW speed		
		hub	*mid*	*tip*	*hub*	*mid*	*tip*	*hub*	*mid*	*tip*
Turbine inlet										
P_0	[bar]		2.23			2.23			2.23	
T_0	[K]		480.0			480.0			480.0	
M_0	[-]		0.17			0.17			0.17	
α	[deg]		0.0			0.0			0.0	
Vane outlet										
P_0	[bar]		2.22			2.22			2.22	
V	[ms^{-1}]	447.5	422.8	400.8	371.4	350.8	332.6	414.0	391.1	370.8
M_0	[-]	1.14	1.06	1.00	0.91	0.85	0.80	1.04	0.97	0.91
α	[deg]	72.7	72.4	72.1	73.0	72.4	71.9	72.9	72.5	72.1
Rotor inlet										
P_{0r}	[bar]	1.23	1.27	1.31	1.43	1.47	1.52	1.50	1.52	1.54
T_{0r}	[K]	405.5	409.1	413.0	423.2	427.0	431.0	429.0	430.5	432.2
W	[ms^{-1}]	224.1	189.5	160.3	153.4	127.8	109.6	262.0	230.9	202.9
M_r	[-]	0.57	0.48	0.40	0.38	0.31	0.26	0.66	0.57	0.50
β	[deg]	53.5	47.6	39.7	44.8	34.0	19.8	62.3	59.4	55.9
Rotor outlet										
P_{0r}	[bar]	1.20	1.25	1.29	1.41	1.46	1.51	1.42	1.48	1.51
W	[ms^{-1}]	315.2	328.3	340.9	218.3	234.9	250.9	222.0	242.9	251.7
M_r	[-]	0.83	0.87	0.90	0.54	0.59	0.63	0.55	0.60	0.63
β	[deg]	62.7	62.2	56.4	62.5	61.7	55.6	62.5	61.8	55.6
Turbine outlet										
P_0	[bar]	0.85	0.86	0.91	1.22	1.24	1.29	1.219	1.237	1.269
T_0	[K]	367.2	367.7	373.0	405.8	407.2	412.3	410.3	408.6	411.0
V	[ms^{-1}]	149.2	156.1	188.6	112.4	123.7	158.9	108.4	122.0	144.0
M_0	[-]	0.39	0.41	0.50	0.28	0.31	0.40	0.27	0.30	0.36
α	[deg]	14.2	10.7	1.6	-26.3	-26.0	-26.9	19.2	19.6	9.2
Turbine parameters										
Π	[-]		2.92			1.92			1.92	
ω	[rpm]		6790			6790			4500	
$\dot{m}$	[kgs^{-1}]		13.6			13.4			13.6	
Power	[MW]		1.51			0.98			0.97	
Re_{vane}	[-]		1.3×10^6			1.2×10^6			1.3×10^6	
Re_{rotor}	[-]		5.5×10^5			4.9×10^5			5.0×10^5	
Φ	[-]		0.49			0.40			0.67	
Ψ	[-]		1.79			1.16			2.58	
DoR_{ms}	[-]		0.29			0.32			0.319	
Ω_r	[-]		1.52			1.83			1.09	

Table 2.6: *Turbine flow by NISRE calculation for the three operating conditions*

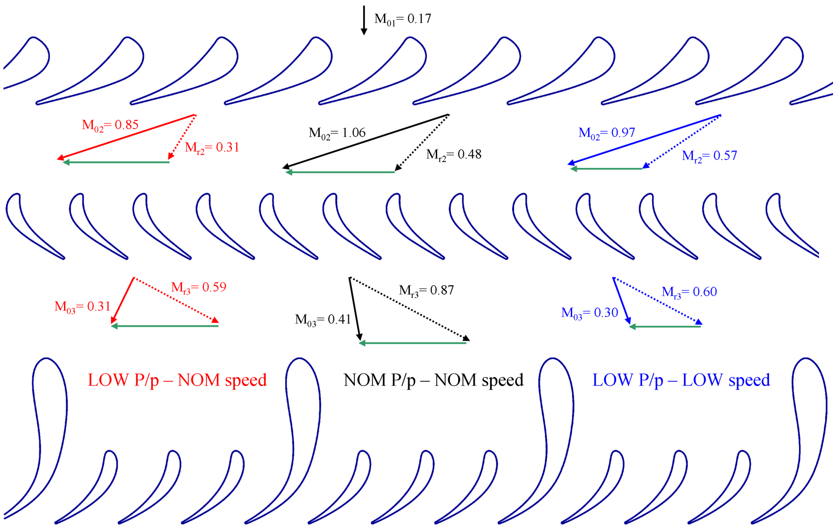

Figure 2.10: *HP turbine velocity triangles for the three operating conditions*

A simple theoretical investigation was carried out to assess the coupling between the turbine and the second stator flow fields. Based on the predictions of the through-flow solver of the single-stage turbine, the variation of the turbine velocities with the total-to-static pressure ratio was represented in Fig. 2.11. The turbine is choked for a pressure ratio of about 2.4, when the HP vane outlet Mach number reaches unity. At higher pressure ratios, the relative rotor exit speed keeps increasing monotonically while the HP vane outlet velocity remains nearly constant once the rotor chokes at a pressure ratio of ~3.3. The flow characteristics at the second stator inlet are estimated by means of a mono-dimensional analysis based on the the rotor outlet Mach number, flow angle, and the second stator geometry. The variation of flow speed and angle through the duct from the rotor exit to the LP vane inlet plane is calculated by applying the conservation of mass flow and angular momentum along a streamline located at the channel mid radius.

Downstream of the strut leading edge the flow is assumed to enter the aero-vane passages with no swirl component, independently of the turbine outlet flow angle since the strut airfoils guide the flow through the passage and redirect it towards axial direction. Mass flow conservation between the LP vane entrance and the aero-vane leading edge yields the flow Mach number at the aero-vane inlet. The radial velocity and angle distribution at the turbine exit and the effect of the duct curvature have been neglected in the present model. No pressure losses have been assumed along the duct and in the stator row.

The condition that limits the pressure ratio at the turbine outlet is the choking of the second stator. As the flow velocity reaches the unity at the stator sonic throat, the aero-vane inlet flow speed must remain below a certain value such that the flow can smoothly accelerate through the vane passage up to the geometric throat. Assuming a one-dimensional isentropic expansion of a perfect compressible fluid through a duct of varying area, the Mach number at a certain section along the aero-vane channel is only a function of the considered section area and the critical area of the passage throat (minimum area, M=1):

$$\frac{A(x)}{A^*} = \frac{1}{M(x)}\left[\frac{2}{\gamma+1}\left(1+\frac{\gamma-1}{2}M^2(x)\right)\right]^{\frac{\gamma+1}{2(\gamma-1)}} \tag{2.2}$$

Eq. 2.2 is used to compute the highest Mach number allowed at the aero-vane inlet section when the second stator is choked. The maximum inlet Mach number is compared with predictions of the flow Mach number normal to the aero-vane inlet section as a function of the turbine pressure ratio. The results of the model predictions are shown in Fig. 2.11. Raising the turbine pressure ratio causes the rotor outlet speed and the meridional Mach number to increase at the aero-vane entry plane. At a pressure ratio of about 3.1, the inlet meridional Mach number exceeds the theoretical limit of 0.37 and the LP vane is choked. Therefore, any further increment in pressure ratio is shown to be theoretically incompatible with the LP vane geometry. The model prediction was actually proved accurate by experiments in the turbine wind tunnel where turbine pressure ratios above 2.95-3.0 could not be finally attained. Therefore, the turbine hardware could not be tested at operative regimes where the rotor outlet flow would be fully supersonic.

2.3.2 Experimental test conditions

The turbine operation was controlled through measurements of the flow conditions in the fixed frame of reference at four axial planes in the test section. Due to the blow-down principle of the short-duration test rig, the instrumentation has been designed to operate with frequency responses ranging between 50 Hz and 500 Hz in order to capture the transient flow variations and measure accurately the quasi-steady performance of the turbine. This section reports only information on the instrumentation used to monitor the turbine operating conditions, whereas a detailed description of the measurement techniques employed for the characterization of the LP multi-splitter vane aero-thermal performances and of the overtip rotor casing flow field is provided in the next chapters.

Fig. 2.12 sketches the location along the machine axis of the measurement planes that are identified with a terminology that will be used in the entire thesis. Plane 01 is positioned at the turbine inlet, $0.66\times C_{\mathrm{HPV,ax}}$ upstream

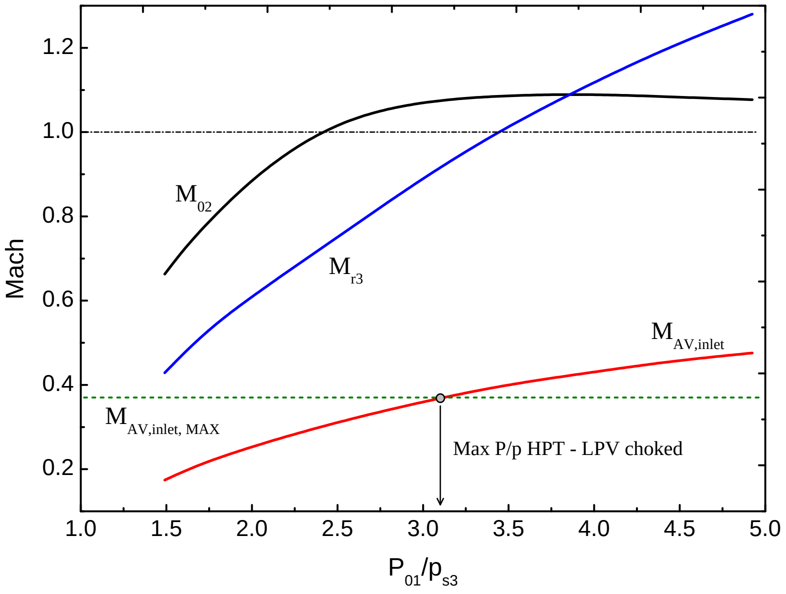

Figure 2.11: *HP turbine flow as a function of the stage pressure ratio (stand-alone configuration) and prediction of the turbine pressure ratio limit (1.5 turbine stage configuration)*

of the nozzle guide vane leading edge. Total pressure and total temperature measurements were carried out at the turbine inlet by means of kiel pneumatic pressure probes and thermocouples. Two reference probes that are equipped with a kiel head pitot probe and a thermocouple sensor were placed at mid-span at two pitch-wise locations in correspondence of the stacking axis of the inlet guide vane (Fig. 2.12). The inlet plane was also instrumented with a 4-head pitot probe and a rake of 4 thermocouples to obtain radial distributions of the total pressure and total temperature. Plane 02 corresponds to the inter-row spacing between the first stator and the rotor and is located $0.035\times C_{\mathrm{HPV,ax}}$ downstream of the first stator trailing edge. No probe was installed in the free-stream flow at this location due to the narrow space available and the risk of high blockage as the stator outlet flow is transonic. The static pressure was measured at the hub and tip endwalls with pneumatic lines and sub-surface mounted fast-response pressure sensors alternately and equally spaced. Ten pressure taps are distributed across one vane pitch as shown in Fig. 2.12. The inlet and exit flow field of the LP vane were monitored in plane 03 and plane 04. The measurement planes are respectively located $0.29\times C_{\mathrm{strut,ax}}$ upstream of the strut vane leading edge (i.e., $0.45\times C_{\mathrm{r,ax}}$ downstream of the rotor trailing edge) and $0.25\times C_{\mathrm{strut,ax}}$ downstream of the aero-vane trailing edge at mid-span. In these planes the total pressure and total temperature were monitored at 50% span with two reference probes and the static pressure was measured at the tip and hub endwalls with two rows of 9 pneumatic taps that cover one full structural vane pitch in two distinct sectors 90 degrees apart. A cross-rake pitot probe with 9 kiel heads was located downstream of the second stator vane at a fixed position.

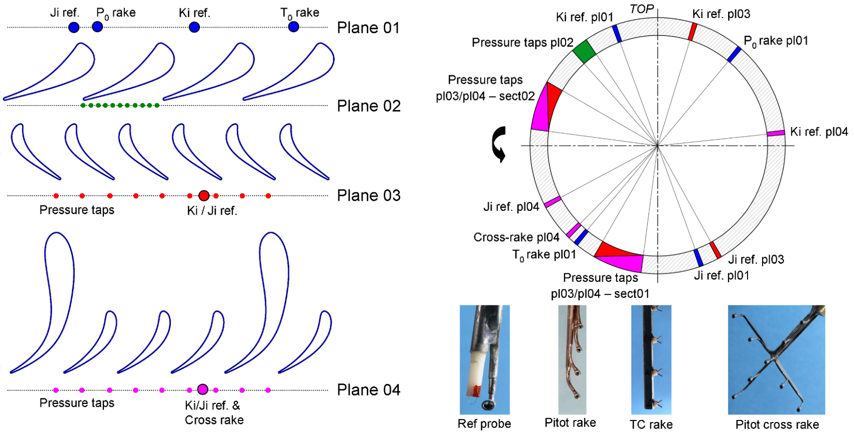

Figure 2.12: *Test section measurement planes and instrumentation for monitoring the turbine operating conditions*

The steady pressure measurements were carried out by means of relative pressure sensors, inexpensive piezo-resistive Sensym 240-PC-006D sensors accurate to 0.1% of the full span, i.e., around ±2.5 mbar (20:1). Total pressure was measured with Kiel head pitot probes. The Kiel head is a vented cylinder that surrounds the pitot tube and serves to improve the dynamic pressure recovery and minimize the probe sensitivity to angle variations. Although the use of the kiel head, the total pressure probes may still lack the recovery of few tenths of a millibar. Pressure taps were drilled normal to the surface wall with a small diameter of 0.8 mm that provides a good compromise between sensor response time, measurement spatial resolution and accuracy. The path and length of the pneumatic lines which connect the measurement points to the transducers outside of the wind tunnel were optimized in order to ensure an acceptable time response for the low-frequency pressure measurements. The pressure gage calibration was performed in-situ by sampling the transducer voltage output in the facility test section prior to each turbine run at vacuum and atmospheric conditions.

The total temperature probes were equipped with thermocouple sensors. Thermocouples are active sensors based on the *Seebeck* effect in which two metal wires of different material are connected at a junction point. A net voltage is generated at the wire extremities that is proportional to the temperature difference between the junction and the two wire ends. For the current research, thermocouple type K (chromel-alumel) were used with a design junction diameter of 25-50 μm for the reference probes and 90 μm for the thermocouple rake. The temperature probe design was specifically suited for accurate temperature measurements in transient wind tunnels and high-speed flows (Paniagua, [40]). Thermocouples were calibrated in a controlled stirred oil bath referenced to a precision mercury thermometer. The thermocouples' readings are compensated for the velocity error through the use of a recovery factor which is function of the flow speed. Once the recovery factor (r) and the flow speed (Mach number) are known, the actual gas temperature can be computed according to the following equation:

$$T_{junction} = T_0 \left[1 - (1-r) \frac{(\gamma - 1) M^2}{2 + (\gamma - 1) M^2} \right] \tag{2.3}$$

The velocity error at the stage inlet is about 1 K, while it raises up to 4-5 K at at the turbine exit and up to 10-12 K at the LP stator outlet where the flow speeds are higher. The overall uncertainty on the total temperature measurements is estimated to be about ±1.0 K, though the measurement repeatability is typically higher (±2 K) due to test-to-test variations and gas temperature fluctuations inside the turbine rig.

The rotor speed and the rotor acceleration were measured by means of a high-frequency infrared photodiode facing a rotor disk system which delivers 126 pulses per rotor revolution [43]. In addition to the photodiode tachometer, the signal of the newly installed capacitance-based tip clearance probe were used to evaluate the turbine rotational speed and acceleration.

The time-average temperature and pressure data in a turbine test were sampled at 1.5 kHz for a duration of 6 s which covers the whole gas blowdown event and starts 3 s before the opening of the shutter valve which provides the trigger event for the acquisition (Fig. 2.3). The experimental data are averaged over a time window of 40 ms just before the end of the test. During this time the turbine inlet total temperature and pressure remain constant and the rotor speed is within its design value.

In order to reduce the uncertainty on the measurements of the turbine operating conditions at the control planes, the flow pressure and temperature result were area-averaged from the different circumferential locations. The stage inlet total temperature and total pressure resulted from the average of the two reference probes' readings and the measurements of the two mid-heads of the rake probes. The static pressure at the hub and tip endwalls in planes 02, 03 and 04 was the average of the pitch-wise distribution across a vane pitch. At the HP stage exit and at the LP vane outlet the total temperature and pressure resulted from the average of the reference probes' readings. The flow Mach number was estimated via the average of the hub and tip endwall static pressure and the total pressure readings at mid-span.

The experimental mean values that define the turbine operating conditions are reported in Table 2.7. The measurement repeatability was estimated with a confidence level of 95% expressed as a percentage of the mean value. The measurement uncertainty on a single measurement was generally smaller than the test-to-test variability. Levels of pressure, temperature and flow speed at the LP vane inlet and outlet planes are reported in Table 2.8.

Condition	P_{01} [bar]	T_{01} [K]	P_{01}/P_{s3}	M_{2hub}	M_{2tip}	ω [rpm]	Acc [rpm^{-1}]	P [MW]
NOM-NOM (LPV)								
Mean	2.248	472.4	2.92	1.09	0.94	6786	1054	1.40
σ (20:1)	0.9%	1.7%	1.1%	0.93%	0.66%	0.2%	1.89%	1.9%
NOM-NOM (Shroud)[*]								
Mean	2.240	471.4	2.92	N.A.	0.97	6786	1067	1.41
σ (20:1)	1.3%	1.7%	0.5%	-	0.67%	0.1%	2.56%	2.5%
LOW-NOM								
Mean	2.253	472.3	1.92	0.90	0.78	6791	645	0.85
σ (20:1)	1.03%	1.79%	0.77%	0.30%	1.06%	0.26%	2.01%	1.94%
LOW-LOW								
Mean	2.238	473.6	1.93	0.97	0.83	4519	971	0.86
σ (20:1)	0.9%	1.5%	0.5%	0.54%	0.77%	0.4%	1.11%	1.2%

[*] No cooling supplied at the HP vane TE

Table 2.7: *Experimental test conditions for the HP turbine stage*

Condition	M_3	M_4	P_{01}/P_{03}	P_{04}/P_{03}	T_{03}/T_{01}	T_{04}/T_{03}
NOM-NOM (LPV)						
Mean	0.38	0.70	2.65	0.973	0.762	0.996
σ (20:1)	1.1%	2.3%	1.0%	2.1%	1.0%	2.0%
NOM-NOM (Shroud)						
Mean	0.38	0.68	2.64	0.967	0.772	0.998
σ (20:1)	1.5%	1.8%	1.7%	2.7%	1.0%	2.4%
LOW-NOM						
Mean	0.29	0.40	1.83	0.941	0.827	0.991
σ (20:1)	3.43%	3.80%	1.86%	1.99%	3.15%	1.71%
LOW-LOW						
Mean	0.31	0.39	1.80	0.993	0.826	0.994
σ (20:1)	4.1%	2.0%	1.4%	0.8%	0.8%	1.3%

Table 2.8: *Experimental test conditions for the LP vane*

In all the tests carried out for the characterization of the aero-thermal performance of the LP multi-splitter vane (see Chapter 5) the cooling ejection was supplied at the stator trailing edge. In the experimental campaign for the study of the rotor overtip flow aero-thermodynamics the turbine article was tested uncooled in order to minimize the complexity of the investigation (see Chapter 4). In the absence of cooling, the mean outlet temperature was slighlty higher as well as the flow velocity. The turbulence level at the stage inlet was measured in previous a previous experimental campaign to be 5% [44].

The span-wise distributions of the total pressure and temperature at the stage inlet plane are shown in Fig. 2.13. Due to the large size of the settling chamber and the symmetry of the turbine rig test section, the inlet flow is assumed axial and uniform in the peripheral direction. The measurement data were normalized by the value measured by the reference probes at mid-span in order to remove the test-to-test variations. The pressure profiles are symmetrical and no apparent variations were observed for distributions measured at different test conditions. The pressure profile also indicated the presence of a thin inlet boundary layer at the nozzle guide vane inlet. The temperature distribution was characterized by an asymmetric profile and by a thick thermal boundary layer, especially at the tip endwall where the total temperature drops by 8% with respect to the mid channel value while in the hub region the temperature reduction is only 2%. The large temperature deficit at the turbine inlet plane is attributed to the relatively long duct upstream of the stator row. The walls of the inlet contraction are at ambient temperature prior to a turbine test, and thus during the blow-down the hot flow is cooled down.

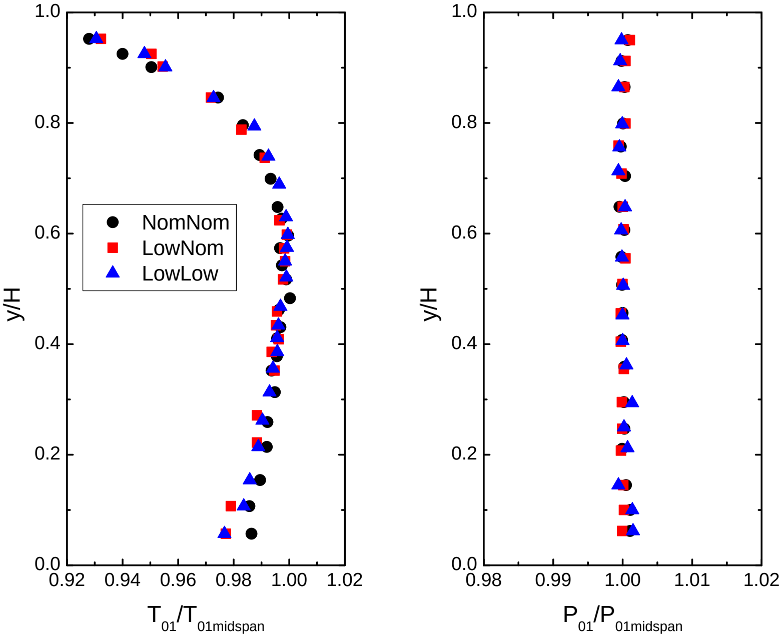

Figure 2.13: *Turbine inlet radial distributions of total temperature and pressure*

2.4 Numerical methods

In order to support the findings of the experimental investigation, two types of numerical simulations were conducted.

Calculations were performed to predict the steady and unsteady flow through the 1.5 turbine stage and assess the interference effects between the HP turbine and the LP multi-splitter vane. Three-dimensional CFD was carried out by ONERA with their in-house solver elsA [45, 46]. This software is capable of solving compressible three-dimensional Reynolds averaged Navier-Stokes equations in the relative frame of reference. The elsA solver uses a multi-domain approach on structured meshes and a cell-centered finite volume scheme. The time integration is accomplished with a backward-Euler scheme coupled to an LU implicit phase technique. The calculations presented in this work have been achieved with the one equation Spalart-Allmaras turbulence model. Unsteady computations were performed with a blade count reduction: the computational domain is composed of 3 HP stators, 4 rotors, 1 structural vane and 3 aero-vanes. Fig. 2.14 shows a view of the computational grid which was meshed with a 63 blocks structured grid including $20{\times}10^6$ points. "O-blocks" were used around the blades, and "H-blocks" filled the rest of the passage as shown on the figure below. The rotor tip clearance gap was also taken into account and a fixed value of h=0.45 mm was used in all the calculations. The values of the normalized distance of first wall cell (y^+) at the blade wall were lower than 2.

The three experimental turbine operating points were investigated. At the turbine inlet the measured total pressure and temperature were prescribed and axial flow was considered. The stage pressure ratio was specified at the hub outlet, and then radial equilibrium was applied. Walls were treated applying a non-slip condition as well as a uniform temperature distribution (T_w=291.5 K). The boundary layer was assumed to be fully turbulent. The unsteadiness induced by the blade passing was taken into account through the use of the reduce blade count approach [47] with a stage reduction matching conditions at the interface between adjacent blade rows. The steady-state 3D calculations were performed with a mixing plane approach.

It has to be remarked that the time-accurate RANS simulations were performed with a relative pitch-wise position between the two stationary vane rows (the so-called clocking or indexation) that did not match the one actually set in the turbine experiments for the instrumented LP vane sector. An offset of 2 degrees exists between the relative positions of the strut vane leading edge with respect to first stator leading edge in the CFD domain and the experimental setup. This angular difference corresponds to a circumferential rotation of the LP vane row equivalent to 36% of the aero-vane pitch or 24% of the HP vane pitch. The prediction of the unsteady flow field in the LP vane and the interaction with the upstream turbine stage are strongly affected by the stator-stator clocking position which modifies the trajectory of the HP stator wake avenue migration and the flow angle incidence on the LP vane profiles [48]. The clocking effect is also enhanced by the multi-profile configuration as the three aero-vane experiences a different unsteady flow-field depending on the strut airfoil location. Therefore, the time-resolved numerical predictions were employed only as a qualitative

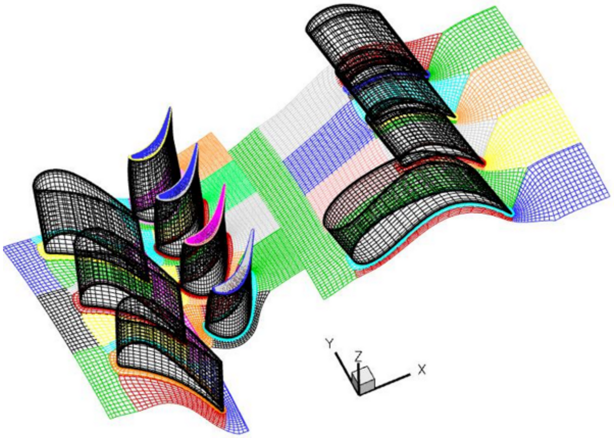

Figure 2.14: *View of the computational grid of the 1.5 turbine stage for numerical simulations with the elsA solver*

support for the interpretation of the experimental results.

A second numerical investigation was conducted to assess the influence of the multi-body architecture on the aerodynamic performance of the LP vane. The multi-splitter stator concept was studied in a one-and-a-half stage turbine configuration by comparing numerical predictions of the multi-profile geometry against predictions of a conventional single-airfoil geometry where the splitter vane is replaced by an aero-vane profile. Simulations were carried out at the turbine design point (NOM P/p - NOM speed) and at three off-design conditions with fixed rotational speed (6790 rpm). Fig.2.15 displays the two turbine configurations. The first model is identical to the geometry experimentally investigated. It consists of 36 blocks, covering the nozzle guide vane and rotor blade passages plus one strut and three aero vanes (Fig.2.15, left). In the second model the strut airfoils were replaced by aero-vanes profiles (Fig.2.15, right). Therefore, only 18 blocks (single NGV, rotor blade and aero-vane) were used to generate the computational domain. The mesh contains around $5{\times}10^6$ and $3{\times}10^6$ grid points for the splitter-vane scheme (model 1) and the aero-vane alone configuration (model 2), respectively. An "O-type" grid topology was selected around the airfoil whereas an "H-type" grid was used in the rest of the domain.

Steady-state computations of the two geometries were performed at the von Karman Institute using the solver FINE, [49]. A mixing plane approach was considered for the coupling of the three row grid interfaces. The one equation Spalart-Allmaras turbulence model was selected. The calculated value of y^+ at the airfoil walls was lower than 5. The experimental total pressure and total temperature were imposed as the inlet boundary conditions. The measured static pressure at hub was used as outlet boundary

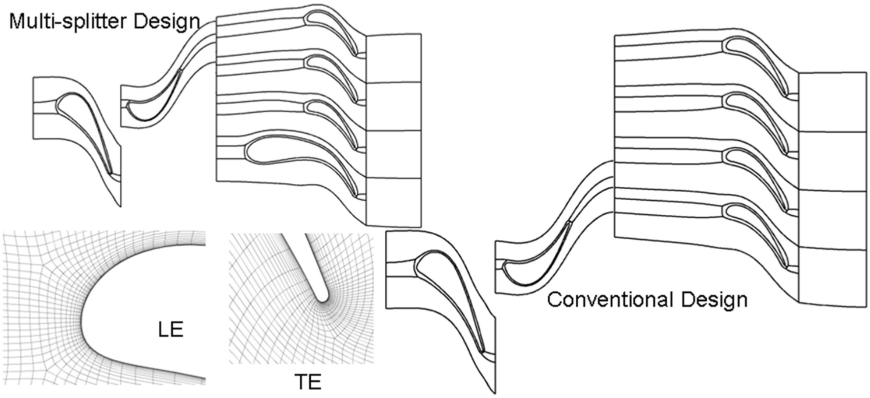

Figure 2.15: *Numerical domain of the multi-splitter (left) and conventional (right) design with details of the grid topology around the aero-vane LE and TE*

condition and radial equilibrium is then applied. A periodic boundary condition was applied at the sides of the domain. Four runs were performed for both models varying the operating pressure ratio of the turbine. The turbine flow conditions of the four operating points and the results of the numerical campaign will be presented and discussed in chapter 5.

Chapter 3

Development of accurate rotor tip clearance measurements

3.1 Introduction

The accurate control of running gaps between static and rotating components is vital to preserve mechanical integrity and ensure a correct functioning of any compact rotating machinery. In modern aircraft propulsion systems, blade tip clearance plays a major role in the characterization and development of reliable and efficient aero-engines. In current turbine stages, hot leakage jet flows above the rotor airfoil tips resulting in 30% of the total aerodynamic losses [50]. Therefore, the gap between the rotor blade tip and the stationary shroud must be minimized. However, turbine designers commonly set a safe minimum gap to prevent mechanical rubbing between the blade tips and the casing that may result in rotor damage or catastrophic failure. Thus, the selection of an optimum tip clearance results from a trade-off between aerodynamic performance and mechanical integrity. Unfortunately, as a consequence of manufacturing and installation tolerances, vibrations, different expansion rates of blades, rotor disk and casing induced by thermal and speed transients, the rotor tip clearance undergoes large variations during engine service operations [51]. Hence, advanced tip clearance active control concepts must rely on accurate real-time clearance measurement systems to achieve highest engine efficiency with increased safety margins. Additionally, blade tip clearance measurements are routinely used in engine development programs to verify the mechanical design and tune numerical predictions [52].

Various sensing principles have been proposed for non-contact gap measurements in large-scale turbomachinery. Optical probes [53, 54] provide the largest resolution and bandwidth. However, optical sensors are complex and expensive as well as being highly vulnerable to particle contamination. Microwave-based sensors [55] are rugged with no sensitivity to debris, but their application to detect small blade thickness is impractical. Ultrasound probes [56] overcome the target size limitation but show dependency on the properties of the gap fluid. Pneumatic sensors measure how the flow is disturbed by the passage of an object to determine its distance [57]. They suffer neither contamination nor electromagnetic fields, but their use in engines is restricted by the low accuracy and slow fluid response. Conversely, eddy current probes are commonly applied for proximity measurements in a wide range of turbomachines due to the simple design, robustness and high signal-to-noise ratio [58]. The main drawback of this type of sensor is its working temperature capability, which is limited by the curie point of rare earth magnets, usually around 500 K.

In aero-engines the most challenging tip clearance measurements are carried out in the high pressure turbine where temperatures, pressures and rotor speeds are the highest. Sensors should thus be capable of withstanding temperatures above 1500 K, have a reduced size and improved working range (0-5 mm), and a high bandwidth to resolve blade passing frequencies of the order of tens of kHz. Tip gap measurements in current gas turbine applications are commonly based on capacitance systems. Similarly to eddy current probes, capacitance-based tip clearance sensors are low cost and rugged devices with the best potential to adapt to harsh working conditions. The technique relies on the measurement of the capacitance between an electrode and a moving metallic target. Different capacitive detection methods have been developed to sense the running tip capacitance. Barranger [59] used the Amplitude Modulation (AM) induced by a sweeping target on a reference signal to quantify the capacitance change due to the blade passage. Capacitive sensors also operate based on phase modulation [60] and dual amplifier feed-back loop [61]. A capacitance gauge utilizing a Frequency Modulated (FM) operating mode was proposed by Barranger [62]. The probe-to-blade tip capacitance is fed into an oscillator whose output frequency carries an imprint of the gap size. Chivers [63] developed a guarded tri-axial FM sensor that minimizes the sensitivity to temperature and vibrations based on Barranger's FM probe. Intense research has targeted the development of capacitive probes for testing in gas turbine engines. Sheard et al. [64] performed accurate blade-to-blade tip clearance measurements on the casing on an HP compressor using a hybrid self-calibrating electromechanical-FM capacitance sensor. Fabian et al.[65] designed and tested a capacitance-based tip clearance measurement system for micro gas turbine applications. Developments of high temperature capacitance probes for tip clearance measurements in engine validation tests were proposed by Bailleul et al. [66], Muller et al. [67], and Sheard et al. [68]. However, no sensors for engine flight have yet been realized [69]. The gas turbine industry therefore has a strong interest for improved tip clearance instrumentation for routine use on in-service engines. Further technology development is needed to provide measurement systems with enhanced accuracy, increased working range and extended lifetime.

This chapter reports the implementation and testing of a novel capacitance-based system to measure single-blade tip clearance over the rotor of a engine-size research HP turbine. The sensing apparatus is composed of a robust capacitive probe connected to the signal conditioning unit via a co-axial cable. The tip clearance instrumentation presented here allows high bandwidth measurements and large distances to be set between the sensor and the electronics without any abatement. The tip clearance probe was calibrated on a simplified test bench to assess the sensor output and determine the measurement uncertainty. In a second phase the probe was mounted on the shroud of a large transonic turbine rotor where tip gap measurements were carried out. A procedure to calibrate the tip clearance probe in-situ by means of wearing gauges is described and a sophisticated technique that ameliorates the calibration data reduction is presented and validated. A technique was also used that enables the capacitance probe self-calibration in-situ when a reference distance is not readily available. The methodology to measure blade-to-blade and average rotor tip clearance and the signal processing procedure were demonstrated through an extensive experimental campaign. The results were used to assess the measurement system performance and characterize the rotor tip clearance variations in a typical run of a short duration turbine rig. The presented methodology can be applied to any rotating machinery.

3.2 Measurement system

3.2.1 Capacitance sensor principle

In the current research work a capacitive probe system, developed by Hytron GmbH [70], was used to perform distance measurements between the rotor blade tip and the casing in gas turbines. The proximity measurement system is based on the detection of the capacitance between a probe and a moving conductive blade. Fig. 3.1a displays a schematic representation of a rotor blade and the tip of a typical capacitance-based probe installed in the turbine engine casing. The sensor head is composed of two co-axial conductors, the round-rod electrode and the guard electrode, separated by an insulator. The guard electrode ensures that the central electrode is electrically insulated from the metallic shroud in which is mounted. As a rotor blade sweeps under the probe head, the sensor electrode and the blade tip establishes a variable capacitance. The resulting capacitor is a function of the plates' geometry, the properties of the medium in between and the gap between the plates. If fringe effects are neglected, the probe-to-target capacitance (C_x) can be expressed by the relationship:

$$C_x = \frac{\varepsilon_r \varepsilon_0 S}{d} \tag{3.1}$$

where ε_r and ε_0 are the permittivity of the medium and the vacuum, S represents the common area between the two plates and d is the probe-to-target distance. The capacitance C_g that forms between the guard electrode and the blade tips can be neglected since the rotor blades are electrically grounded to the engine casing via roller bearings and seals. Thus, the total capacitance sensed by the proximity measurement system is the sum of the shunt capacitance of the probe alone (C_0) and the probe-to-target capacitance (C_x). The total system shunt capacitance C_0 depends on the geometry of the probe head, the insulator material between the cylindrical electrodes, the length of the cabling and is typically in the order of 500-1000 pF. Conversely, the passage of a rotor blade results in a small capacitance change to be measured at the probe head, approximately three orders smaller than the system shunt capacitance.

The proximity sensor presented in this work adopts a novel concept to accurately detect such narrow capacitance variations. A high frequency signal is transmitted trough a co-axial cable to the probe and then reflected back at the sensor tip. The close passage of a moving target modifies the probe response and modulates the reflected signal content. The input and probe-modulated signals are subsequently compared and processed by means of a heterodyne technique that yields direct information of the instantaneous tip clearance.

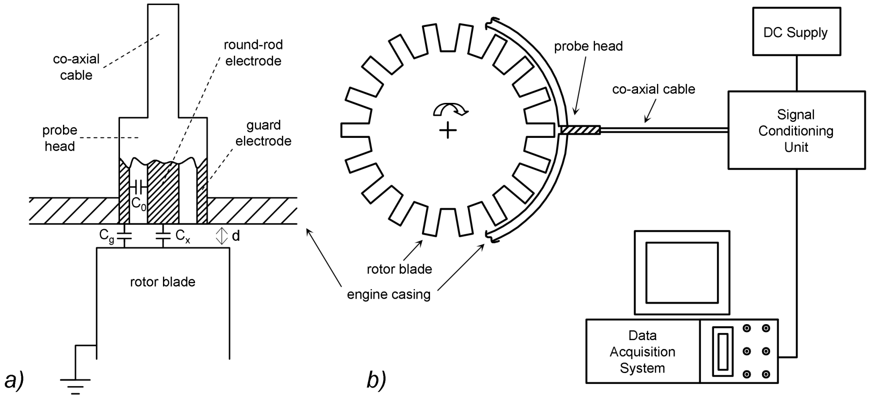

Figure 3.1: *Sketch of the proximity measurement system: a) cut view of the sensor head and b) tip clearance measurement system block*

3.2.2 System specifications

The configuration of the tip clearance capacitive measurement system is represented in Fig. 3.1b as a simplified block diagram. The system is composed of three main elements: a sensing probe, a cable and a signal conditioning unit. The sensing probe surface is mounted in the turbine shroud, located immediately above the rotor blades whose clearances are to be measured.

The probe head is connected via co-axial cable to the signal conditioning electronics fed by a DC power supply. The probe head is composed of two co-axial cylinders made of steel and separated by an electrical insulator of PTFE (Poly-Tetra Fluoro Ethylene). This ensures that the probe can withstand a maximum temperature of 530 K, which is below the operative temperature levels encountered in the turbine test rig used for the experiments. The probe has an external diameter of 10 mm and the outer screen has a threaded surface in order to facilitate the mounting in the rotor casing (Fig. 3.2a). The diameter of the inner sensing electrode, 5 mm, has been selected as an optimum value that offers a small probe size and a wide measurement range, typically estimated as half of the central electrode diameter, Fig. 3.2b.

The connection between the sensor head and the conditioning unit is provided by a co-axial cable made out of copper with PTFE as insulator, covered by an outer screen of FEP (Fluorinated Ethylene Propylene) that guarantees flexibility and mechanical protection. The cable has a total length of 8 m and allows transmitting high frequency signals for long distances with no loss in performances. The overall system shunt capacitance (probe head + cable) amounts to about 900 pF while the capacitance change induced by a blade passage is less than 100 fF.

The small capacitance variations are detected by the conditioning unit, the core component of the measurement system. The signal conditioning unit is composed of several sub-units that serve specific functions and are strictly interconnected as shown in Fig. 3.2c. The Clock-Generator module generates a low distorted and phase-stable sine wave at high frequency (60 MHz) that is fed into the sensor head, with the frequency selected according to the probe characteristics and the total cable length. The oscillator signal is also used to synchronize all the other circuitry. In the Input Stage unit, the probe-modulated reflected HF (high frequency) signal and the original input from the oscillator are overlapped to generate a heterodyne signal that carries the tip-to-sensor distance information. The raw signal is then amplified by multi-stage operational amplifiers (HF Process sub-unit), digitalized in the Flash Analogue-Digital-Converter (12 bit resolution, 10 MHz sample rate), and sent to the Digital Control unit. At this step the amplified digital signal undergoes further processing to compensate for all the spurious alterations of the original blade-to-sensor capacitance. This function is carried out by a Field Programmable Gate Array (FPGA) circuit that executes a combination of operations in both the time and frequency domains to generate a signal that performs the compensation. The auxiliary signal is fed back via a fast Digital-Analogue-Converter to the HF Process unit to compensate the HF signal from the input stage. In the current set-up, the output signal is sampled by a Data Acquisition System from a bypass analog output located after the HF Process stage.

The feedback loop is an essential feature of the current system working principle. It is based on the tracking of the signal ”idle” working point, when no target faces the sensor, to calculate an auto-compensation function. Therefore, the system is able to correctly measure only time-varying clearances, which corresponds to a minimum operating frequency of approximately 160 Hz for the current application. However, this approach allows canceling out measurement capacity errors caused by a number of spurious factors such as probe shunt capacitance drifts due to temperature changes or vibrations, mechanical stress on the cabling, or crosstalk interference with other electronics. The use of modern FPGA technology and a high frequency clock-oscillator module extend the sensor frequency bandwidth up to 60 kHz. The upper frequency bandwidth of the sensor is limited by the minimum time window required by the analogue peak detector to identify either a passing target or the "idle" mode (no object faces the sensor). The settling time of the measurement system can be adjusted depending on the required sensor bandwidth and measurement accuracy. In the current application the system settling time was set to approximately 8 μs which guarantees the best sensor performances for accurate tip clearance measurements on the investigated turbine article.

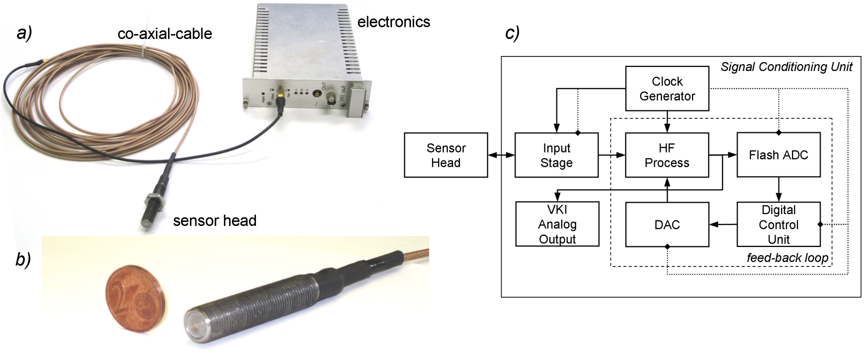

Figure 3.2: *Proximity measurement system: a) Capacitive probe head, cable and electronics b) picture of the sensor head c) conditioning unit scheme*

3.3 Data processing

3.3.1 Conventional calibration procedure

The characteristics and performance of the proximity measurement system were first evaluated in a simplified calibration bench that allows the run of a full probe calibration under controlled operative conditions. This also served to develop a robust methodology for the processing of the capacitance probe raw signal and to optimize the system set-up for measurements in the turbine test rig.

Preliminary calibration tests were run on a lathe driving a small cogwheel (Fig. 3.3a). A brass wheel with twelve teeth was manufactured with an external diameter of 70 mm and a tooth height of 10 mm. An inter-tooth spacing of 10 mm was considered in order to test the ability of the capacitance probe to correctly detect the idle position between two passing targets. The cogwheel was mounted on a 15 mm-shaft and clamped into the chuck of the lathe on one side and on the tailstock on the other side. The probe head was fitted on a support, mounted on the lathe's cross slide to permit its independent displacement. An absolute reference gap between the capacitance probe and the bladed wheel is determined using a thin metallic wire of known length mounted in the proximity of the probe sliding support. The wire is moved towards the rotating blading till contact occurs, thus datuming the sensor tip on the longest tooth. The calibration data set was obtained traversing the measurement head at 0.10 mm intervals over the sensor operating scale (0.2-3 mm). Tests were performed at shaft speeds ranging between 1000 rpm and 3000 rpm to guarantee a minimum tooth passage frequency of 200 Hz and the safe operation of the sensor. During the calibration, the voltage output for a set of known distances between the probe tip and the cogwheel was recorded. The capacitance sensor signal was sampled with a 12 bit data acquisition system for 2 s at 250 kHz that corresponds to a frequency resolution of 0.5 Hz. This ensures that the unsteady signal features are well captured and a sufficient number of wheel turns is available for statistical analysis. Fig. 3.3b shows a typical trace of the raw voltage output, acquired during a calibration step. As a tooth sweeps under the probe sensing area, the voltage increases proportionally to the actual target distance. The signal does not show any abrupt discontinuity, rather a gradual variation as the sensor-to-target area variation is non-linear [71]. The raw signal was digitally low-pass filtered before performing any further treatment with the cut-off frequency selected to be approximately 15 times the target passing frequency, to remove the high-frequency noise while preserving unaltered the blade-by-blade signal variations. The measurement system calibration is generated by performing a curve fit through the data set associated to the longest wheel tooth using a least-square optimization routine. The equation that describes the relationship between the sensor output (ΔV) and the gap (D) between the probe tip and the target is assumed to be:

$$D = A_1 + \frac{1}{A_2 + A_3 \Delta V} \tag{3.2}$$

where *A1*, *A2* and *A3* are the coefficients of the curve fit. The form of eq. 3.2 was selected from others as it provided the best fit of the available calibration data sets. The physics of a capacitor suggests that as the distance between two plates approaches zero the capacitance must tend towards infinity. Likewise, a thorough analysis of the data exposed that the voltage variation across a tooth passage was a more robust parameter than the maximum peak-to-peak voltage to represent the sensor response. Indeed, the voltage amplitude is a direct function of the capacitance change induced by the actual target proximity [62]. Once a calibration test is completed, a routine was programmed to perform the required data reduction. The software sorts through the data sets to identify the longest blade corresponding to the largest signal amplitude. Usually 10 to 20 data sets were

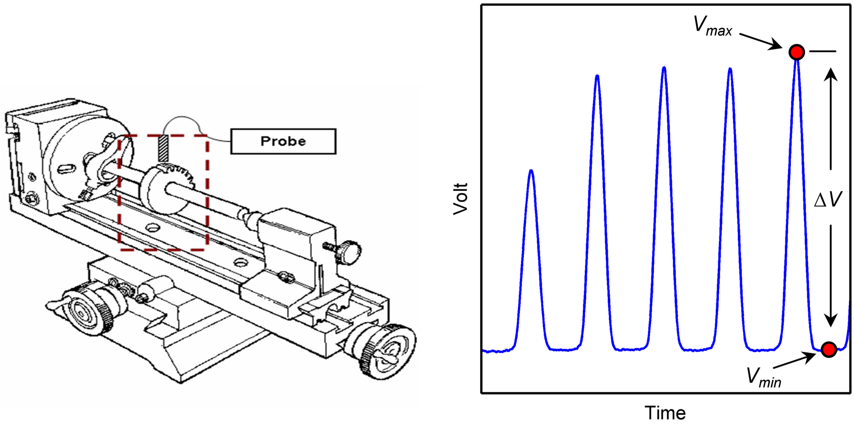

(a) (b)

Figure 3.3: *Simplified calibration set-up: a) Calibration rig set-up and b) example of typical sensor output*

used to obtain a reliable probe calibration. At this point the actual distance of the probe head to the other tooth's tips is unknown and therefore a conventional calibration curve fit is based only on the longest tooth data points as displayed in Fig. 3.4a.

3.3.2 Advanced calibration refinement

An advanced calibration refinement method was implemented in the data reduction routine, which allows the voltage values of each wheel tooth to be included into the calibration fit. This procedure is based on the research work of Sheard et al. [72]. The entire data set of a calibration run can be organized in a matrix $[V]$ that contains in each row the voltage values associated to a single tooth, and in each column the voltage value obtained at each traverse position. Once a preliminary calibration becomes available from the longest tooth curve fitting, a matrix of distances $[C1]$ can be defined. A second distance matrix $[C2]$ can be generated that has the same first column of $[C1]$ and the remaining columns computed by adding to the value of the first column the known offset distance traversed during the calibration. The distance matrices would be ideally identical but small differences exist due to calibration inaccuracies. An error matrix $[E]$ is calculated from the difference between $[C2]$ and $[C1]$. The rows of $[E]$ represent the distance error over a single tooth at each probe step while the columns account for the error in distance of the entire blading at a certain calibration point. Each row is averaged to provide a resulting row $[F1]$ that represents

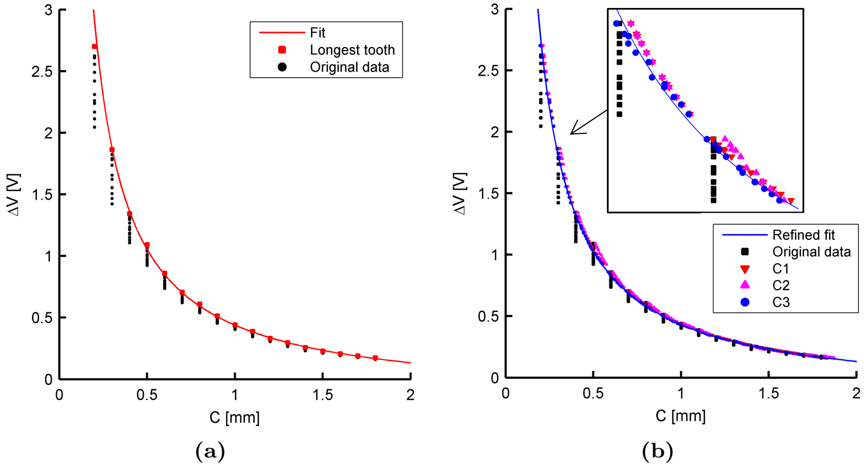

(a) **(b)**

Figure 3.4: *Sensor calibration procedure: a) classical probe calibration b) calibration refinement procedure*

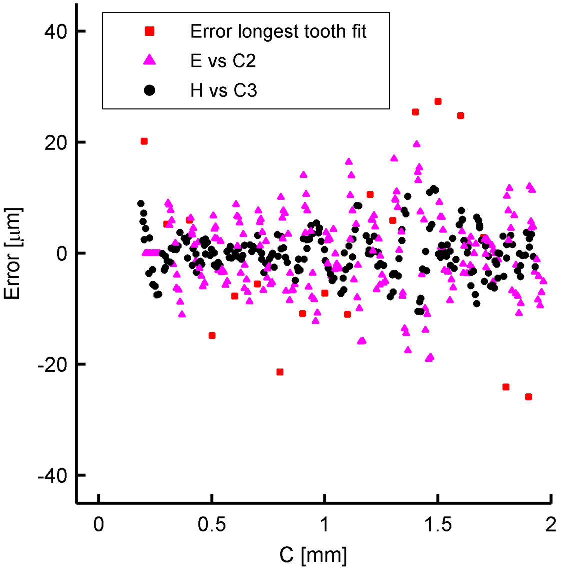

Figure 3.5: *Calibration error reduction through the calibration refinement procedure*

the error due to the proximity sensor readings. Likewise, each column of the error matrix is averaged to generate a column vector which provides an estimate of the error due to the probe traversing position. The initial matrix $[C1]$ is modified by subtracting from each column the vector $[F1]$ and from each row the vector $[F2]$ to generate a third distance matrix $[C3]$. Finally, a new set of refined calibration coefficients is calculated by performing a second curve fit, using $[V]$ and the matrix of corrected clearance $[C3]$. As previously done for $[E]$, a second error matrix $[H]$ is calculated by subtracting $[C3]$ from matrix $[C4]$, which represents the clearances obtained via the refined calibration coefficients.

Fig. 3.4b displays all the steps of the reduction procedure for the sensor calibration refinement. The capacitance probe output $[V]$ is plotted against the corrected distance matrices $[C2]$ and $[C3]$ together with the original and refined calibration laws. It is apparent that the proposed procedure has significantly enhanced the quality of the calibration result. The improved methodology enables to generate the probe calibration based on the entire data set available, thus providing a more robust estimation of the calibration coefficients.

The calibration error distribution can be appreciated by plotting $[C2]$ against $[E]$ and $[C3]$ against $[H]$ together with the clearance error associated with the calibration based only on the longest tooth as depicted in Fig. 3.5. After the last calibration refinement, the data scatter has visibly reduced from ±25 μm (longest tooth calibration) to ±10 μm. The ±10 μm error band can be reasonably assumed as an indication of the sensor accuracy achievable over the calibration range.

3.3.3 Sensor self-calibration

In-situ calibration of a capacitive-based proximity sensor may become a very challenging task in a real turbine test rig where it is often impossible to measure the actual distance between the sensor and the longest blade. An experimental procedure developed by Sheard [73] was implemented in this work that allows the self-calibration of the tip clearance probe. The technique relies upon the functioning principle of capacitance-based sensors. The physics of a capacitor dictates that the capacitance should tend to infinity as the distance between the capacitor's plates becomes zero, eq. 3.1. In the case when the actual distance between the sensor head and the rotating targets is a priori not known, it is convenient to assign an arbitrary clearance C_{guess} to the calibration data point which corresponds to the minimum distance between the probe and the investigated target (first calibration point). The position of each calibration data point relative to the first one is obtained by measuring the probe relative displacement during the calibration traverse. The sensor calibration can be then estimated using the data reduction methodology described in section 3.3.2. It is assumed that the value at which the calibration curve goes to infinity ($A1$, eq. 3.2) corresponds exactly to the opposite of the difference between the actual clearance and the first clearance guess:

$$C_{actual} - C_{guess} = -A_1 \tag{3.3}$$

and thus, the final self-calibration law can be obtained by setting to zero the *A1* coefficient of eq. 3.2.

This technique was validated using the experimental data from the calibration test bench. Fig. 3.6 displays an example of a probe self-calibration performed using the original voltage datasets and imposing that the clearance between the sensor and the longest wheel tooth is not known a priori, thus initially set to zero. Once the calibration coefficient refinement is completed (blue solid line), the final calibration curve (red dotted line) is directly obtained by setting the coefficient *A1* to zero. The calibration curve obtained by means of the self-calibration technique is in excellent agreement with the original calibration curve (black solid line) based on the known distance between the longest tooth and the sensor. The close match between the actual calibration and the one originated by the self-calibration technique was observed for repeated calibration experiments. This gave confidence that the methodology could actually provide a reliable set of calibration coefficients in the case a reference clearance is not available. The assumption that the sensor output should tend to infinity as the clearance approaches zero was verified ensuring that the value of the *A1* coefficient was zero within the measurement uncertainty for all the experimental calibrations. This ensures that the sensor self-calibration yields the correct calibration coefficients, and any discrepancy remains contained within the measurement system uncertainty (±10-25 μm, see section 3.5) as shown in the zoom snapshot in Fig. 3.6. In general, this methodology might be employed for the calibration of sensors which working principle mimics the capacitor's one.

3.3.4 Measurement data reduction

Once the calibration law is available, the capacitance probe output raw voltage is converted into the running tip gap by identifying the voltage amplitude peaks and applying the calibration coefficients (eq. 3.2). The time-varying tip gap signal is further treated in order to assign to each single voltage peak the corresponding blade number.

In the current work, a data processing technique was implemented to automatically track the rotor blade index. The technique is based on the recognition of the correct blade index by comparing the rotor radius signature measured in rotation with a known distribution of the rotor blade radius. The blade radius signature can be obtained by static measurements of the blade radii carried out with a dial gauge. The correct indexation of the blade passage events in a tip gap measurement is found as the indexation that minimizes the difference between the reference blade height distribution

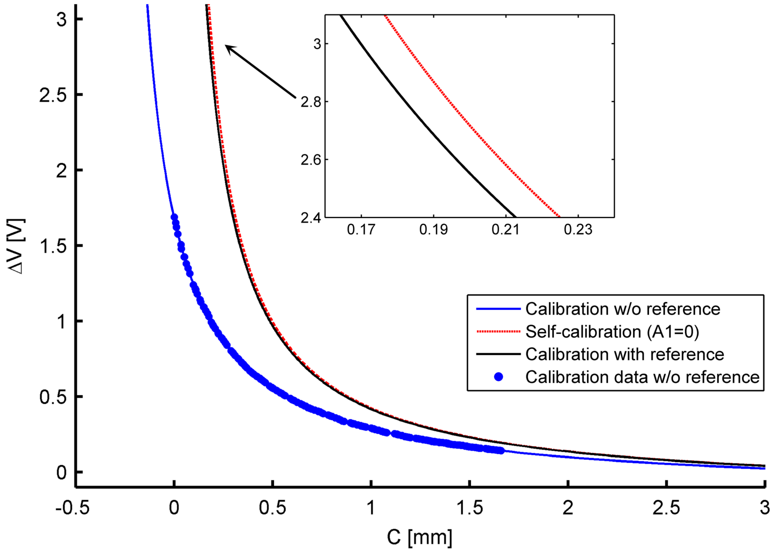

Figure 3.6: *Self-calibration of the capacitance-based proximity sensor*

and the one measured in rotation. A one-revolution trigger pulse, generated by a tachometer, can be used to verify that the rotor blade height signature measured in static condition remain the same in rotation. If this condition is not matched, the tachometer reading can still provide the rotor signature to be used as a reference at a particular rotor speed. The capacitance probe output is also utilized to extract the rotational speed and the acceleration of the rotor disk based on the blade passing signal.

3.4 Probe performance

The system performances can be described by considering the results of the capacitance sensor calibration in the small spinning rig. Calibration tests were run to verify the performance of the measurement system at increased working temperatures.

The probe head and the bladed disk were directly exposed to a hot air jet blown by a heat gun during the calibration. Thermocouples were used to monitor both the air and probe head temperatures. Calibrations were performed at two air temperatures, 500 K and 600 K, with the probe head temperature reaching the same level of approximately 360 K in both cases. The resulting calibrations superimposed with calibrations performed at room temperature. Fig. 3.7a indicates that the selected system is insensitive to temperature variations of 300 K. The sensor electronics is actually able to compensate for capacitance drifts due to variations with temperature of the electrical properties of the probe head components. Results also suggested that changes in the probe-to-target capacitance due to variation of the air dielectric characteristics with temperature are negligible over the tested temperature range.

Fig. 3.7b shows calibration curves for tests performed at two different disk speeds. Comparison of calibrations run at 1000 rpm and 2500 rpm reveals that the sensor response remains unaltered when the system is operated at low rotor speed that corresponds to target passing frequency (200 Hz), close to the lower bandwidth limit of the probe. Calibrations performed by the manufacturer ensured that the measurement system output is independent of the target passing speed for frequencies below 60 kHz. Repeatability on the calibration law coefficients was judged excellent.

The amount of voltage change with clearance size provides the probe sensitivity. At a working clearance of 0.5 mm, the signal voltage amplitude is approximately 0.8 V and probe sensitivity is typically 1.5V/1mm. At extended range, the capacitance sensor signal approaches the system noise floor, estimated to be around 10 mV. Thus, the signal-to-noise ratio is normally 80. The 5 mm diameter capacitance probe is able to operate over a range of 2.5 mm. As the distance between the sensor tip and the rotor increases, the probe sensitivity degrades. As such, a voltage pulse induced by a passing target becomes more and more difficult to distinguish from a random noise peak. At clearances below 0.2 mm, the amplifiers in the signal conditioning unit saturate.

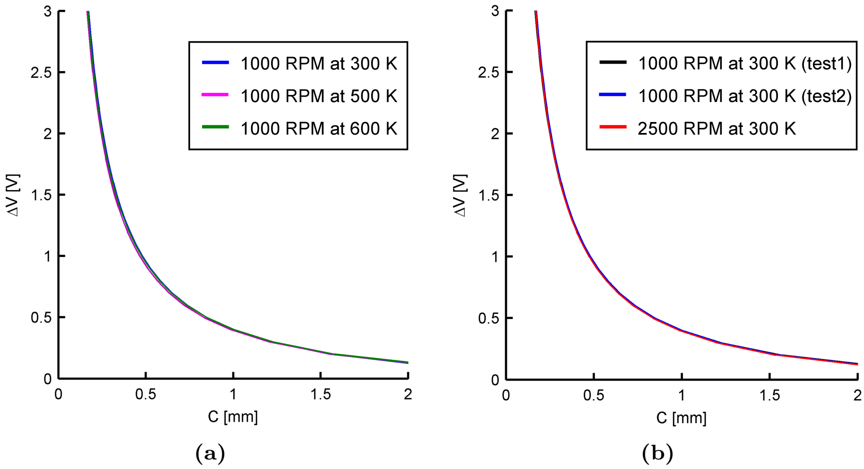

(a) **(b)**

Figure 3.7: *Capacitance probe calibrations performed at different working conditions: a) effect of environmental temperature b) effect of rotational speed*

3.5 Uncertainty analysis

The accuracy of the clearance measurement sensor is limited by a number of errors that arose during probe calibration, system installation and data reduction.

The error generated in the calibration process can be thought of as the uncertainty of the standard used to datum the probe relative to a known reference distance. This uncertainty is estimated as half of the reading resolution of the instrument used to monitor the probe displacement. For measurements carried out in the calibration test bench, the proximity probe traversing is recorded by a dial gauge with a typical resolution of 10 μm. Thus, the reading error amounts to ±5 μm (20:1). In the turbine test rig, the sensor displacement is measured by a precision micrometer screw with a resolution of ±20 μm, thus a reading error of ±10 μm (20:1). Uncertainties due to the deviation between the real blade and disk geometry and the calibration rig are not accounted for in this analysis since the proximity probe was calibrated in-situ.

During the operation of the system, uncertainties are introduced by changes in the gas dielectric properties that affect the sensed capacitance as described by eq. 3.1. Errors of the order of 0.5% of the full scale can be engendered by variations in the air humidity [74]. Likewise, large air temperature and pressure changes result in slight variations of the measured capacitance, usually less than 0.1% in standard turbine applications [63].

In the turbine rig operation, installation uncertainties are generated in the measurement of the sensor head setback inside the rotor shroud. The knowledge of the probe position inside the casing is used to retrieve the actual distance between the blade tip and the rotor endwall from the capacitance probe measurements. The probe setback is measured prior to each test with a precision of ±5 μm (20:1).

System noise and signal treatment routines introduce a random error in the identification of the peak-to-peak voltage amplitude from the measurement readings. The uncertainty on the data reduction process can be statistically determined from repeated measurements performed at fixed operating conditions during the system calibration. For a large number of samples, the random error associated to the blade-induced voltage change is estimated by the standard deviation of the voltage amplitude values logged for a single blade. The levels of the voltage data scatter are observed to remain nearly constant over the probe working range, $\sigma_v = \pm 5$ mV. The propagation of the data-reduction error trough to the final result, according to eq. 3.2, yields an uncertainty of ±18 μm (20:1) on the tip gap measurement at 1 mm probe working distance. Lastly, during the data reduction process, the conversion of the measured voltage amplitude into clearance generates an error, estimated by means of the precision interval associated to the calibration curve fit. Thanks to the use of the calibration refinement technique, the calibration uncertainty is reduced to approximately ±10 μm (20:1).

An RSS (Root of Sum of Squares) method is applied to combine all the error contributions [75], and Table 3.1 provides a summary of the bias and random uncertainties of the measurement system. The total systematic uncertainty amounts to ±12 μm (20:1) and the major contribution comes from the calibration standard used to datum the probe position. The largest influence on the random uncertainty is ascribed to the noise/data-reduction error that can easily dominate the overall uncertainty.

Fig. 3.8 displays the overall system error as a function of the probe range. As the operating gap increases, the probe sensitivity reduces, and thus the random error becomes increasingly significant. However, because of systematic errors, reducing the probe operational distance below 0.5 mm does not yield a significant reduction of the total uncertainty. The uncertainty analysis suggests that an optimum working range for the proximity sensor exists that allows maximizing the measurement accuracy and the probe sensitivity by keeping acceptable safety margins.

Error source	**Type**	**Uncertainty** [μm] (20:1)
Calibration standard	Bias	± 10.0
Calibration curve fit	Random	± 10.0
Probe head installation	Bias	± 5.0
System Noise / Data reduction	Random	± 18.0
Digitalization error	Bias	± 0.05
Gas effect - air humidity	Bias	± 5.0
Gas effect - air Temperature & Pressure	Bias	± 0.5
Random error		**± 20.0**
Bias error		**± 12.0**
Total system uncertainty*		**± 25.0**

* *For a nominal working clearance of 1 mm*

Table 3.1: *Proximity measurement system uncertainty analysis*

3.6 Turbine measurements

3.6.1 Sensor installation and in-situ calibration

The proximity measurement system was installed on the casing of the compression tube turbine facility to provide detailed measurements of the rotor tip clearance.

The airfoils height is 54 mm at the corresponding measurement location and the inter-blade spacing is 38.8 mm at the blade tip. The airfoil thickness varies along the chord and in correspondence of the proximity probe location is 6.7 mm. For aerodynamic testing purposes, the turbine was investigated at two design speeds of 4500 rpm and 6790 rpm. For high speed testing

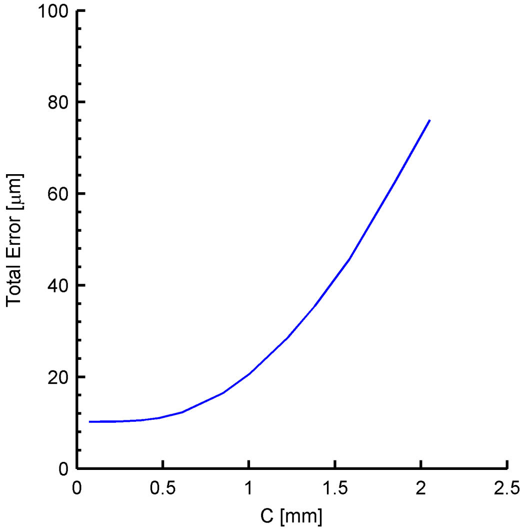

Figure 3.8: *Capacitance-based proximity measurement system total error as a function of the sensor range*

this corresponds to a blade passing frequency of approximately 7400 Hz. In order to properly detect the passage of a single blade and resolve the running tip clearance fluctuations, the sensor signal was sampled with a 16 bit acquisition card at 1 MHz, i.e., a minimum of 135 samples per blade passage event.

Fig. 3.9 displays an example of the rotor speed and acceleration history over 3.5 s after the blow-down start and the typical variation of the mean rotor tip clearance during a turbine test. In a typical test cycle, the test section is initially under vacuum. The turbine rotor is spun up to nearly its design speed by an auxiliary power turbine. As a consequence of the work exchange with high enthalpy flow, the rotor accelerates during the test blow-down reaching a maximum speed of 7500 rpm (highest design speed testing). The rotor blades strains under the effect of the centrifugal loads and at the maximum rotor speed the rotor tip clearance is nearly zero. Once all the mass-flow from the upstream piston has been discharged, air brakes are activated that slow down the rotor disk.

The experimental set-up and the tip clearance system installation in the turbine test section were designed to enable the calibration of the capacitance probe in-situ. This entails the advantage of calibrating the sensor against the actual blading geometry and minimizes the system installation uncertainties. The tip clearance measurement installation on the turbine stage was performed by fitting the probe head into an extension support, Fig. 3.10a. The probe-support assembly is guided trough the turbine casing to the rotor shroud. The sensor external surface is equipped with a screw

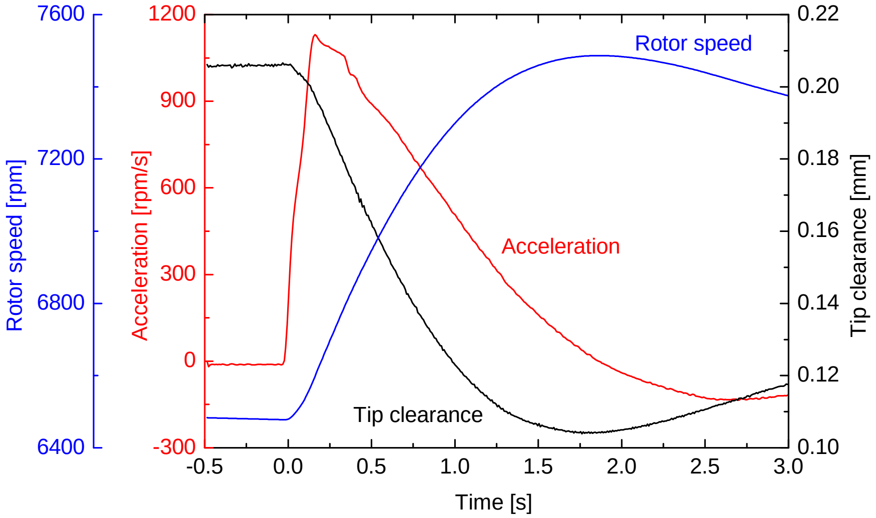

Figure 3.9: *Typical rotor speed, acceleration and rotor tip clearance levels during a blow-down test*

that allows the correct positioning and displacement of the probe head inside the turbine casing. The capacitance probe can be mounted on three different slots located in the casing at equally spaced circumferential positions, Fig. 3.10b. The exact position of the probe head was measured by a precision micrometer that, mounted on the outer casing surface, measures the radial displacement of the external extension support that carries the sensor (Fig. 3.10a).

The in-situ calibration was performed thanks to wear gauges fitted in the rotor shroud in proximity of the sensor head. The wear gauge consists of a thin metallic wire attached to a small support that can be fit inside the rotor casing ring (Fig.3.11). Two wear gauges were installed in the close proximity of each of the three circumferential positions where the capacitance probe sensor can be mounted. One wear gauge was positioned at the same axial probe location (75% $C_{ax,r}$) and the second one was located at 25% $C_{ax,r}$, Fig. 3.10b. As the rotor speed increases, the wear tip is gradually machined by rubbing with the longest blade.

The calibration was performed by rotating the rotor disk at increasing speeds that result in increasing wearing of the reference gauges. At the end of each run-up, the actual distance between the wear gauge tip and the sensor head was measured, thus providing a zero reference to datum the capacitance probe position. The rotor shroud endwall was covered with a thin layer of abradable liner. This allows performing a planned blade-abradable erosion procedure at the beginning of the experimental campaign once the clearance system calibration is completed. When the rotor disk spins up

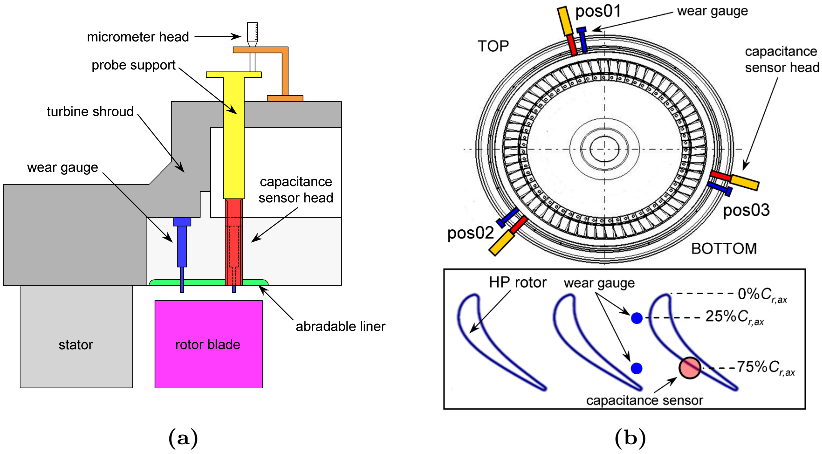

Figure 3.10: *Installation of the proximity measurement system on the turbine rig: a) design of the capacitance sensor and wear gauge arrangement on the rotor shroud for in-situ calibration b) circumferential and axial locations of the capacitance probe and the wear gauges*

to its maximum speed, the blade tips rub the abradable liner resulting in a defined running clearance, Fig.3.11. To avoid damage to the probe in the event of a tip rub, the sensor head was positioned recessed 0.7 mm within the casing during the experimental test campaign for the investigation of the aerothermodynamics of the multi-splitter low pressure vane (see chapter 5). The capacitance tip clearance sensor head was replaced at the end of the test campaign due to a failure. In a second test campaign dedicated to the experimental characterization of the rotor casing aerothermodynamics (see chapter 4), the second capacitance sensor was calibrated by means of the self-calibration technique since there was no possibility to restore the abradable liner and utilize the wear gauges as a clearance reference.

In order to perform the self-calibration of the capacitive sensor in the turbine wind tunnel, the probe head is initially set flushed with the casing endwall. Then a run-up test is started and the the rotor is spun up to a rotational speed close to design speed (6000 rpm). Once the rotor speed is stabilized, the probe is traversed radially at increasing distances from the rotor blade tip at steps of 0.05-0.1 mm. The probe displacements are accurately monitored thanks to the micrometric screw mounted on the external turbine casing. Ten to fifteen calibration points were used to perform the calibration curve fitting. Additional calibrations tests run at different rotational speeds confirmed that the sensor calibration is not dependent on the blade passing frequency.

The coefficients that defines the calibration curves used for the data reduction of the tip clearance measurements obtained during the experimental campaigns are reported in Table 3.2. The difference between the two calibration laws was due to the probe head replacement and to different configuration of the sensor control unit set by the manufacturer.

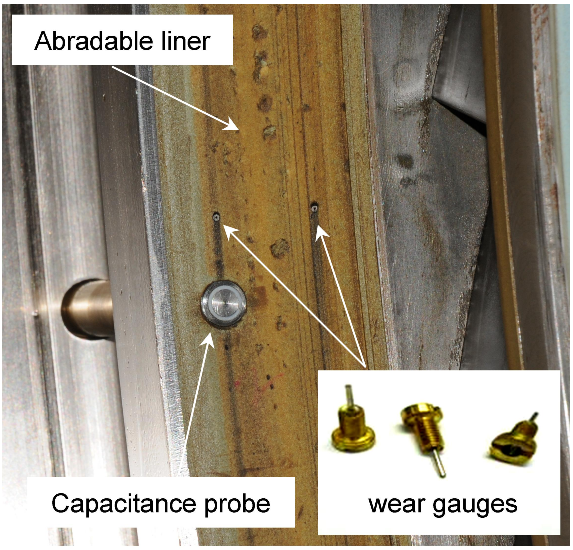

Figure 3.11: *View of the capacitance probe installation in the rotor casing at the end of the in-situ calibration procedure. The wear gauges are worn out and flushed with the abradable liner.*

	A1	*A2*	*A3*	R^2
Probe 01 (wear gauges)	0.0009	0.2274	1.4572	0.99987
Probe 02 (self-calibration)	0.0000	0.1466	2.1392	0.99994

Table 3.2: *Coefficients of the capacitance sensor turbine in-situ calibrations*

3.6.2 Mean rotor tip clearance

The experimental program served to verify the performance of the proximity measurement system in a engine-representative environment and to provide a detailed investigation of the tip clearance levels that characterize the operation of a short duration wind tunnel. Furthermore, the gathered data is fundamental to correlate with turbine efficiency and unsteadiness levels.

For the duration of the test campaigns, the rotor tip clearance was monitored during the turbine rig operation at increasing rotational speeds and during the blow-down test phase. The raw output voltage amplitude was reduced to a data set of tip clearances associated to the corresponding blade passage event. The time-varying tip clearance signal was also utilized to estimate the rotor speed and acceleration. The single clearance data was averaged over one rotor revolution to provide a mean value representative of the 64-blade rotor tip clearance variation during a turbine test run.

Fig. 3.12 depicts the typical variation of the rotor tip clearance, normalized by the blade height, measured during the turbine test rig operation as a function of the rotor speed. The blade radius grows with the rotational speed as the centrifugal loads increase following a parabolic law. The tip clearance was observed to vary approximately 0.6% of blade span (0.32 mm) as the rotor accelerates from rest to the design speed of 6790 rpm. Analysis of the experimental data confirmed that the capacitive sensor output is virtually not affected by the blow-down of a hot air flow occurring during the test phase (Fig. 3.12).

A finite element stress calculation of the rotor disk has been used to estimate the rotor blade deformation under centrifugal load and the predicted tip clearance is also plotted in Fig. 3.12 as a function of the rotational speed. Discrepancies exist between the computed tip clearance and the experimental data. The numerical predictions overestimate the blade radius growth rate and a difference of 0.1% of blade span with the experimental value was observed at 6790 rpm. Tip clearance measurements are of crucial importance to obtain high accuracy correlations between the flow measurement data and the true tip gap value as this is one of the main objectives of the experimental investigation into the rotor casing aero-thermodynamics (chapter 4).

As the rotor disk speed constantly increases during a test, it is convenient to select as a reference, hereby referred to revolution "0", the rotor revolution in which the turbine speed reaches the target design value, 4500 rpm or 6790 rpm. Fig. 3.13 shows typical trends of the average blade tip clearance for the two operative speeds. As the turbine speed increases, the tip clearance reduces due to larger centrifugal loads and consequent growth of the rotor blades and disk. A constant clearance shift of approximately 0.2 mm was observed between high and low speed regimes, while the variation during a test run was similar for the two speed levels, around 0.045-0.050 mm for a rotational speed change of about 400 rpm.

In order to investigate the test-to-test repeatability, the mean tip clearance traces during the blow-down test were further averaged on a window of 8 rotor revolutions around the revolution zero, Fig. 3.14. The data exhibited a scatter of 0.1 mm over a large number of tests, for both low and high rotor speed regimes. This test-to-test variation was more than twice the estimated uncertainty in tip gap measurements at a working distance of 1.0-1.2 mm. A further examination of the test running conditions revealed that part of the data scatter was due to the warming up of the wind tunnel when repeated tests were performed in a single day. In fact, the short duration

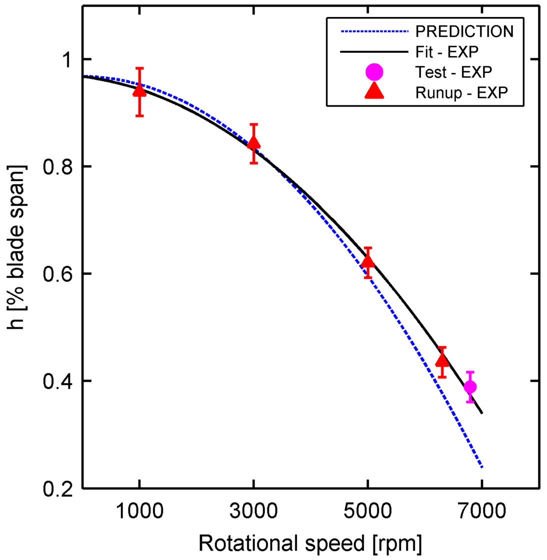

Figure 3.12: *Experimental and predicted tip clearance envelope during a facility run*

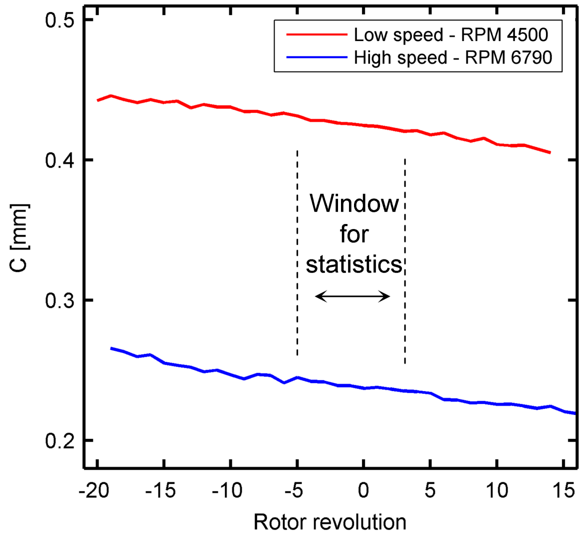

Figure 3.13: *Mean rotor tip clearance: typical tip clearance variation during a wind tunnel test*

facility allows running up to 6-7 tests a day. At every test, a hot gas blowdown releases a considerable amount of heat towards the colder test section surfaces being the turbine entry gas temperature around 480 K. The test section increasingly warms up during the day, thus causing a thermal growth of both the turbine casing and the rotor disk.

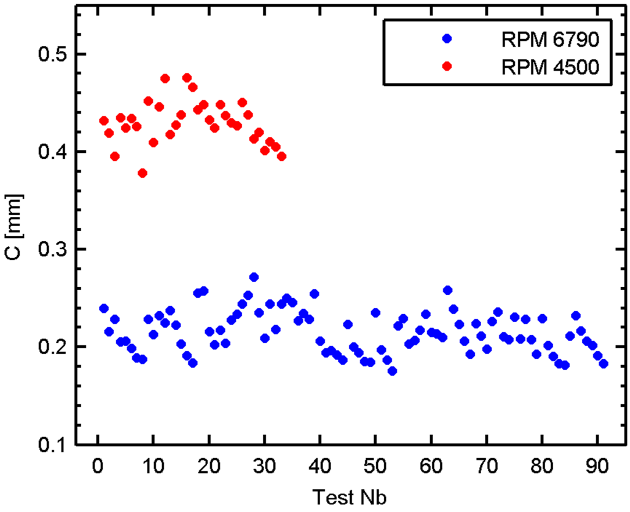

Figure 3.14: *Mean rotor tip clearance: test-to-test repeatability*

Fig. 3.15 shows again the test-to-test tip clearance variations at high-speed testing, but data are grouped according to the time a test was run during a day. The fifth, sixth and seventh test of the day were grouped together due to their small number. After ranking the tests, the results clearly displayed a significant reduction of the data scatter. The turbine tip clearance measurements showed a test-to-test repeatability variation of 45 μm, consistent with the capacitance probe error of ±25 μm (20:1) predicted by the uncertainty analysis. On a daily basis, the mean tip clearance level was shown to vary by as much as 50 μm because of the wind tunnel thermal transient. Table 3.3 summarizes the repeatability results for both rotor speed conditions. The tip clearance exhibits a reduction as the wind tunnel heats up during the day. This phenomenon is due to the different thermal dilatation of the rotor and the turbine casing. The thermal expansion for a metal is function of three variables, the initial length, the coefficient of thermal expansion and the temperature change. In the present case, the casing has a larger diameter than the rotor as well as a slightly higher thermal coefficient. Therefore, the rotor tip gap reduces because the rotor assembly (blades + disk) temperature increases more than the turbine shroud temperature as tests are performed in a day. This hypothesis is consistent with the fact the rotor surface, directly exposed to the incoming hot flow, absorbs more heat than the shroud and the heat produced by the bearings is preferably conveyed from the shaft to the rotor disk. The thick turbine casing has a much larger thermal capacity than the rotor disk which dumps the temperature increase due to the hot gas flow. On the other hand, the rotor assembly is thermally insulated from the rest of the facility and the heat absorbed during the blow-down can only be dissipated in between two consecutive tests through natural convection.

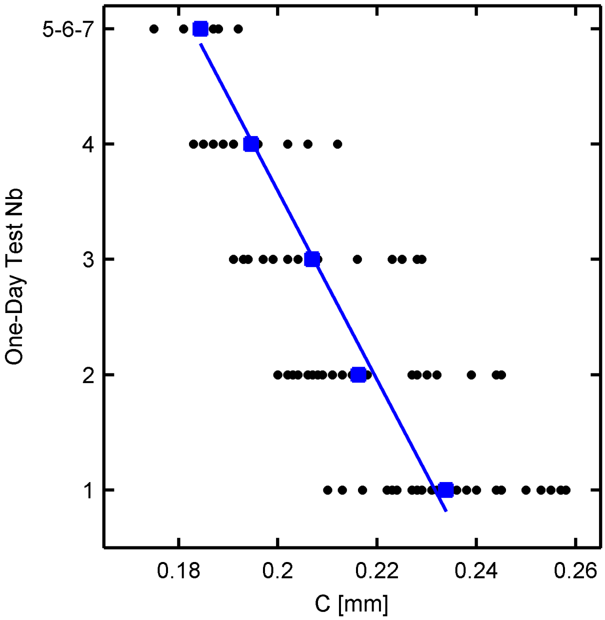

Figure 3.15: *Corrected tip clearance test-to-test repeatability, high-speed tests*

The experimental average rotor tip clearance as a function of the circumferential probe position is reported in Table 3.4 for tests performed at 6790 rpm. The measurements indicated the presence of a static rotor eccentricity as there is an unequal tip clearance distribution around the rotor annulus. The largest maximum tip gap variation was found between position 02 and position 03 and amounted to 0.06 mm. The cause for the static rotor eccentricity can be ascribed to the stator bore ovality and incorrect positioning of the rotor during the installation phase.

3.6.3 Blade-to-blade rotor tip clearance

The capacitance sensor was used to measure the individual tip-to-casing gap over the 64 blades of the turbine stage. Every blade passing event

Test number in a day	*1st*	*2nd*	*3rd*	*4th*	*5-7th*
High Speed 6790 rpm					
Mean TC [mm]	0.234	0.216	0.207	0.195	0.184
Test count	30	25	16	9	7
Repeatability [μm] (20:1)	± 28	± 28	± 29	± 23	± 13
Low Speed 4500 rpm					
Mean TC [mm]	0.456	0.449	0.422	0.416	0.411
Test count	4	8	11	4	6
Repeatability [μm] (20:1)	± 43	± 36	± 28	± 47	± 52

Table 3.3: *Mean tip clearance statistics*

	Pos01	*Pos02*	*Pos03*
Mean tip clearance [mm]	0.173	0.220	0.156

Table 3.4: *Mean tip clearance at the three circumferential probe locations*

was assigned to the corresponding blade index by means of the automatic blade-tracking technique previously described. The tip clearance of each blade was averaged over 8 rotor revolutions around the design rotor speed in order to yield a unique value for each test. The test-to-test repeatability was taken into account in the averaging process. Tests were ranked following the procedure described in the previous section to isolate the daily tip gap drift due to the thermal growth of the rotor assembly. Fig. 3.16 illustrates the average tip gap distribution over the 64-blade rotor measured at 6790 rpm. During a typical testing day, the thermal transient of the turbine rig causes a tip gap reduction of approximately 50 μm which equally affects every rotor blade. The rotor exposed a maximum blade-to-blade clearance variation of approximately 0.30 mm, i.e., 0.6% of the blade height. On the other hand, except for a few blades, the tip gap variation over the 64-blade rotor was within 0.1 mm. The blade-by-blade tip clearance envelopes measured in rotation at the high and low speed regimes are plotted together with the static blade height deviation measured using a dial gauge against the blade number, Fig. 3.17, as offset with respect to the longest blade. The dynamic and static data sets showed a high degree of overlap, the largest deviation being within the ±25 μm error of the probe, giving confidence on the accuracy of the capacitance sensor to measure running single-blade tip clearance. The observed match between the static and dynamic rotor signatures also indicates that the working positions of the rotor blades, pin-fixed to the rotor disk, remain unaffected by the high centrifugal load.

The ±25μm sinusoidal variation in tip clearance around one rotor revolution seen in Fig. 3.16 is thought to be engendered by the rotor geometry and not by the rotor assembly dynamic eccentricity. In fact, the same blade height distribution was found in the static measurements performed by a dial gauge as shown in Fig. 3.17. Therefore, it was concluded that the dynamic rotor eccentricity was negligible and the rotor center of rotation was properly set. Based on the smallest blade height variation detected by both the capacitance system and the dial gauge, the measurement system resolution can be estimated to be approximately 10 μm.

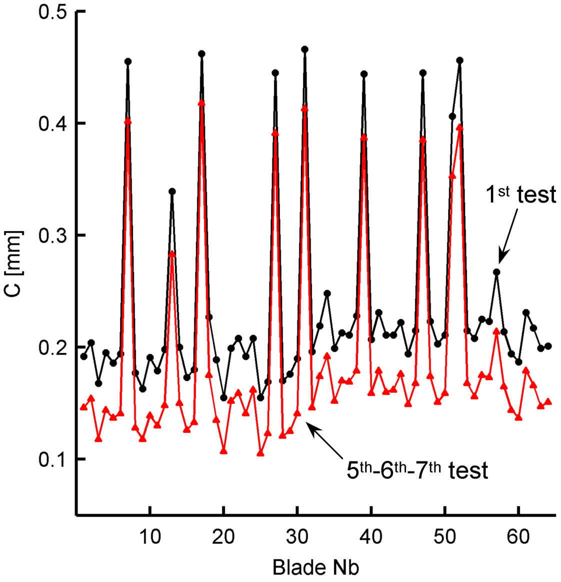

Figure 3.16: *Blade-to-blade tip clearance at high speed testing, daily variation*

The high bandwidth of the probe enables to correctly detect small tip clearance fluctuations in the range of tenths of kilohertz. Therefore, the unsteady sensor signal can provide information of the rotordynamic effects. The Fourier spectrum of the raw capacitance measurements was used to determine the relative size of fundamental and harmonic frequencies and to highlight phenomena that are not rotor periodic. The frequency analysis is presented for a typical test run at high speed condition in Fig. 3.18. The plot shows the power spectrum density of the raw output voltage for varying frequencies up to 100 kHz. The rotor fundamental frequency clearly shows the largest amplitude as the blade tip passage represents the main event that triggers the probe response. With regards to harmonics, the contribution of the rotor blade passing is relatively small and becomes negligible at frequencies higher than the second harmonic. The frequency spectrum in Fig. 3.18 shows that the contribution of frequencies other than the blade passing is almost negligible. The rotor shaft frequency at 110 Hz is hardly detectable, around two orders of magnitude smaller than the rotor fundamental and of comparable size with the system noise peak level at 150 Hz.

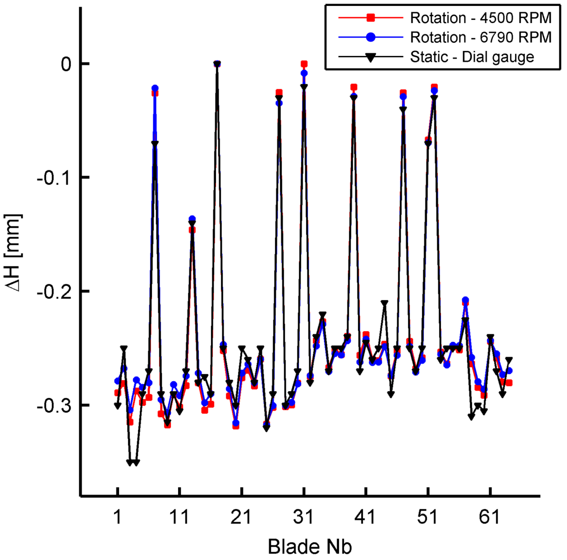

Figure 3.17: *Offset of the rotor blades from the longest blade for static (dial gauge) and running (capacitance probe) measurements*

This observation suggests that vibrations of the turbine rotor were kept to a minimum, in agreement with the fact that the rotor disk was accurately balanced before starting the experimental campaign. The frequency spectrum analysis also confirmed the hypothesis that the sinusoidal variation observed in the data sets of Fig. 3.16 was caused by the static geometrical shape of the rotor assembly.

3.7 Conclusions

The main purpose of the research work presented in this chapter was to experimentally determine the tip clearance variations that characterize a typical test run in a short duration turbine facility. A capacitance-based proximity measurement sensor was successfully used to detect tip clearance over individual blades around a rotor.

The measurement system components was described and its performances accurately evaluated by means of repeated calibrations in a simplified test rig. An advanced procedure to calibrate the capacitance probe was implemented that allows producing a set of refined calibration coefficients based on the data sets available from all the blades. Additionally, a methodology that allows the self-calibration of the capacitance probe was introduced described, tested and validated. The technique exploits the physical working principle of a capacitor and enables calibration to be performed without the

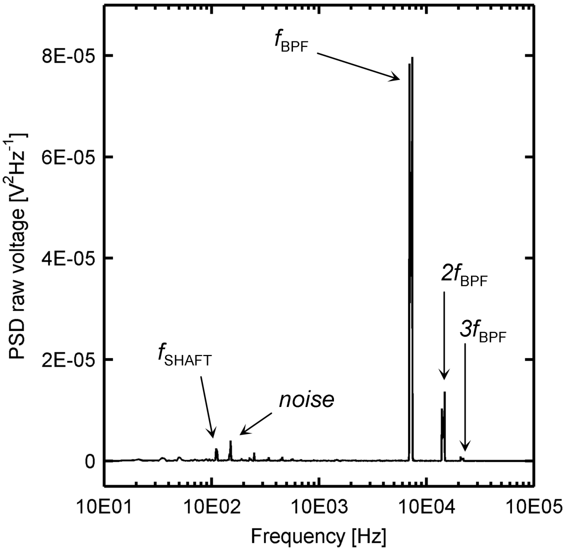

Figure 3.18: *Power spectrum density of the sensor raw voltage at high speed testing*

knowledge of an absolute clearance reference.

Calibrations at different working conditions proved that the system electronics fully compensate for temperature drifts of the gas temperature and of the probe head. A methodology to assess the measurement system uncertainty was proposed and the bias and random error sources were identified and quantified. The analysis predicted that running gaps can be measured within ±25 μm (20:1) at a working distance of 1 mm. Experience on a real running turbomachine gave confidence that this uncertainty was actually achieved in practice.

The tip clearance sensor was mounted on the shroud of the high pressure turbine stage and calibrated in-situ using wear gauges fitted into the casing endwall. Blade tip clearance measurements were carried out in the von Karman Institute short duration turbine test rig where the rotor speed constantly increases during a test. Results showed that the tip clearance decreases approximately 0.05 mm from the blow-down start till the moment the rotor reaches the design speed. The tip gap was observed to vary 0.2 mm for tests run at 4500 rpm and 6790 rpm, with typical mean levels of about 0.45 mm and 0.20 mm respectively. The mean tip clearance was found to vary as much as 0.06 mm along the circumferential direction because of static rotor eccentricity. Test-to-test repeatability revealed that the tip clearance level is sensitive to the thermal conditions of the wind tunnel as the test section warms up when hot gas blow-downs are repeated in a day. Because of this phenomenon the tip clearance was found to reduce up to 0.05 mm as the rotor assembly becomes hotter than the casing.

The blade-by-blade tip clearance measurements showed a maximum variation of 0.30 mm over the 64 rotor blades. Measurements showed that the turbine rotor maintains the same blade radius signature over one rotor revolution in the investigated speed range. Comparison of the blade heights measured in static condition and in rotation allowed to estimate the probe resolution to be 10 μm. Based on the frequency spectrum content of the raw sensor output, the vibration levels acting on the rotor disk were found to have negligible effect on the time-varying tip clearance.

Overall, the experimental investigation pointed out that tip clearance significantly change during the operation of a short duration wind tunnel and accurate measurements are required to support and validate aero-thermal experiments in such turbine test rigs.

Chapter 4

Aero-thermal flow field in the overtip casing of a transonic rotor

4.1 Introduction

The management of aerodynamic performance and thermal loads on the rotor blade tip and rotor casing remain an extraordinary challenge. Rotor tip and overtip casing of an unshrouded transonic turbine are susceptible to considerable unsteady temperatures. The understanding of the complex flow phenomena and heat transfer occurring at the blade tip gap is therefore crucial to develop new turbine designs with enhanced blade lifetime [76]. The assessment of the heat loads at different engine operative conditions becomes of utmost importance to run reliable thermal analysis that ameliorate endwall cooling strategies [77] and support design solutions for improved turbine shroud durability [78].

Noteworthy investigations have been devoted to analyze the unsteady flows on the rotor tip and shroud at the behest of the reliability and performance betterment. A substantial number of publications report studies in low speed environments or subsonic cascades [79]. Alas, low speed testing is not adequate to simulate the true high-speed flow structures inside the tip gap at engine representative Mach number [80]. The existence of shock patterns due to the overexpansion inside the tip gap have been revealed through water table experiments [81], and numerical investigations of low and high speed tip flows for a high pressure turbine [82, 83]. Heat transfer measurements on rotor blade tips have been performed mainly in high speed linear cascades, as an alternative to the onerous rotating rig. Regarding the fundamental flow topology, Newton et al. [84] observed the highest levels of heat transfer near the pressure side at the bubble reattachment. The combined experimental and numerical work done by Zhang et al. [85] revealed the presence of oblique shock waves, initiated near the pressure-side and reflected multiple times between the casing and the blade. In order to mimic the real engine conditions, experiments need to be performed in rotating test rigs at engine representative Mach and Reynolds numbers. Krishnababu et al. [86], and Zhang et al. [87], demonstrated with CFD significant differences in local heat transfer with a stationary or moving casing. One of the first studies on a fully scaled rotating transonic turbine stage was presented by Guenette et al. [88]. The authors assessed the effects of the blade passing and of the Reynolds number on the casing heat transfer. Metzger et al. [89] measured local tip and shroud heat fluxes at engine representative conditions. Didier et al. [90] performed measurements of the heat transfer on the rotor blade, hub and tip surfaces at the von Karman Institute in the transonic turbine stage investigated in this research work.

The recovery temperature is proven to be fundamental in determining the work processes occurring at the blade tip gap [91, 92]. Thorpe et al. [93, 94] presented both time-averaged and time-resolved values for the adiabatic wall temperature and heat transfer coefficient on the casing endwall, showing a decrease in temperature as work is extracted through the rotor passage. Moreover, their results reveal that the absolute stagnation temperature within the tip gap flow can rise above the turbine inlet total temperature due to the work processes performed by the blade tip. The rotor tip leakage flow can be held responsible for more than 50% of the total heat load on the casing. Recent studies performed by Wheeler [82] and Krishnababu [95] indicate a significant influence of the size of the tip clearance gap on the thermal and aerodynamic performances.

In the present research simultaneous measurements of the steady and unsteady adiabatic wall temperature, true Nusselt number, static pressure and instantaneous local tip clearance at the casing of a transonic turbine are presented. The study focuses on the understanding of the aero-thermal overtip flow and investigates the existence of correlations between the thermal and aerodynamic flow field with the rotor gap size. The experimental data were used to validate a model that predicts the flow temperature fluctuations generated by the overtip work processes. Hence, the effect of the tip leakage flow aerodynamics on the casing unsteady thermal load was evaluated. Furthermore, the implications for the design of rotor blade tip sections are discussed.

4.2 Experimental approach

4.2.1 Experiment design

Simultaneous measurements of heat transfer, static pressure and blade tip clearance were carried out on the shroud of the large high-speed turbine stage. Such turbine stage experiments are of paramount importance to reproduce the overtip flow problem at fully scaled engine conditions. The experimental testing incorporated the effects of the turbine parameters such as the radial pressure gradients, the centrifugal forces, the flow speed, the Reynolds number, and the relative casing motion that characterize the actual tip flow physics. More importantly, the flow temperature fluctuations induced by the work processes at the rotor blade tip were correctly simulated [92].

The main novelty of the proposed study is to investigate the effect of the rotor tip gap size on the unsteady casing heat transfer. An important goal of the experimental programme was to identify the individual effects of the flow-field and the gas temperature on the heat transfer generation by measuring the local adiabatic temperature and the adiabatic Nusselt number. A technique was adopted in this work that allows determining the flow driver temperature through repeat experiments at different casing wall temperatures. This procedure and the development of the suited instrumentation are described in the following sections.

The turbine was tested at a single flow regime selected to be representative of the in-flight conditions of a modern aero-engine. The stage was run at nominal pressure ratio and nominal rotor speed as described in section 2.3.2 where the main turbine flow parameters are reported. The turbine stage was tested uncooled in order to minimize the complexity of the flow and heat transfer data analysis. Accurate measurements of the single blade rotor tip clearance during the turbine run were available thanks to the capacitive-based proximity measurement system installed on the turbine shroud. Extensive data were gathered to characterize the tip clearance variations during the wind tunnel operation. At the design speed of 6790 rpm the circumferentially averaged tip clearance was about 0.2 mm, i.e., ~ 0.4% of blade span, representative of modern unshrouded large civil engines [96]. As the rotor achieves the maximum speed at the end of a test, the tip gap reduces to about 0.1 mm. The release of a hot gas through the test section warms up the rotor assembly. Because the tip clearance was observed to decrease on average 0.05 mm after six consecutive tests, a sufficient time was left between two runs to minimize the test-to-test tip gap variations in the present measurement campaign. One of the goals of this research relied upon the fact that the rotor geometry had a relatively large blade-by-blade running tip clearance variation and thus allowed the direct investigation of the effects of the tip gap parameter on the overtip aerothermodynamics. The rotor row is composed of 64 twisted blades which blade tip section is flat (Fig. 2.7) and the blade root is pin-fixed to the rotor disk. Fig. 4.1 shows the relative blade height variations against the blade number, namely the offset with respect to the longest blade measured in static and running conditions. The rotor geometry exhibits blade-to-blade tip gap variations as large as 0.3 mm. Such blade-to-blade variability allows testing the effect of tip clearance in a range comprised between 0.3% and 0.9% of the blade span in a single experiment. The tip clearance measurement system were used in all tests to record the actual single blade tip gap. Further information on the turbine test conditions and the rotor geometry are reported in Table 4.1.

Tip clearance measurements were retained of crucial importance for this research in order to correlate with high accuracy the aero-thermodynamics data with the true tip gap value. As a matter of fact, the observed discrepancies between the experimental data and the numerical prediction of the tip gap evolution in the turbine rig, the tip clearance variation caused by the facility thermal transient, and the need to evaluate the rotor tip gap signature in rotation (the blade root is pin-attached therefore it adopts the true

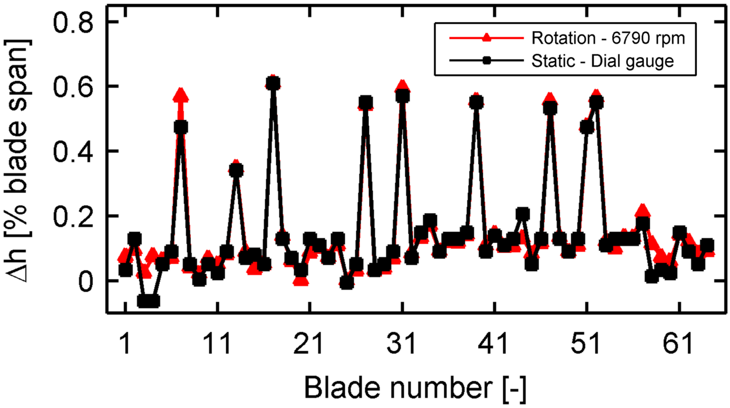

Figure 4.1: *Blade-to-blade radius signature in static and running conditions*

working position only when centrifugally loaded) would have prevented any conclusion on the correlation between the casing heat transfer and the rotor gap magnitude if accurate tip clearance measurements were not available.

Turbine operating condition		*Nom P/p - Nom speed*
Cooling massflow	[% main flow]	0.0
Design rotational speed	[rpm]	6790
Blade tip peripheral speed	[m/s]	280
Mean blade height	[mm]	54
Blade thickness at measurement axial location	[mm]	6.7
Mean tip clearance (at rest)	[mm]	~ 0.5 (1%H)
Mean tip clearance (at design speed)	[mm]	~ 0.2 (0.4%H)
HPV exit Reynolds number* (tip)	[-]	1.35×10^6
HPV exit Mach number (tip)	[-]	0.97
HPV exit flow angle (tip)	[deg]	72
Rotor relative inlet flow angle (tip)	[deg]	39
Rotor relative exit flow angle (tip)	[deg]	-56
$\Delta H/T_{01}$	[Jkg^{-1}K^{-1}]	258

*Based on chord and outlet velocity

Table 4.1: *Test conditions for the casing overtip flow investigation*

4.2.2 Rotor casing instrumentation

The investigation combined different measurement techniques such as high-frequency response surface temperature gauges, micro-thermocouples, fast-response pressure sensors, and high-frequency bandwidth blade tip clearance. Access to the overtip casing flow was provided by the three cylindrical slots (10 mm diameter) around the turbine annulus originally designed for the fitting of the tip clearance probe. Fig. 4.2a displays the three circumferential positions monitored during the experiments. The three slots are positioned at the same axial distance. The center line is at 75% of the rotor axial chord as depicted by Fig. 4.2b. Two novel probes were developed to measure the heat transfer and the static pressure. An extension support holds the probe head where the sensors and the cabling are contained. The probe-support assembly is guided through the turbine casing to the rotor tip, as illustrated in Fig. 4.2c. The probe head external surface was equipped with a thread that permits the precise adjustment of the sensors' radial position.

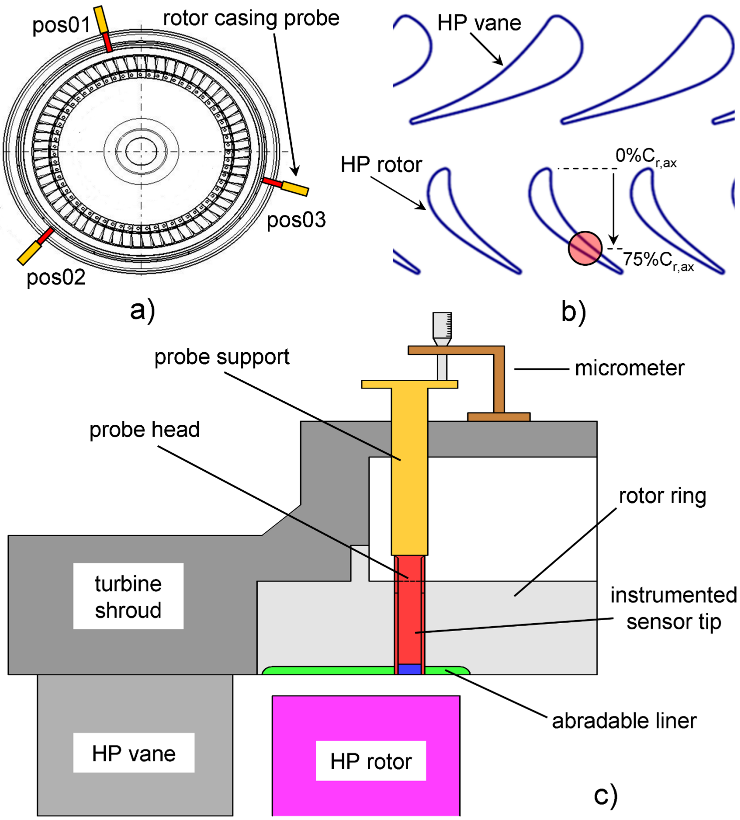

Figure 4.2: *Installation of the casing instrumentation in the turbine rig: a) circumferential locations of the instrumented probe b) axial location of the probe c) meridional view of the turbine test section*

4.2.2.1 Heat transfer probe

The rotor casing temperature were measured with high frequency bandwidth using platinum single layer thin-film gauges. The gauges consist of a thin platinum temperature resistors fired onto a ceramic substrate [97]. MACOR has been selected as the ceramic substrate due to the low thermal conductivity (enhancing surface temperature variations), electrical insulation, and easy machining. The ceramic support is shaped to be fit and held by a metallic probe head. Fig. 4.3 displays the substrate's geometry and the final probe assembly. Two thin-film sensors are set onto the ceramic substrate as shown in the right side of Fig. 4.3. The small size of the thin film gauges (1.6 mm × 0.3 mm × 0.1 μm) guarantees a large frequency bandwidth in excess of 50 kHz and high spatial and temporal resolution, required for measurements of heat flux fluctuations occurring at the rotor blade passing frequency (>7 kHz).

The understanding of the physical processes that control the heat flux generation in the endwall area requires the evaluation of the local flow temperature and convective heat transfer coefficient. The knowledge of these two parameters permits to decouple the aerodynamic from the thermal effects. A methodology, recently proposed in [93], was applied to experimentally determine the adiabatic wall temperature from a linear fit of the heat flux rates measured at different wall temperatures. A miniaturized heating system embedded inside the casing probe support was designed to allow varying the ceramic substrate temperature and thus, the wall temperature. A cylindrical cartridge heater (Firerod Watlow) with a diameter of 3.1 mm and a length of 30 mm was fitted inside a copper case, Fig. 4.3. The copper case, equipped with a pin at one of its extremities, is inserted inside a cavity dug in the ceramic substrate. The heat released by the cartridge is absorbed by the copper socket and conveyed to the MACOR block via the copper pin. The level of heating can be changed by varying the electrical power supplied to the heater and thus the wall temperature can be adjusted to different values. A power of 5 W was enough to establish a wall temperature of 340 K. The thickness of the ceramic insert resulted from a trade-off between the required thickness to ensure the semi-infinite assumption in 1D heat transfer calculations, and the maximum wall temperature achievable within a safe operation of the gauges' wiring inside the probe.

The MACOR block was also instrumented with four embedded thermocouples located at 1.5 mm and 3 mm far from the thin film sensor surface as shown in Fig. 4.3. The thermocouples provided useful information on the thermal field and the temperature gradients generated in the ceramic block. This also provided an effective tool to correct measurement drifts of the thin-film gauges. An additional thermocouple was attached in proximity of the copper case pin to monitor the metal temperature of the case during the probe operation.

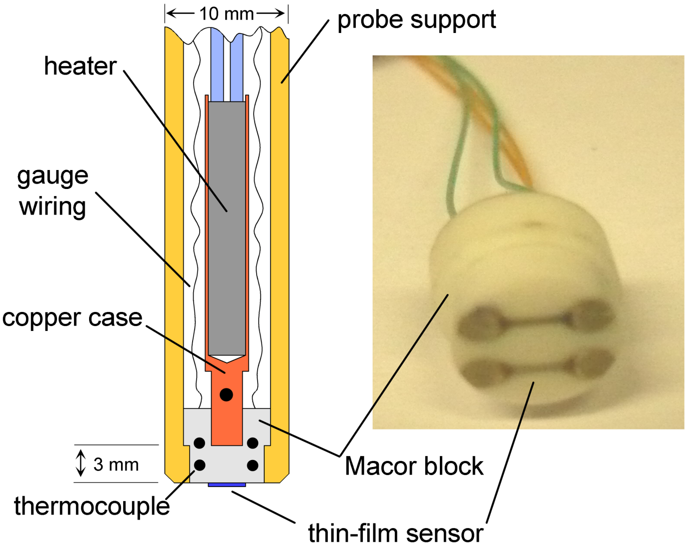

Figure 4.3: *Heat transfer probe design and instrumented ceramic insert*

4.2.2.2 Aerodynamic probe

The unsteady pressure on the rotor shroud was also measured in order to support the analysis of the heat flux data. A second probe was developed based on the same design concept as the heat transfer probe allowing simultaneous measurements at an equivalent location. A metallic insert was instrumented with two fast-response pressure sensors (Kulite® type XCQ-062) and fit into the probe head as shown in Fig. 4.4a. The pressure sensors were not flush mounted but recessed inside the metallic block by 0.2 mm underneath a 0.6 mm pressure tap. This configuration offers protection against possible damages due to the close proximity of the rotating blades and still guarantees an adequate frequency response to capture the pressure fluctuations induced by the blade passage. The probe was also equipped with a pneumatic pressure tap to facilitate the calibration of the fast-response sensors. Fig. 4.4b shows the aerodynamic probe installed on the rotor casing prior to a turbine test.

4.2.2.3 Tip clearance probe

The influence of the rotor tip clearance on the casing flow is a priority in this research. The tip clearance sensor used in this work was successfully tested in previous experiments, and the measurement system performance have been already described in chapter 3. The capacitive probe sensing element has a diameter of 5 mm and this sets its optimal working range, 0.15 - 2 mm. The sensor was positioned recessed 0.2 mm within the rotor ring

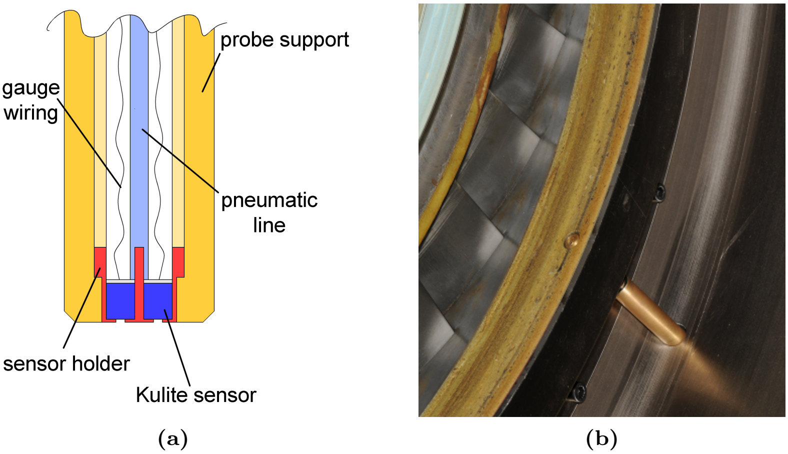

Figure 4.4: *The fast-response pressure probe: a) cut view of the probe measurement head and b) its installation on the rotor casing*

during this experimental campaign to enhance the measurement sensitivity and preserve a safety margin.

4.2.3 Measurement basics and data reduction

4.2.3.1 Measurement data acquisition

The wall temperature, static pressure and tip clearance were monitored over the entire wind tunnel operation, including the pre-test rotation (~450-500 s), the test run and the turbine slow down phase. The signals were split in three components in order to maximize the resolution of the low, medium and high frequency fluctuations during the test, and capture variations at the time scale of the test sequence (several minutes), actual blow-down duration (~0.5 s), and of the blade passing event (<0.2 ms). The low frequency content of the thermal transient was sampled on a dedicated acquisition system during 1250 s at 100 Hz. The medium frequency content, which corresponds to the transient occurring during the blow-down (similar to a step function), was low pass-filtered at 700 Hz and sampled at 2 kHz for 6 s. The high frequency signal, used to analyze the unsteady component, was high-pass filtered at 100 Hz, amplified by a factor of 10, and subsequently sampled at 1 MHz for 1.5 s where the starting of the acquisition is set to 0.5 s before the blow-down. An analog low-pass filter at 100 kHz provided the anti-aliasing filter for the high-frequency data. The tip clearance signal was directly sampled at 1 MHz. Additionally, acquisitions of the unsteady signals were made at different rotational speeds during the rotor pre-test spinning up. Once the rotor speed was stabilized, static pressure, heat transfer and tip clearance signals were acquired at 1 MHz for a duration of 2 s. Sampling the unsteady signals at high frequency was retained crucial to appropriately resolve the fast flow variations on the casing region. A minimum of 135 samples were acquired per blade passage event that corresponds to a spatial resolution of ~0.3 mm over the rotor tip area (~24 samples). The nominal blade tip thickness at the probe location is 6.7 mm.

4.2.3.2 Heat transfer measurement

The sensing thin-film gauge acts as a variable resistance thermometer which is monitored by a dedicated Wheatstone bridge. The variation of the electrical resistance with temperature was calibrated for each gauge in the range 290-360 K using a temperature controlled room where the whole heat transfer probe is placed ($T = a_T R + b_T$). Appropriate calibrations required several annealing cycles which resulted in calibration curve fits with correlation coefficients above 0.9999. Because the absolute value of the thin-film resistance (~45-50 Ω) is typically one or two orders of magnitude larger than the resistance variation generated by the blow-down of hot gas (~1 Ω), the sensor electronics can operate in two modes of amplification. In the first mode the overall resistance of the gage is measured with a gain a_{R0} =~ 0.010 Ω/V ($R_0 = a_{R0} V_0 + b_{R0}$). In the second operation mode the Wheatstone bridge is first balanced (*auto-zero* phase, the bridge outputs zero voltage), and then only resistance variations are measured with a gain 50 times higher than for the absolute operation mode ($a_{\Delta R}$ =~ 0.50 Ω/V, $\Delta R = a_{\Delta R} V + b_{\Delta R}$). The electronic board output was calibrated with a resistance reference that yields the voltage-resistance linear relationship for the two operating modes. The sensor voltage is also modulated in the electronic board by an analogue filter that has a gain shape increasing with frequency [98]. A Matlab routine was used to retrieve the original demodulated thin-film resistance that is then converted into temperature applying the calibration laws. Finally, the time-varying temperature was denoised by a digital low-pass filter. Fig. 4.5 shows an example of the post-processing steps to retrieve the wall temperature from the thin-film signal of a blow-down test. The procedure for the reconstruction of the wall temperature is identically applied to all the thin-film gauge signals acquired at the three sampling rates.

During the processing of the thin-film sensors a methodology was devised to correct eventual drifts of the wall temperature measurements. The temperature measured before a test run (when the turbine rig is under thermal equilibrium) by the thermocouples embedded in the ceramic substrate was used to correct the initial wall temperature reading. Once the thin-film voltage is converted into temperature, the wall temperature signal is offset by an amount such that the average temperature of the four thermocouples and of the corrected thin-film sensor, measured at the start of the test sequence, is equal. This type of correction is applicable only if the test-to-test signal

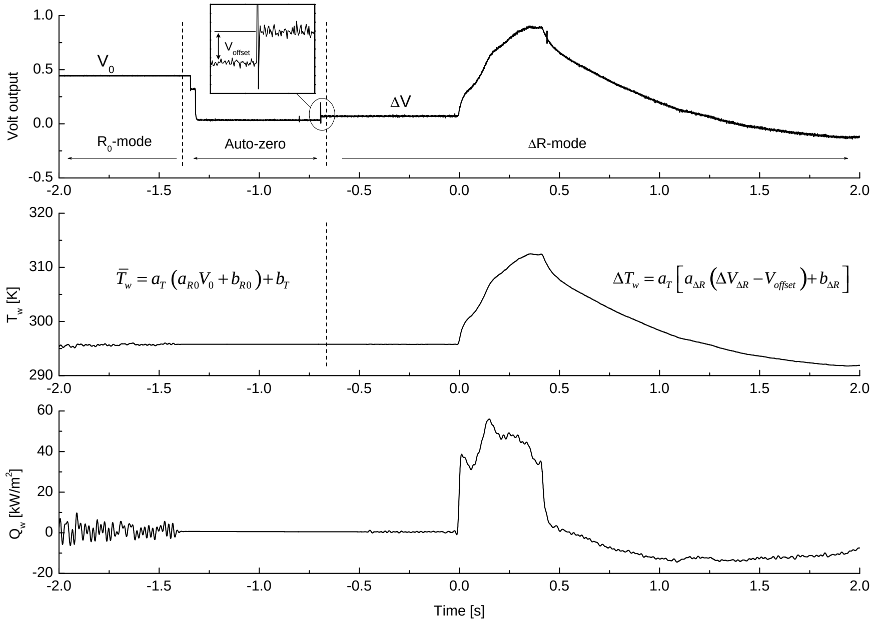

Figure 4.5: *Example of the heat transfer data reduction procedure for a typical time-averaged signal during a blow-down experiment*

drifts are not due variations of the gauge temperature sensitivity, and the four thermocouples actually measure a uniform temperature in the ceramic substrate. These conditions were always verified during the correction procedure and it was ensured that, after the compensation, the temperature difference between the thin-film and the embedded thermocouples was actually within ±1.0-1.5 K at the end of the turbine run (wind tunnel returns to thermal equilibrium but residual temperature distributions may still exist in the substrate). Fig. 4.6 illustrates an example of the correction methodology by comparing the thin-film and the embedded thermocouples readings at the beginning and at the end of the turbine test sequence.

The heat transfer at the casing wall was determined from the wall temperature data by solving the 1D unsteady heat conduction equation for a single layer substrate with known thermal properties (Macor, $\sqrt{\rho c k} = 2073$, Dénos [99]):

$$\frac{1}{\alpha}\frac{\partial T}{\partial t} = \frac{\partial^2 T}{\partial x^2} \tag{4.1}$$

A set of initial and boundary conditions are needed to solve the 1D equation. At the wall, the measured thin-film temperature is imposed, $T_w(0,t)$. Assuming a second boundary condition at the inner side wall $T(x = x_{max}, t)$, the heat conduction equation is solved with a Crank-Nicholson numerical

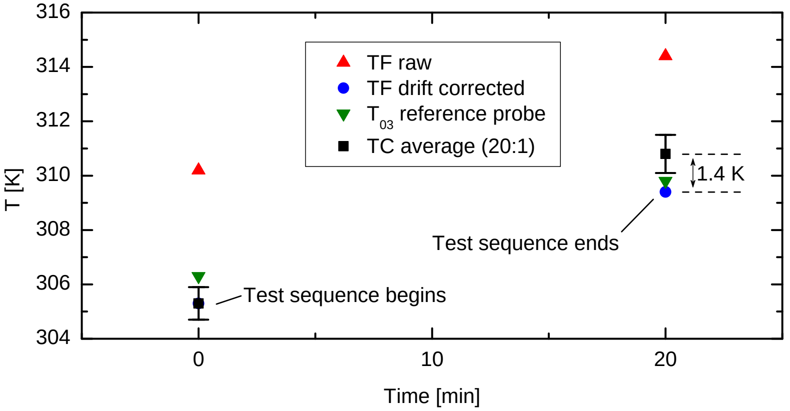

Figure 4.6: *Correction of the thin-film sensor offset based on the temperature readings of thermocouples embedded in the ceramic substrate*

discretization that provides the evolution in time of the temperature field in the substrate. The assumption of a semi-infinite boundary condition at the inner solid wall is valid as long as the duration of the transient heat transfer process remains shorter than the thermal penetration depth, estimated by $L_{\infty} = 3.648\sqrt{\alpha t}$, [99]. In the present case, being the ceramic substrate thickness 3 mm (wall to copper pin tip distance), the semi-infinite assumption holds for the blow-down time scales, i.e., test duration (0.5 s) and rotor revolution event (<10 ms). In order to calculate the heat flux during the pre-rotation, the average temperature evolution measured by the two thermocouples at 3 mm from the wall is imposed at the rear solid wall. The wall heat flux at the sensor location is derived from the Fourier law:

$$\dot{Q}_w = -k_{macor}\left(\frac{\partial T}{\partial x}\right)_{x=0} \tag{4.2}$$

where the temperature spatial derivative is calculated with a third order forward difference scheme. The resulting time-averaged heat transfer over the whole test run is reconstructed as the sum of the spinning up heating and the blow-down contribution, Solano and Paniagua [100].

The time-mean heat flux and wall temperature signals were averaged over a time window of 40-80 ms near the end of the blow-down test (t~0.4 s). The unsteady heat flux measurements were ensemble-averaged to produce a set of individual blade events that represent only the deterministic fluctuations generated by the rotor blade passage [101]. The analysis of the unsteady heat flux periodicity revealed significant blade-to-blade variations that periodically repeat every complete rotor revolution. Fig. 4.7 shows the typical frequency content of the unsteady casing wall temperature measured during a blow-down. Nearly all the signal energy is concentrated at the first (1 rotor revolution) and the second (64 blade events) engine orders. The heat transfer oscillations generated by the blade tip passage are strongly modulated by the rotor signature meaning that the fluctuations' pattern periodically repeats every rotor turn. Therefore, the averaging of the unsteady component was performed on a full rotor revolution cycle, i.e., on a phase equivalent to 360 degrees. The raw unsteady heat flux data of the blow-down measurements were averaged over 20 rotor revolutions, corresponding to 20 × 64 = 1280 rotor blade passages.

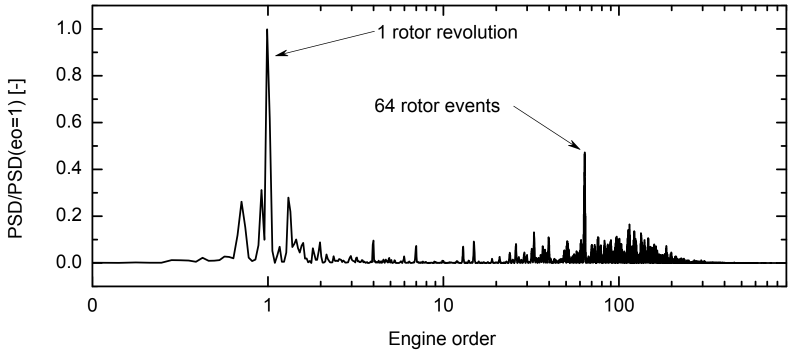

Figure 4.7: *Power spectrum density of the unsteady wall temperature at the rotor casing for a blow-down test*

An estimation of the wall temperature and heat flux measurement accuracy is provided in the following. The uncertainty analysis is based on the methodology proposed by Coleman and Steel [75], all estimates are given at the 95% confidence level and the bias and precision errors are distinguished. The measured wall temperature T_w is determined from the thin-film gauge voltage through the temperature-resistance calibration of the heat transfer sensor and the calibration of the control electronic board output. The overall measurement accuracy can be deducted by application of the following data reduction equation:

$$T_{wall} = \underbrace{a_T\left(a_{R0}V_0 + b_{R0}\right) + b_T}_{\bar{T}_{wall}} + \underbrace{a_T\left(a_{\Delta R}\left(\Delta V_{\Delta R} - V_{offset}\right) + b_{\Delta R}\right)}_{\Delta T_{wall}} \qquad (4.3)$$

The measurement system allows to monitor either the absolute wall temperature ($\bar{T}_w$) either variations of the gauge resistance ($\Delta\, T_w$). Therefore, the uncertainty limit is evaluated separately depending upon the operation mode of the wheatstone bridge. The errors introduced by the surface sensor finite thickness and the non-uniformity of the platinum layer deposition have been neglected in this analysis. The heat transfer gauge is assumed to have a repeatable response without hysteresis. When the absolute value of the thin-film resistance is monitored, the accuracy in $\bar{T}_w$ depends on the errors introduced by the gauge temperature-resistance calibration and the electronic board calibration (voltage-to-resistance linear relationship). These errors appear in $\bar{T}_w$ as bias uncertainty once eq. 4.3 is applied. Error in the measurement of the gauge voltage output is generated by the signal noise, thus considered as a random uncertainty. The uncertainty of each parameter is reported in Table 4.2 together with the corresponding error engendered in the wall temperature measurement. Typical uncertainties for the temperature-resistance calibration coefficients a_T and b_T are 0.5% and 2.3% respectively, which are principally due to the temperature non-uniformity within the calibration room (±0.1 K) and the accuracy of the reference thermometer (±0.1 K). The values of a_{R0} and b_{R0} are calibrated for each channel of the wheatstone bridge board. Precision uncertainty in the reading of the output voltage V_0 is estimated to be 0.02% of the mean voltage value. The uncertainty in the absolute wall temperature $\bar{T}_w$ can be obtained by combining all the individual errors through the use of a Root of Sum of Squares (RSSs) method.

For the current experimental conditions, the total uncertainty in $\bar{T}_w$ has a relatively high value of ±4 K, and the uncertainty due to the intercept of the resistance calibration b_T (±3.2 K) is the largest contributor. However, there exists a number of procedures to reduce the error on the wall temperature offset. The thin-film gauge resistance can be directly measured prior to a test to provide a reference value to adjust the thin-film calibration. Another method that guarantees low uncertainty on the gauge temperature intercept consists in monitoring the gauge excitation current as proposed in [102]. In the present case the wall temperature offset is corrected prior to a test with the temperature measured by the embedded thermocouples in the Macor substrate. This allows to estimate the thin-film offset with an error of ±0.2 K, generated by the thermocouple reading dispersion (±0.15 K) and by the thermocouple sensor accuracy (±0.1 K). In this way the uncertainty on $\bar{T}_w$ was reduced to ±2.4 K.

Measurement of ΔT_w is affected by errors in: gauge resistance-temperature sensitivity, electronic board calibration, gauge voltage, and voltage offset needed to correct the residual unbalance of the wheatstone bridge. The overall error in ΔT_w is estimated to be ±0.15 K, dominated by the uncertainty in a_T.

In order to improve the accuracy in the wall temperature measurements it is convenient to perform accurate temperature calibrations of the gauge resistance with more than 10 temperature points uniformly spaced across the calibration range that should encompass the expected measurement range. More importantly, the evolution of the thin-film resistance during a blowdown test should be preferably monitored using the relative operational mode (ΔR) of the wheatstone bridge.

The uncertainty in the wall heat flux measurement is evaluated according to the following equation:

$\bar{T}_w = a_T\left(a_{R0}V_0 + b_{R0}\right) + b_T$					
Parameter		*Mean*	$\Delta\theta_i$ [%*mean*]	$\frac{\Delta T_w[\%]}{\Delta\vartheta_i[\%]}$	$\frac{\partial T_w}{\partial\vartheta_i}\Delta\vartheta_i\ [K]$
a_T	K/Ω	10.08	0.50%	1.47	2.177
b_T (cal. interc.)	K	-139.71	2.29%	0.47	3.202
b_T (TC correction)	K	-139.71	0.14%	0.47	0.201
a_{R0}	Ω/V	99.78	0.15%	1.48	0.679
b_{R0}	Ω	-0.56	14.09%	0.02	0.789
V_0	V	0.44	0.02%	1.48	0.111
$\bar{T}_w$ (cal. interc.)	K	300.00			±**4.01** (20:1)
$\bar{T}_w$ (TC correction)	K	300.00			±**2.42** (20:1)
$\Delta T_w = a_T\left(a_{\Delta R}\left(\Delta V_{\Delta R} - V_{offset}\right) + b_{\Delta R}\right)$					
Parameter		*Mean*	$\Delta\theta_i$ [%*mean*]	$\frac{\Delta T_w[\%]}{\Delta\vartheta_i[\%]}$	$\frac{\partial T_w}{\partial\vartheta_i}\Delta\vartheta_i\ [K]$
a_T	K/ohm	10.08	0.50%	1.0	0.149
$a_{\Delta R}$	Ω/V	2.02	0.08%	1.0	0.023
$b_{\Delta R}$	Ω	0.01	60.23%	0.002	0.032
ΔV	V	1.52	0.02%	1.0	0.008
V_{offset}	V	0.05	0.39%	-0.03	-0.004
ΔT_w	K	30.00			±**0.15** (20:1)
T_w (TC correction)	K	300.00			±**2.43** (20:1)

Table 4.2: *Wall temperature uncertainty*

$$\dot{Q}_w = \frac{\sqrt{\pi}}{2}\sqrt{\rho c k}\frac{\Delta T}{\sqrt{\Delta t}} \tag{4.4}$$

Eq. 4.4 describes the relationship between the heat flux and the measured parameters in the case of an heat transfer step with mono-dimensional heat conduction through a semi-infinite substrate. Heat transfer measurements are affected by uncertainties in the measured wall temperature change (ΔT_w) and in the thermal product of the substrate ($\sqrt{\rho c k}$), which appear as fixed bias errors. Only wall temperature variations must be considered for the determination of the heat flux since the initial substrate temperature does not to affect the heat flux evolution in the investigated experimental temperature range. Hence, the contribution of the wall temperature error can be considered negligible. Previous measurements for Macor ceramic have shown that the uncertainty in the thermal product is about ±6% (20:1) [99]. The numerical algorithm used in the heat flux data reduction introduces minor errors. The effect of the thin-film layer thickness on the flow status is also considered negligible [97]. The largest source of uncertainty in $\dot{Q}_w$ comes from the thermal product and the overall uncertainty in heat transfer is ±6.0%. Table 4.3 summarizes the contribution of the measured parameters to the wall heat flux uncertainty.

4.2.3.3 Adiabatic wall temperature and Nusselt number measurement

The flow on the overtip casing of a shroudless turbine is intrinsically unsteady as the rotor blade motion induces fierce fluctuations of the aero-

		$Q_w = \frac{\sqrt{\pi}}{2}\sqrt{\rho c k}\frac{\Delta T}{\sqrt{\Delta t}}$			
Parameter		*Mean*	$\Delta\theta_i$ $[\%mean]$	$\frac{\Delta Q_w[\%]}{\Delta\vartheta_i[\%]}$	$\frac{\partial Q_w}{\partial\vartheta_i}\Delta\vartheta_i$ $[kW]$
$\sqrt{\rho c k}$	$\mathrm{Jm^{-2}K^{-1}s^{-0.5}}$	2073	6.00%	1.0	5.23
$\Delta \mathrm{T_w}$	K	30	0.51%	1.0	0.45
$\mathrm{Q_w}$	kW	87.00			±**6.0%** (20:1)

Table 4.3: *Wall heat flux uncertainty*

dynamic conditions in this region. The heat transfer is therefore highly time-dependent because of temporal variations in convective heat transfer coefficient (velocity and pressure fluctuations), and temporal changes of flow recovery temperature (unsteady work processes). It is apparent that the measurement of heat flux is not sufficient to capture the physical origin of the heat transfer fluctuations. Hence, the measurement of the adiabatic wall temperature and the adiabatic local convective coefficient becomes a primary goal for this research.

The determination of the time-resolved adiabatic wall temperature is based on the measurement of the heat flux at a number of casing wall temperatures. This requires multiple tests to be run in the turbine rig with the local wall temperature adjusted to a different level before each blow-down. The time-mean heat transfer rate and the time-mean wall temperature of each test are averaged over a time window of 40-80 ms to yield single values representative of the heat transfer and wall temperature when the turbine operates at correct aerodynamic conditions. The average heat flux is added to the time-periodic component dataset (zero-mean) to reconstruct the time-resolved heat flux over a rotor revolution. Hence, the time-resolved heat flux of each test can be plotted against the rotor phase and the average wall temperature. At a certain rotor phase, the change in wall heat flux can be modeled as a linear function of the wall temperature over the investigated temperature range [103]:

$$\dot{Q}_w\left(\varphi\right) = h_{aw}\left(\varphi\right)\left(T_{aw}\left(\varphi\right) - T_w\right) \tag{4.5}$$

where the adiabatic wall temperature is determined as the wall temperature that yields zero heat flux [102]. The local convective heat transfer coefficient is the gradient of the linear regression line that fits the experimental data as prescribed in eq. 4.5. The Nusselt number can be determined based on the adiabatic wall temperature as:

$$Nu = \frac{\dot{Q}_w}{\left(T_{aw} - T_w\right)}\frac{C_{ax,r}}{k_{air}} \tag{4.6}$$

This procedure can be applied to all the rotor phase instants assuming that the boundary layer is always in a quasi-steady state. This assumption can be considered valid if the response time of the boundary layer is sufficiently short compared to the time-scale of the aerodynamic periodic fluctuations. In the case of thin high-speed boundary layers typically found in highly loaded turbines, the boundary layer time response is very fast (few microseconds), and relatively slow flow fluctuations happening at the blade frequency (~0.10-0.15 ms) can be tolerated [94, 104].

An example of the procedure for the adiabatic wall temperature data reduction is given in Fig. 4.8 for a particular value of the rotor phase (0.52). It should be noted that the adiabatic wall temperature can be related to the total temperature through a recovery factor that is function of the Mach number. The adiabatic wall temperature can be interpreted as the local flow total temperature in the close proximity of the casing endwall if the Mach number is known [93]. The difference in these two temperatures would be less than 2.5% at a Mach number of 1 and assuming a recovery factor of 0.86. Therefore, the adiabatic wall temperature provides a qualitative representation of the flow thermodynamics and can be used to investigate the work exchanges undergone by the fluid across the rotor row. In the following the adiabatic wall temperature will be also referred as the local driver temperature.

The determination of the adiabatic wall temperature and heat transfer coefficient is based upon the fit of the experimental heat flux and wall temperature data through the use of eq. 4.5. Therefore, the uncertainty in these parameters is influenced by a number of factors: the number of measurement points employed to define the linear fit, the wall temperature range spanned in the experiments, the error in the heat flux measurement and the repeatability of the experimental conditions in the turbine wind tunnel.

A statistical analysis was carried out using a Monte Carlo type approach to investigate the propagation of the error in each measurement parameter in the resulting uncertainty in T_{aw} and h_{aw} for typical experimental scenarios. The following analysis provides useful guidelines to design experiments for the determination of the adiabatic wall temperature and convective coefficient. A baseline case was selected which represents the actual experimental conditions. The influence of each parameter on the uncertainty in T_{aw} and h_{aw} was separately studied as a function of the adiabatic wall temperature. A fixed convective heat transfer coefficient was considered in the calculations (h_{aw}=2000 $\mathrm{Wm^{-2}K^{-1}}$).

The results of the parametric uncertainty analysis are illustrated in Fig. 4.9. The number of experimental data points has a significant effect on the precision uncertainty in T_{aw} and h_{aw}. As a larger number of data points is used, the error in the experimental data fit reduces. However, use of a larger number of data points becomes truly beneficial only when the adiabatic wall temperature does not fall within the spanned wall temperatures, i.e, the T_{aw} is found by extrapolation. Increasing the wall temperature range leads to a reduction of the random uncertainty in both T_{aw} and h_{aw}. As an example, the upper middle plots of Fig. 4.9 shows that if an adiabatic wall temperature of 450 K has to be measured, the random uncertainty

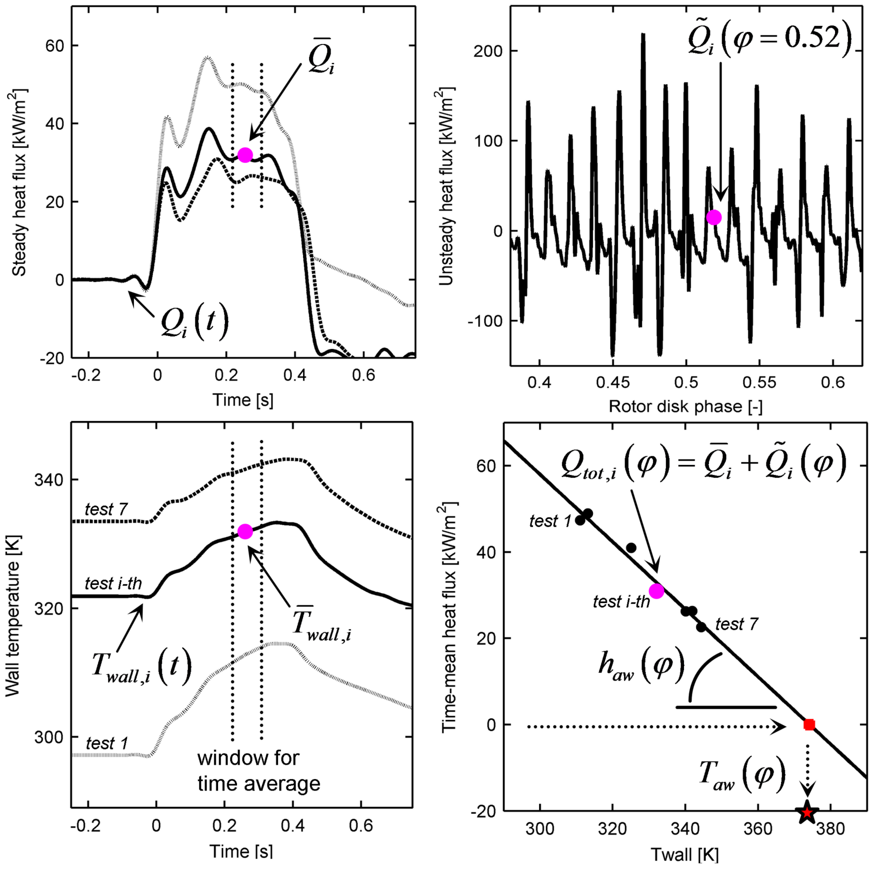

Figure 4.8: *Procedure for heat transfer and adiabatic wall temperature data reduction*

in T_{aw} drops from ±40 K to ±5 K when the T_w range is extended from ±25 K ±100 K (around the same mean T_w=325 K). The error in convective coefficient reduces from 30% to 5%.

Because the measurement of the adiabatic wall temperature is based on a multiple test strategy, the random error is significantly affected by the repeatability of the aero-thermodynamic conditions established in the turbine experiment. According to eq. 4.5, the factors related to the test-to-test variability are the Reynolds number (change in h_{aw}), the turbine inlet total temperature (change in T_{aw}), and the rotor tip clearance (change in T_{aw} and h_{aw}). The variations in run conditions are assumed to generate normally distributed random errors into the measurement of the wall heat flux and thus in T_{aw} and h_{aw}. Analysis of the uncertainty propagation of the test-to-test variability into T_{aw} and h_{aw} was carried out for three heat flux repeatability levels. The baseline case (±4%) is representative of the actual performance of the turbine wind tunnel. The lower middle plots of Fig. 4.9 display the overall uncertainty in T_{aw} and h_{aw} as a function of the random error in $\dot{Q}_w$. The run-to-run repeatability has a great impact on the uncertainty in T_{aw} and h_{aw} when the adiabatic wall temperature falls outside the spanned T_w range. The bias error in the measured heat transfer rate does not influence the measurement of adiabatic wall temperature. In contrast the bias error in ΔT_w propagates through the data reduction equation (eq. 4.5). However, the resulting bias error in T_{aw} is negligible. The measurement of h_{aw} is affected by bias errors in $\dot{Q}_w$ and T_w. The bias errors in ΔT_w and $\dot{Q}_w$ propagate into T_{aw} and h_{aw}:

$$\begin{aligned}
[\Delta T_{aw}]_{T_w} &= \frac{\partial T_{aw}}{\partial T_w}\Delta T_w \approx 0 \\
[\Delta h_{aw}]_{T_w} &= \frac{\partial h_{aw}}{\partial T_w}\Delta T_w \approx 0 \\
[\Delta h_{aw}]_{\dot{Q}_w} &= \frac{\partial h_{aw}}{\partial \dot{Q}_w}\Delta \dot{Q}_w = h_{aw}\frac{\Delta \dot{Q}_w}{\dot{Q}_w}
\end{aligned} \tag{4.7}$$

Improvement of the test condition repeatability would always increase the overall accuracy in the adiabatic wall temperature measurement. In contrast, the lowest total error in convective heat transfer coefficient is limited by the bias error in wall heat transfer (error in the thermal product).

The effect of two additional factors on the measurement error in adiabatic wall temperature and convective heat transfer coefficient was also investigated: the change of the thermal product value with temperature, and the non-linear variation of the convective coefficient as a function of the substrate wall temperature. It must be noted that these two parameters do not introduce a statistical uncertainty, but rather an offset in the measured T_{aw} and h_{aw}.

The thermal properties of the ceramic substrate are usually assumed to remain constant over the spanned wall temperature range and a fixed value of $\sqrt{\rho c k}$ from calibration at ambient temperature (300 K) is used through the data reduction. However, the thermal product of Macor has been shown to vary with temperature at a rate of 0.1% per degree Kelvin [97, 105]. Therefore, the thermal product varies proportionally with the wall substrate temperature. Here, for the sake of simplicity, it is assumed that the wall temperature variation during a single experiment does not cause a change in the thermal product value. The corrected values of T_{aw} and h_{aw} can be estimated via the following equations:

$$\begin{aligned}
\dot{Q}_w^{'} &= \dot{Q}_w + \dot{Q}_w Y \left(T_w - T_{ref}\right) \\
T_{aw}^{'} &= T_{w,1} - \frac{\dot{Q}_{w,1}\left[1 + \left(Y\left(T_{w,1} - T_{ref}\right)\right)\right]}{h_{aw,\exp}} \\
h_{aw}^{'} &= \frac{\dot{Q}_{w,2}\left[1 + \left(Y\left(T_{w,2} - T_{ref}\right)\right)\right] - \dot{Q}_{w,1}\left[1 + \left(Y\left(T_{w,1} - T_{ref}\right)\right)\right]}{\left(T_{w,2} - T_{w,1}\right)}
\end{aligned} \tag{4.8}$$

where Y ([1/K]) is the rate of change of $\sqrt{\rho c k}$, T_{ref} is the temperature at which the thermal product calibration is performed, and the subscripts 1 and 2 denote the heat flux measured at the lowest and largest wall temperatures. The error in T_{aw} associated to the thermal product variation with temperature remains below ~2 K for adiabatic wall temperatures within the wall temperature range (bottom left plot of Fig. 4.9). However, the adiabatic wall temperature is significantly overestimated when the wall temperature range does not encompass T_{aw}. The error in h_{aw} is directly proportional to the variation of the thermal product with temperature (bottom right plot of Fig. 4.9). In the investigated wall temperature range, using a value for $\sqrt{\rho c k}$ calibrated at temperatures close to the mean wall temperature (T_w=325 K) provides almost no improvement. It is important to remark that the error due to changes of thermal product with temperature only affects the time-average adiabatic wall temperature and convective heat transfer coefficient. Large unsteady fluctuations in T_{aw} and h_{aw} at blade passing frequency generate instantaneous heat flux oscillations to which correspond wall temperature variations below 1 K in the present application. On the other hand, this error can be reduced by using a modified value of the thermal product in the heat flux data reduction as a function of the initial substrate temperature.

In order to determine the adiabatic wall temperature and the convective heat transfer coefficient a straight least-square fit is performed on the experimental wall heat flux and temperature data. This procedure assumes that a linear relationship exists between the measured heat flux and the wall temperature, i.e., the heat transfer coefficient is constant over the spanned wall temperature range. Fitt et al. [106] demonstrated that for a flat plate at constant free-stream Reynolds number and flow total temperature, the ratio of convective heat transfer coefficients at two wall temperatures is:

$$\frac{h_{aw,1}}{h_{aw,2}} = \left(\frac{T_{w,1}}{T_{w,2}}\right)^{-0.25} \tag{4.9}$$

Eq. 4.9 illustrates that in reality h_{aw} is not ideally constant over a defined wall temperature range, and therefore a non-linearity error is introduced when eq. 4.5 is applied to the experimental measurements. The error that is introduced is twofold: 1) the h_{aw} determined as the slope of the experimental data fit can be considered as the average of the convective coefficients that would be measured at the different experimental wall temperatures.

Therefore, an error is introduced since the variation of the convective coefficient is not linear with the wall temperature. 2) An additional error arises if the mean wall temperature does not correspond to the actual wall temperature that is used for the definition of the target gas-to-wall temperature ratio.

The error in h_{aw} can be determined through eq. 4.9 considering uniformly spaced wall temperature samples, and that a temperature difference exist between the mean experimental wall temperature ($T_{w,mean}$) and the reference wall temperature ($T_{w,ref}$) that defines the gas-to-metal temperature ratio of the experiment:

$$\begin{aligned}
\Delta h_{aw,range} &= h_{aw,\exp}\left\{1-\frac{1}{2}\left[\left(\frac{T_{w,1}}{T_{w,mean}}\right)^{-0.25}+\left(\frac{T_{w,2}}{T_{w,mean}}\right)^{-0.25}\right]\right\}\\
\Delta h_{aw,ref} &= h_{aw,\exp}-\left[h_{Tw,range}\left(\frac{T_{w,ref}}{T_{w,mean}}\right)^{-0.25}\right]\\
\Delta h_{aw,nonlin} &= h_{aw,\exp}-\Delta h_{aw,range}-\Delta h_{aw,ref} \qquad (4.10)
\end{aligned}$$

The modification of the convective coefficient implies also the correction of the adiabatic wall temperature that can be estimated through:

$$\Delta T_{aw,nonlin} = T_{aw,\exp}-\frac{\dot{Q}_{w,mean}}{(h_{aw,\exp}-\Delta h_{aw,range}-\Delta h_{aw,ref})} \qquad (4.11)$$

The errors in the estimation of the adiabatic wall temperature and convective heat transfer coefficient are plotted in Fig. 4.9. The calculations were performed considering a $T_{wall,ref}$=300 K. The error in T_{aw} is relatively small (-5 K < ΔT_{aw} < 10 K for 250 K < T_{aw} < 600 K) compared to the total uncertainty that affects the measurements. The impact of the wall temperature range is of minor importance. The error in the convective heat transfer coefficient is also limited (<2-4%), is independent of the adiabatic wall temperature value, and is feebly affected by the wall temperature range. It has to be noted that the corrections for T_{aw} and h_{aw} proposed here are only an approximation of the real problem. However, eq. 4.10 and 4.11 provide a simple tool to assess the magnitude of the deviation between the actual T_{aw} and h_{aw} and the experimental values determined by means of the multi-test strategy.

The experimental conditions of the turbine study were T_{aw} ~370 K and 300 K ≤ T_w ≤ 350 K and typically 7 data points were used to perform the data fit. The overall uncertainty in the time-average adiabatic wall temperature is estimated to be less than ±5 K. However, for unsteady T_{aw} fluctuations beyond 500 K the error rises above ±25 K. Typical values for the total uncertainty in convective heat transfer coefficient are 10% at moderate T_{aw} (350-400 K), increasing above 20% for T_{aw} > 550 K.

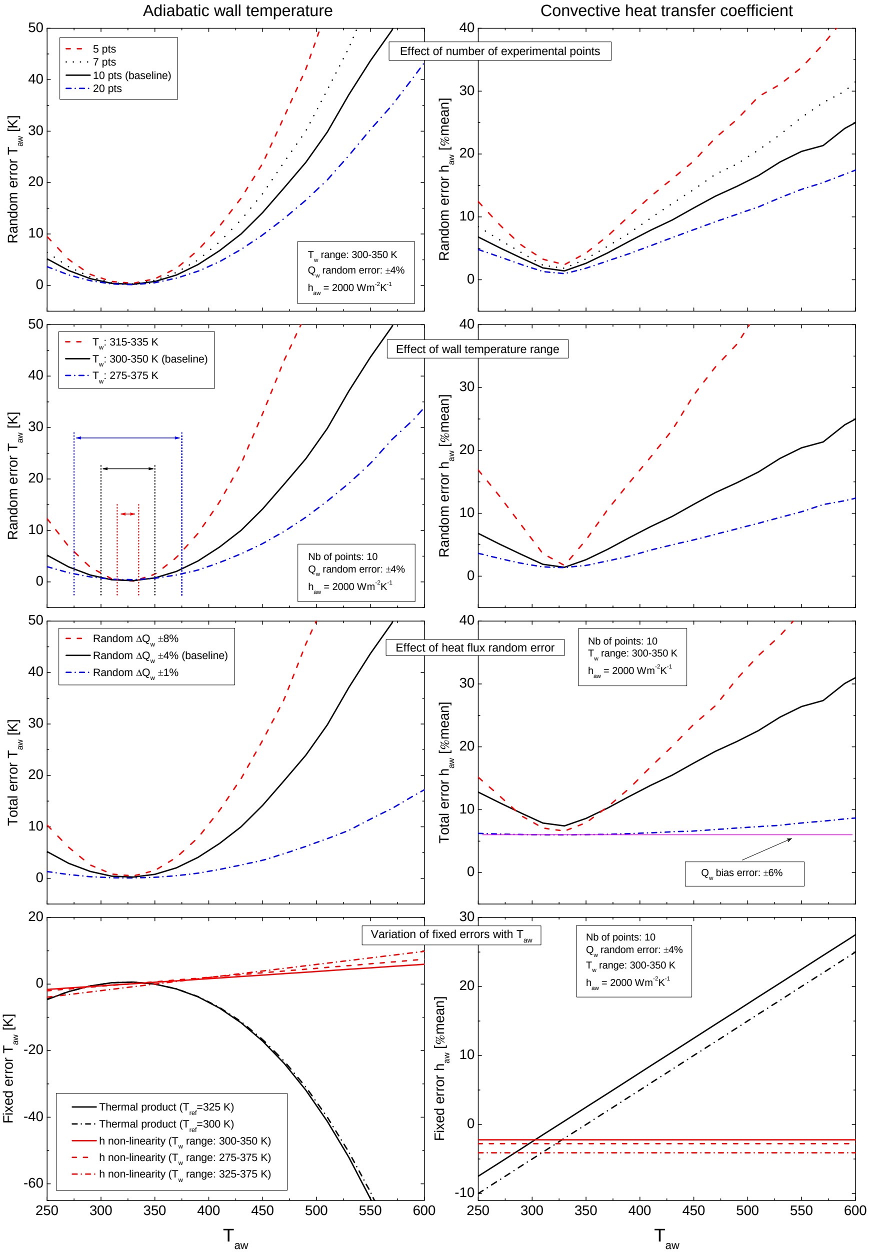

Figure 4.9: *Parametric analysis of the adiabatic wall temperature and convective heat transfer coefficient uncertainty*

4.2.3.4 Static pressure measurement

The time-resolved static pressure fluctuations in the rotor casing were measured with fast-response strain gauge Kulite transducers (Fig. 4.10a). The pressure sensor is composed of four piezo-resistors arranged in a Wheatstone bridge as shown in Fig. 4.10b. Two of the four sensing elements work in compression while the other two experience tension. The overall bridge resistance remains unaltered but the bridge unbalance is directly proportional to the pressure applied on the gauge surface. These semi-conductor sensors are known to be temperature sensitive. Both the zero offset and sensitivity of the gauge are affected, and therefore a compensation of the temperature effect is needed to perform accurate pressure measurements. This becomes of particular importance for measurements in the short-duration turbine rig where large temperature transients occur. In order to monitor the pressure and the temperature of the sensor membrane, a double wheatstone bridge configuration is adopted with an external resistor that measures the bridge sensitivity to temperature (V_s, Fig. 4.10b). A data-reduction procedure was used that allows a precise control of the temperature-induced error by including the span and offset sensitivities to temperature into the calibration of the fast-response pressure gauge:

$$P_{kul} = (a_1 V_s + b_1) V_p + (a_2 V_s + b_2) \tag{4.12}$$

The calibration of the piezo-resistive pressure transducer was performed in-situ during a rotor spinning up cycle where pressure and temperature transients are generated by releasing into the test section, initially under vacuum, the air supply of the turbine aero-brakes. Due to the friction between the air and the rotating blades (ventilation losses), the gas temperature increases. The sensor voltage output (V_p and V_s) is monitored during the entire duration of the pressure and temperature transient. At the same time, a pressure measurement is performed by means of a pressure tap located in proximity of the Kulite sensor and connected via a pneumatic line to a slow-response transducer outside the test section. The pneumatic measurement, insensitive to temperature, provides the reference pressure for the calibration of the fast-response gauge. The four coefficients (eq. 4.12) of the fast-response sensor calibration are determined through an optimization routine that minimizes the difference between the two pressure measurements. An example of a typical calibration for a Kulite transducer is illustrated in Fig. 4.10c. Details on this compensation technique are given by Ainsworth et al. [107] and Dénos [108]. The data reduction procedure for the temperature compensation ensures an accuracy of ±10-15mbar (20:1) in the DC part of the kulite pressure measurement, the most affected by the thermal drift [101]. The time-resolved pressure component has also been calibrated using the full set of calibration coefficients according to eq.4.12. The error in pressure increases as the temperature transient is larger. However, temperature variations happening at the time-scale of a rotor revolution can be considered very limited and thus, the uncertainty on the unsteady pressure fluctuations is estimated to reduce to ±5mbar (20:1).

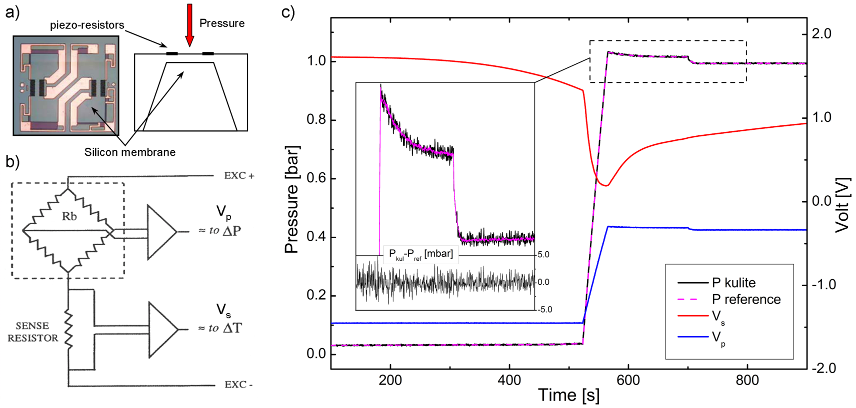

Figure 4.10: *Fast-response Kulite pressure gauge: a) structure of the piezo-resistive sensor b) circuitry operating principle c) example of sensor calibration for temperature correction*

The fast-response pressure sensor was embedded inside the the casing probe support for safety purposes. However, this arrangement produces a reduction of the instrumentation promptness due to the presence of a cavity between the sensor membrane and the surface pressure tap. The small volume of the cavity introduces a resonance frequency in the transducer response limiting the sensor bandwidth. Fig. 4.11 shows the frequency content of a typical unsteady pressure measurement on the rotor casing during a test. The cavity resonance band is visible at around 90 kHz while the transducer natural frequency is located at approximately 290 kHz. The aerodynamic probe can be considered prompt up to 70 kHz without digital compensation. This means that up to 10 harmonics of the blade passing frequency (7.2 kHz) can be captured. All the unsteady pressure data have been digitally low-pass filtered at 70 kHz before applying any further data reduction.

The data processing of the casing static pressure data follows the same procedure adopted for the thin-film measurements. The time-average kulite signal is first calibrated and then averaged over a time window of 40 ms close to the test end. The unsteady signal component is low-pass filtered and then phase-lock averaged at the rotor disk passing frequency over 20 rotor revolutions.

4.2.3.5 Tip clearance

The capacitive tip clearance probe provided the individual tip-to-casing gap over the 64 blades of the turbine stage. The sensor was calibrated in situ

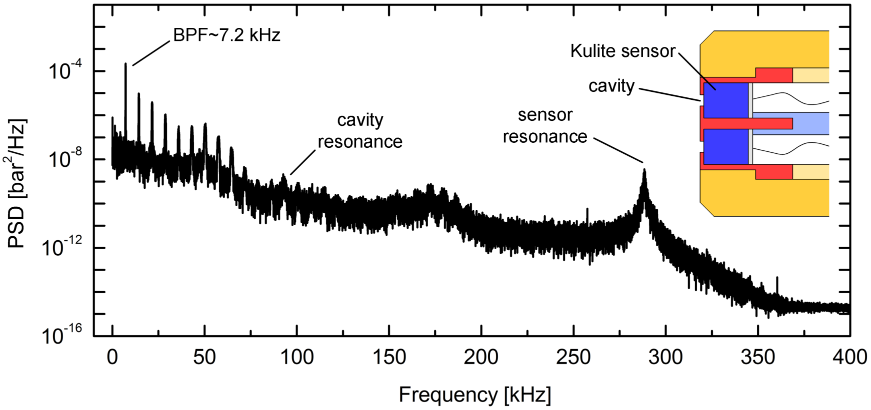

Figure 4.11: *Example of the frequency content of an unsteady pressure signal measured at the rotor casing during a blow-down*

thanks to the self-calibration technique proposed in section 3.3.3 since at the moment of the experimental campaign wear gauges at the rotor casing were not available. The self-calibration is performed by displacing the proximity measurement probe inside the rotor casing ring at several positions during a spinning-up procedure at a stabilized rotor speed close to the test design value of 6790 rpm.

Once the probe calibration is available, the capacitance sensor voltage is converted into tip clearance. The time-varying tip gap signal is further processed to yield the blade-average and the blade-to-blade tip clearance information together with the rotor speed and acceleration for the entire test duration. The phase-averaged heat transfer and static pressure data are synchronized with the tip clearance signature in rotation allowing direct comparison for each single blade. In order to obtain the actual value of the single blade tip clearance at each of the three peripheral measurement locations, the relative difference in circumferential tip clearance is subtracted from the real-time blade tip gap measured by the proximity probe at its current position.

The uncertainty associated to the tip clearance measurements is discussed in detail in section 3.5. The error largely depends on the sensor operating range and for the rotor casing measurements the overall uncertainty is estimated to be less than $\pm 15\mu$m (20:1) being the probe tip recessed 0.2 mm inside the rotor casing.

A methodology that relies on the capacitance sensor output was devised to provide a rough estimate of the relative pitch-to-pitch variations (i.e., blade-to-blade changes of the rotor passage width) in rotation. The distance between two passing blades is estimated as the temporal difference between two consecutive local maxima in the raw tip clearance signal. Local peaks in the capacitance sensor output are representative of the instantaneous passage of the blade underneath the capacitance probe tip. In order to account for the variation of the rotational speed during the test, the blade-to-blade pitch variation is normalized by the mean blade passage width at each rotor turn. Although the capacitance sensor signal shape is not especially suited for accurate detection of the blade passing event, the blade-to-blade pitch signature showed a high level of repeatability both at subsequent rotor revolutions and at different rotor speeds. This gave confidence that the applied methodology was reliable. Fig. 4.12 shows the pitch-to-pitch variability with repeatability levels on 16 tests (95% confidence level). The investigation of the rotor geometry variability was completed by the measurement of the blade thickness of each of the 64 rotor airfoils. A high-resolution photo-camera was installed on a fixed location in proximity of the rotor blading where optical access to the airfoil rear tip profile was available. The blade thickness was measured based on the number of pixels contained within the blade profile. The processed images had a resolution of ~70 pixels/mm. The measured blade-to-blade profile thickness variation is also plotted in Fig. 4.12.

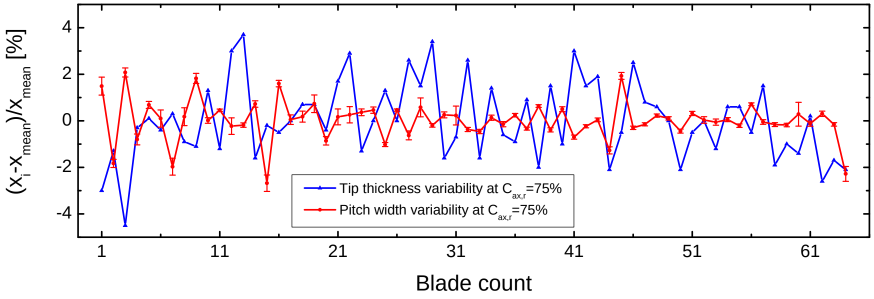

Figure 4.12: *Blade-to-blade rotor pitch and thickness variations at the casing measurement location ($x/C_{ax,r}$=0.75)*

4.3 Results

The collected measurement dataset is analyzed focusing first on the time-averaged data, and then on the time-resolved measurements. In the following discussion emphasis is given to the unsteady character of the heat transfer and aerodynamics in the casing region related to the rotor passage events and the tip clearance fluctuations.

4.3.1 Time-average results

The heat transfer data were used to reconstruct the evolution in time of the local driver temperature and convective coefficient (expressed through the adimensional parameter Nusselt number) during a blow-down. An example is illustrated in Fig. 4.13. Both T_{aw} and Nu rise at the beginning of the experiment as hot gas enters the test section and the correct aerodynamic conditions establish in the turbine. The heat transfer parameters are sensitive to fluctuations of the turbine temperature and speed levels, and remain constant for about 150 ms around t~0.2-0.35 s. The measured adiabatic wall temperature is close to the total temperature measured at the rotor outlet and in line with the expected total temperature value at the tip region ($T_{03,tip} = 370K$) based on a NISRE calculation.

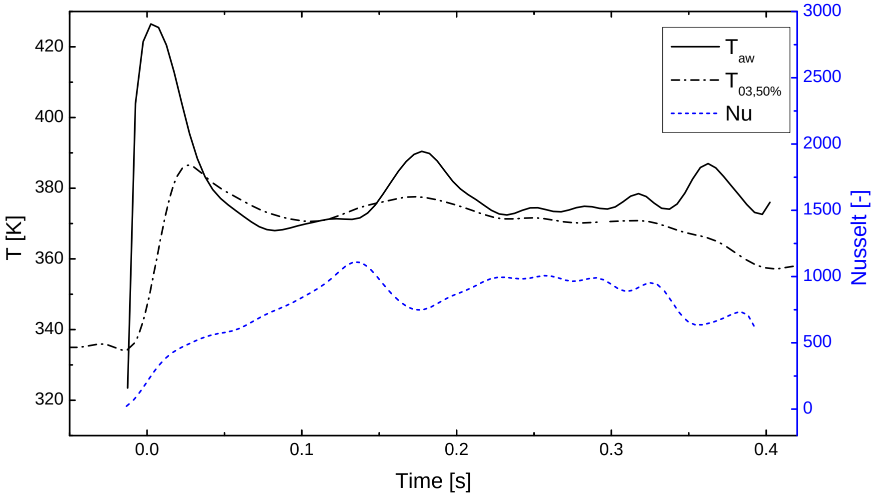

Figure 4.13: *Evolution of rotor casing adiabatic wall temperature and Nusselt number during a turbine blow-down*

The time-average values of the adiabatic wall temperature, Nusselt number and static pressure are presented in Table 4.4 together with the blade-average tip clearance. The heat transfer and static pressure were measured with the two probe sensor pair (both thin-film and fast-response pressure sensors) aligned with the turbine axis in order to maximize the sensitivity to blade-induced fluctuations. The circumferentially-averaged tip clearance was measured to be 0.35% of the blade span over the 64 rotor blades at 6790 rpm. Tip gap measurements at the three circumferential positions revealed a limited static rotor eccentricity (less than 0.1% of the blade span) due to the casing bore ovality and positioning of the rotor disk. The dynamic eccentricity was estimated to be negligible in the investigated rotor speed range (see chapter 3). The time-average heat transfer data showed that the adiabatic wall temperature at position 01 and 02 is 1%- 3% above the total temperature measured at mid-span of the rotor outlet (T_{03} ~360 K). The experimental observation reflects the decay in flow total temperature along the axial direction as work is extracted by the rotating blades. The adiabatic wall temperature varies 2% of T_{01} (~9 K) depending upon the circumferential position. This can be explained by different relative locations of the shroud casing instrumentation with respect to the upstream high-pressure vane. The rotor-stator interaction is the driving mechanism that generates circumferential local flow distortion as already observed by Thorpe et al. [93], who measured peripheral temperature variations in the range of ~8 K at 80% of the rotor axial chord and 10% variation for the local Nusselt number. In this study, the experimental Nusselt number exposed a negligible change at two casing locations, below 1%. Hence, it appears that the small difference in average tip clearance between position 01 and 02 (0.1% of blade span) does not influence the convective heat transfer processes in the investigated clearance range (0.3-0.4% h/H). The average local Nusselt number measured at 75% of the rotor axial chord is around 980. This is in agreement with the experimental values of casing convective heat transfer coefficients measured in the experimental investigations of Guenette et al. [88] and Chana et al. [96] on a transonic turbine stage.

The time-averaged static pressure at the rotor casing is also reported in Table 4.4, normalized by the inlet total pressure. The data showed again a subtle change depending on the circumferential position of about 2.5% of P_{01}. The static pressure mean value is strongly dependent on the amplitude of the unsteady static pressure fluctuations. The rotor tip clearance gap size is one of the key parameters that control the aerodynamics of the tip flow, by defining the geometry of the duct for the tip leakage jet. The investigated HP rotor has a highly subsonic exit blading (Mach number 0.9 at the tip section) and transonic speed can be expected on the blade suction side. As demonstrated by Wheeler et al. [82], for large blade width-to-gap ratios (s/h ~32 in the present case) the flow is likely to be transonic within the tip gap itself. Thus, a variation of the mean tip clearance will also impact on the time-averaged static pressure field. Moreover, it has to be noted that the average static pressure field was weakly affected by the signature of the vane exit flow on the aft part of the rotor blade, as observed by Thorpe [93].

	Casing circumferential position		
P_{01}/P_{s3}		2.92	
T_{03}/T_{01}		0.77	
	Pos01	*Pos02*	*Pos03*
h/H	0.32%	0.41%	0.29%
P_s/P_{01}	-	0.387	0.363
T_{aw}/T_{01}	0.768	0.796	-
Nu	989	973	-

Table 4.4: *Time-averaged results at the rotor casing ($75\%C_{r,ax}$) and measured stage inlet conditions*

4.3.2 Time-resolved results

4.3.2.1 Time history analysis

Fig. 4.14 shows the adiabatic wall temperature, the Nusselt number and the static pressure ensemble averaged fluctuations measured on the rotor casing as a function of the rotor phase. On the left side, the phase-locked traces are displayed over a full rotor revolution (360 degrees), while on the right side the same traces are represented only over a partial phase window to enhance the detail of the signal fluctuations. The static pressure, the convective heat transfer coefficient and the local driver temperature show a steep rise and fall, periodic with a blade-passing cycle ($\varphi = 1/64$). The maximum signal amplitudes are measured during the rotor tip traverse, while the low level regions are obtained in the blade passage. The highest peak in local driver temperature occurs near the corner of the tip suction side edge (thick blue line) as the leakage flow exits the rotor tip gap, while the gradient on the pressure surface edge (dotted red line) appear of smaller magnitude. The average size of the adiabatic wall temperature peaks is comparable with the turbine inlet total temperature. This has to be expected as the work processes engendered by the interaction of the hot flow with the rotor blade can lead to a strong "compression" of the flow in the overtip region in the stationary frame of reference and thus, to a significant increase of the absolute stagnation temperature [91]. The Nusselt number follows approximately the same trend as the local driver temperature. The evolution of the Nusselt number over a blade passage is strongly influenced by the traverse of the rotor blade tip. As the blade tip suction side edge approaches the sensor, the convective heat transfer coefficient experiences a sharp rise and reaches a peak within the overtip gap. The steep increase in Nusselt number at the suction side edge is due to the sudden arrival of the blade surface that disrupts the endwall boundary layer that has developed in between two blade tip passages (thick boundary layer, low thermal convection) and the recreation of a new started boundary layer (thin boundary layer, high thermal convection). The tip leakage flow enters the blade gap from the blade pressure side and significantly accelerates to high transonic speeds. Therefore, the boundary layer gets thinner and thinner along the blade thickness as shown by the convective heat transfer coefficient fall as the blade tip traverses. Within the blade passage the convective heat transfer is generally higher in the proximity of the blade pressure surface and reaches a minimum toward the suction side passage. The sudden flow acceleration in the blade tip gap is also captured by the static pressure signal that shows a rapid drop starting from the blade pressure side edge. Along the rotor passage the pressure change is relatively gradual from suction to pressure side.

A striking feature of the measured data is the considerable dispersion of the amplitude of the adiabatic wall temperature and Nusselt number. The majority of the blade passages show a maximum fluctuation of the adiabatic wall temperature between 0.7 and 0.9 of the inlet total temperature, in close agreement with the adiabatic wall temperature levels measured by Thorpe et al. [92]. For some other blades the driver temperature raises to exceptionally high levels, for a few of them around 150 K above the inlet total temperature (470 K) as shown in Fig. 4.14. Local overtip flow temperatures above the stage inlet total temperature are to be expected as the tip leakage flow is "compressed" by the rotor blade passage. Previously, [83, 94], adiabatic wall temperature amplitudes on the rotor shroud were reported to be 10-15% higher than the inlet total temperature. Few other works investigated the unsteady heat transfer at the shroud of a high speed turbine at fully matched engine conditions ([88, 96, 109]). All reported very high heat flux fluctuations across the overtip region ($150 - 400 kW/m^2$), in line with the heat flux levels measured in the present investigation (top right of Fig. 4.8). Although the previous works did not provide the adiabatic wall temperature, the heat flux levels would be compatible with large instantaneous local flow temperatures and convective heat transfer coefficients. Nevertheless, no previous research reported the signature of the shroud heat transfer above the rotor tip, with adiabatic wall temperatures 40% higher than the stage inlet total temperature. The Nusselt number over a rotor revolution oscillates between 80% and 140% of its time-average value and the amplitude of the convective heat transfer coefficient fluctuations also present large blade-to-blade variations that vary between 20% and 50% of the time-average value. In order to confirm that the experimental data were repeatable and representative of the real flow physics, measurements were repeated and data double-checked. The phase averaging of the unsteady wall temperature measurements (reads unsteady heat flux) over a full rotor revolution was excellent, with correlation coefficients typically above 0.99.

4.3.2.2 Analysis of the blade-to-blade pressure and heat transfer

In order to understand the physical mechanisms behind such large blade-to-blade differences, the peak-to-peak maxima values of the adiabatic wall temperature and Nusselt number were tracked over one rotor phase and associated to the respective blade number. The same procedure was applied to the unsteady static pressure signal measured at the same location. The data were subsequently plotted against the tip clearance. Fig. 4.15 shows the distribution of the maximum adiabatic wall temperature (left plot) and the Nusselt number (center plot), measured during the test and at two different rotational speeds during the spinning up period, normalized by their time-average values. It is clear that the heat transfer parameters show no apparent correlation with the tip clearance size in the investigated range. For the same clearance level, both the Nusselt and driver temperature peak values scatter on a very large band. This was observed to happen for both the blow-down and for the pre-rotation measurements when the turbine test section is at vacuum level (~ 30 mbar) under moderate thermal equilibrium.

Conversely, in the case of a turbine test, the casing endwall static pres-

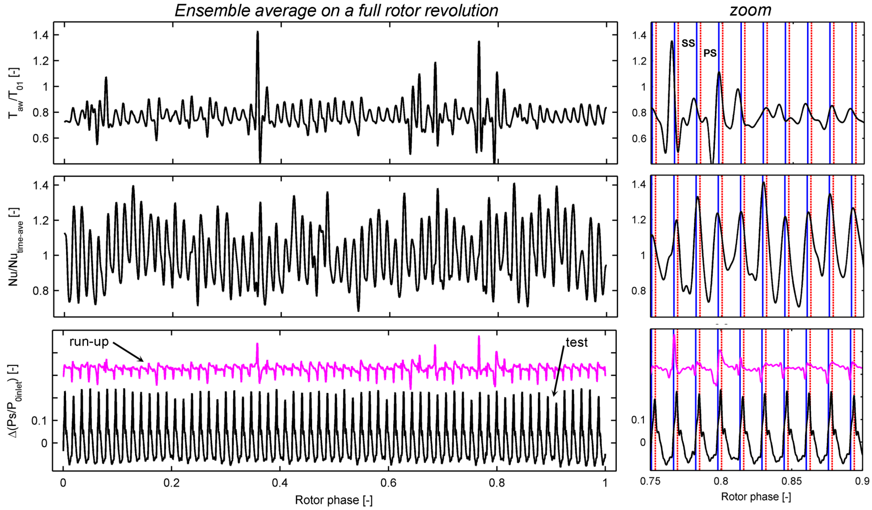

Figure 4.14: *Measured time-resolved casing adiabatic wall temperature, Nusselt number and static pressure as a function of rotor phase*

sure showed a good correlation with the tip clearance as depicted on the right picture of Fig. 4.15. The plot displays the amplitudes of the pressure oscillations, normalized by the inlet total pressure, generated by a single blade passage. For a turbine test, this quantity represents the load difference between pressure and suction side and can be reasonably assumed as an estimate of the local flow speed across the rotor tip gap. The static pressure amplitude drops as the tip clearance becomes larger. Data showed a reduction of almost 25% in the driving pressure load as the tip gap size increase by 0.6% of the blade span.

Fig. 4.16 illustrates the signature of the adiabatic wall temperature, Nusselt number and static pressure amplitudes against the tip clearance size as a function of the blade number during a turbine test (left plot) and for a run-up (right plot). For the test case, the static pressure and the tip clearance signatures present a good match indicating that the aerodynamic flow field is strongly modulated by variations of the gap size. On the other hand, the signature of the adiabatic wall temperature and Nusselt fluctuations do not match the tip gap size variations. Therefore, it seems that the origin of the heat transfer fluctuations cannot be directly explained by a change in tip clearance or static pressure. However, the distribution of the blade-to-blade driver temperature preserves a distinct trend that is maintained during the blow-down experiment and the pre-rotation tests.

Interestingly, the static pressure fluctuations measured during the spinning-up process (normalized by the total pressure in the turbine test section, approximately 30 mbar) present a high degree of overlap with the adiabatic wall temperature signature as illustrated in Fig. 4.16, right. A large static pressure oscillation is observed to occur in correspondence of a high adiabatic wall temperature swing as depicted in Fig. 4.14, bottom right. As the blade suction side approaches, the air is suddenly compressed and the local driver temperature experiences a steep rise. However, the static pressure field during the run-up phase still maintains a weak correlation with the tip clearance magnitude and a moderate reduction of the pressure amplitude can be observed as the tip clearance gets larger (Fig. 4.15, right). The comparison of the run-up and blow-down data suggests that the blade-to-blade variability in the adiabatic wall temperature and static pressure are generated by a flow mechanism that is independent of the tip clearance size. When the rotor blades are loaded during the blow-down test, the static pressure field in the overtip region is imposed by the tip leakage flow. Hence, the pressure signature observed in the run-up case is hidden by the established pressure load difference at the rotor tip section and the effect of tip clearance variations becomes predominant. On the contrary, the signature of the adiabatic wall temperature during the blow-down is scarcely affected by the established overtip leakage flow as it remains the same as in the run-up case. This indicates that the blade-to-blade variability of the heat transfer data is mainly attributable to the same work process that originates the adiabatic wall temperature fluctuations during the no-flow phase, and whose effects appear to largely dim any variation of the overtip heat transfer induced by changes of the tip leakage flow structure with different tip gap levels.

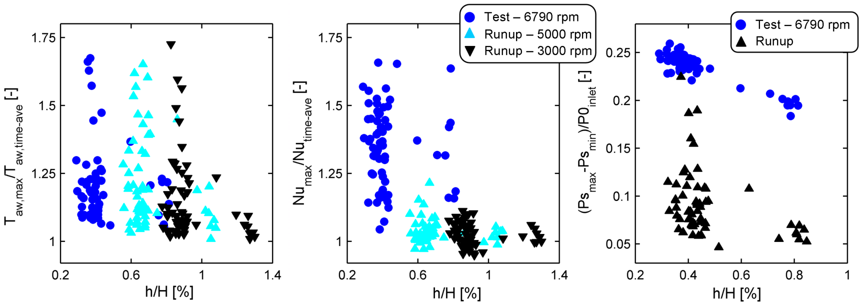

Figure 4.15: *Adiabatic wall temperature, Nusselt number and static pressure correlation with the blade-to-blade tip clearance*

The correlation between the aerodynamic field and the thermal load in the rotor spinning up phase was also assessed by comparing the run-to-run repeatability of the heat flux and the static pressure signatures. Fig. 4.17 depicts the relative blade-to-blade variation of the static pressure and heat flux oscillations, averaged on 24 tests, and the corresponding uncertainty band at 95% confidence level for both run-up and blow-down experiments. The run-up signatures result from the average of all the tests performed at different rotational speeds (3000/5000/6300 rpm). The very high repeata-

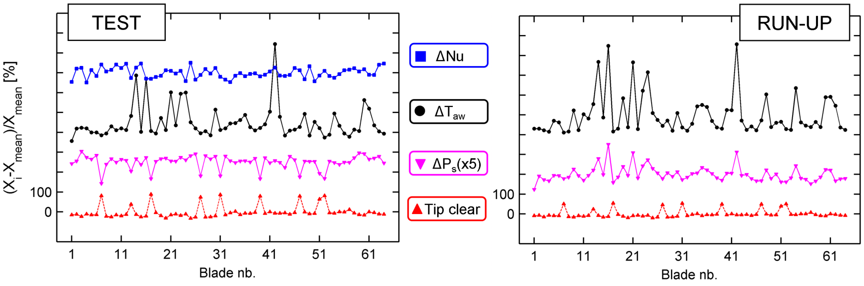

Figure 4.16: *Blade-to-blade signature of adiabatic wall temperature, Nusselt number, static pressure and tip clearance for a blow-down experiment (left) and for a run-up (right)*

bility proves that the rotating static pressure and heat transfer patterns are unchanged by rotor speed variations. In the spinning up phase the heat flux and pressure amplitude traces are almost identical. As the tip leakage flow establishes during the blow-down, the pressure signature is exclusively driven by the tip clearance variations. Conversely, as for the adiabatic wall temperature, the unsteady heat flux signature is not affected by the tip gap flow.

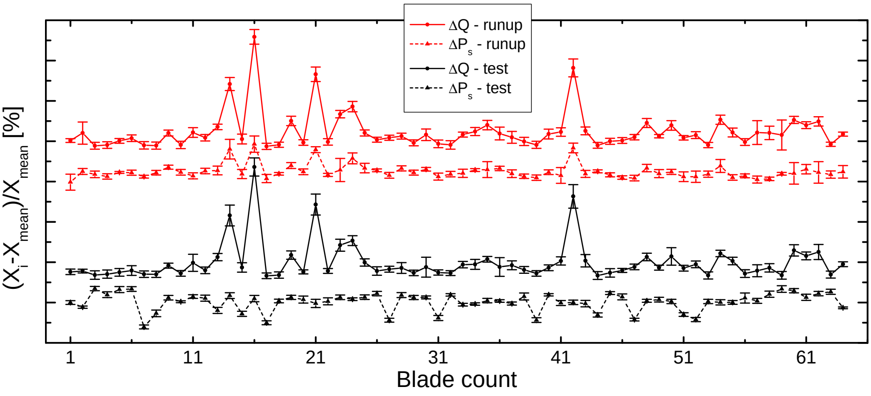

Figure 4.17: *Run-to-run repeatability of the blade-to-blade unsteady heat flux and static pressure variations for a test and a turbine run-up (at different rotor speeds)*

There could be a number of factors that might be held responsible for causing such significant variations between blade passages, and consequently hide the tip clearance effect. The excellent repeatability of the heat transfer and pressure signature of the 64-blade rotor suggests that the generation of the blade-to-blade variability is likely to be related to geometrical dissimilarities of the rotor row other than the tip clearance. The unsteady patterns of the static pressure and heat transfer signals were also confronted with the blade-to-blade pitch and blade thickness variations available from the measurements described in section 4.2.3.5. Fig. 4.18 displays the adiabatic wall temperature, Nusselt number and static pressure amplitudes of the 64 rotor blades as a function of the corresponding blade pitch and blade thickness. Both the thermal and aerodynamic data spread in a random fashion against the measured pitch and blade thickness variations. This indicates that the observed aero-thermal flow data are also uncorrelated with modest changes in rotor pitch (±2%) or blade thickness (±3%).

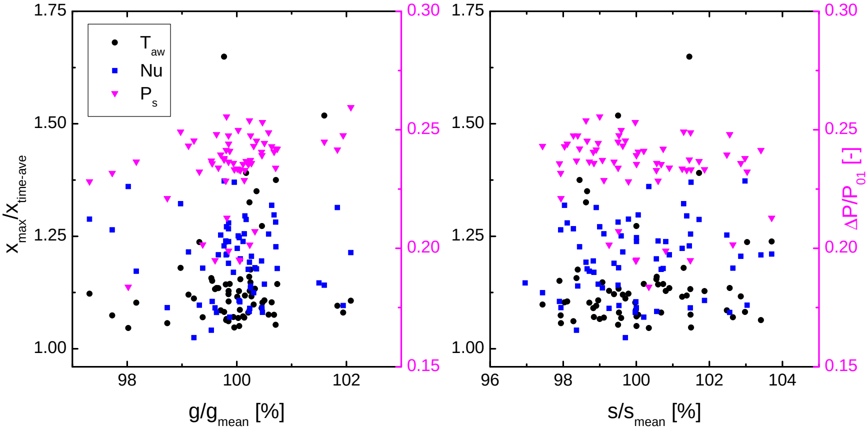

Figure 4.18: *Adiabatic wall temperature, Nusselt number and static pressure correlation with the rotor pitch (left) and blade thickness (right) blade-to-blade variations*

Small geometrical variations of the rotor tip surface can significantly alter the overtip flow topology as large pressure and velocity gradients occur over the tight gap between the blade tip surface and the rotor shroud. However, no apparent evidence of geometry irregularities could be found after careful inspection of the rotor row. This means that the casing heat transfer processes might be very sensitive to small variations of the rotor blade geometry at the tip section.

A deeper analysis of Fig. 4.15 reveals that the adiabatic wall temperature exposes a subtle trend in function of the rotor disk speed. The heat transfer data were rearranged against the rotor speed at which they were acquired. Fig. 4.19 shows the mean value of the adiabatic wall temperature maxima, averaged over a rotor phase, i.e. 64 blades, while the ticked band represents the data scatter contained within a 66% confidence level. The data collected at additional speeds during the pre-rotation shown in Fig. 4.19 revealed the existence of a relationship between the heat transfer and the rotational speed. It has to be noted that, although the data distribution for the run-up at 6300 rpm manifests an excessive scatter due to a measurement error, its mean value appears to be consistent with the trend visible in the other datasets at different rotor speeds. Fig. 4.19 illustrates that local driver temperature increases with the rotor speed in a non-linear fashion. It is also observed that the blade-to-blade variation grows as the rotational speed increases. Indeed, a significant unsteady heat flux component is observed on the overtip region already at relatively low rotational speeds during the pre-rotation phase. The experiments suggest that the unsteady heat generation during the pre-rotation is probably related to a process dependent on the peripheral tip speed magnitude.

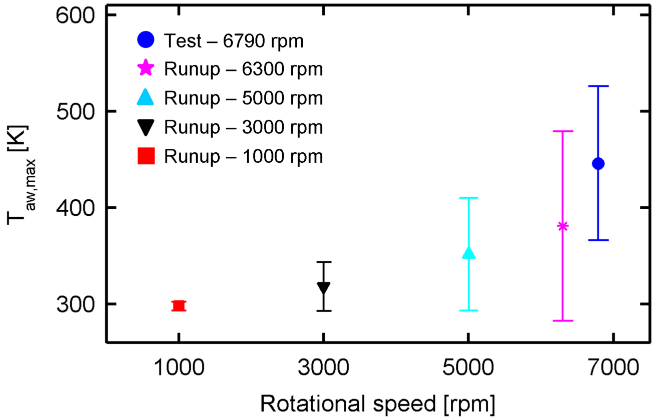

Figure 4.19: *Adiabatic wall temperature correlation with rotor speed*

4.4 Models for overtip heat transfer predictions

4.4.1 Zero-dimensional overtip flow model

In order to understand the physical flow processes responsible for the high adiabatic wall temperature fluctuations and support the analysis of the experimental data, a zero-dimensional model is proposed based on the Euler's work equation:

$$\Delta H_0 = U\left(\Delta V_\theta\right) = c_p \Delta T_0 \tag{4.13}$$

Equation 4.13 relates the tip peripheral speed and the variation of the absolute tangential velocity to a change in total temperature. The equation is applied to the case of a pre-rotation measurement where the turbine test is at low pressure and the flow time-averaged temperature can be reasonably assumed to be close to the ambient temperature. As illustrated in the sketch of Fig. 4.20, a particle in the test section will have approximately zero axial and tangential velocity in the absolute frame of reference in between two blade passage events. In contrast, a particle in the proximity of the rotor casing will be dragged by the rotor tip as a blade traverses and will acquire a certain tangential speed. The velocity that the particle would achieve can be reasonably assumed equal to the blade tip peripheral speed $V_m = U$, Fig. 4.20. Thus, the flow total temperature rise due to a blade passage can be predicted as:

$$\Delta T = (T_{local} - T_{amb}) = \frac{U^2}{c_p} \tag{4.14}$$

The calculation is performed at a number of rotational speeds and results are reported in Table 4.5. Additionally, the above flow model can be used to roughly estimate the increase of the total temperature due to the shear stress work generated in the overtip region. A steady viscous flow is considered between two parallel plates (the casing endwall and the rotor tip surface) separated by a distance h, namely the blade tip clearance. This situation corresponds to the well-known Couette flow and an analytical solution for the velocity distribution inside the tip gap assuming a velocity U at tip surface and zero velocity at the casing endwall can be derived. If no pressure gradient exists in the moving-wall direction as it is the case for a run-up test, the maximum flow temperature can be determined as:

$$T_{\max} - T_{amb} = \frac{1}{8}\frac{\mu V^2}{k_{air}} \tag{4.15}$$

Calculations show that the shear stress work only contributes for a small amount (~7%) to the overall predicted temperature variation. Comparison with the experimental values of the blade-average peak adiabatic wall temperature (to which a reference temperature of 300 K is subtracted) shows a good match for the spinning up cases. However, the no-flow model fails in predicting the blow-down levels. This indicates that the heat transfer generation mechanism is essentially driven by the tip speed if no leakage flow takes place across the blade tip.

On the other hand, the aerothermodynamics of the overtip flow can still be described by applying eq. 4.13 to the blow-down case as originally proposed in the work of Thorpe et al. [94]. The change in total temperature corresponding to the work exchange between the rotor tip and the crossing leakage flow can be expressed as:

$$\Delta T_0 = T_{0,tip} - T_{02} = \frac{1}{c_p} U \left[(U + w_{tip} \sin\delta) - V_2 \sin\alpha_2 \right] \tag{4.16}$$

where V_2 and α_2 are the absolute velocity and flow angle at the vane exit and w_{tip} and δ are the speed and angle of the leakage flow in the relative frame, Fig. 4.20, right. Eq. 4.16 is used to calculate the rise in absolute total temperature for a range of leakage flow relative Mach numbers and

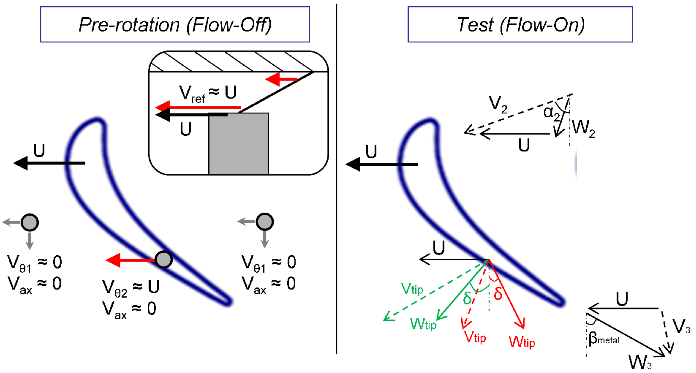

Figure 4.20: *Model of the flow work process on the rotor tip for a run-up test and a blow-down*

		Prediction			*Exp*
RPM $[rpm]$	U $[m/s]$	ΔT Euler $[K]$	ΔT shear stress* $[K]$	ΔT tot $[K]$	$T_{aw} - T_{ref}$ $[K]$
1000	41.9	1.7	0.2	1.9	-2
3000	125.7	15.7	1.4	17.1	18
5000	209.4	43.6	3.9	47.5	51
6300	263.9	69.2	6.2	75.4	86
6790**	284.4	80.4	7.2	87.6	151

$^{\star} h = 0.25mm$

$^{\star\star} Test(flow - on)$

Table 4.5: *Predicted and experimental flow total temperature rise in the overtip region for no-flow conditions*

flow angles at fixed vane exit conditions. Predictions are shown in Fig. 4.21, left. This graph is used to estimate the tip leakage flow characteristics that could explain the high adiabatic wall temperature variations observed in the experiments. An overtip maximum temperature of about 450 K, corresponding to the average experimental value, could be expected for a tip leakage flow angle through the gap of about zero degrees (no tangential speed component) and a variety of flow speeds. This would be in agreement with relative flow angles that can be expected on the rear part of the rotor profile where the blade load has greatly reduced. The model can therefore provide predictions of the total temperature in the overtip regions for a given tip leakage flow structure.

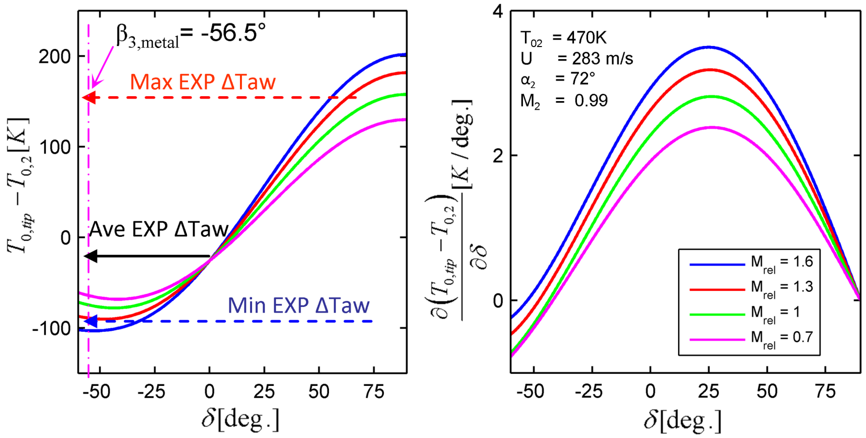

Figure 4.21: *Predicted leakage flow absolute total temperature variations for a range of Mach numbers and flow angles, temperature variations sensitivity to change in tip leakage flow angle at different Mach numbers*

The model was also used to roughly estimate the variation of the overtip total temperature due to changes in tip leakage flow angle and speed induced by different tip clearance levels. Even assuming a significant flow angle variation of 30 degrees over a range of flow Mach numbers between 0.7 and 1.3, the largest predicted overtip temperature variation would not exceed 50 K, i.e. 10% of T_{01} (see Fig. 4.21, left). Fig. 4.22 shows the relative Mach number and flow angle evolution across a rotor pitch at the mid-gap section at 75% of the rotor chord predicted by the steady-state CFD computation with a fixed tip clearance of 0.45 mm. This flow scenario is expected to be representative of the largest tip clearance levels measured in the experiments. The flow angle is nearly constant across the tip gap (~+10 deg.) and supersonic. According to the work process model, this flow regime would correspond to an overtip total temperature of about 480 K, 10 K above the measured local flow temperature averaged over the 64 rotor blades with a mean tip clearance of 0.2 mm. This is an indication that the expected overtip flow temperature variations induced by a tip clearance change of 0.3 mm is limited. This analysis also supports the conclusion that the large scatter of the blade-to-blade adiabatic wall temperature amplitudes (50% of T_{01}) cannot be exclusively originated by variations of the tip leakage flow aerodynamics with the tip gap magnitude.

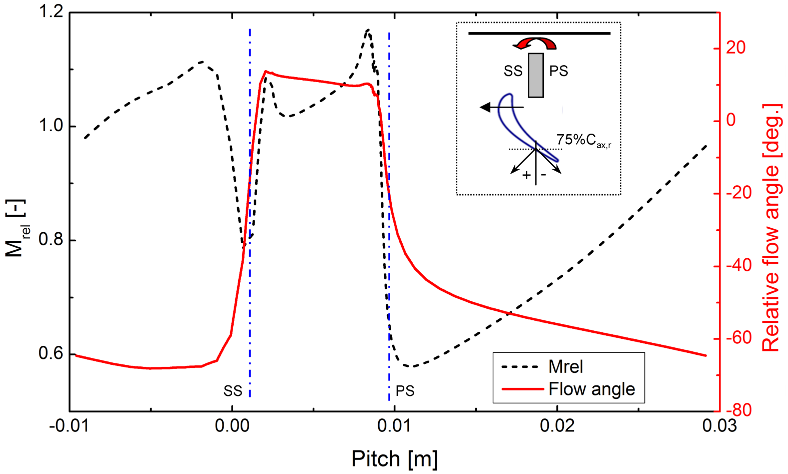

Figure 4.22: *CFD prediction of the relative Mach and flow angle at the rotor mid tip gap at 75%$C_{ax,r}$ for a tip clearance of 0.45 mm*

4.4.2 Turbine design implications

In order to better understand the impact of the tip leakage aerodynamics on the casing unsteady heat transfer, the sensitivity of temperature variations to the tip leakage flow angle is investigated. Fig. 4.21-right illustrates how the total overtip temperature would react to a change in leakage flow angle at a given flow angle. It is possible to identify a region between -10 degrees and +60 degrees where the total temperature change will be enhanced by flow angle variations. In particular, at a working angle of about +30 degrees, a high leakage flow speed will magnify this effect. Therefore, a large unsteadiness in the casing heat transfer can be expected at axial locations where the tip leakage flows is within this angle range. Additionally, there exists a range of flow angles between -20 degrees and +20 degrees for which the induced total temperature variations will be practically unaffected by the flow speed magnitude. On the contrary, a speed reduction for leakage flows at angles lower than -20 degrees would result in higher overtip flow temperatures closer to the vane exit total temperature.

The physics associated with the overtip work processes offers turbine designers a great potential to control the magnitude and uniformity of the overtip thermal loads through optimization of the tip leakage flow aerodynamics [110]. Designs targeting relatively low tip leakage losses at transonic regimes [111] must therefore consider the effect of increased tip flow speeds on the unsteady overtip heat transfer.

4.5 Conclusions

An experimental investigation of the time-resolved heat transfer on the casing of a transonic high-pressure turbine stage was conducted in a short duration rotating rig at engine-like conditions. The heat flux was measured by single-layer thin-film sensors at three circumferential locations around the rotor casing endwall. The probe for heat transfer measurements is equipped with a miniaturized heating system that allows varying locally the wall temperature, thus the adiabatic wall temperature and the true Nusselt number were determined. In order to support the understanding of the heat transfer data, simultaneous measurements of unsteady static pressure and running tip clearance were simultaneously performed at equivalent locations as for the heat transfer.

The time-averaged adiabatic wall temperature was observed to vary 10 K between two circumferential positions around the casing due to the vane clocking. The Nusselt number has also been measured and its time-averaged value showed slight variations depending on the casing position.

A large variation of the blade-to-blade time-resolved adiabatic wall temperature and Nusselt number was observed. Local flow temperature peaks 40% higher than the turbine total inlet temperature were measured in the overtip gap region. The fluctuations of the local driver temperature and Nusselt number exposed no plain correlation with the tip gap size in a range of tip clearances between 0.3% and 0.9% of the blade span. On the contrary, the static pressure field was strongly modulated by the tip gap size when the rotor blade tip is loaded during a turbine test. However, the shroud static pressure showed a clear match with the adiabatic wall temperature and heat flux signatures during the rotor spinning-up phase. This indicated that the blade-to-blade variability was likely to be generated by a flow mechanism that was active in both the run-up and the blow-down experiments, independent of the tip clearance size. The aerodynamic and heat transfer data were also shown to be uncorrelated with rotor pitch and blade thickness blade-to-blade variations which were measured in-situ.

The magnitude of the unsteady adiabatic wall temperature amplitudes was also observed to be dependent on the rotor speed. A simple model based on Euler's work equation predicts the change of adiabatic wall temperature for a pre-rotation test. The same model was adapted to describe the turbine test case where strong tip leakage flows take place. Hence, overtip flow temperatures above the stage inlet temperature can be explained through a simplified work process mechanism. The experimental 64-blade average maximum flow temperature could be predicted assuming the tip leakage flow had no tangential speed component across the rotor gap at $75\% C_{ax,r}$.

The prediction tool is used to illustrate possible scenarios related with the design of high-performance transonic blade tip sections. It is concluded that high-load rotor blades can be designed with relatively low tip leakage loss and reduced overtip thermal loads through optimization of the tip leakage flow aerodynamics.

Chapter 5

Aero-thermal flow field of a downstream multi-splitter LP vane

5.1 Introduction

Aero-engine designers pursue stringent objectives, increase component efficiency to lower fuel consumption and environmental impacts, while reducing engine size, weight and manufacturing costs.

Current and future design architectures rely upon the concept of ultra high by-pass ratio aero-engines [112]. In this perspective, larger fan diameters demand a reduction in rotational speed to maintain an acceptable tip velocity. Hence, the low pressure turbine radius must be increased in order to preserve high levels of efficiency [113]. Furthermore, to reduce the axial length of the whole machine with larger radial offset, a swan-neck diffuser is adopted to link the low-radius HP turbine to the high-radius LP guide vane. Hence, the inter-turbine transition duct presents a high hade angle. This is particularly evident in the first low-pressure vane or intermediate pressure vane in a three-spool engine configuration (Miller et al. [114]). S-shape ducts need improved design to minimize losses, prevent flow separation and deliver uniform flow to the next turbine stage. Many investigations report on the aerodynamic flow field in aggressive swan-neck diffusers. Among them research on this topic has been carried out by Dominy et al. [115], Miller et al. [33], Göttlich et al. [116], and Axelsson [117].

In conventional engine designs transition ducts are equipped with bulky pylons that are used to support the engine frame, route service, oil piping and instrumentation (Norris et al. [118]). The large size of the thick struts represents an effective obstacle for the compressible flow released by the high-pressure turbine, and high aerodynamic losses are generated in the inter-stage diffuser. In a ulterior attempt to further reduce the low pressure turbine size, the LP vane row is located inside the duct. Some fundamental research was dedicated to the investigation of the flow field in ducts with integrated struts and the interaction with an upstream turbine stage. Miller et al. [119] carried out an experimental and numerical characterization of the rotor flow migration through an inter-stage diffuser with integrated turning vanes. Marn et al. [34] reported a similar study on a duct with 18 struts. Ubertini and Desideri [120] also investigated the effect of struts in the transition duct performance. Britchford et al. [121] researched an outlet guide vane integrated duct at the fan.

In the frame of new engine architectures, an innovative stator for the LP turbine is proposed and studied with a multi-profile configuration. The conventional thick struts have been re-designed from an aerodynamic point of view and included in the LP vane together with small aero-vanes. The LP vane is placed inside an S-shaped transition duct downstream of a high-pressure turbine stage. Fig. 5.1 displays the evolution of the multi-profile row concepts and three possible architectures are shown in the plot. To reduce the turbine length, the vane row is moved inside the duct closer to the pylons (Fig. 5.1a). Higher aerodynamic performance can be achieved through redesign of struts' profile which provide also flow turning (Fig. 5.1b). A compromise between the need for large structural airfoils and an efficient aerodynamic low pressure vane can be found by including the two types of profile into one single vane row (Fig. 5.1c).

Little research has been carried out on multi-airfoil rows and there is no open literature on multi-splitter configurations applied to aero-engine turbine components. The aerodynamics of a turbine low-pressure vane with multiple profiles has not been previously studied at engine-like conditions, and thermal investigations for this type of stator architecture is nonexistent. One of the pioneer works on splitter vanes has been provided by Zhou et al. [122, 123]. The airfoil design, blade placement and number of splitter vanes to be used for such configuration were explained for the case of impulse steam turbines. The authors investigated numerically the three configurations shown in Fig. 5.1 and quoted a profile loss reduction of ~0.8% for the multi-splitter case with respect to the tandem profile arrangement. In their work the authors proposed to maintain the same mass flow to pass in every vane passage, i.e. the pitch must be the same for each blade-to-blade channel. Numerical calculations also provided velocity distributions and profile losses for three vane configurations with one, two and three smaller aero-vanes. A numerical analysis was performed by Barber [124] on a non-uniform cascade to investigate the potential distortion induced by the strut. Ng et al. [125] experimentally observed that the upstream potential field of a bulky strut, placed downstream of a stator, has a stronger effect on the rotor pressure field than the stator itself. Kodama et al. [126] studied a non-uniform spaced vane row to control and improve the performance of the strut-stator system. Cerri et al. [127, 128] and Parry et al. [129] suggest that rotor-stator-strut row interactions can be reduced by using non-uniform re-staggering of the airfoils along the circumferential direction. Ro et al. [130] proposed to control the horse shoe vortex generation by applying cut splittered vanes at the endwalls in between the blade passage. However, multi-profile designs have already been applied to radial turbomachinery. In particular, the use of splitter airfoils is common in radial impellers. Miyamoto et al. [131] performed an experimental characterization of centrifugal impellers with and without splitter blades in which the pressure field and flow angle were presented. Tjokroaminata et al. [132] performed a design study for a radial turbine with splitter blades. The study shows that the splitter blades give more flexibility for tailoring the loading on the main blades. Asuaje et al. [133] numerically investigated the effects of splitter blades on the velocity and pressure fields of a centrifugal pump.

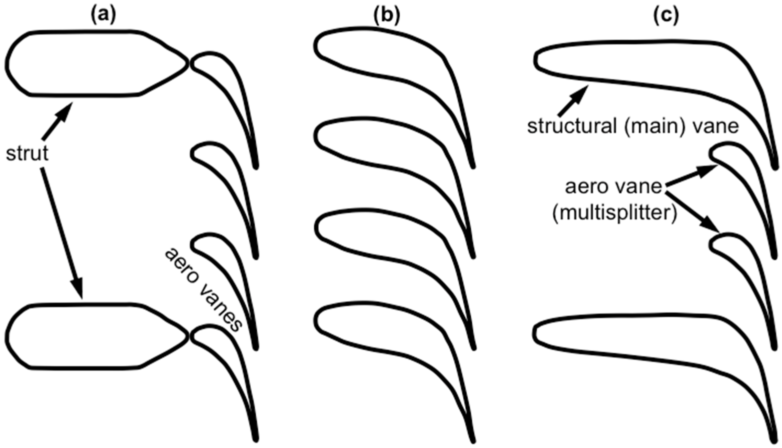

Figure 5.1: *Evolution of the multi-profile design*

The quest for higher performances and durability for modern aero-engines requires the understanding of the complex flow field experienced by the gas turbine stages. The LP vane is tested in a one-and-a-half turbine environment and one of the objectives of the present work is to assess the effects of the high-pressure turbine stage flow on the steady and unsteady performance of the multi-splitter vane. The periodic convection of wakes coming from the upstream stage and the unsteadiness introduced by the trailing edge shock system have a strong influence on the flow field of the next blade row. An intense research activity has been carried out by different research groups on the characterization of the flow field of a single stage turbine. Among them Giles [134], Hilditch et al. [7], Dénos et al. [135], Miller et al. [8], Paniagua et al. [9]. Less work has been done on the effect of the HP turbine on the downstream components and their mutual interaction. Billiard et al. [30] investigated the effect of clocking on one and a half turbine stage. The author reports the positive effect of the vane-vane interaction on the LP stator performance when the first stator wake avenue impinges on the leading edge of the second stator. Similar conclusions on the potential benefit of clocking were drawn by other researchers in a number of experimental and numerical studies (Reinmöller et al. [136], Bohn [137]). Few works have treated specifically the interaction mechanisms between a HP turbine and a second stator positioned in an s-shaped diffuser. In a numerical investigation Davis et al. [138] described the effect of shock waves generated by the rotor on the flow field of the transition duct and in the LP stator. Miller et al. [28, 31] experimentally investigated the potential interaction of the downstream vane on the unsteady pressure field around the rotor. Haldeman et al. [32] studied the effect of clocking on the unsteady pressure loadings on a LP vane and on the inter-turbine duct.

The assessment of the heat transfer on the novel multi-airfoil configuration is of crucial importance to design efficient cooling strategies for this turbine component and optimize the thermal load distribution. Furthermore, the knowledge of the heat flux on the LP vane surfaces permits to gain information on the boundary layer along the vane airfoils. Adequate predictions of the boundary layer status and location of the boundary layer transition point are necessary to evaluate the profile loss across turbine passages. The published research has provided insight into the heat transfer mechanisms in a highly unsteady environment, flow migration across turbine rows and wake and shock interactions. Ladisch et al. [139] investigated the heat transfer related to pressure side recirculation bubbles in a linear cascade. Additionally, Joslyn and Dring [140], Johnston and Fleeter [141] and Blair et al. [142] performed experiments at low speed in multistage configurations. Measurements of time-mean heat flux and aerodynamics are seldom performed in 1.5 stage turbines, because of the necessary complexity of the experimental setup. Only few works in the open literature report on aerothermal measurements on a low-pressure vane component downstream of a high-pressure stage: Jouini et al. [143] analyzed the stator and rotor clocking in a scaled two-stage turbine configuration; Povey et al. [144], Chana et al. [145] and Haldeman et al. [146] performed aerodynamic and heat transfer measurements on an intermediate pressure vane downstream of a high-pressure turbine in a rotating annular facility.

In the current study the flow field in the innovative multi-splitter stator located downstream of a high pressure turbine was experimentally investigated in a engine-size research turbine. The turbine experiments were carried out at three operating conditions. Time-averaged and time-resolved surface pressure and heat transfer measurements were used to characterize the steady and unsteady aero-thermal performances. Additionally, the performance of the multi-profile design was examined and compared with a conventional single-airfoil stator geometry. This analysis is of utmost interest for the design of compact s-shaped transition ducts with an integrated structural low-pressure vane. The present investigation also aims at providing an experimental database to improve future civil aero-engine design and validate CFD simulations and transition models.

5.2 Analysis of the LP vane aerodynamics

The aerodynamics of the second LP stator was investigated through steady and unsteady static pressure measurements around the four vane profiles.

Experiments were performed at three turbine operating points by varying the turbine pressure ratio and the rotor speed.

5.2.1 Airfoil pressure instrumentation

The pressure loadings around the aero-vanes' surfaces were measured locally by means of 19 pneumatic taps connected to piezo-resistive transducers (Sensym 240-PC-006D), and 17 piezo-resistive pressure transducers (Kulite type XCQ-062) distributed around 2 aero-vanes (Fig. 5.2, left). A structural vane is equipped with 27 pneumatic taps and a second one is instrumented with 25 piezo-resistive transducers. All the static pressure instrumentation was located at mid-span of the airfoils. The number and locations of the fast-response transducers were selected based on cost, sensor size, airfoil machining, and minimum vane thickness. Fig. 5.2, right, shows the distribution of the measurement locations around the vanes. The instrumented airfoils could be easily mounted into the LP vane measurement sector which comprises one strut vane and three adjacent aero-vanes. The LP vane airfoils were extractable allowing fast interchange of the instrumented vanes at different measurement positions. The kulite sensors were not flush-mounted but recessed 0.4 mm underneath a 0.8 mm diameter pressure tap. This instrumentation arrangement offers a better protection with a high spatial resolution at the price of a limited frequency response due to the cavity resonance at 35-40 kHz.

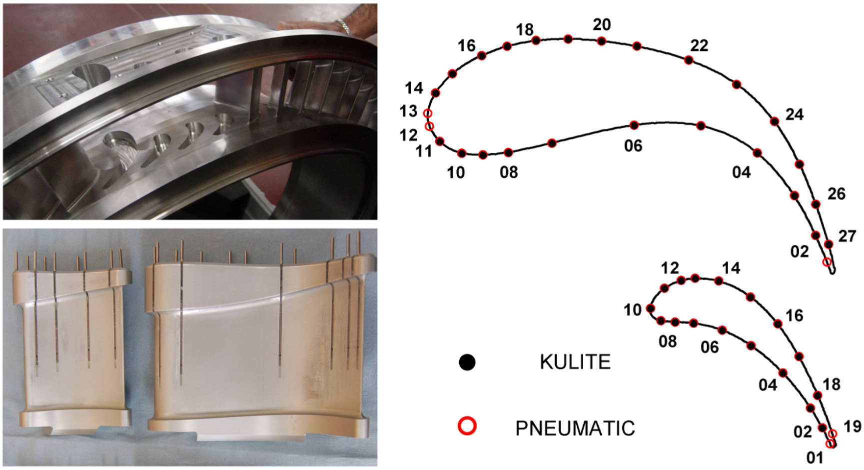

Figure 5.2: *Extractable LP vanes and locations of the pressure sensors*

The steady static pressure measurements were acquired with a sampling rate of 1.5 kHz. The unsteady pressure signals, sampled at 300 kHz for 250 ms, were first high-pass filtered at 100 Hz and then amplified by 10.

The slow-response piezo-resistive transducers were calibrated in-situ prior to and after each facility run. The kulite fast-response pressure sensor were calibrated applying the methodology for the temperature effect compensation described in chapter 4. The steady results are time averaged for a duration of 40 ms. The unsteady raw pressure signals were low-pass filtered at 35 kHz to remove any spurious oscillation linked to the measurement system dynamics. The filtered signals were phase-locked averaged (PLA) at the blade passing frequency over three rotor revolutions (192 blade periods) to distinguish the deterministic periodic fluctuations from the random ones. Frequency analysis on the unsteady pressure data was carried out by means of the Fourier transform.

5.2.2 Time-average pressure field

Measurements of surface pressure around the structural vane airfoil along the mid-span section are shown in Fig. 5.3, top, for the three operating conditions. Pressure side and suction side pressure envelopes are plotted in separated graphs. The normalized measured static pressure at each gauge location is plotted as a function of the normalized curvilinear abscissa (S/S_{max}). The CFD predictions are also reported. Overall, the agreement with the experimental data is very satisfactory.

At *Nom-Nom* condition three regions can be identified in the strut pressure distribution: in the front part of the airfoil (zone I) a steep acceleration occurs for both suction and pressure side promoted by the large curvature of the strut leading edge and the positive flow incidence. Then, the flow decelerates between S/S_{max}~-0.10 and S/S_{max}~-0.50 on the pressure side (zone II-PS) and between S/S_{max}~0.15 and S/S_{max}~0.45 on the suction side (zone II-SS). The increase of area in the transition channel is not counterbalanced by the low curvature of the strut profile resulting in diffusion. In the rear part (zone III), the flow is well guided by both strut and small aero-vane profiles. The turning imposed by the airfoils is enough to oppose the diffusion generated by the inter-turbine channel and accelerates the flow up to the geometric throat. The same considerations can be extended to the pressure field measured at *Low-Low* off-design condition. At this regime the load on the strut decreases being the turbine pressure ratio reduced.

When the turbine operates at *Low-Nom* regime, the rotor outlet flow angle changes significantly. The flow impinges on the strut with a large negative incidence (~-26 degrees). Consequently, the flow separates on the strut pressure side. Fig. 5.4a displays computed instantaneous turbulent to laminar viscosity ratio contours. CFD indicates that the whole vane passage is affected by the separation and the flow field of the adjacent aero-vane is strongly altered. The recirculation region extends along the entire strut pressure surface span. Fig. 5.4c presents numerical static pressure distributions along two lines at the tip endwall. Line *l1* runs near the strut pressure side and follows the geometric middle passage between the strut and aero-vane *C*. Line *l2* traces a similar path but through the passage between aero-vane *C* and *B*. At the inlet of the s-shape duct, in the proximity of the strut pressure side (line *l1*), the flow abruptly accelerates moving around the vane profile and then separates. The static pressure plateau, that closely follows the velocity peak at x/L_{duct}=0.15, identifies the size of the recirculation bubble at the duct wall (0.16< x/L_{duct} <0.32). Once the boundary layer reattaches the increasing annular cross section imposes a steep pressure rise to the flow. In the aero-vane passage the flow re-accelerates thanks to the turning given by the aero-vane profile. Conversely, the static pressure evolution along line *l2* is not affected by the separation but shows a smooth pressure recovery up to the aero-vane leading edge (x/L_{duct}=0.38).

Likewise, the detrimental effect of the flow instability can be clearly recognized on the strut pressure profile (Fig. 5.3, top right). The stagnation point moves to the suction side (S/S_{max}=0.07). The flow abruptly accelerates on the pressure side leading edge region. At S/S_{max}~-0.15 the boundary layer detaches because of the strong adverse pressure gradient that closely follows the velocity peak. Similarly to what has been observed at the tip wall, experimental data exhibit a constant static pressure region between S/S_{max}~-0.18 and S/S_{max}~-0.35. Again, this gives an estimate of the recirculation bubble extension affecting the strut pressure surface. At S/S_{max}=-0.40 the flow reattaches and decelerates due to the combined effect of low profile curvature and high diffusion imparted by the transition duct. In the rear profile, the presence of the aero-vanes imposes a strong turning to the flow (60 degrees) that accelerates up to the TE. On the suction surface, the flow remains attached and smoothly accelerates up to the throat region. Comparison between the numerical results and the measurements show that the largest discrepancy is found at *Low-Nom* condition on the pressure side profile. However, although CFD predicts lower static pressure levels, the general trend is fairly captured.

The steady pressure fields around three small aerofoils are displayed in Fig. 5.3, bottom. The presence of the large structural vane alters appreciably the aerodynamic field of the small vanes in the front part. The outlet rotor flow structures are disturbed as the flow enters the low aspect-ratio vane. The struts cause an evident blockage effect and worsen the circumferential non-uniformity of the aero-vane inlet flow field. Hence, the flow field in the aero-vanes' leading edge region is distorted. Fig. 5.5 shows numerical predictions of the absolute flow angle and Mach number variations along a strut pitch in two axial planes, one upstream of the strut LE (plane *P01*), one in between the strut and the aero-vane LE (plane *P02*). Both the experimental and the CFD results confirm the existence of strong pitchwise gradients (flow incidence and flow velocity) at the aero-vane inlet flow field induced by the strut vane. The surfaces adjacent to the strut profiles (pressure side of vane *A* and suction side of vane *C*) are the most affected. The experimental results show large velocity peaks for aero-vane *A* on the

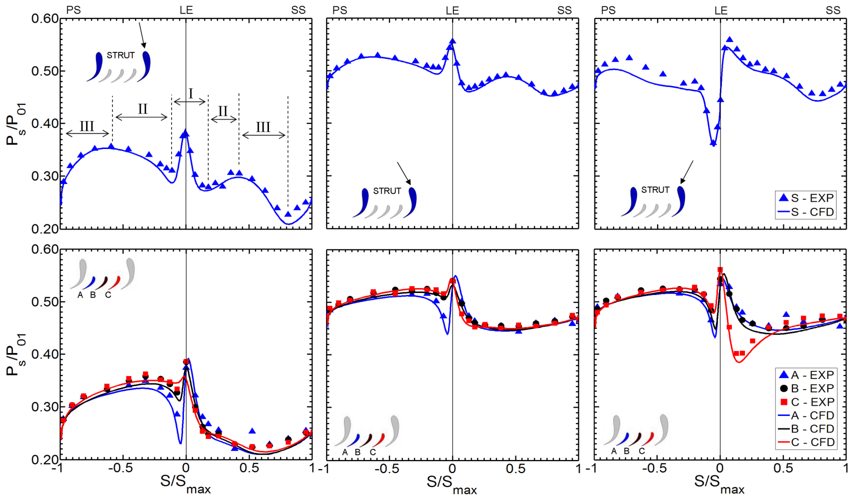

Figure 5.3: *Steady static pressure distributions on the stator strut (top) and aero-vanes (bottom) at three operating conditions:* Nom-Nom *(left),* Low-Low *(center) and* Low-Nom *(right)*

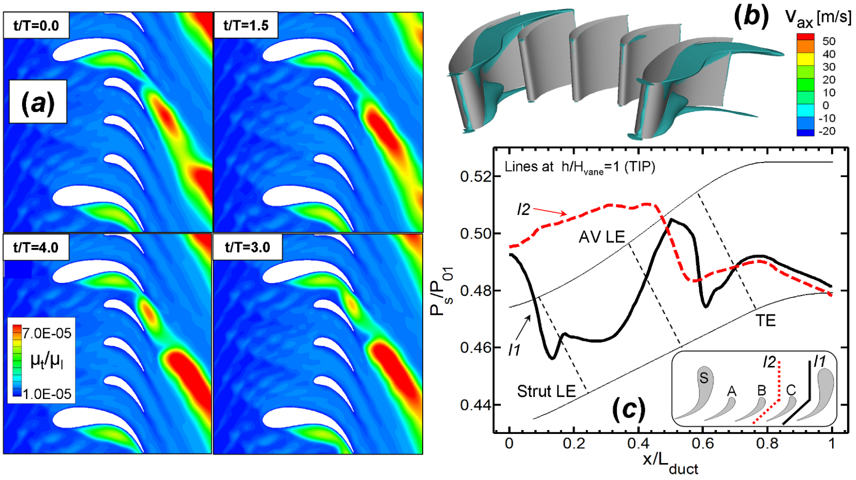

Figure 5.4: *Prediction of flow separation on the strut pressure side at* Low-Nom *condition: a) instantaneous contour plot of turbulent to laminar viscosity ratio at 50% span, b) Iso-surface of flow velocity, and c) casing static pressure distribution at two circumferential positions*

pressure side measurements. This can be explained by the directed inlet flow. The flow accelerates and turns as it follows the profile of the strut. Thus, it impinges to the vane A with a locally large negative incidence as confirmed by CFD calculations (α=-18 degrees, see Fig. 5.5a). The velocity peak reduces for aero-vane B and C due to the decreased flow incidence. The velocity peak on aero-vane A is nearly 3 times larger than the ones on the other two aero-vanes. While the experiments show a similar pressure drop on the front pressure side for aero-vane B and C, i.e. similar flow incidence (see Fig. 5.3, bottom left), numerical computations seem to underpredict the velocity peak at aero-vane C probably because the angle of attack is slightly overestimated. On the suction surface the three aero-vanes present similar trends. At *Low-Low* condition the vane load is different but smooth flow accelerations are preserved. Indeed, both inlet flow angle and Mach number follow the same trend observed for the *Nom-Nom* regime with less severe circumferential variations, as shown in Fig. 5.5.

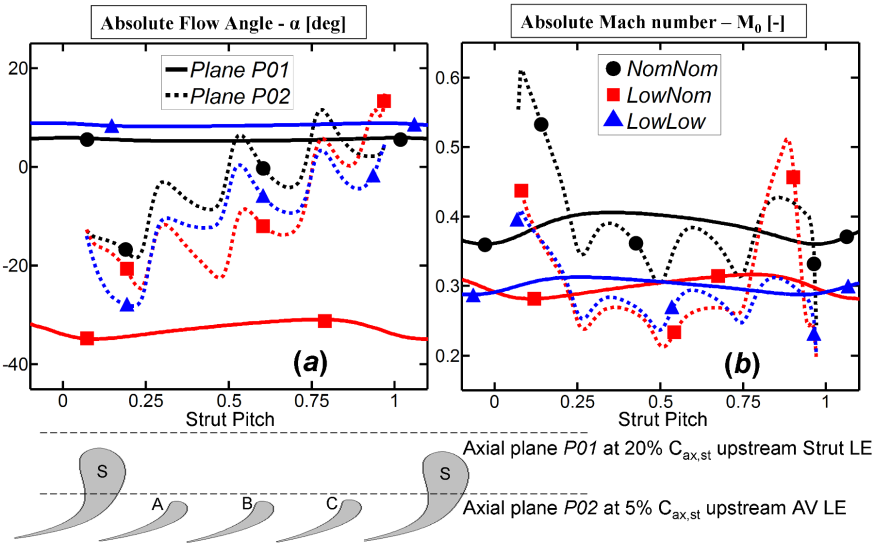

Figure 5.5: *Numerical results for absolute flow angle (a) and Mach number (b) variation along the circumferential direction at two axial planes upstream and downstream the strut LE*

Fig. 5.3, bottom right, presents the steady pressure distribution around the LP stator aero-vanes at *Low-Nom*. The suction side of vane C is substantially affected by the flow structure distortion imposed by the structural vane. The resulting velocity profile is dominated by a large velocity peak in the leading edge neighborhood. The low-speed recirculation structure obstructs a wide portion of the vane passage as clearly shown by CFD unsteady calculations in Fig. 5.4a. The flow steeply accelerates on the vane C

suction surface due to this blockage effect. In fact, the Mach number can reach peak value above 0.5 in the middle passage adjacent to the strut PS (Fig. 5.5b). However, the flow still attacks the three aero-vanes with negative incidence. The velocity peak measured on the aero-vane A pressure side is very similar to what is observed for the positive incidence off-design case, being the inlet flow angle and Mach number nearly unchanged (α=-25 deg, M_0=0.26-0.28). On the other hand, the high-speed flow entering the aerovane C- strut passage intensifies the acceleration rate on the vane C front pressure side. The stagnation pressure measured at the vane C LE at *Low-Nom* condition is therefore increased with respect to the *Low-Low* regime. At negative incidence off-design regime the aerodynamic effect of the structural vanes diminishes in the middle strut pitch. Although strut-induced pitchwise gradients still exist, flow angle and flow velocity variations between aero-vane A and B have tailed off. Hence, aero-vane B and A show velocity peaks of comparable magnitude in the front pressure side. At the rear part of the airfoils, the pressure levels are very similar and they merge after S/S_{max}=0.40-0.50. This characteristic is present for all conditions. The flow analysis of the multi-splitter LP vane has highlighted the main interaction mechanisms occurring between struts and downstream aero-vanes. The bulky structural vanes have been observed to cause a marked pitchwise aperiodicity on the aero-vane inlet flow. The investigation at off-design regimes points out two important considerations. Firstly, the circumferential gradient imposed by the strut on the aero-vane inlet flow angle always acts in the same direction (increasing incidence from strut SS to strut PS), independently of the rotor exit flow. Secondly, a dramatic variation of the LP vane flow incidence ($\Delta\alpha=\alpha_{3,lowlow}$- $\alpha_{3,lownom}$=45 degrees) does not change significantly the pitchwise velocity distribution inside the strut passage unless a flow instability establishes. This can be observed in Fig. 5.5b by comparing the Mach number variations in the vane passages adjacent to the strut suction side and to the strut pressure side at *Low-Nom* and *Low-Low* conditions.

5.2.3 Time-resolved pressure field

The unsteady performances of the LP stator are determined by the interaction with the upstream high-pressure turbine. The novel multi-profile LP vane configuration introduces a strong mutual effect among the stator vanes, in particular between the large strut vane and the small aero-vanes. The discussion on the complex interaction mechanisms is based on the phase-lock pressure fluctuations measured around the second stator surfaces for the four vanes (strut and vane A, B and C). Because of the large amount of data (4 blades × 3 conditions × 17-25 sensor locations), the analysis is carried out focusing on few key pressure sensors (*02-04-07-10-11-14-16-18* for the aero-vanes and *02-05-07-11-14-19-24-27* for the strut-vane) under nominal regime. The investigation is extended to the two off-design conditions by comparing the minimum and maximum envelopes of the deterministic pressure fluctuations together with the random component (rms).

In the present research the HP turbine works in the transonic domain at design regime. While the HP stator exit is dominated by a shock system ($M_{2,\mathrm{hub}}$=1.06, Table 2.7), the rotor outlet flow is highly subsonic (M_{r3}=0.87). However, the rotor exit Mach number may experience unsteady excursions in the transonic region when the rotor passes in front of the LP vane and shock waves from the rotor TE may reach the front part of the large strut. Gadea et al. [147] investigated the pressure field of a second stator downstream the present HP turbine stage tested at similar flow conditions. The authors calculated the rotor relative exit Mach number by means of a simple model based on numerical and experimental data. They demonstrate that at 15% span the rotor operates temporarily in the transonic domain. Shock interaction was found to drive the unsteady interaction with the stator downstream. The same model has been applied at the present case but at rotor mid-span height. The method consists of using measurements of P_{02}, P_{s2}, T_{02} and α_2 performed downstream of the HP stator alone (Valenti et al. [148]) together with the measured static pressure P_{s3} downstream of the turbine stage. Assuming no pressure losses across the rotor ($P_{03r,is}$=P_{02r}) allows calculating the time-average flow quantities at the rotor exit. A detailed description of the model and its validation is given in [11]. Fig. 5.6 displays the computed rotor relative exit Mach number variation across a vane pitch (50% span). It is shown that the outlet rotor flow remains subsonic.

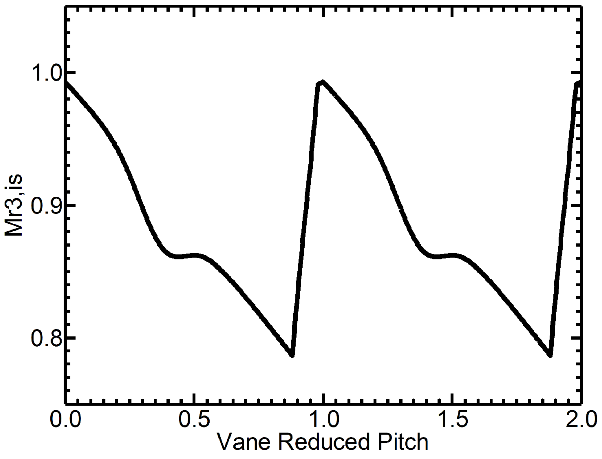

Figure 5.6: *Isentropic relative Mach number at the rotor exit, 50% span*

Tiedemann and Kost [149] reports no rotor TE shock activity for the same rotor geometry with higher degree of reaction resulting in a higher rotor exit velocity (M_{3r}=0.94). The large axial gap existing between the strut LE and the turbine stage exit (Table 2.5) also contributes to weaken the pressure perturbations shed by the rotor outlet. Besides, the strut vane LE might be positioned in a region such that pressure gradients are attenuated as suggested by Hummel [14]. In Fig. 5.7 the pressure fluctuations measured at leading edges of the strut and aero-vane B and C are compared. At the aero-vane leading edges, located $1.56C_{ax,r}$ downstream the rotor, larger pressure variations than at the strut are measured. It is unlikely that compression waves may travel far downstream in the stator passage and still cause high pressure oscillations. It can be concluded that shock activity does not affect the time-resolved pressure field of the LPV.

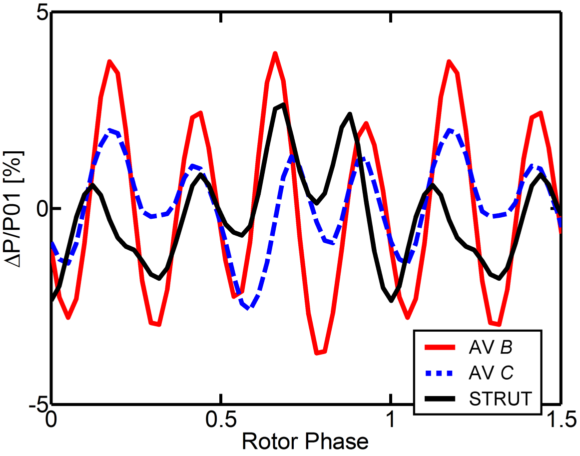

Figure 5.7: *PLA traces at LE of strut and aero-vane* B *and* C *at design condition*

Experimental measurements of time-resolved surface pressure around the LP stator airfoils are shown in Fig. 5.8 for design condition. The plot displays the time history of the LP vanes' surface pressure as the rotor sweeps one aero-vane passage. The pressure fluctuations are normalized by the inlet total pressure (P_{01}) and plotted against the rotor phase ϕ_r. The zero phase corresponds to the time when the rotor blade stacking axis is aligned with the leading edge of one aero-vane, the phase equal to 1 corresponds to the time when the next rotor blade is aligned to the same aero-vane.

The measured unsteady surface pressure depends on the vane position. The analysis of the periodic pressure distribution shows a complex evolution in time. In the pressure traces up to four peaks per rotor passage can clearly be distinguished. This behavior is marked on the leading edge and pressure side of both the aero-vanes and the strut. The rotor unsteadiness does not convect with the flow speed indicating that the rotor wake viscous effect is not dominant on the pressure side. On the contrary, the suction side variations assume a fundamental wave-like shape. The peaks are still present but of small relative amplitude compared to the main pressure variation.

The negative jet effect [150], caused by the sweeping of the rotor wake on blade surface, helps to explain for this experimental observation. The largest pressure fluctuations are measured at the LE of aero-vane B (7% P_{01} peak-to-peak). On the strut LE the maximum variation amounts to 5% of P_{01} (sensor *S11-S14*), the same as for aero-vane A and C (sensor *AV10*). The differences in terms of pressure amplitude and phase between the four vanes become more relevant from leading to trailing edge. This characteristic is more evident for the suction side gauges. On the pressure side, exposed to the unsteadiness shed by the rotor, the fluctuations are larger (sensor *S05-07*, *AV04-07*). On the pressure side the magnitude of the fluctuations keeps almost unchanged (about 4-5% P_{01}) up to the trailing edge. On the aero-vanes' suction side an attenuation is observed on the rear profile (sensor *AV18*).

The experimental data show that the time-resolved pressure field structures vary remarkably depending on the LPV airfoil circumferential position. Two main interaction mechanisms are responsible for this feature: firstly, the presence of the large strut alters the transport and mixing out processes of the unsteady flow structures generated by the upstream stage. The rotor traversing across the strut leading edge region disturbs locally the static pressure field in the rotor-stator gap. Secondly, there exists an "indexing" effect because the LP vane to HP vane count ratio is not an integer. It is known that the phasing between rotor wakes and first stator wake avenues only depends on the clocking position [151]. In the present case each LP stator airfoils is at a different relative position with respect to the first stator (see Fig. 5.8); thus it experiences a different unsteadiness generated by the HP turbine. It is acknowledged that clocking for optimum aerodynamics occurs when the NGV wake impinges on the downstream stator LE and some researchers related this to the clocking-induced unsteadiness variations. However, in these investigations contradictory results are drawn on whether the random fluctuation level should be the highest [152, 153] or the lowest [149, 154]. In the current investigation any attempt to isolate the single contributions of clocking and strut-induced flow distortion based on the periodic and random pressure fluctuations would be extremely difficult. However, it must be remarked that the strut cannot generate additional periodic unsteadiness, which is solely created by the movement of the rotor row. Thus, the strut affects the unsteady LP vane in a similar manner as clocking, i.e. the strut can only modify the spatial periodicity of the unsteady structures.

An interesting finding of this research is the experimental evidence that the adoption of a multi-splitter configuration does not affect dramatically the unsteady aerodynamics of the LP vane. One can argue that the combined effect of clocking and multi-body stator layout induces a spatial aperiodicity on the unsteady pressure field. Nevertheless, the strut time-resolved pressure distribution does not show significant differences compared to the aero-vanes. At the strut crown (sensors *S11-S14*), where the rotor disturbances are expected to be stronger, the magnitude of the pressure variations is in the same order of the ones measured on the aero-vanes (around 5% of P_{01}).

The unsteady aerodynamics of the LPV at off-design conditions is investigated by comparing the minimum and maximum envelope of the periodic pressure variations measured at each sensor locations together with the associated random unsteadiness (Fig. 5.9). The general structure of the unsteady pressure field is very similar for all the conditions. When the pressure ratio is reduced (*Low-Nom*), an overall drop of the pressure amplitudes (~1.5-2% of P_{01}) as well as for the random fluctuations (~0.5% of P_{01}) is observed with respect to the design regime. When the rotational speed is lowered to 4500 RPM the periodic and the random fluctuations are further reduced. The leading edge region is most affected by a change in the operating conditions due to the variation of the incidence angle. At design condition the highest fluctuations are found for aero-vane B and the strut in the front part of the profile. At *Low-Nom* condition the pressure fluctuations measured at the LE of aero-vane A are as large as the one on the strut LE. The peak in aero-vane B LE has disappeared. In fact, for this regime, the flow attacks the LP stator with a strong negative incidence. Thus, the LE of aero-vane A is directly exposed to the rotor unsteadiness while aero-vane B and C benefit from the obstruction of the strut. At *Low-Nom* condition the strut pressure side is affected by a wide separation zone. Fig. 5.4a illustrates the unsteady behavior of the recirculation region. The extent of the recirculation zone varies by the rotor movement. The turbulent low-speed fluid gathers on the vane passage and it is periodically released to the downstream flow field. The separation zone sweeps on the suction side of vane C almost impinging on the vane crown. The pressure fluctuations experienced by vane C are mostly influenced by the separated zone time scale. The periodicity dictated by the rotor movement has a weak effect. Thus, high rms values (2.5% of P_{01}) associated to low pressure amplitudes are found for aero-vane C front suction side. On the other hand, pressure oscillations, periodic with the rotor movement, are dumped by the separated zone acting directly on the strut pressure surface. That is why in this region low pressure magnitudes and relatively low random variations are measured. The separated region has a strong effect on aero-vane A which shows large pressure variations, up to 7%, on the pressure side mid-chord. The shedding of the recirculation structure alters the circulation around the strut blade and this may intensify the interaction between the strut potential field and the rotor flow unsteadiness. The pressure fluctuations are then enhanced on aero-vane A and dumped for aero-vane C. At *Low-Low* conditions the intensity of the unsteadiness is further reduced and the mean fluctuation level drops to ~0.5% of P_{01}. All the three aero-vanes experience lower pressure fluctuations than the strut in the leading edge region.

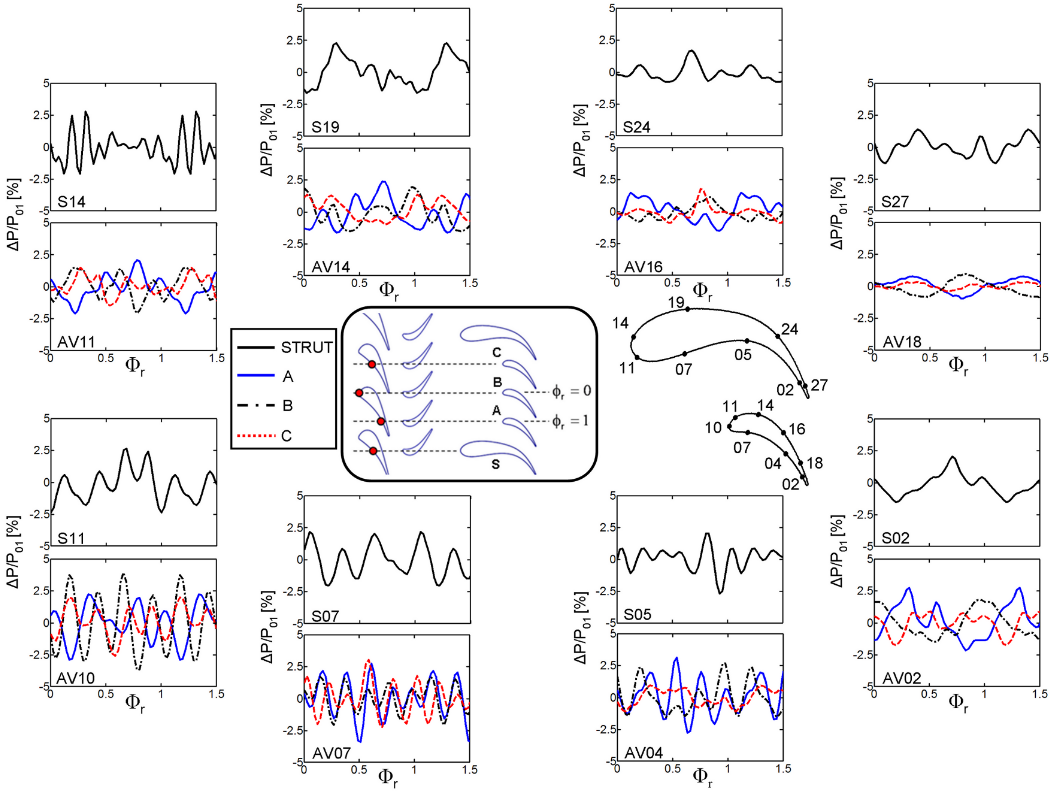

Figure 5.8: *Measured pressure fluctuations on LPV airfoils, 50% span and design condition*

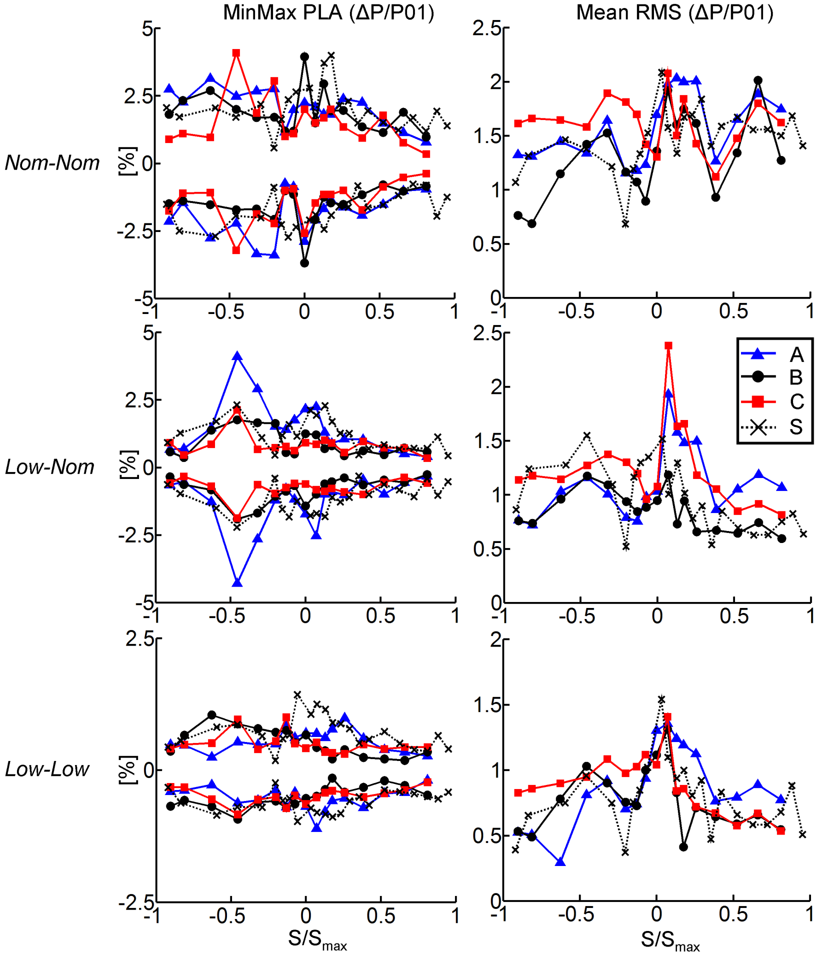

Figure 5.9: *Periodic pressure envelopes and mean rms along the LPV airfoils for the three turbine regimes*

5.2.4 Spectral analysis of the pressure field

The Fourier spectrum of the raw pressure measurements is used to determine the relative size of fundamental and harmonic frequencies and to highlight phenomena that are not rotor periodic. The frequency analysis is presented for the LP vane profiles at the three tested conditions in Fig. 5.10. The plot shows the amplitude of the normalized pressure for varying frequencies up to 30 kHz. The blade passing frequency (7.2 kHz and 4.8 kHz for nominal and low rotational speeds) and its harmonics are well captured.

At *Nom-Nom* condition, the fundamental frequency is stronger than the harmonics for almost all the gauges on the strut airfoil. However, the amplitude content of the harmonics remains considerable up to the third (29 kHz) and for some gauges it becomes comparable, if not larger, than the fundamental. This behavior is more evident for the three aero-vanes. The harmonics amplitudes dominate the spectrum in a defined zone of the vanes' profile. Indeed, the second and third harmonic show the highest peaks (0.2-0.3% of P_{01}) in a region between the middle pressure side (aero-vane A), front pressure side (aero-vane B) and vane crown (aero-vane C). The extension of this region is nearly the same for the three aero-vanes but its location depends on the vane position. The large energy content of the harmonics is reflected as several pressure peaks on the time-varying periodic signals in Fig. 5.8. In the suction side and in the rear pressure side the blade passing becomes the strongest frequency again. Additionally, at the rear suction side at all positions low frequency components appear to increase in magnitude towards the trailing edge. After the geometric throat the flow is less guided and undergoes expansion in the vane passage. This might enhance the boundary layer instability and account for the augmented low-frequency pressure oscillations. The peak frequency and magnitude differ depending on the position indicating a link with the multi-splitter stator configuration. At vane A, the peak appears spread around 400 Hz whereas the peak frequency increases to 600 Hz and 1000 Hz at vane B and C, respectively. On vane C the peak size is in the order of the blade passing (0.2%) while for the strut the levels remain relatively small (0.05%).

At off-design condition *Low-Nom*, the spectrum distribution shows large differences for each airfoil. The fundamental frequency has the largest amplitudes on the suction side of strut and aero-vane A and C. On aero-vane B suction side the amplitudes of the first and second harmonic are of the same size as the blade passing frequency. On the pressure side, the second and third harmonic present the largest amplitudes for strut and aero-vane A. For aero-vane B and C the fundamental frequency and the harmonics show approximately the same amplitude level. On the strut pressure side high amplitude levels can be observed at low frequency. The peaks are spread in a frequency band ranging between 500 Hz and 1600 Hz. Obviously these large amplitudes are not related with the rotor passing event but are caused by the separated flow region that affects the strut pressure side. The separation modifies the potential field of the strut and its effects extend up to the vane crown. It is thought that the frequency band in which these amplitudes manifest is imposed by the time-scale of the wide recirculation zone. As shown in Fig. 5.4a, numerical calculations are capable of capturing this phenomenon. The shedding of the recirculation zone seems to have a periodicity of nearly four rotor passages (corresponding to the CFD sampling period) corresponding to 1800 Hz (7240/4=1800) in the frequency domain. Fair agreement exists with the experimental evidence. The effect of the separation region extends its influence to the adjacent vane C. High amplitude peaks are observed at around 1000-1200 Hz. On the vane crown the peaks are much stronger than any other frequency in the whole spectrum with magnitudes of 0.3-0.4% (sensor *AV 11-12-13*). The contraction and spreading of the separation zone periodically modify the blockage in the vane passage. Thus, the inlet flow of vane *C* strongly varies in terms of flow speed and flow angle enhancing the pressure fluctuations.

When the rotor speed is reduced (*Low-Low* condition) the frequency spectrum structure changes once again. The peak amplitudes of the fundamental frequency are globally smaller than for *Nom-Nom* and *Low-Nom* conditions. The blade passing frequency (4.5 kHz) dominates only at the rear suction side and at the vanes' crown. The contributions of the harmonics vary according to the vane position. In aero-vane *B* the 1st harmonic has a major effect on the pressure surface whereas on the suction side the third harmonic is as large as the fundamental. The spectrum distributions of aero-vane *A* and *C* are similar with significant first harmonic amplitudes on the front suction side. However, the largest peak amplitudes are observed in a wide low frequency band spread between 200 Hz and 2000 Hz. The low frequency content is present around all the vanes' profiles. The strongest peaks are found on the front pressure side of all the vanes. The size of the peaks (0.08-0.1%) is also similar and generally higher than the blade passing. On the pressure and rear suction surface, the amplitude of the low frequency decreases around 0.03%. Indeed, a closer look reveals the presence of this low frequency band also for *Nom-Nom* and *Low-Nom* conditions. The physical reason for this phenomenon does not seem straightforward and further investigation is necessary.

5.2.5 Aerodynamic forces on the LP vane

The airfoil forces have been computed by integrating the measured time-resolved pressures on strut and aero-vanes. A linear variation of pressure has been assumed between the consecutive gauges. Fig. 5.11, left, shows that the mean axial force is unaltered for all conditions and similar for the three aero-vanes. The force fluctuation magnitudes are reduced when the pressure ratio is lower. The strut, that has a lower acceleration rate, shows lower axial force than the aero-vanes for all conditions. Likewise, Fig. 5.11, right, depicts a similar level of tangential forces for all airfoils at *Nom-Nom*. Aero-vane *B* has the lowest force variation, 8% of the mean level. The separation at *Low-Nom* condition causes a negative tangential force on the strut. When the rotational speed is lower, the mean level of the tangential force on the strut is eight times smaller than the one at *Nom-Nom* turbine operating point. Aero-vane *A* experiences the maximum variation over the aero-vanes at *Nom-Nom* and *Low-Nom*. When tangential and axial forces are obtained, the modulus of the force and the acting angle are computed and depicted in Fig. 5.12. The airfoil forces are the largest at *Nom-Nom* due to the higher pressure gradient across the vanes. Especially on the strut, the force variations are quite significant as ±20% of the mean level. When the

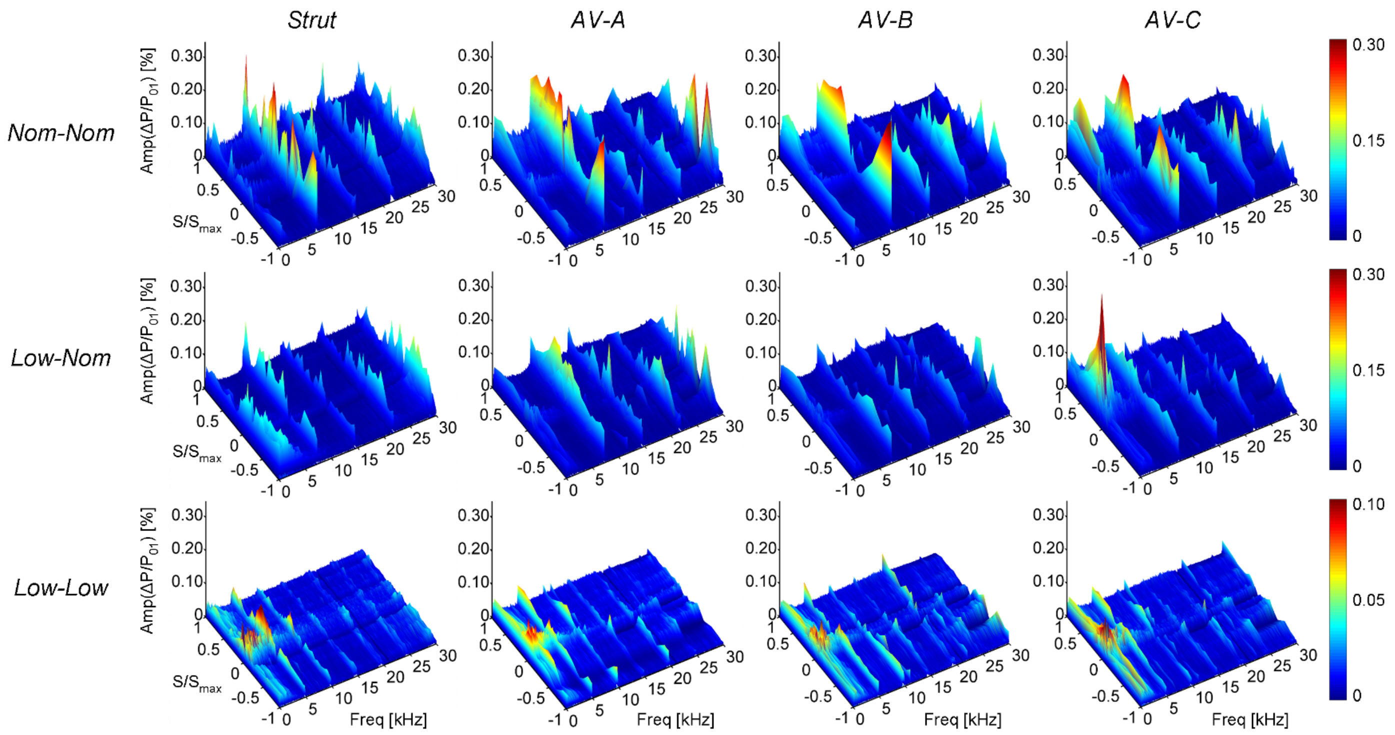

Figure 5.10: *Amplitude spectrum of surface pressure on LPV airfoils at the three operating conditions*

pressure ratio reduces, the mean levels of forces that act on the aero-vanes decrease smoothly. The rotational speed does not have an influence on the mean level but it affects the magnitude of the force oscillations. On the other hand, the strut shows a negative force at *Low-Nom* due to the large flow separation on the pressure side. When the flow incidence is corrected by changing the rotational speed, the force becomes positive again and its magnitude is drastically lower compared to the one at *Nom-Nom*. The angular variation is rather small for the aero-vanes compared to the one for the strut. The force angle on the strut changes significantly at *Low-Low* conditions. However this variation is not dramatic since the force magnitude is very small.

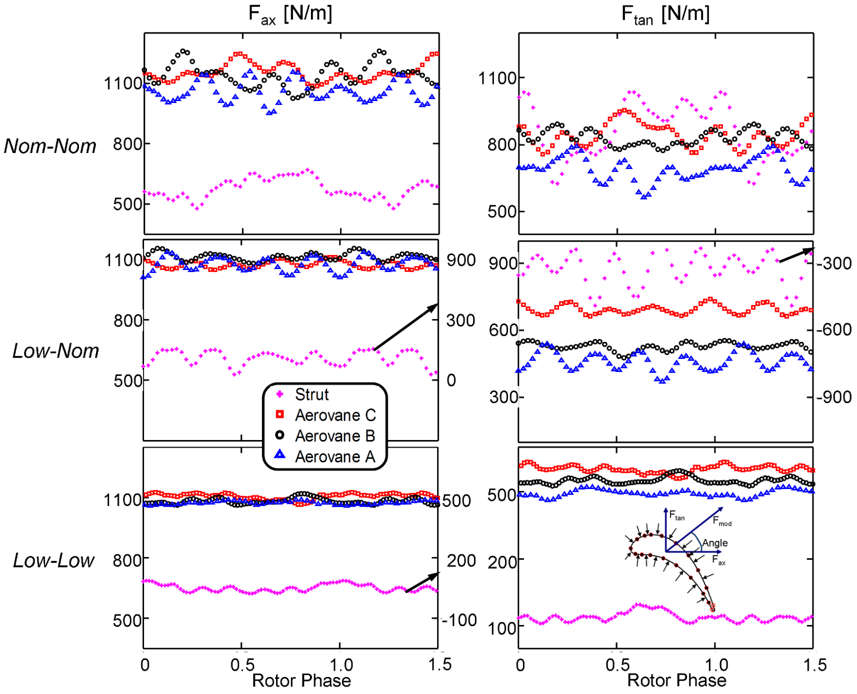

Figure 5.11: *Tangential and axial forces on the four airfoils*

The force acting on the whole LP stator row is derived by knowing the airfoil force variation over a rotor phase. When the reference vane is at rotor phase 0, the force of each vane at the stator row is interpolated using Fig. 5.12 based on their position relative to the rotor blade. The stator force is equal to the sum of each vane force at a certain position. If the position of the reference vane is changed step by step over a rotor pitch, the stator force variation is plotted. Fig. 5.13 shows the result of such calculation. When the pressure ratio is lowered by approximately 35%, the forces applied on the stator decrease by about 30%. Moreover the force variation reduces as

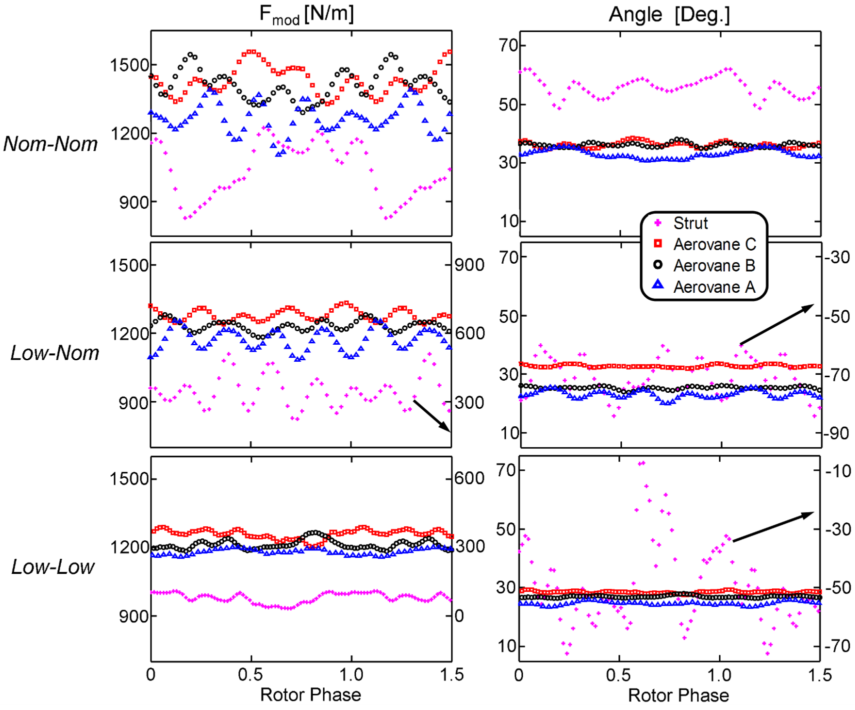

Figure 5.12: *Force modulus and angle acting on the four airfoils*

it goes from 9% of the mean level (*Nom-Nom*) to 7% of the mean level (*Low-Nom*) and 2.5% of the mean level (*Low-Low*). The force angle almost remains constant at *Low-Low* conditions. The total force variation depends highly on the airfoil periodicity between two rows. If a periodicity exists like the one in this study (64 rotor blades - 64 LP vanes: 1-1 periodicity), the periodic vanes always experience the same force. Therefore, the number of forces that define the total force at a given time is linked to the periodicity of the stator. When the number of vanes in the periodicity increases, each airfoil force is better distributed over a rotor phase. In such a case, the total force variations are also dumped. The lowest fluctuations are achieved for non-periodicity arrangement.

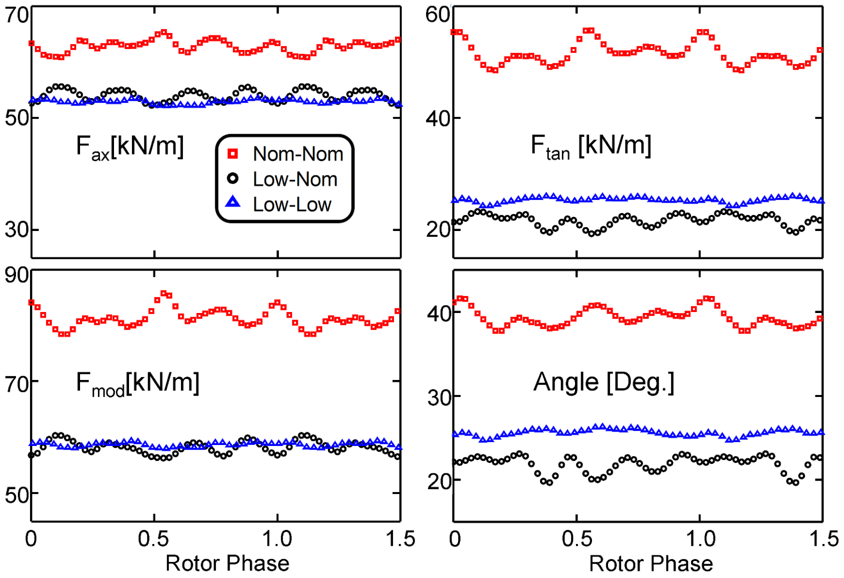

Figure 5.13: *Module and angle of the total force acting on the LP vane row*

5.3 Thermal loads through the LP vane passages

The time-average and time-resolved heat transfer on the multi-splitter LP vane is presented here. The heat flux measurements are used to derive the Nusselt number distributions along the vane profiles and quantify the unsteady heat flux fluctuations. The boundary layer status and its evolution across the LP vane passages is analyzed and the effect of the HP turbine-vane unsteady interaction on the convective heat transfer levels is discussed.

5.3.1 Heat transfer instrumentation and data reduction

Measurement of the heat transfer on the LP vane is performed with single layer thin-film gauges which consist of thin platinum temperature resistors fired onto a ceramic substrate. An extensive description of this type of heat transfer sensors has been given in section 4.2.3.2 of this thesis. The thin-film sensors are located at the airfoils' mid-span section and Macor is selected as the ceramic substrate. The entire blade could be manufactured in ceramic for cascade testing (Arts et al. [155]), or inserts could be fitted into metallic blades (Dénos, [99]). In the current measurement campaign, a Macor insert is used to reproduce a portion of the vane airfoil which is fitted into the remaining part of the metallic profile. Fig. 5.14, top, presents the test specimens instrumented for the heat transfer measurements. A sketch of the low pressure vane with the position of the sensors is also included in Fig. 5.14, bottom, which allows the definition of the four stator passages where the heat transfer is analyzed.

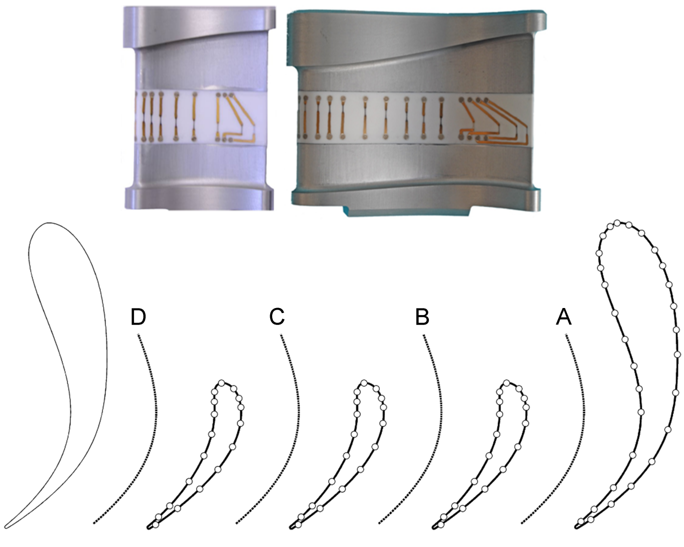

Figure 5.14: *LP vane airfoils instrumented with single-layer thin film gauges (top), definition of the LP vane passages (*A, B, C *and* D*) and location of the heat transfer gauges*

The heat transfer was recorded during the turbine test duration using the same settings applied for the sampling of the vanes' static pressure measurements. The wall temperature was finally derived from the thin-film data following the processing methodology described in section 4.2.3.3. The heat flux is determined from the wall temperature time-history using the numerical solution of the unsteady heat conduction equation in the gauge substrate. In order to reconstruct the time-average heat flux distribution around the vane profiles, the global approach developed by Solano and Paniagua [100] was considered. This data reduction technique consists of solving the 2D unsteady heat conduction equation in the cross sectional area of the vane, using as a boundary condition the reconstructed temperature history provided by the thin film gauges in the contour of the airfoil. This methodology enables to account for radial conduction effects actually present at the leading edge of the airfoil (Buttsworth and Jones, [156]) and for the failure of the semi-infinite assumption in the trailing edge region.

A weighted residual (Galerkin) approach is used to derive the finite element equations from the governing differential equation (eq. 4.2), as stated by Rao [157]. The solution of the resulting algebraic system provides the time-dependent temperature distribution inside the body and subsequently, the normal heat flux to its external boundary:

$$\dot{Q}_w\left(x, y, t\right) = -k_{macor} \cdot \vec{n}\nabla T \tag{5.1}$$

Due to the complexity of measuring the adiabatic wall temperature in the present experiment, the Nusselt number is expressed in function of the vane upstream total temperature. The driving temperature (T_{03}) is obtained using the thermocouple probe placed upstream of the LP vane row at 50% span-wise position. The local hydraulic diameter of the passages is chosen as the dimension to define the Nusselt number at each gauge position:

$$Nu_{Dh} = \frac{\dot{Q}_w}{T_{03} - \bar{T}_w}\frac{D_h}{k_{air}} \tag{5.2}$$

To highlight the shortcomings of a purely one-dimensional approach, the heat flux distributions along the aero-vane and structural vane profiles were computed, prescribing the analytical wall temperature evolution in a flat plate which applies to a heat flux step. This solution is reported by Doorly and Oldfield [158] for a 1D semi-infinite substrate. Therefore, it discards any lateral heat conduction phenomenon. Fig. 5.15a depicts this analytical wall temperature evolution evaluated for a Macor substrate and a wall heat flux step $\dot{Q}_w$=30 kWm^{-2} extended over 0.5 s. These magnitudes are representative of the short duration tests in the compression tube facility. Fig. 5.15b presents the wall heat flux evolution retrieved by the 1D solution of the heat conduction across the Macor substrate (Iliopoulou et al., [159]) and the equivalent result obtained in the stagnation point of the aero-vane with the 2D methodology of Solano and Paniagua.

Whereas the solution of the 1D semi-infinite substrate fully reconstructs the wall heat flux step, the 2D solution decays short after the commencement of the test, owing to the radial heat conduction effects present in the stagnation point of the aero-vane. At t_f= 0.5 s, the 2D solution is 16.6% lower than the prescribed heat flux at this position. The heat flux distribution at the end of the test is shown in Fig. 5.15c for the aero-vane and

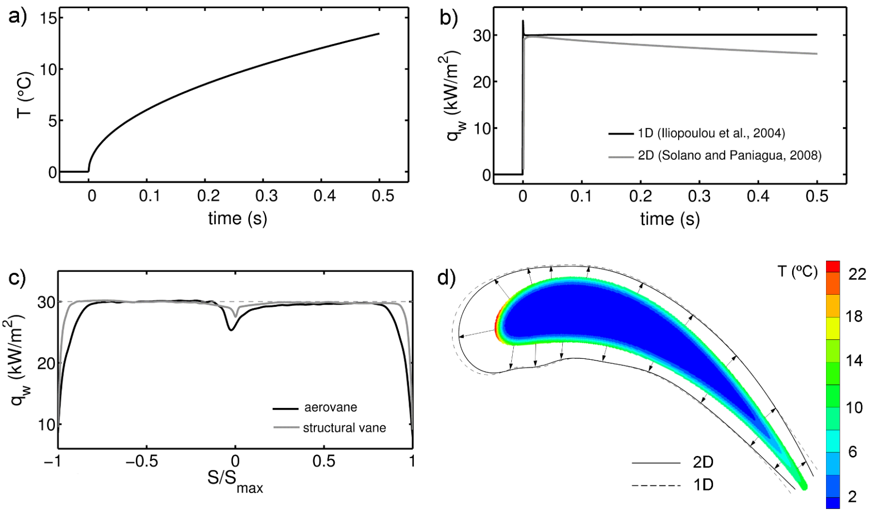

Figure 5.15: *Comparison of 1D and 2D heat flux distribution on a vane profile: a) Analytical wall temperature evolution for an heat flux step b) wall heat flux computed in 1D and 2D ceramic substrates c) 2D computation of the wall heat flux around the aero-vane and strut airfoils d) 2D computation of the wall heat flux and substrate temperature distribution*

for the structural vane. The results show that the expected heat flux step is reconstructed in wide regions of the pressure and suction sides of both airfoils during the whole test duration, proving that these regions fulfill the 1D hypothesis. As previously shown, the wall heat flux evolution around the leading edge does not comply with the 1D model. However, the curvature effects are less pronounced in the structural vane as a result of the higher leading edge radius. The results in the trailing edge of the airfoils also underpredict the 1D solution by approximately 25%, owing to the failure of the semi-infinite assumption for the reduced airfoil thickness. The present methodology solves the 2D effects, relevant to critical sensors of the airfoil. Fig. 5.15d depicts 1D and 2D heat flux distributions around the first aero-vane (passages A-B) at nominal turbine operating conditions. The temperature distribution in the cross sectional area of the airfoil reveals the lateral heat conduction phenomena present in the stagnation point. The temperature diffusion phenomena that actually occur in the trailing edge of the airfoil also justifies the adequacy of a 2D approach for a turbine blade heat transfer calculation.

The flow conditions across a vane passage are modulated by the periodic movement of the rotor blades occurring at the blade passing frequency and therefore the heat transfer measurements contain frequencies related to the rotor flow disturbance. Hence, the unsteady heat flux is analyzed by decomposing the unsteady fluctuations into two fundamental components: the deterministic time-periodic heat flux fluctuations induced by the rotor movement that repeat for each blade passage or each rotor revolution; the random heat flux unsteadiness generated by random features in the flow such as turbulence.

The effect of the rotor passing event on the deterministic heat flux unsteadiness is revealed by the frequency spectrum of the wall temperature unsteady signal. Fig. 5.16 shows that the unsteady heat transfer in the low-pressure vane is dominated by the rotor unsteady flow field. The highest frequency content is found at two dominant frequencies corresponding to 1 and 64 rotor blade events per revolution. The heat flux variation happening at the rotor speed frequency implies that the low-pressure vane is exposed to different flow conditions at each rotor blade passage. These differences are originated by the blade-to-blade variability of the rotor geometry which imposes perfect periodic conditions only once per rotor turn. The blade-to-blade heat transfer variations are mainly engendered by changes of the rotor blade tip gap size which result in tip leakage jets and vortices with different temperature and strength. Additionally, variations of the blade passage geometry and rotor trailing edge thickness may alter the size and the energy of the 2D unsteady structures shed at the rotor outlet. The 64 events per revolution reveal interactions caused by the passage of each rotor airfoil, namely the potential flow field, wake and compression waves.

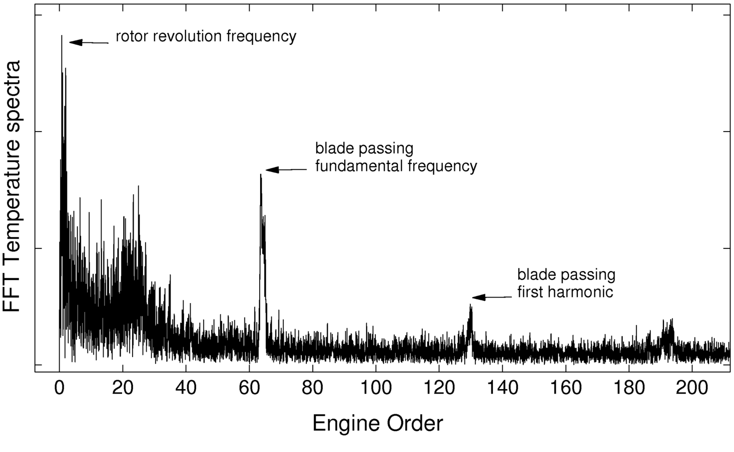

Figure 5.16: *Typical frequency spectrum of an unsteady wall temperature signal on a LP vane airfoil*

The current analysis concerns the time-periodic component of the unsteady measurements. The unsteady deterministic heat flux is obtained through application of phase-locked averaging performed on a dataset that includes three full rotor revolutions and thus, 192 rotor blade passage events are used to form one phase-locked average signal. The ensemble averaging is performed at the blade passing frequency since the final goal of the measurements is to assess the contribution of the rotor-induced flow unsteadiness on the LP vane unsteady heat flux.

The data reduction procedure is illustrated in Fig. 5.17. The final step demonstrates the results of the time-resolved heat flux compared with the original raw unsteady signal. The method commences with the analysis of the raw unsteady wall temperature (Fig. 5.17a) where the rotor speed is selected as the dominant frequency for the fluctuations which repeat every rotor turn. Therefore, the unsteady wall temperature signal is ensemble averaged on a time period corresponding to a full rotor revolution, Fig. 5.17b. The phase-locked trace contains 64 oscillations, each of them generated by a certain rotor blade. Based on the ensemble average of the wall temperature, the rotor-periodic heat flux is determined over one full rotor revolution, Fig. 5.17c. It has to be noted that the low-frequency oscillations in wall temperature are naturally dumped in the conversion to heat flux. As the heat flux is a function of the time derivative of the wall temperature, high frequency temperature fluctuations result in larger unsteady heat flux for the same temperature variation. Fig. 5.17d finally presents the ensemble average of the 64 heat flux oscillations over one rotor revolution, i.e., the phase-locked averaged heat flux for a blade passing event. In this case, the good agreement between the raw and the periodic signal indicates a low contribution from random unsteadiness.

5.3.2 Mid-span time-average heat transfer

The experimental investigation was carried out at three turbine operating conditions which have been reported and described in chapter 2. The time-average heat flux measured on the four airfoils of the LP vane is first studied at design conditions (*Nom-Nom* condition) where the low-pressure vane is choked. The effect of reducing the pressure ratio is studied at nominal rotational speed (*Low-Nom* condition) and at lower speed (*Low-Low* condition). Due to the multi-splitter architecture of the low-pressure vane, the large structural vane alters substantially the flow field entering the aero vanes, notably at the passages next to the structural vanes (passage A and D). Therefore, the analysis is carried out considering the heat flux distribution on each of the four vane passages. This in contrast with the common approach adopted for conventional mono-profile stator geometries where the heat flux evolution is studied referring to a single airfoil (suction and pressure side) and not to a vane passage.

The measured time-mean heat flux is confronted with well-known correlations of local Nusselt number for simultaneously developing flow in ducts subject to uniform heat transfer. The solution for laminar developing flow is accounted for with the correlation of Churchill and Ozoe [160]:

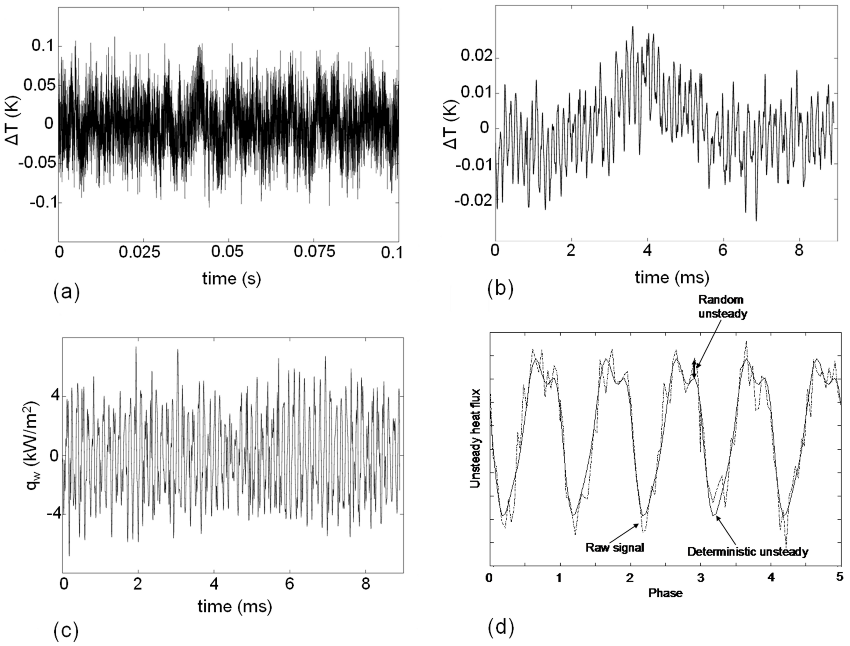

Figure 5.17: *Data reduction for the unsteady vane surface heat flux: a) raw unsteady wall temperature b) unsteady deterministic wall temperature over one rotor revolution c) unsteady deterministic heat flux over one rotor revolution d) phase-locked average heat flux at the blade passing frequency*

$$\frac{Nu_x}{4.364\left[1+(Gz/29.6)^2\right]^{\frac{1}{6}}}=\left\{1+\left[\frac{Gz/19.04}{\left[1+(\mathrm{Pr}/0.0207)^{\frac{2}{3}}\right]^{\frac{1}{2}}\left[1+(Gz/29.6)^{\frac{1}{3}}\right]^{\frac{1}{3}}}\right]^{\frac{3}{2}}\right\}^{\frac{1}{3}} \tag{5.3}$$

In turbulent flows, the solution proposed by Bhatti and Shah [161] is adapted for the computation of the local Nusselt number:

$$\frac{Nu_x}{Nu_\infty}=1+0.234\left(\frac{D_h}{x}\right)^{0.76} \tag{5.4}$$

where Nu_∞ denotes the fully developed Nusselt number.

Static pressure (P_s/P_{03}) and Nusselt number distributions along the mid height channel are depicted in Fig. 5.18, at nominal conditions. The static pressure distribution describes the pressure gradient driving the boundary layer development. Local values along pressure side and suction side of passages A, B, C and D are presented as a function of the axial coordinate $x/C_{ax,strut}$.

The highest heat flux level is measured in the stagnation region, where the boundary layer begins to develop. Maximum values of Nusselt number of the order of 2000 are found at the leading edges. In the front section of the passage a steep acceleration occurs for both the suction and pressure sides. Hence, the Nusselt number decays abruptly as the laminar boundary layer develops along both sides of the passage. The comparison with the data correlation helps to identify the transition location in each side. Along passage A, a sudden increase of the Nusselt number in the pressure side for $x/C_{ax,strut}$~0.15 indicates transition onset with further turbulent boundary layer development. This is caused by the flow deceleration from $x/C_{ax,strut}$~0.1 to $x/C_{ax,strut}$~0.5 inferred from the pressure distribution. Such adverse pressure gradients promote the onset of transition, resulting in heat transfer enhancement. This onset of transition is also noticeable by a peak in the rms of the unsteady data. The further acceleration of the flow from $x/C_{ax,strut}$~0.5 towards the rear part of the pressure side stabilizes and thickens the turbulent boundary layer, leading to a decrease of the Nusselt number. Along the suction side of the passage, the Nusselt number decreases continuously from the leading edge of the aero-vane up to $x/C_{ax,strut}$~0.8. This evolution is well predicted by the laminar correlation (eq. 5.3), with the exception of the gauge located at the leading edge of the aero-vane, submitted to the stagnation of the flow that approaches the aero-vane. From this point towards the rear part of the suction side, transition occurs and further thickening of the turbulent boundary layer is observed.

Concerning passage B, the Nusselt number distribution along the suction side in nominal conditions presents a similar pattern to that reported for passage A, with an earlier onset of transition at $x/C_{ax,strut}$~0.7. It is worth noting that both correlations predict accurately the local Nusselt number values in regions where the boundary layer is purely laminar or turbulent, respectively. In the front part of the suction side, the Nusselt number decreases continuously from the leading edge up to $x/C_{ax,strut}$~0.7, indicating the growth of a laminar boundary layer. Further enhancement of the Nusselt number towards the rear part of the suction side reveals the onset of transition and the development of a fully turbulent boundary layer. Pressure measurements along pressure side of passage B indicate that large velocity peaks occur in the front side of the passage. The adverse pressure gradient promotes early transition to turbulence in the pressure side, at $x/C_{ax,strut}$~0.5, From this point onwards, turbulent boundary layer stabilized and thickens progressively, leading to a decrease of the local Nusselt number. Passage C shows a similar scenario to passage B on the pressure side heat transfer. However, on the suction side the onset of transition to turbulent boundary layer is delayed and occurs only at the rear part of the profile ($x/C_{ax,strut}$~0.9) when the flow starts decelerating downstream of the aerovane passage throat.

In regards to passage D, the transition onset in the suction side is found at about $x/C_{ax,strut}$~0.15, corresponding to the flow deceleration observed in the pressure distribution. The increase of area in the transition channel is not counter-balanced by the low curvature of the structural vane profile in that zone, resulting in diffusion. The turning imposed by the airfoils is enough to oppose the diffusion generated by the inter-turbine channel and accelerates the flow up to the geometric throat. The heat transfer characteristics along the pressure side of the channel is similar to that observed in passage B.

When the turbine operates at off-design pressure ratio and design rotor speed conditions, the rotor outlet flow angle changes significantly. The flow impinges on the structural vane with a large negative incidence (-26 degrees). The detrimental effect on the aerodynamics is clearly visible on the pressure profile: the stagnation point moves towards the suction side in all passages as displayed by Fig. 5.19. The pressure levels are very similar at the rear part of the passages. Regarding passage A, the flow abruptly decelerates on the pressure side at $x/C_{ax,strut}$~0.1. This results in boundary layer detachment because of the strong adverse pressure gradient that closely follows the velocity peak. Early transition to turbulence in the suction side is promoted at approximately $x/C_{ax,strut}$~0.65. The flow approaching towards the suction side is also over accelerated, and impinges in the leading edge at higher velocities than for the other aero-vanes. This effect enhances the heat flux in this region. The separated region extends along most part of the structural vane pressure side, which is supported by both the CFD simulations and oil visualizations presented in Fig. 5.21. The detached flow region evidently affects the suction surface. The flow distortion imposed by the low-speed recirculation structure obstructs a wide portion of the vane passage. Hence, the resulting suction side velocity profile is dominated by a large velocity peak in the leading edge. The Nusselt number distribution reveals the poor performance for this operating regime. The front part of the pressure side presents local values of Nusselt number higher than those found at the leading edge, due to the separation of the boundary layer. Reattachment and development of the turbulent boundary layer is found for values of $x/C_{ax,strut}$~0.5. Owing to the blockage effect originated by this low-velocity region, the flow is steeply accelerated along the suction side of the passage A. The flow still approaches the aerovane with a negative incidence, and early transition is promoted from $x/C_{ax,strut}$~0.6 to $x/C_{ax,strut}$~0.75. On passage B, the trend is similar to the nominal conditions, although the flow still approaches the aero-vanes with negative incidence. Thus, the velocity peak on the pressure side is larger than what has been measured for the nominal conditions. Passage C is the least affected by the change of the turbine pressure ratio. The Nusselt number distribution along the passage closely resembles the levels observed in passage B with slightly lower heat flux on the pressure surface.

The heat flux on the LP vane passages at *Low-Low* conditions is shown in Fig. 5.20. Overall, the levels of Nusselt number in the aero-vane passages remain nearly the same as in the design conditions. The heat flux past the strut surfaces is observed to decrease by almost 25-50% as a consequence of the reduced flow speed at positive flow incidence. The largest effect of pressure ratio and positive flow incidence is found on the Nusselt number evolution of the two central passages. With respect to the design case, the suction side of passage B and C experience earlier transition to turbulent boundary layer, at $x/C_{ax,strut}$~0.5 and $x/C_{ax,strut}$~0.6 respectively. This is thought to be caused by the slightly higher flow incidence at the aerovane front part and mostly by the reduced favorable pressure gradient as the flow speed has decreased.

The correlations reported in eq. 5.3 and eq. 5.4 agree with the experimental observation, which is more evident for passage B and C where the flow is guided by both aero-vane surfaces, thus closely resembling the flow in a pipe. As expected, the central passages appear to be the most efficient in a multi-profile stator configuration from a heat transfer point of view. For all passages, the abrupt decrease of the Nusselt number due to the thickening of the laminar boundary layer is also well predicted. Overall, the experimental data are found to lie within the heat transfer levels estimated by the laminar and turbulent correlations. Therefore, results give confidence that Nusselt levels predicted by correlations for laminar and turbulent flow in a pipe may still provide an effective indication of the heat transfer variations found in turbine rows. Additionally, the static pressure distributions provide a guideline to assess the onset of boundary layer transition. On the other hand, the largest discrepancy between the correlations and the experimental data is found in the region where transition occurs, suggesting that the correlations are only valid for fully laminar and turbulent boundary layers.

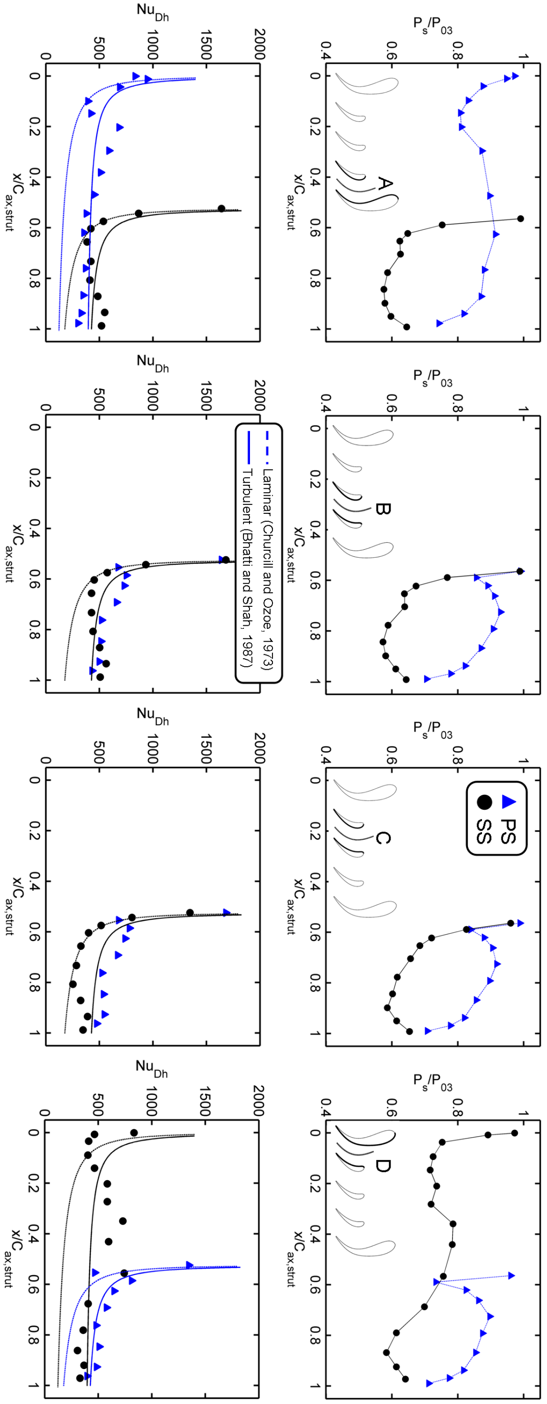

Figure 5.18: *Time-average Nusselt number distributions at Nom-Nom conditions*

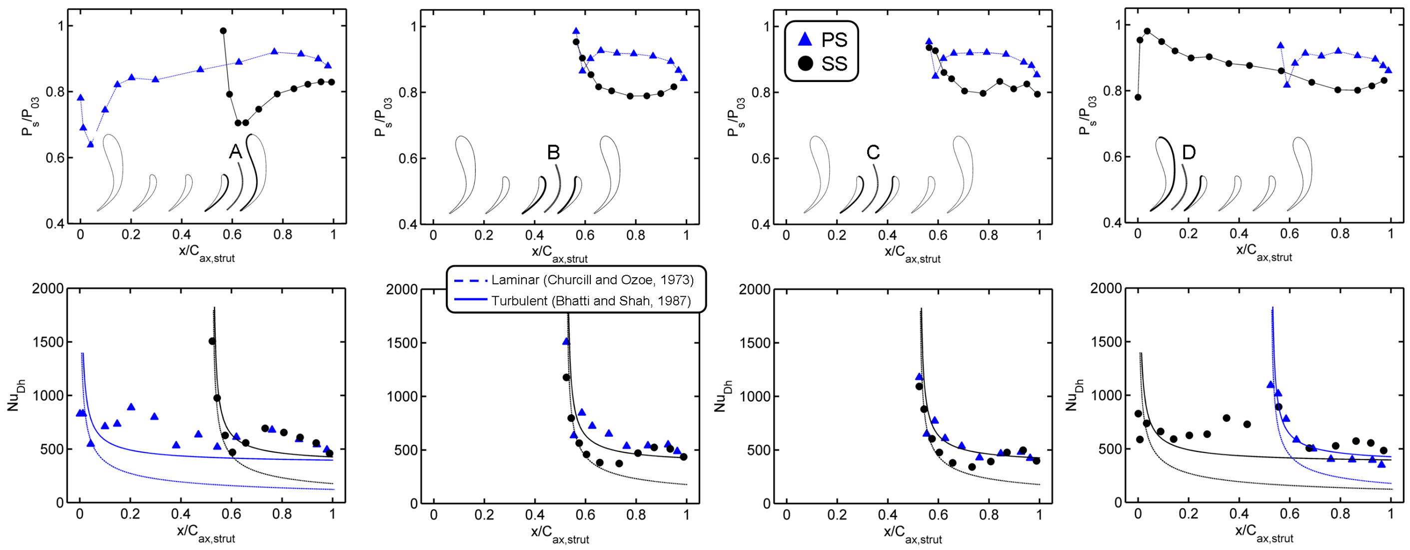

Figure 5.19: *Time-average Nusselt number distributions at* Low-Nom *conditions*

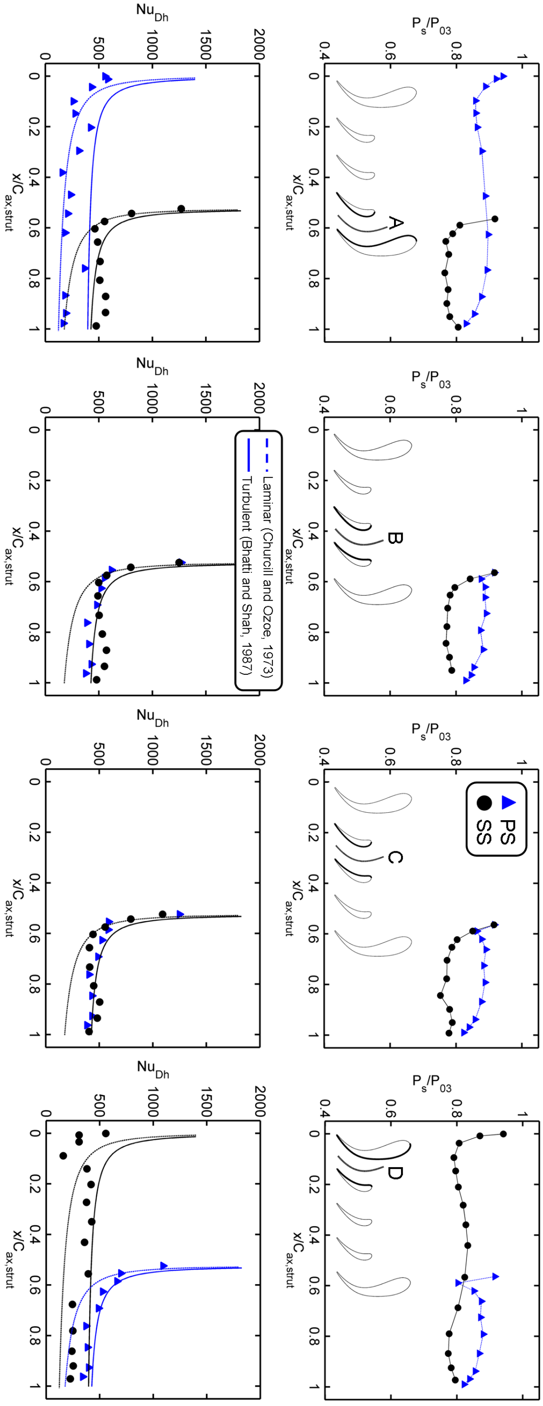

Figure 5.20: *Time-average Nusselt number distributions at* Low-Low *conditions*

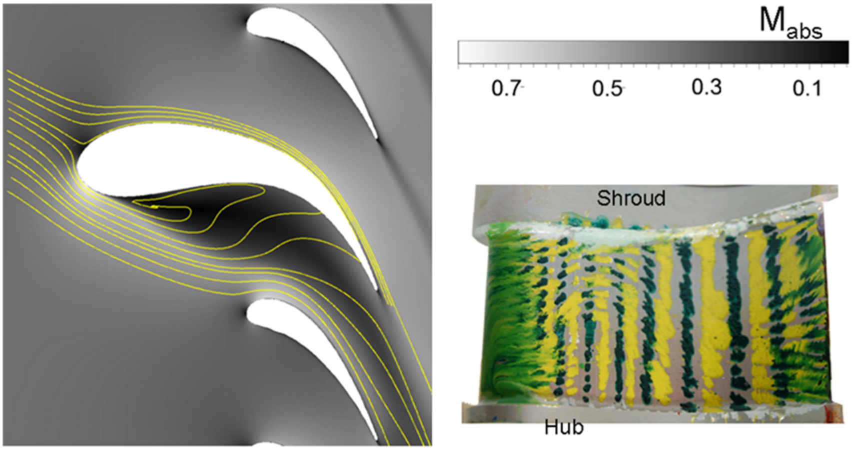

Figure 5.21: *Mach number distribution and streamlines at 50% span at off-design* Low-Nom *conditions (left), flow visualization of the separated region on the structural vane pressure side (right)*

5.3.3 Mid-span time-resolved heat transfer

Fig. 5.22 displays the Fast Fourier Transform (FFT) of the heat fluxes at design and off-design (*Low-Nom* condition) in several gauges across the passages, in the range of frequencies between 0 to 25 kHz. The fundamental frequency of the rotor blade passing and two harmonics are well captured in the measurements. The amplitude of the fundamental frequency tends to increase along the suction side. This phenomenon is related to the boundary layer status. As it is shown in the time averaged results, once transition occurs, the boundary layer becomes more energetic and the convective terms are stronger than in a laminar boundary layer. In a laminar boundary layer the amplitude of the unsteadiness is low in comparison to a turbulent boundary layer, due to a lack of convective movement towards the wall. The high convective movement in a turbulent boundary layer enhances the transport of the external fluctuations towards the wall. At off-design conditions, the blade passing frequency is also noticed in the FFT, where a frequency band at around 1 kHz appears on the suction side of passage A. This frequency band is related to the appearance of a separation bubble in the pressure side of the structural vane and its effect is particularly visible on the front suction side of aerovane C adjacent to the strut airfoil.

This information can be translated to the phase domain in order to have information of the different phenomena and their relative position in phase. Fig. 5.23 displays the time resolved fluctuations along the suction side in passages A and C. The heat flux shows a similar trend along the rear suction side of the two aero vanes. All heat flux signals are characterized by a clear peak as one rotor blade sweeps one aero-vane pitch. The amplitude of the heat flux peak grows larger from the aero-vane mid passage, 2-3 $\mathrm{kWm^{-2}}$, towards the trailing edge, where the heat flux rises to approximately 8 $\mathrm{kWm^{-2}}$. In Fig. 5.23 the dotted line shows the location of the local maximum in the heat transfer traces along the rear suction side of passages *A* and *C*. It should be noted that the heat flux fluctuations do not manifest any convective pattern. As the rotor sweeps across on vane pitch, the perturbation that originates the heat flux variations appears to move upstream. Therefore, the unsteady heat flux field in the low-pressure vane is governed by a potential interaction between the rotor and stator rows.

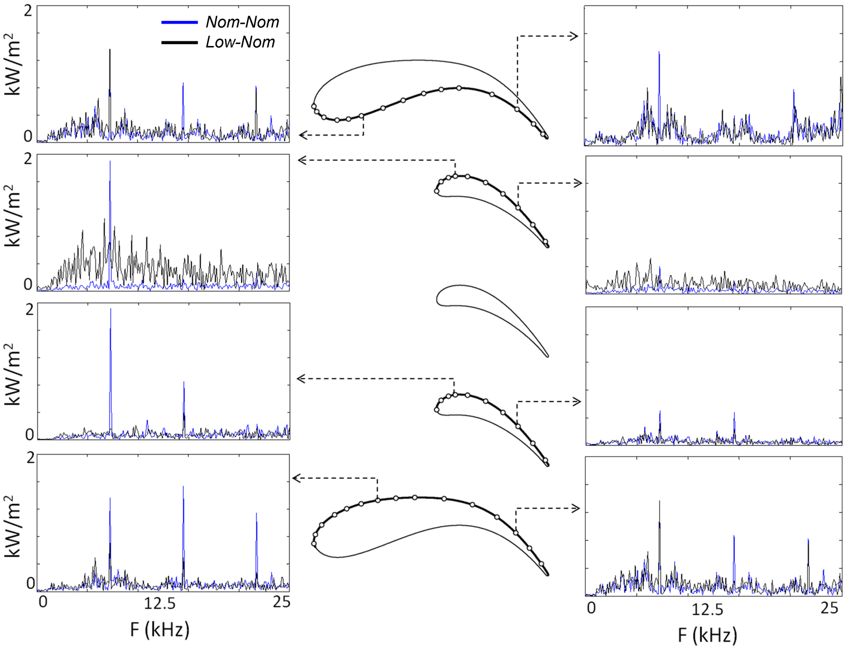

Figure 5.22: *Frequency spectra at design and off-design (*Low-Nom*) conditions*

The viscous effects due to the sweeping of the unsteady rotor wake in the rear suction side are not observed in the time-resolved data at the blade passing frequency. Additionally, the time-resolved heat transfer data differ depending on the airfoil position relative to the structural vane. The large airfoil generates a strong potential field that locally modifies the interactions between the unsteady flow structures periodically released at the rotor outlet and the aero-vanes.

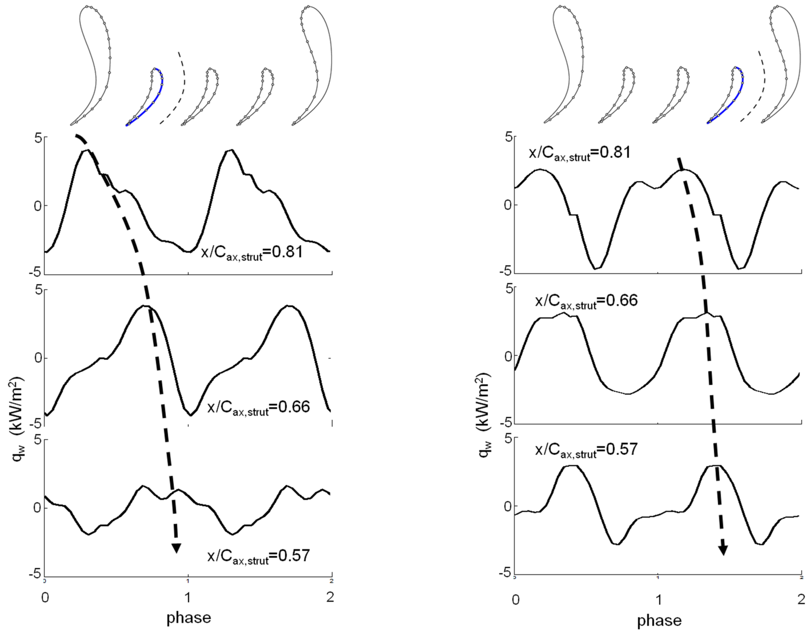

Figure 5.23: *Phase-locked averaged heat flux on two different passages at design conditions*

5.4 Loss analysis of the multi-profile LP vane

In this section the aerodynamic performance of the low-pressure multi-splitter vane is numerically investigated using 3D Reynolds-Averaged Navier-Stokes computations. The main goal of this study is to evaluate the aerodynamic behavior of the multi-profile architecture when the HP turbine operates at off-design conditions. In addition, numerical simulations are employed to assess the impact of the bulky strut profile on the losses and outlet flow quality of the stator in comparison with a conventional single-airfoil stator geometry.

5.4.1 Numerical campaign and CFD calibration

The simulations were performed at design and off-design conditions on two LP vane geometries: the first geometry has a multi-splitter layout (Model 1, experimentally investigated) and the second one has a conventional design with only aero-vane profiles (Model 2, derived from the multi-splitter vane geometry). Extensive description of the CFD settings and details of the mesh topologies have been given in section 2.4. Four numerical runs were performed for both models varying the turbine operating pressure ratio at constant rotor speed (6790 rpm). The investigated turbine flow conditions are summarized in Table 5.1. Case 02 and 04 reproduce two experimental test conditions, *Nom P/p - Nom speed* and *Low P/p - Nom speed* respectively. In Case 01 the flow from the HP turbine stage enters the LP stator with a positive incidence with respect to the design case. As the pressure ratio (total-to-static) is reduced, the rotor outlet flow enters the LP vane with increasing negative flow incidence.

	Multi-splitter Design (model1)						Conventional Design (model2)			
	1	2*	2exp	3	4	4exp	1	2	3	4
P_4/P_{01}	0.22	0.27	0.27	0.37	0.48	0.48	0.22	0.27	0.37	0.48
P_{03}/P_{01}	0.36	0.38	0.38	0.45	0.55	0.55	0.36	0.38	0.45	0.54
M_{03}	0.4	0.37		0.32	0.29		0.4	0.38	0.32	0.3
α_3	-13	-7		12	32		-13	-8	11	30
M_{04}	0.86	0.71		0.53	0.4		0.86	0.71	0.53	0.41
α_4	64	63		62	59		64	63	63	62

* *Design Condition*

Table 5.1: *Summary of the CFD test matrix with flow quantities at mid-span*

The solver is first calibrated using experimental data. Airfoil loadings and downstream pressure fields are compared for both models. The pitchwise static pressure distribution is measured at the exit of the rotor and at LP stator outlet, respectively at $0.45C_{ax,r}$ (plane 03) and $3.96C_{ax,r}$ (plane 04) downstream of the rotor trailing edge. The measurements are taken over a strut pitch at two different peripheral locations in order to monitor the circumferential periodicity. Then, they are duplicated to cover 1.5 pitches. Data are normalized by the inlet total pressure at mid-span to account for test-to-test variations. Pitchwise static pressure distributions measured upstream of the LP stator are presented in Fig. 5.24. The different symbols are used to distinguish two peripheral locations. The CFD predictions for the multi-splitter vane model are in good agreement with the experiments both at hub and tip. The strut vane is observed to sensibly alter the aerodynamic potential field close to the rotor outlet. This is due to the large size of the airfoil and its proximity to the rotor blade row. The pitchwise static pressure in plane 03 at the shroud endwall clearly shows a pressure variation (approximately 2% of P_{01}) along a strut vane pitch (Fig. 5.24). At the hub endwall the static pressure variation becomes weaker since the strut leading edge is located further downstream than at tip.

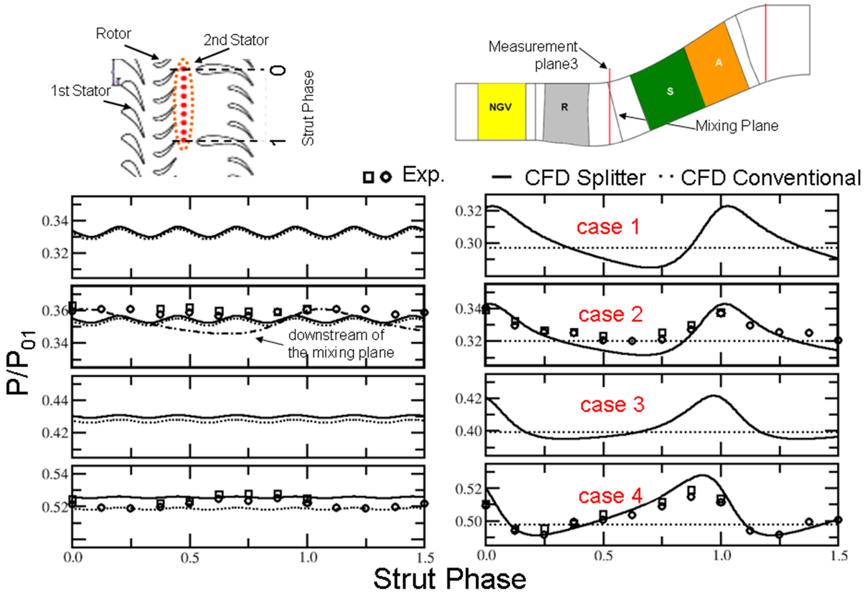

Figure 5.24: *Pitchwise pressure distribution upstream of the LP vane at hub (left) and tip (right)*

Fig. 5.25 depicts the static pressure distribution downstream of the LP stator at hub and tip endwalls. The LP stator outlet shows a rather uniform pressure distribution except for Case 01 when the second stator outlet is transonic close to the hub region. Numerical predictions indicate that the splitter configuration causes a slight variation on the downstream pressure field only at higher outlet Mach number (Case 01 - hub). The presence of the strut vane causes the outlet flow speed to reduce at a strut phase of 1.

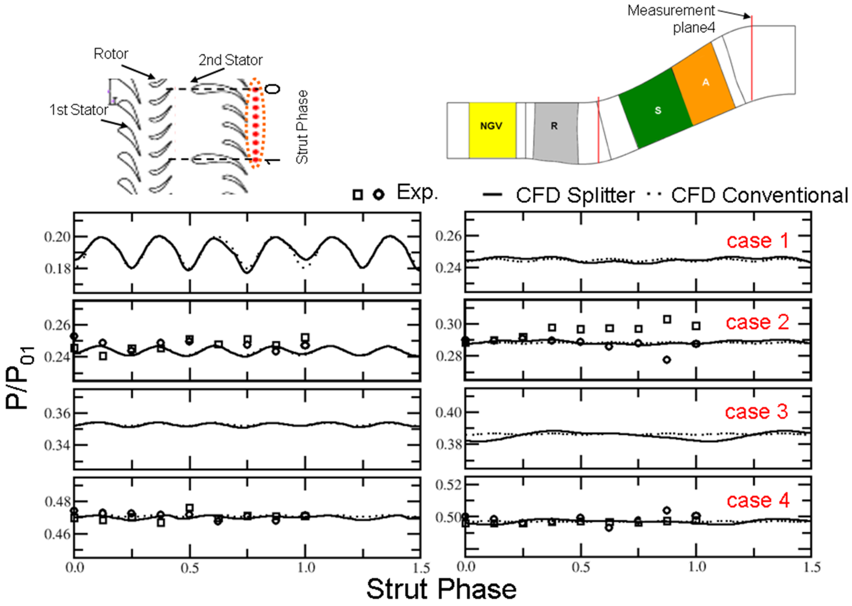

Figure 5.25: *Pitchwise pressure distribution downstream of the LP vane at hub (left) and tip (right)*

The predicted airfoil static pressure distribution for all cases is plotted in Fig. 5.26 at mid-span. Good agreement is achieved with the experimental data (Case 02-04). At design conditions (Case 02), flow accelerates rapidly at the leading edge region due to curvature effect. The flow that enters the strut passage maintains its speed until it enters the aero-vane passage. Then, it speeds up into the aero-vane passage smoothly until the trailing edge. Comparison between the multi-splitter and the conventional LP vane geometry shows that the strut airfoils primarily affects the flow field in the aero-vanes crown region. In fact, the struts modify the aero-vanes' incidence angle depending on the aero-vane's circumferential position since the flow is turned inside the strut passage upstream of the aero-vanes (see section 5.2.2). When the stator runs at low pressure ratio, the incidence angle changes drastically from -7 degrees to +32 degrees, which causes a high diffusion rate close at the shroud due to the coupled effect of the s-shape duct area increase and leading edge curvature. Therefore, the flow separates on the pressure side of the strut.

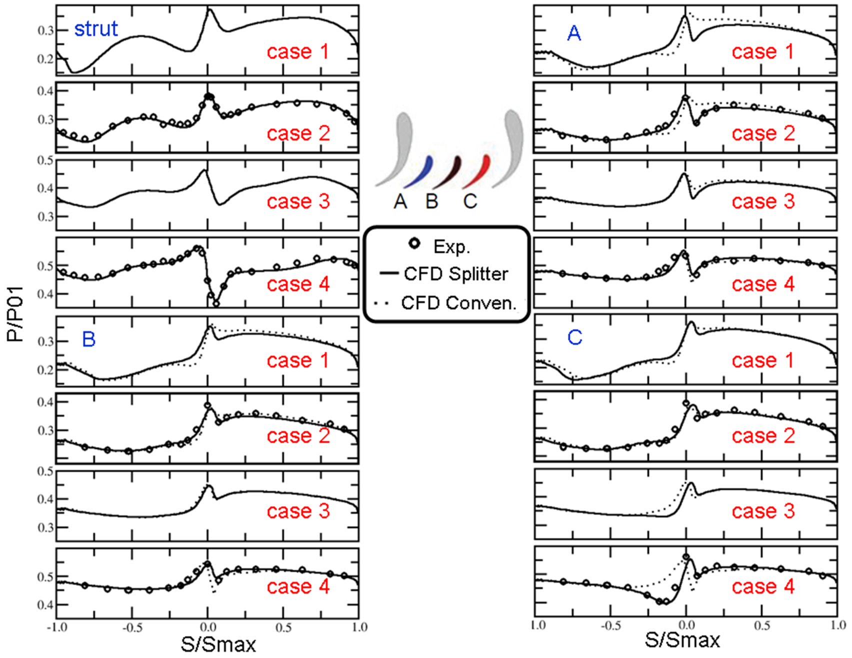

Figure 5.26: *Static pressure distribution around the three aero-vane and strut at mid-span*

5.4.2 Impact of the multi-airfoil geometry on the vane outlet flow

Fig. 5.27 represents the flow angle difference between the conventional LP vane geometry and the multi-profile configuration over a strut pitch. In the conventional vane model the flow angle in the circumferential direction remains uniform from the rotor outlet plane plane (plane 03) till 10% of the aerovane axial chord upstream of the aerovane leading edge; from that point onwards, each vane experiences similar distortion. On the contrary, in the multi-profile model, the strut profile already causes a perturbation of the flow angle immediately downstream of the strut passage entrance ($1.54C_{ax,r}$). However, the outlet flow remains uniform for both configurations, except in the case where a large separation occurs on the strut pressure side due to the high negative flow incidence (multi-splitter model, case 03 and case 04).

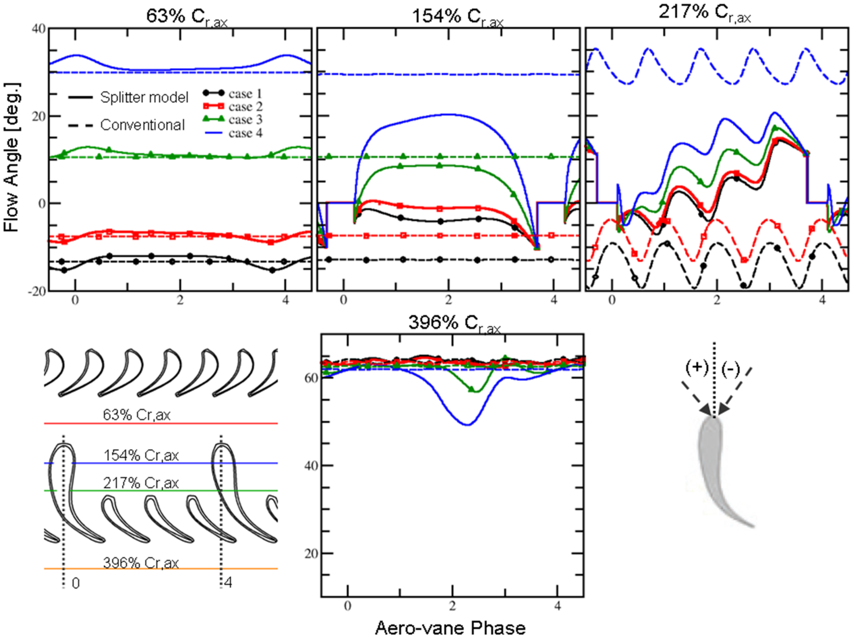

Figure 5.27: *Pitchwise flow angle distributions for multi-splitter and conventional vane geometries*

Fig. 5.28 and Fig. 5.29 plot the total pressure field at the outlet plane (plane 04) of the two LP vane models. The multi-splitter configuration generates different flow fields at the outlet of each stator passage. The effect of the multi-airfoil design is easily observed by comparing the total pressure maps of the two flow passages adjacent to the strut vane (S) pressure side (flow passage *S-C*) and suction side (flow passage *S-A*). This dissimilarity in the outlet flow field is found to be significant at all the investigated turbine regimes. However, the flow in the passages between the aero-vanes (*B-C* and *A-B*) does not suffer any strong change and keeps very similar to the aerovane-alone model. A positive flow incidence on the strut profile (Case 01) does not affect the quality of the outlet flow field. The flow is transonic close to the hub region. The trailing edge shock system causes a low pressure region. The structural-vane shock system has a stronger impact on the pressure field when the incidence angle becomes positive.

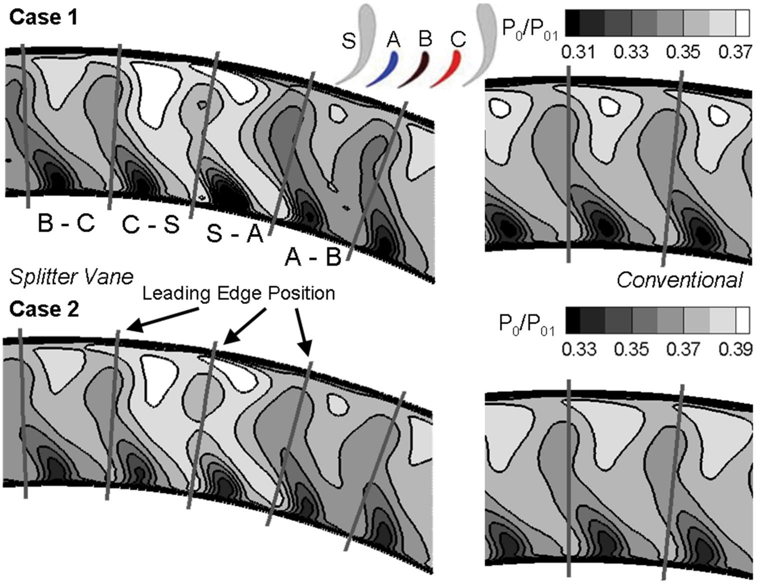

Figure 5.28: *Non-dimensional total pressure field downstream of multi-splitter and conventional LP vane models for CFD case 01 and 02*

Due to the large thickness of the strut profile, the strut airfoil is very sensitive to negative flow incidence (Case 03 and 04). The displacement of the stagnation point towards the suction side, the combination of large leading edge curvature of the strut vane and the high diffusion rate at the tip endwall triggers the flow separation in the vane passage *S-C*, Fig. 5.21. The separation starts close to shroud region when the flow angle goes from -7 degrees to 12 degrees (case 03) as shown in Fig. 5.29, top. This region tends to migrate towards the mid-span when the pressure ratio is further reduced (case 04). The separation bubble almost blocks the upper half of the channel between the strut airfoil and aerovane *C*. The blockage effect reduces the effective flow area so that the flow accelerates more on the lower half of the passage. On the other hand, the conventional design is free of any separated flow and shows insensitivity to the inlet flow incidence for the

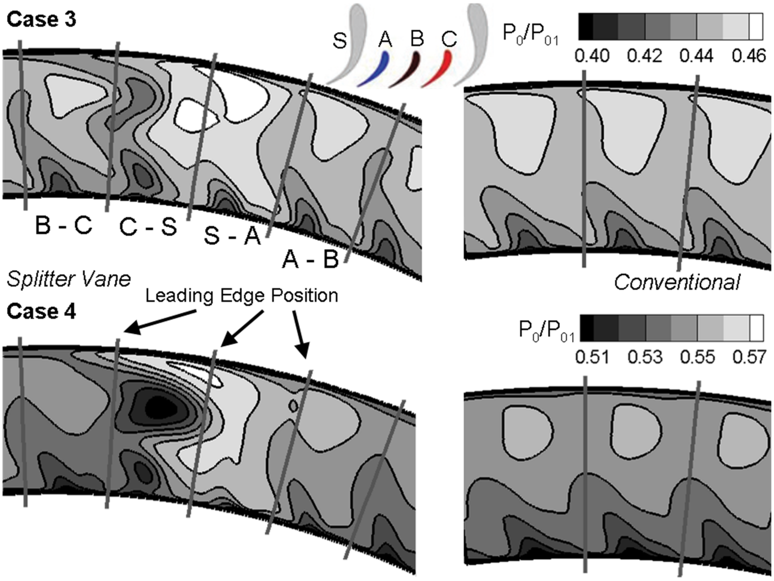

Figure 5.29: *Non-dimensional total pressure field downstream of multi-splitter and conventional LP vane models for CFD case 03 and 04*

investigated off-design conditions.

5.4.3 Performance evaluation and comparison

5.4.3.1 Methodology for the performance estimation

Traditional performance evaluation methods focus on the flow analysis around an airfoil. However, such approach is not useful for innovative geometries with non-periodic passages. In the case of non-periodic flow generated by a multi-profile architecture, the pressure losses are evaluated on a domain that includes the ducted passage between the suction side and the pressure side of two neighboring airfoils. The use of this procedure allows the analysis of the streamlines through the passage and the estimation of the losses associated with them. The domain limits are defined at the inlet and outlet planes of the LP vane using streamlines on blade to blade cuts at 27 different radial locations. At both inlet and outlet planes the rectangular flow channels are generated using the span-wise domain limits of two consecutive blade-to-blade cuts. The radial profiles of the flow properties are obtained by performing pitchwise and mass averaging in each individual rectangular channel. The height of the stream tubes at the inlet and the outlet are adjusted considering a mass flow balance.

5.4.3.2 Pressure losses

The kinetic losses were computed according to Traupel [162]:

$$\zeta = 1 - \frac{1 - \left(\frac{P_{s,out}}{P_{0,out}}\right)^{\frac{\gamma-1}{\gamma}}}{1 - \left(\frac{P_{s,out}}{P_{0,inlet}}\right)^{\frac{\gamma-1}{\gamma}}} \tag{5.5}$$

Eq. 5.5 is used to compute the loss coefficient on each stream-tube along the span-wise direction. The size of the stream-tubes in the circumferential plane is adjusted according to the mass flow distribution in the four different vane passages characterizing a full LP vane pitch (multi-splitter vane design). The same procedure is also applied for the conventional design case for comparison purposes. Inlet conditions are extracted downstream of the mixing plane. Hence, the inlet plane is slightly shifted downstream of plane 03 to avoid calculations to be performed on the CFD domain interface where the mixing plane is located. The outlet conditions are taken at the measuring plane 04 (Fig. 5.24 and Fig. 5.25).

Fig. 5.30 shows the inlet and outlet mass flow and kinematic loss distributions along the span. The pressure loss and mass flow distributions are reported for each of the four individual passages together with the overall value corresponding to a full strut pitch. The global performance of the new multi-profile stator design are compared to the performance of the conventional stator geometry. The mass flow distributions are normalized by the total mass flow of each passage.

The conventional model performs generally better than the novel multi-splitter architecture. The pressure loss level and distribution are particularly different in the top part of the vane channels. At design conditions (case 02), the aero-vane passages *B*-*C* and *A*-*B* show similar loss distribution to the "aero-only" passage. The same consideration holds when comparing the other two passages (*A*-*S* and *C*-*S*) up to mid-span. In the upper part of these vane passages, the losses are larger and present the same trend as the single-airfoil calculation. The loss rise in this region also characterizes the performance of the multi-splitter vane model. When the stagnation point moves towards the pressure side (case 01), the loss profiles do not change significantly. The performance of the passage between strut and aerovane *C* is enhanced above the mid-span. On the other hand, the passage *S*-*A* shows increased loss penalty in the hub region (approximately up to 20% of the vane span). This loss rise is probably due to the detrimental effect of transonic flow conditions occurring in this area. The outlet mass flow is equally distributed in the radial direction for both cases.

The strut vane performance is drastically altered when the flow has a negative incidence (case 03-04). A separation region appears at the shroud. The extension of the separation region appear to be proportional to the flow incidence magnitude. The recirculation zone obstructs a wide portion of the vane passage adjacent to the strut airfoil pressure side (passage S-C). Consequently, the radial mass flow distribution is strongly altered, not only in the passages adjacent to structural-vanes (passages S-A and S-C), but also in the central passage B-C. The separation causes an increase of the flow speed in the lower mid-channel. Since the inlet mass flow rate is nearly the same as in the other vane passages and the separation region blocks the upper half of the channel, the flow which enters the passage close to the shroud is confined in a region between 25% and 60% of the span. Although the flow quality in the vane channels that comprise the strut profile is significantly penalized by the flow angle change, the impact on the global performance of the multi-airfoil LP vane is limited, and the pressure losses are only doubled.

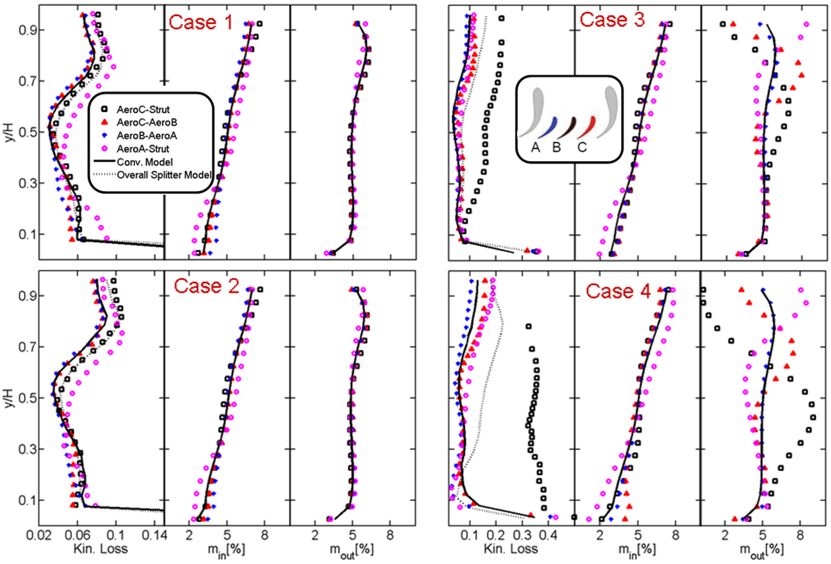

Figure 5.30: *Kinematic loss and mass flow distribution for all cases*

The radial loss distribution is massflow-averaged in order to study the global performance of each passage. Fig. 5.31 displays the global stator kinetic loss as a function of the pressure ratio. The kinetic losses are plotted with two different scales in order to highlight the comparison between the single-profile and the multi-splitter stator configurations (Fig. 5.31, left), and improve the visualization of the passage-to-passage losses (Fig. 5.31, right).

The multi-airfoil vane model shows higher losses for all the operating conditions. However, the performance gap with the conventional model is less than 1% at design conditions and for positive incidence flow angles. The performance penalty rapidly increases when the HP turbine flow approaches the LP vane with a negative incidence. The aerodynamics of the "aero-vane only" geometry is observed to be more robust to large negative flow angles. The performance of the conventional design remains unaltered for inlet flow angle with moderate negative incidence (Case 03, α_4=11 degrees). The four vane passages of the multi-splitter configuration generate similar kinetic losses for positive incidence angles. The central aero-vane passages C-B and A-B of the multi-splitter stator show improved performances with respect to the conventional single-airfoil situation. The strut profile modifies the flow direction in the channel upstream of the aero-vanes. This helps to smooth the detrimental effect of strong flow incidences on the aero-vane airfoils, which results in a reduction of the pressure losses compared to "aero-vane only" model. The highest increase of kinetic loss is observed for the passage between the strut pressure side and the aerovane suction side (passage S-C), about 4 times higher than in the other three vane passages at the highest pressure ratio.

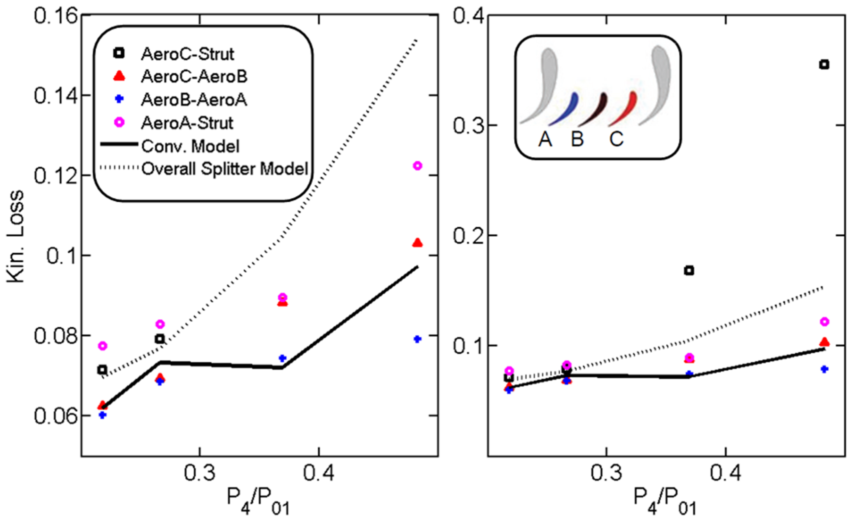

Figure 5.31: *Variation of the LP vane performance with pressure ratio for multi-profile and conventional geomtries*

5.5 Conclusions

The steady and unsteady aero-thermal field in an innovative multi-profile LP stator was measured in a short duration test rig in the presence of a fully rotating high-pressure turbine operated at two pressure ratios and two rotor speeds. The experiments reproduced the relevant engine non-dimensional numbers, namely Reynolds number, Mach number and temperature ratios.

The experimental investigation showed that the struts cause an evident blockage effect resulting in a circumferential non-uniformity of the aero-vane inlet flow field. The surfaces adjacent to the strut profiles are the most affected. At the rear part of the airfoils the pressure levels are similar and the vane outlet field is uniform for all the operating conditions. The structural vane is sensitive to the negative incidence. The flow separates at strut pressure side when the rotational speed is reduced and a strong acceleration is observed on the suction side of the aero-vane *C*. CFD computations revealed that the strut profiles impose a circumferential gradient on the aero-vane inlet flow angle. The flow incidence on the aero-vanes always increases from strut pressure side to strut suction side independently of the rotor outlet flow angle. At the aero-vane inlet, the flow velocity shows similar pitchwise distributions when the operating condition changes. Results suggest that multi-body stator concept might offer designers a practical solution to design LP vanes with robust off-design performances.

A complex flow structure was observed for the unsteady pressure field. The combined effect of multi-splitter configuration and clocking modifies the spatial periodicity of the unsteadiness structure shed by the upstream stage. The amplitude and shape of the periodic signals significantly depend on the circumferential position of the airfoil. Up to four pressure fluctuations affect the phase-locked traces. However, the presence of the strut does not cause a dramatic change on the global unsteady performances. Strut and aero-vanes show generally similar pressure variations. The largest unsteady loadings are found to occur on the pressure side and the leading edge regions, more exposed to the rotor disturbances. Surprisingly, the strut vane does not suffer the highest unsteadiness although its leading edge is closer to the rotor. The frequency analysis has highlighted that the amplitude of blade passing is not always the dominant frequency. Depending on the airfoil position and on the testing regime, the amplitude size of the harmonics can be far larger than the fundamental. No significant differences appear between the strut and aero-vanes spectra. However, when the flow separates on the strut pressure side, large size amplitude levels are observed in a low frequency band between 500 and 1600 Hz. The recirculation region extends its influence on the adjacent vane C causing the appearance of a strong peak at 1200 Hz around the vane crown.

The unsteady forces acting on the four profiles were computed based on the periodic pressure data. The three aero-vanes experience similar axial forces, two times larger than the one of the strut. For all the conditions aero-vane *A* presents the lowest mean level of tangential force but the weakest fluctuations are found for aero-vane *B*. The force modulus was shown to be the largest for the aero-vanes but again, the unsteady variation is stronger on the strut (40% of the mean level). At *Low-Nom* the force applied on the strut becomes negative due to the wide separated region on the pressure side. Reducing the turbine pressure ratio also lowers the force fluctuations on the aero-vanes. When the rotor speed is also decreased, the force acting on the strut is almost insignificant. This counter-balances the strong unsteady angle variations and no dramatic effects on the strut unsteady loading are expected. The angle variation magnitude for the aero-vanes is rather small at all the turbine regimes. The total force acting on the whole LP stator was seen to drop 30% when the pressure ratio was reduced.

Time-average and time-resolved heat transfer measurements on the LP vane were carried out by means of fast-response thin-film gauges mounted on a ceramic substrate. In combination with the airfoils' pressure loads, the heat transfer information helps to characterize the boundary layer status and the main driving mechanisms in the boundary layer transition. The steady heat flux data were compared to existing correlations for ducted flows, which allowed the detection of the onset of transition. A good match was observed between the experimental values and the correlations. The results showed that by-pass transition is mainly triggered by adverse pressure gradients. The separated flow region found at the strut pressure side at off-design condition (negative flow incidence) has a significant impact also on the thermal loads of the LP vane. The unsteady heat transfer data showed the presence of low frequency heat flux fluctuations related to non-identical rotor blade geometries. The time-resolved heat flux at the blade passing frequency yielded information about potential effects on the vanes due to the interaction with the rotor.

Numerical simulations were carried out to evaluate the aerodynamic performance of the multi-splitter low-pressure stator at design and off-design conditions. Additionally, the CFD study was extended to a conventional single-airfoil stator architecture and comparison of the results helped to determine the performance penalty introduced by the presence of the bulky strut profile. Four turbine pressure ratios were investigated which corresponds to different inlet flow swirl levels at the LP vane inlet. The CFD was validated against the collected experimental data.

The CFD results showed the effect of the strut profile on the aero-vane inlet flow conditions and served to quantify the flow angle non-uniformity across the full stator vane pitch. The static pressure and flow angle distribution at the multi-splitter stator outlet is rather uniform in the pitchwise direction (±2 degrees), and the potential interaction of the strut airfoil is limited unless large flow separation occurs on the strut pressure side. The multi-profile stator geometry results in non-uniform outlet total pressure distribution among the four vane passages. However, the vane passages bounded by the aero-vane profiles perform similarly to the passage in the single-airfoil configuration. The structural-vane is highly sensitive to the negative incidence and thus the multi-splitter vane configuration result in poor aerodynamic performance due to the appearance of a separated flow region on the strut pressure side. The recirculation region partially blocks the flow passage on the upper half of the channel on the pressure side of the strut airfoil modifying the mass flow and pressure distribution in the span-wise direction.

A methodology was introduced that allows the evaluation of pressure losses in a multi-airfoil environment. The performance penalty associated to the multi-splitter vane configuration were quantified and compared to the conventional, single-airfoil, LP vane model. The two stator geometries showed similar efficiency levels at design and positive incidence conditions. When the pressure ratio reduces, the flow becomes locally transonic and penalizes the performance. The multi-profile vane configuration rapidly loses its performance when the stagnation point moves towards the suction side whereas the "aero-only" design is more robust to flow angle changes. On the other hand, the multi-airfoil design approach enhances the performance of the central passages at off-design conditions.

Chapter 6

Conclusions

The present research has addressed the experimental characterization of the aerothermal flow field in a one and a half turbine stage environment. The investigated module is composed of a high-speed HP turbine stage and a low pressure vane with an innovative multi-airfoil design, integrated in a s-shape transition duct.

The turbine experiments were performed in the large short-duration rotating turbine rig at the von Karman Institute. A series of experiments were conducted to investigate the unsteady heat transfer and pressure field on the casing of the transonic shroudless rotor. Another extensive test campaign was dedicated to the analysis of the aerodynamic and thermal performance of the multi-body LP vane in an engine-like scenario.

Special attention was paid to the development of accurate rotor tip clearance measurements in the transient turbine wind tunnel:

- A capacitance-based proximity measurement sensor was successfully used to resolve the tip gap variations over single rotor blades. The measurement system was installed on the shroud of the turbine stage and calibrated in-situ using two different techniques: 1) calibration by means of an absolute clearance reference provided by wear gauges fitted on the rotor casing ring, 2) sensor self-calibration with no absolute clearance reference. An advanced data reduction technique was used to improve the calibration accuracy using the full rotor blade dataset available.

- A methodology was introduced for the estimation of the uncertainty in the tip clearance measurements. Theoretical predictions and turbine measurements showed that the tip clearance could be measured within ±15 μm (20:1) at a working range below 1 mm.

- The blade-average rotor tip clearance was measured to be around 0.2 mm during a typical blow-down run at 6790 rpm and 0.45 mm for tests at 4500 rpm.

- Experiments revealed that the tip clearance level is sensitive to the thermal conditions of the wind tunnel as repeated hot gas blow-downs are performed. The tip clearance was observed to reduce up to 0.05 mm in a day as the rotor assembly becomes hotter than the casing.

- The blade-to-blade tip clearance measurements showed a maximum variation of 0.30 mm over the 64 rotor blades and the blade radius signature over one rotor revolution remains unchanged from static to rotating conditions.

The investigation of the rotor casing flow has provided original observations on the overtip heat transfer and aerodynamics:

- The adiabatic wall temperature and the true Nusselt number were determined at three circumferential locations around the rotor casing. The analysis of the heat transfer data was supported by simultaneous measurements of unsteady static pressure and running blade-to-blade tip clearance.
- Local unsteady adiabatic wall temperature peaks 40% higher than the turbine total inlet temperature and Nusselt number fluctuations between 80% and 140% of the Nusselt time-average value were measured in the overtip gap region.
- A large variation of the blade-to-blade time-resolved adiabatic wall temperature and Nusselt number was observed. The fluctuations of the local driver temperature and Nusselt number showed no correlation with the tip gap size in a range of tip clearances comprised between 0.3% and 0.9% of the blade span.
- The shroud static pressure is strongly modulated by the tip clearance variation during a turbine blow-down.
- The shroud static pressure showed a clear match with the adiabatic wall temperature and heat flux signatures during the rotor spinning-up phase. This feature pointed out that the blade-to-blade heat transfer variability is likely to be generated by a flow mechanism that is active in both the run-up and the blow-down experiments, independently of the tip clearance size. The magnitude of the unsteady adiabatic wall temperature amplitudes was also observed to be dependent on the rotor speed.
- A theoretical model based on Euler's work equation was used to predict the flow total temperature change for a pre-rotation test and a turbine run where strong tip leakage flows take place.

Analysis of the steady and unsteady aero-thermal flow field in the multi-profile low-pressure stator vane lead to the following conclusions regarding the novel stator architecture and its interaction with an upstream high-pressure turbine stage:

- The strut profiles cause an evident blockage effect and worsen the circumferential non-uniformity of the aero-vane inlet flow field. Identical rear profiles for the four vane airfoils ensure uniform outlet flow angles.

- The bulky strut vane is sensitive to the negative incidence and a large separated flow region appears on the strut pressure side. The vane passages adjacent to the strut profiles are the most affected.

- The strut airfoil offers a beneficial effect at off-design conditions by adjusting the flow swirl at the aerovane inlet section always towards design values.

- The combined effect of the multi-splitter configuration and clocking modifies the spatial periodicity of the unsteadiness structures shed by the high-pressure stage.

- The amplitude and shape of the periodic pressure signals significantly depend on the circumferential position of the airfoil. However, the strut does not cause a dramatic change on the global unsteady performances and it does not experience the highest unsteadiness although it is closer to the rotor. The largest unsteady loadings are found to occur on the pressure side and leading edge regions of the four airfoils. The three aerovanes experience similar axial forces, two times larger than for the strut, which in turn, is subject to higher amplitude unsteady load fluctuations.

- The amplitude of the pressure fluctuations at the blade passing frequency is not always the dominant frequency component. Depending on the airfoil position and on the testing regime, the amplitude size of the harmonics can be far larger than the fundamental. The recirculation region on the strut pressure side causes the appearance of low frequency fluctuations in the pressure and heat flux spectra. The recirculation region affects the unsteady aero-thermal field on the adjacent aerovane.

- The time-average heat transfer on the vane airfoils could be predicted with existing correlations for ducted flows that allows to detect the onset of boundary layer transition. By-pass transition is mainly triggered by adverse pressure gradients. When a large flow separation occurs on the strut pressure side, the thermal loads are significantly increased on the adjacent vane passages.

- CFD analysis of the multi-profile geometry showed that the total pressure distribution at the LP vane outlet is not uniform among the four vane passages. However, the vane passages bounded by the aerovane profiles perform similarly to a conventional single-airfoil configuration.

- The multi-splitter architecture provides efficiency levels comparable to an "aerovane-alone" arrangement (no struts) at design and positive incidence conditions. However, the conventional LP vane configuration is more robust to inlet flow swirl with negative incidence. Despite this, the multi-airfoil design approach enhances the performance of the central passages at off-design conditions.

This work has provided a significant contribution on two research topics relevant to the design and performance analysis of future aero-engine HP-LP turbine modules. Instrumentation and data reduction tools were specifically developed for the measurement of rotor tip clearance in a transient wind tunnel. It was concluded that accurate tip gap measurements are required to support aero-thermal experiments in such turbine test rigs. The experimental research on the casing heat transfer of a transonic shroudless turbine has reported original findings on the physics and flow mechanisms of the overtip aero-thermal flow field at very tight tip clearances ($<1\% h/H$). Prediction tools are used to illustrate possible scenarios related with the design of transonic blade tip sections. The steady and unsteady aero-thermal dynamics of an innovative multi-profile LP stator vane was measured in engine similarity. The novelty of the observed flow patterns should serve to redesign new families of LP turbines with multi-splitter profiles. Results suggest that the multi-body stator concept might offer designers a practical solution to design LP vanes with robust off-design performances and with no significant aerodynamic penalty compared to conventional single-airfoil architectures. Furthermore, the validity of correlations for heat transfer predictions in turbomachinery passages was assessed providing a powerful tool for engineering evaluations of the thermal loads and cooling requirements.

Bibliography

[1] T. Povey. *On advances in annular cascade techniques.* PhD thesis, Department of Engineering Science, University of Oxford, 2003. 2

[2] P. F. Beard, T. Povey, and K. S. Chana. Turbine Efficiency Measurement System for the QinetiQ Turbine Test Facility. *Journal of Turbomachinery*, 132(1), 2010. 2

[3] A. H. Epstein, G. R. Guenette, and R. J. G. Norton. The MIT BlowdownTurbine Facility. *ASME paper*, (84-GT-116), 1984. 2

[4] C. W. Haldeman and M. G. Dunn. High-Accuracy Turbine Performance Measurements in Short-Duration Facilities. *Journal of Turbomachinery*, 120(1):1–10, 1998. 2

[5] M. D. Polanka, D. A. Hoying, M. Meininger, and C. D. MacArthur. Turbine Tip and Shroud Heat Transfer and LoadingPart A: Parameter Effects Including Reynolds Number, Pressure Ratio, and Gas-To-Metal Temperature Ratio. *Journal of Turbomachinery*, 125(1):97–106, 2003. 2

[6] R. Dénos, G. Paniagua, T. Yasa, and E. Fortugno. Determination of the Efficiency of a Cooled HP Turbine in a Blow-Down Facility. *ASME paper*, (GT2006-9046), 2006. 2

[7] M. A. Hilditch, G. C. Smith, and U. K. Singh. Unsteady Flow in a Single Stage Turbine. *ASME paper*, (98-GT-531), 1998. 2, 99

[8] R. J. Miller, R. W. Moss, R. W. Ainsworth, and C. K. Horwood. Time-Resolved Vane-Rotor Interaction in a High-Pressure Turbine Stage. *Journal of Turbomachinery*, 125(1):1–13, 2003. 99

[9] G. Paniagua, T. Yasa, A. de la Loma, and T. Castillon, L.and Coton. Unsteady Strong Shocks Interactions in a Transonic Turbine: Experimental and Numerical Analysis. *Journal of Propulsion and Power*, 24(4):722–731, 2008. 2, 99

[10] M. G. Dunn, C. W. Haldeman, R. S. Abhari, and M. L. McMillan. Influence of Vane/Blade Spacing on the Heat Flux for a Transonic Turbine. *Journal of Turbomachinery*, 122(4):684–691, 2000. 2

[11] R. Dénos and G. Paniagua. Effect of Vane-Rotor Interaction on the Unsteady Flow Field Downstream of a Transonic HP Turbine. *Proc. Inst. Mech. Eng., Part A*, 219(6):431–442, 2005. 2, 107

[12] S. J. Payne, R. W. Ainsworth, R. J. Miller, R. W. Moss, and N. W. Harvey. Unsteady Loss in a High Pressure Turbine Stage. *International Journal of Heat and Fluid Flow*, 24(5):698–708, 2003. 2

[13] G. Pullan. Secondary Flows and Loss Caused by Blade Row Interaction in a Turbine Stage. *Journal of Turbomachinery*, 128(3):484–491, 2006. 2

[14] F. Hummel. Wake-Wake Interaction and Its Potential for Clocking in a Transonic High-Pressure Turbine. *Journal of Turbomachinery*, 124(1):69–76, 2002. 2, 108

[15] M. G. Dunn. Convective Heat Transfer and Aerodynamics in Axial Flow Turbines. *Journal of Turbomachinery*, 123(4):637–686, 2001. 2

[16] A. De la Loma, G. Paniagua, D. Verrastro, and P. Adami. Transonic Turbine Stage Heat Transfer Investigation in Presence of Strong Shocks. *Journal of Turbomachinery*, 130(3):310–320, 2008. 2

[17] R. S. Abhari and A. H. Epstein. An Experimental Study of Film Cooling in a Rotating Transonic Turbine. *ASME paper*, (92-GT-201), 1992. 2

[18] C. W. Haldeman, R. M. Mathison, M. G. Dunn, S. A. Southworth, J. W. Harral, and G. Heltland. Aerodynamic and Heat Flux Measurements in a Single-Stage Fully Cooled Turbine – Part II: Experimental Results. *Journal of Turbomachinery*, 130(2):684–695, 2008. 2

[19] J. H. P. Ong, R. J. Miller, and S. Uchida. The Effect of Coolant Injection on the Endwall Flow of a High Pressure Turbine. *Journal of Turbomachinery*, 134(5), 2012. 2

[20] G. Paniagua, R. Denos, and S. Almeida. Effect of the hub endwall cavity flow on the flow-field of a transonic high-pressure turbine. *Journal of Tturbomachinery*, 126(4):578–586, 2004. 2

[21] M. Pau, G. Paniagua, D. Delhaye, A. de La Loma, and P. Ginibre. Aerothermal Impact of Stator-Rim Purge Flow and Rotor-Platform Film Cooling on a Transonic Turbine Stage. *Journal of Turbomachinery*, 132(2):1–12, 2010. 2

[22] M. D. Barringer, K. A. Thole, and M. D. Polanka. Experimental Evaluation of an Inlet Profile Generator for High Pressure Turbine Tests. *Journal of Turbomachinery*, 127(2):382–393, 2007. 2

[23] T. Povey and M. I. Qureshi. A Hot-Streak (Combustor) Simulator Suited to Aerodynamic Performance Measurements. *Transactions of the Institution of Mechanical Engineers, Part G, Journal of Aerospace Engineering*, 222(6):205–220, 2008. 2

[24] P. F. Beard, A. Smith, and T. Povey. Impact of Severe Temperature Distortion on Turbine Efficiency. *ASME paper*, (GT2011-45647), 2011. 2

[25] R. M. Mathison, C. W. Haldeman, and M. G. Dunn. Aerodynamics and Heat Transfer for a Cooled One and One-Half Stage High-Pressure Turbine – Part I: Vane Inlet Temperature Profile Generation and Migration. *Journal of Turbomachinery*, 134(1), 2012. 2

[26] T. Povey, K. S. Chana, and T. V. Jones. The Effect of Hot-Streaks on HP Vane Surface and Endwall Heat Transfer: An Experimental and Numerical Study. *Journal of Turbomachinery*, 129(1):32–43, 2007. 2

[27] R. M. Mathison, C. W. Haldeman, and M. G. Dunn. Aerodynamics and Heat Transfer for a Cooled One and One-Half Stage High-Pressure Turbine – Part III: Impact of Hot-Streak Characteristics on Blade Row Heat Flux. *Journal of Turbomachinery*, 134(1), 2012. 2

[28] R. J. Miller, R. W. Moss, R. W. Ainsworth, and N. W. Harvey. Wake, Shock, and Potential Field Interactions in a 1.5 Stage Turbine – Part II: Vane-Vane Interaction and Discussion of Results. *Journal of Turbomachinery*, 125(1):40–47, 2003. 3, 100

[29] C. W. Haldeman, M. Dunn, J. W. Barter, B. R. Green, and R. F. Bergholz. Experimental Investigation of Vane Clocking in a One and One-Half Stage High Pressure Turbine. *Journal of Turbomachinery*, 127(3):512–522, 2005.

[30] N. Billiard, G. Paniagua, and R. Dénos. Impact of Clocking on the Aero-Thermodynamics of a Second Stator Tested in a One and a Half Stage HP Turbine. *Journal of Thermal Science*, 17(2):97–110, 2008. 3, 99

[31] R. J. Miller, R. W. Moss, R. W. Ainsworth, and N. W. Harvey. Wake, Shock, and Potential Field Interactions in a 1.5 Stage Turbine – Part I: Vane-Rotor and Rotor-Vane Interaction. *Journal of Turbomachinery*, 125(1):33–39, 2003. 3, 100

[32] C. W. Haldeman, M. L. Krumanaker, and M. G. Dunn. Influence of Clocking and Vane/Blade Spacing on the Unsteady Surface Pressure Loading for a Modern Stage and One-Half Transonic Turbine. *Journal of Turbomachinery*, 125(4):743–753, 2003. 3, 100

[33] R. J. Miller, R. W. Moss, and R. W. Ainsworth. The Development of Turbine Exit Flow in a Swan-Necked Inter-Stage Diffuser. *ASME paper*, (GT2003-38174), 2003. 3, 97

[34] A. Marn, E. Göttlich, D. Cadrecha, and H. P. Pirker. Shorten the Intermediate Turbine Duct Length by Applying an Integrated Concept. *Journal of Turbomachinery*, 131(4):041014, 2009. 3, 97

[35] J. D. Denton. Some Limitations of Turbomachinery CFD. *ASME paper*, (GT2010-22540), 2010. 4

[36] Rolls Royce plc, editor. *The Jet Engine.* Rolls Royce plc, 2005. 5

[37] T. V. Jones, D. L. Schultz, and A. D. Hendley. On the Flow in an Isentropic Light Piston Tunnel. Technical report, Aeronautical Research Council of Great Britain, 1973. 7

[38] D. L. Schultz, T. V. Jones, M. L. G. Oldfield, and L. C. Daniels. A New Transient Cascade Facility for the Measurement of Heat Transfer Rates. *AGARD Symposium on "High Temperature Problems in Gas Turbine CP No. 229*, 1977. 7

[39] C. H. Sieverding and T. Arts. The VKI Compression Tube Annular Cascade Facility CT3. *ASME paper*, (92-GT-336), 1992. 7

[40] G. Paniagua. *Investigation of the Steady and Unsteady Performance of a Transonic HP Turbine.* PhD thesis, Von Karman Institute for Fluid Dynamics, 2002. 7, 23

[41] T. Povey and G. Paniagua. Method to Improve Precision of Rotating Inertia and Friction Measurements. *Mechanical Systems and Signal Processing*, 2012. 10

[42] R. Martet and T. Coton. Report on the Design of the Second Stator. Technical report, SNECMA Moteurs, 2005. 13

[43] T. Yasa. *Efficiency of a HP Turbine Tested in a Compression Tube Facility.* PhD thesis, Von Karman Institute for Fluid Dynamics, 2008. 23

[44] T. Yasa, G. Paniagua, and R. Denos. Application of Hot-Wire Anemometry in a Blow-Down Turbine Facility. *Journal of Engineering for Gas Turbines and Power*, 129(2):420–427, 2007. 24

[45] L. Cambier and M. Gazaix. elsA: An Efficient Object-Oriented Solution to CFD Complexity. In *AIAA Aerospace Sciences Meeting & Exhibit, 40 th, Reno, NV*, 2002. 26

[46] L. Cambier and J. P. Veuillot. Status of the elsA CFD Software for Flow Simulation and Multidisciplinary Applications. In *46th AIAA Aerospace Sciences Meeting and Exhibit*, 2008. 26

[47] A. Fourmaux. Assessment of a Low Storage Technique for Multi-Stage Turbomachinery Navier-Stokes Computations. In *ASME, Winter Annual Meeting, Chicago, IL, Nov. 6-11, 1994*, number 1994-157, 1994. 26

[48] N. Billiard. *Blade Row Interference and Clocking Effect in a One and Half Stage Turbine.* PhD thesis, von Karman Institute for Fluid Dynamics, 2007. 26

[49] Numeca International. User Manual, Fine Turbo v8.7. 2009. 27

[50] J. D. Denton. Loss Mechanisms in Turbomachines. *Journal of Turbomachinery*, 115(4):621–656, 1993. 1. 29

[51] T. C. Booth. *Importance of Tip Clearance Flows in Turbine Design.* Number 03 in Tip Clearance Effects in Axial Turbomachines. Von Karman Institute for Fluid Dynamics, Rhode Saint Genese, Belgium, April 1985. 2. 29

[52] B. Glezer. *Transient Tip Clearance Analysis and Measurement Techniques.* Number 02 in Turbine Blade Tip Design and Tip Clearance Treatment. Von Karman Institute for Fluid Dynamics, Rhode Saint Genese, Belgium, January 2004. 29

[53] H. S. Dhadwal and A. P. Kurkov. Dual-Laser Probe Measurement of Blade-Tip Clearance. *Journal of T*, 121(3):481–486, 1999. 29

[54] T. Pfister, L. Büttner, J. Czarske, H. Krain, and R. Schodl. Turbo Machine Tip Clearance and Vibration Measurements Using a Fibre Optic Laser Doppler Position Sensor. *Measurement Science and Technology*, 17:1693–1705, 2006. 3. 29

[55] A. Maslovskiy. Microwave Turbine Tip Clearance Measuring System for Gas Turbine Engines. *ASME paper*, (GT2008-50354), June 913 2008. 4. 29

[56] T. Tagashira, N. Sugiyama, Y. Matsuda, and M. Matsuki. Measurement of Blade Tip Clearance Using an Ultrasonic Sensor. *AIAA paper*, (97-0165), January 6-9 1997. 5. 29

[57] L. C. Hall and B. E. Jones. An Investigation Into the Use of a Cone-Jet Sensor for Clearance and Eccentricity Measurement in Turbomachinery. *Proc. Inst. Mech. Eng.*, 190(1976):23–30, 1976. 6. 29

[58] M. M. Hastings and H. B. Jensen. A Novel Proximity Probe Unaffected by Shaft Electromagnetic Properties. *ASME paper*, (GT-96-004), 1996. 7. 30

[59] J. P. Barranger. An In-Place Calibration Technique to Extend The Temperature Capability of Capacitance Sensor System. In *Soc. Automotive Engineers Aerospace Meeting vol. SAE Paper 781 003*, page 14, San Diego, CA, November 27-30 1978. 9. 30

[60] R. N. Demers. Compressor Blade Clearance Measurement Using Capacitance and Phase Lock Techniques. In *AGARD Advanced Instrumentation Aero Engine Components*, volume vol. AGARD-CP-399, page 10, Philadelphia, PA, May 1923 1986. 10. 30

[61] G. R. Sarma and J. P. Barranger. Capacitance-Type Blade-Tip Clearance Measurement System Using a Dual Amplifier with Ramp/DC Inputs and Integration. *IEEE Trans. Instrum. Meas.*, 41(5):674–678, 1992. 11. 30

[62] J. P. Barranger. Low-Cost FM OScillator for Capacitance Type of Blade Tip Clearance Measurement System. Technical Report Tech. Rep. NASA-TP-2746, NASA, 1987. 12. 30, 35

[63] J. W. H. Chivers. A Technique for the Measurement of Blade Tip Clearance in a Gas Turbine. *AIAA paper*, (89-2916), July 1012 1989. 13. 30, 42

[64] A. G. Sheard and B. Killeen. A Blade-by-Blade Tip Clearance Measurement System for Gas Turbine Applications. *Journal of Engineering for Gas Turbines and Power*, 117:326–331, 1995. 15. 30

[65] T. Fabian, F. B. Prinz, and G. Brasseur. Capacitive Sensor for Active Tip Clearance Control in a Palm-Sized Gas Turbine Generator. *IEEE Trans. Instrum. Meas.*, 54(3):1133–1143, 2005. 27. 30

[66] G. D. Bailleul and S. Albijat. Review of Progress in the Development of Capacitive Sensors for Blade Tip Clearance Measurement. *ASME paper*, (96-TA-1), 1996. 16. 30

[67] D. Mueller, A. G. Sheard, S. Mozumdar, and E. Johann. Capacitive Measurement of Compressor and Turbine Blade Tip to Casing Running Clearance. *Journal of Engineering for Gas Turbines and Power*, 119(4):877–884, 1997. 17. 30

[68] A. G. Sheard, S. G. ODonnell, and J. F. Stringfellow. High Temperature Proximity Measurement in Aero and Industrial Turbomachinery. *Journal of Engineering for Gas Turbines and Power*, 121:167–173, 1999. 18. 30

[69] R. R. Roberts. *The Potentials of Tip-Timing and Tip Clearance Measurements for Aero Propulsion Gas Turbines.* Number 03 in Tip Timing and Tip Clearance Problems in Turbomachines. Von Karman Institute for Fluid Dynamics, Rhode Saint Genese, Belgium, February 2007. 14. 30

[70] A. Steiner. Techniques for Blade Tip Clearance Measurements with Capacitive Probes. *Measurement Science and Technology*, 11:865–869, 2000. 39. 31

[71] C. P. Lawson and P. C. Ivey. The Use of Commercially Available Capacitance Tip-Clearance Probes for Tip-Timing of Aero-Engine Compressor Blades. *AIAA paper*, (2002-3730), July 7-10 2002. 19. 35

[72] A. G. Sheard, G. C. Westerman, and B. Killeen. An On-Line Calibration Technique for Improved Blade by Blade Tip Clearance Measurement. In *38th International Instrumentation Symposium*, volume 1, pages 31–51, Las Vegas, NV, April 26-30 1992. 38th International Instrumentation Symposium. 20. 36

[73] A. G. Sheard. Blade by Blade Tip Clearance Measurement. *International Journal of Rotating Machinery*, 2011, 2011. 38

[74] K. Chana. *Fundamentals of Tip-Timing and Tip Clearance Sensors.* Number 03 in Tip Timing and Tip Clearance Problems in Turbomachines. Von Karman Institute for Fluid Dynamics, Rhode Saint Genese, Belgium, February 2007. 21. 42

[75] H. W. Coleman and W. G. Steele. *Experimentation, Validation, and Uncertainty Analysis for Engineers.* Wiley, third ed. edition, 2009. 43, 68

[76] B. Glezer. *Thermal-Mechanical Design Factors Affecting Turbine Blade Tip Clearance.* Turbine Blade Tip Design and Tip Clearance Treatment. Von Karman Institute for Fluid Dynamics, 2004. 57

[77] M. K. Chyu. Heat Transfer Near Turbine Nozzle Endwall. *Annals of the New York Academy of Sciences*, 934:27–36, 2001. 57

[78] M. Malak, J. Liu, and E. Zurmehly. Turbine Shroud Durability Analysis Using Time Unsteady CFD and Si-C Testing. *ISABE paper*, 2011(1706). 57

[79] R. Bunker. A Review of Turbine Blade Tip Heat Transfer. *Annals of the New York Academy of Sciences*, 934(1):64–79, 2001. 57

[80] J. Moore, J. G. Moore, G. S. Henry, and U. Chaudhry. Flow and Heat Transfer in Turbine Tip Gaps. *Journal of Turbomachinery*, 111:301, 1989. 57

[81] J. Moore and K. M. Elward. Shock Formation in Overexpanded Tip Leakage Flow. *Journal of Turbomachinery*, 115(3):392–399, 1993. 57

[82] A. P. S Wheeler, N. R. Atkins, and L. He. Turbine Blade Tip Heat Transfer in Low Speed and High Speed Flows. *Journal of Turbomachinery*, 133:041025, 2011. 57, 58, 83

[83] V. Shyam, A. Ameri, and J. P. Chen. Analysis of Unsteady Tip and Endwall Heat Transfer in a Highly Loaded Transonic Turbine Stage. *Journal of Turbomachinery*, 134:041022, 2012. 57, 85

[84] P. J. Newton, G. D. Lock, S. K. Krishnababu, H. P. Hodson, W. N. Dawes, J. Hannis, and C. Whitney. Heat transfer and aerodynamics of turbine blade tips in a linear cascade. *Journal of Turbomachinery*, 128:300, 2006. 57

[85] Q. Zhang, D. O. ODowd, L. He, A. P. S. Wheeler, P. M. Ligrani, and B. C. Y. Cheong. Overtip Shock Wave Structure and Its Impact on Turbine Blade Tip Heat Transfer. *Journal of Turbomachinery*, 133:041001, 2011. 57

[86] S. K. Krishnababu, W. N. Dawes, H. P. Hodson, G. D. Lock, J. Hannis, and C. Whitney. Aerothermal Investigations of Tip Leakage Flow in Axial Flow Turbines – Part II: Effect of Relative Casing Motion. *Journal of Turbomachinery*, 131:011007, 2009. 57

[87] Q. Zhang, D. O. ODowd, L. He, M. L. G. Oldfield, and P.M . Ligrani. Transonic Turbine Blade Tip Aerothermal Performance With Different Tip GapsPart I: Tip Heat Transfer. *Journal of Turbomachinery*, 133:041027, 2011. 57

[88] G. R. Guenette, A. H. Epstein, and R. J. Norton. Time Resolved Measurements of a Turbine Rotor Stationary Tip Casing Pressure and Heat Transfer Field. *AIAA paper*, (85-1220), 1985. 57, 83, 85

[89] D. E. Metzger, M. G. Dunn, and C. Hah. Turbine tip and shroud heat transfer. *Journal of Turbomachinery*, 113(3):502–507, 1991. 58

[90] F. Didier, R. Dénos, and T. Arts. Unsteady Rotor Heat Transfer in a Transonic Turbine Stage. *Journal of Turbomachinery*, 124(4):614–623, 2002. 58

[91] S. J. Thorpe, R. J. Miller, S. Yoshino, R. W. Ainsworth, and N. W. Harvey. The Effect of Work Processes on the Casing Heat Transfer of a Transonic Turbine. *Journal of Turbomachinery*, 129:84–91, 2007. 58, 84

[92] S. J. Thorpe and R. W. Ainsworth. The Effects of Blade Passing on the Heat Transfer Coefficient of the Overtip Casing in a Transonic Turbine Stage. *Journal of Turbomachinery*, 130:041009, 2008. 58, 85

[93] S. J. Thorpe, S. Yoshino, R. W. Ainsworth, and N. W. Harvey. An Investigation of The Heat Transfer and Static Pressure on the Over-Tip Casing Wall of an Axial Turbine Operating at Engine Representative Flow Conditions (I): Time-Mean Results. *International Journal of Heat and Fluid Flow*, 25(6):933–944, 2004. 58, 62, 72, 83

[94] S. J. Thorpe, S. Yoshino, R. W. Ainsworth, and N. W. Harvey. An Investigation of The Heat Transfer and Static Pressure on the Over-Tip Casing Wall of an Axial Turbine Operating at Engine Representative Flow Conditions (II): Time-Resolved Results. *International Journal of Heat and Fluid Flow*, 25(6):945–960, 2004. 58, 72, 85, 91

[95] S. K. Krishnababu, P. J. Newton, W. N. Dawes, G. D. Lock, H. P. Hodson, J. Hannis, and C. Whitney. Aerothermal Investigations of Tip Leakage Flow in Axial Flow Turbines –Part I: Effect of Tip Geometry and Tip Clearance Gap. *Journal of Turbomachinery*, 131:011006, 2009. 58

[96] K. S. Chana and T. V. Jones. An Investigation on Turbine Tip and Shroud Heat Transfer. *Journal of Turbomachinery*, 125(3):513–520, 2003. 59, 83, 85

[97] D. L. Schultz and T. V. Jones. *Heat-Transfer Measurements in Short-Duration Hypersonic Facilities.* ADVISORY GROUP FOR AEROSPACE RESEARCH AND DEVELOPMENT PARIS (FRANCE), 1973. 62, 70, 74

[98] V. Iliopoulou. *High Frequency Gas Temperature and Surface Heat Flux Mesurements.* PhD thesis, Von Karman Institute for Fluid Dynamics, 2005. 65

[99] R. Dénos. *Aerothermal Investigation of The Unsteady Flow in The Rotor of a Transonic Turbine Stage.* PhD thesis, Von Karman Institute for Fluid Dynamics, 1996. 66, 67, 70, 119

[100] J. P. Solano and G. Paniagua. Novel Two-Dimensional Transient Heat Conduction Calculation in a Cooled Rotor: Ventilation PreheatingBlow-Down Flux. *Journal of Heat Transfer*, 131:081601, 2009. 67, 120

[101] G. Persico. *Unsteady Aerodynamic Stator-Rotor Interaction in High Pressure Turbines.* PhD thesis, Von Karman Institute for Fluid Dynamics, 2007. 67, 78

[102] S. J. Thorpe, S. Yoshino, R. W. Ainsworth, and N. W. Harvey. Improved Fast-response Heat Transfer Instrumentation For Short-Duration Wind Tunnels. *Measurement Science and Technology*, 15:1897, 2004. 69, 71

[103] G. A. Thomas, N. R. Atkins, S. J. Thorpe, R. W. Ainsworth, and N. W. Harvey. The Effect of a Casing Step on the Over-Tip Aerothermodynamics of a Transonic HP Turbine Stage. *ASME paper*, (GT2007-27780), 2007. 71

[104] H. Schlichting and K. Gersten. *Boundary-Layer Theory.* Springer Verlag, 2000. 72

[105] C. G. Miller. Comparison of Thin-film Resistance Heat-Transfer Gauges With Thin-Skin Transient Calorimeter Gages in Conventional Hypersonic Wind Tunnels. Technical Memorandum 83197, NASA, 1981. 74

[106] A. D. Fitt, C. J. P. Forth, B. A. Robertson, and T. V. Jones. Temperature Ratio Effects in Compressible Turbulent Boundary Layers. *Journal of Heat and Mass Transfer*, 29:159–164, 1986. 75

[107] R. W. Ainsworth, R. J. Miller, R. W. Moss, and S. J. Thorpe. Unsteady Pressure Measurement. *Measurement Science and Technology*, 11:1055, 2000. 78

[108] R. Dénos. Influence of Temperature Transients and Centrifugal Force on Fast-Response Pressure Transducers. *Experiments in Fluids*, 33(2):256–264, 2002. 78

[109] M. D. Polanka, J. P. Clark, A. L. White, M. Meininger, and T. J. Praisner. Turbine Tip and Shroud Heat Transfer and Loading: Part B – Comparisons Between Prediction and Experiment Including Unsteady Effects. *ASME paper*, (GT2003-38916), 2003. 85

[110] N. Harvey. *Aero-thermal Implications of Shroudless and Shrouded Blades.* Turbine Blade Tip Design and Tip Clearance Treatment. Von Karman Institute for Fluid Dynamics, 2004. 95

[111] Q. Zhang and L. He. Overtip Choking and Its Implications on Turbine Blade-Tip Aerodynamic Performance. *Journal of Propulsion and Power*, 27(5):1008, 2011. 95

[112] J. Kurzke. *Preliminary Design.* Aero-Engine Design: from State of the Art Turbofans towards Innovative Architectures. Von Karman Institute for Fluid Dynamics, 2008. 97

[113] P. De la Calzada. *Aerothermodynamic Design of Low Pressure Turbines.* Aero-Engine Design: from State of the Art Turbofans towards Innovative Architectures. Von Karman Institute for Fluid Dynamics, 2008. 97

[114] R. J. Miller, R. W. Moss, R. W. Ainsworth, and N. W. Harvey. Time-Resolved Vane-Rotor-Vane Interaction in a Transonic One-and-a-Half Stage Turbine. *Proceedings of the Institution of Mechanical Engineers, Part A: Journal of Power and Energy*, 215(6):675–685, 2001. 97

[115] R. G. Dominy, D. A. Kirkham, and A. D. Smith. Flow Development through Inter-Turbine Diffusers. *Journal of Turbomachinery*, 120(2):298–304, 1998. 97

[116] E. Göttlich, A. Marn, F. J. Malzacher, O. Schennach, and F. Heitmeir. Experimental Investigation of the Flow through an Aggressive Intermediate Turbine Duct Downstream of a Transonic Turbine Stage. In *Proceedings of 7th European Conference on Turbomachinery Fluid Dynamics and Thermodynamics*, 2007. 97

[117] L. U. Axelsson and T. G. Johansson. Experimental Investigation of the Time-Averaged Flow in an Intermediate Turbine Duct. *ASME paper*, (GT2008-51340), 2008. 97

[118] G. Norris, Dominy R. G., and A. D. Smith. Strut Influences Within a Diffusing Annular S-Shaped Duct. *ASME paper*, (98-GT-425), 1998. 97

[119] R. J. Miller, R. W. Moss, R. W. Ainsworth, and N. W. Harvey. The effect of an upstream turbine on a low-aspect ratio vane. *ASME paper*, (GT2004-54017), 2004. 97

[120] S. Ubertini and U. Desideri. Experimental Performance Analysis of an Annular Diffuser With and Without Struts. *Experimental Thermal and Fluid Science*, 22(3):183–195, 2000. 97

[121] F. M. Britchford, J. F. Carrotte, J. H. Kim, and P. M. Hield. The Effect of Operating Conditions on the Aerodynamic Performance of an Integrated OGV and a S-Shaped Duct. *ASME paper*, (2001-GT-0347), 2001. 97

[122] D. M. Zhou, Z. G. Zhang, and Y. S. Li. Design and Calculation for Splittered Axial Turbine Cascade. *ASME paper*, (93-GT-311), 1993. 98

[123] D. M. Zhou, Z. G. Zhang, and Y. S. Li. Numerical Prediction of Profile and Endwall Losses for Multi-Splitter Turbine Cascades. *ASME paper*, (93-GT-255), 1993. 98

[124] T. J. Barber and H. D. Weingold. Vibratory Forcing Functions Produced by Nonuniform Cascades. *Journal of Engineering for Gas Turbines and Power*, 100:82–88, 1978. 98

[125] W. F. Ng, W. F. OBrien, and T. L. Olsen. Experimental Investigation of Unsteady Fan Flow Interaction with Downstream Struts. *Journal of Propulsion and Power*, 3(2):157–163, 1987. 98

[126] H. Kodama and S. Nagano. Potential Pressure Field by Stator/Strut Interaction. *Journal of Turbomachinery*, 111(2):197–203, 1989. 98

[127] G. Cerri and W. F. OBrien. Sensitivity Analysis and Optimum Design Method for Reduced Rotor-Stator-Strut Flow Interaction. *Journal of Turbomachinery*, 111(4):401–408, 1989. 98

[128] G. Cerri, C. Boatto, W. F. OBrien, and A. Sorrenti. Optimization of Rotor-Stator-Strut Potential Flow Interaction Including Rotor Feedback Effects. *ASME paper*, (94-GT-274), 1994. 98

[129] A. B. Parry and R. H. Bailey. The Use Of Cyclic Variations In Strut Stagger To Reduce Coupled Blade-Vane-Strut-Pylon Interaction And System Losses. *ASME paper*, (97-GT-470), 1997. 98

[130] M. S. Ro and Y. S. Hong. The Control of Secondary Flow by Application of Splitter Vanes in the Turbine Stator Passages. In *Proceedings of Yokohama International Gas Turbine Congress*, volume 2, pages 81–84, Japan, 1995. 98

[131] H. Miyamoto, Y. Nakashima, and H. Ohba. Effects of Splitter Blades on the Flows and Characteristics in Centrifugal Impellers. *JSME International Journal*, 35:238–246, 1992. 98

[132] W. D. Tjokroaminata, C. S. Tan, and W. R. Hawthorne. A Design Study of Radial Inflow Turbines with Splitter Blades in Three-Dimensional Flow. *Journal of Turbomachinery*, 118(2):353–362, 1996. 98

[133] M. Asuaje, F. Bakir, S. Kouidri, F. Kenyery, and R. Rey. 3D Quasi-Unsteady Flow Simulation in a Centrifugal Pump. Influence of Splitter Blades in Velocity and Pressure Fields. In *Proceedings of the ASME Heat Transfer/Fluids Engineering Summer Conference*, volume 2, pages 1081–1090, 2004. 99

[134] M. B. Giles. Stator/Rotor Interaction in a Transonic Turbine. *Journal of Pr*, 6(5):621–627, 1990. 99

[135] R. Dénos, T. Arts, G. Paniagua, V. Michelassi, and F. Martelli. Investigation of the Unsteady Rotor Aerodynamics in a Transonic Turbine Stage. *Journal of Turbomachinery*, 123(1):81–89, 2001. 99

[136] U. Reinmöller, B. Stephan, S. Schmidt, and R. Niehuis. Clocking Effects in a 1.5 Stage Axial Turbine Steady and Unsteady Experimental Investigations Supported by Numerical Simulations. *Journal of Turbomachinery*, 124(1):52–60, 2002. 99

[137] D. Bohn, J. Ren, and M. Sell. Influence of Stator Clocking on the Unsteady Three-Dimensional Flow in a Two-Stage Turbine. *Journal of Turbomachinery*, 127(1):156–163, 2005. 99

[138] R. L. Davis, J. Yao, Clark J. P., G. Stetson, J. J. Alonso, A. Jameson, Haldeman C. W., and Dunn M. G. Unsteady Interaction Between a Transonic Turbine Stage and Downstream Components. *International Journal of Rotating Machinery*, 10(6):495–506, 2004. 99

[139] H. Ladisch, A. Schulz, and H. Bauer. Heat Transfer Measurements on a Turbine Airfoil With Pressure Side Separation. *ASME paper*, (GT2009-59904), 2009. 100

[140] D. Joslyn and R. Dring. Three-Dimensional Flow in an Axial Turbine: Part 1Aerodynamic Mechanisms. *Journal of Turbomachinery*, 114(1):61–70, 1992. 100

[141] D.A . Johnston and S. Fleeter. Turbine Blade Unsteady Heat Transfer Change Due to Stator Indexing. *ASME paper*, (99-GT-376):376, 1999. 100

[142] M. F. Blair, R. P. Dring, and H. D. Joslyn. The Effects of Turbulence and Stator/Rotor Interactions on Turbine Heat Transfer: Part IDesign Operating Conditions. *Journal of Turbomachinery*, 111(1):87–97, 1989. 100

[143] D. B. M. Jouini, D. Little, E. Bancalari, M. Dunn, C. Haldeman, and P. D. Johnson. Experimental Investigation of Airfoil Wake Clocking Impacts on Aerodynamic Performance in a Two Stage Turbine Test Rig. *ASME paper*, (GT2003-38872), 2003. 100

[144] T. Povey, K. S. Chana, and T. V. Jones. Heat Transfer Measurements on an Intermediate Pressure Nozzle Guide Vane Tested in a Rotating Annular Turbine Facility and the Modifying Effects of a Non-uniform Inlet Temperature Profile. *Proc. Instn. Mech. Engrs. Vol. 217 Part A: Journal of Power and Energy*, 217:421–431, 2003. 100

[145] K. Chana, U. K. Singh, and T. Povey. Measurements and Predictions for a 1.5 Stage Configuration. *ASME paper*, (GT2004-53951), 2004. 100

[146] C. W. Haldeman, M. G. Dunn, J. W. Barter, B. R. Green, and R. F. Bergholz. Aerodynamic and Heat-flux Measurements with Predictions on a Modern One and One-Half State High Pressure transonic Turbine. *Journal of Turbomachinery*, 127(3):522–532, 2005. 100

[147] J. Gadea, R. Dénos, and C. H. Paniagua, G.and Sieverding. Effect of Clocking on the Second Stator Pressure Field of a One and a Half Stage Transonic Turbine. *ASME paper*, (GT2004-53463), 2004. 107

[148] E. Valenti, J. Halama, R. Dénos, and T. Arts. Investigation of the 3D Unsteady Rotor Pressure Field in a HP Turbine Stage. *ASME paper*, (GT2002-30365), 2002. 107

[149] M. Tiedemann and F. Kost. Some Aspects of Wake-Wake Interactions Regarding Turbine Stator Clocking. *Journal of Turbomachinery*, (3):526–533, 2001. 107, 109

[150] H. P. Hodson and W. N. Dawes. On the Interpretation of Measured Profile Losses in Unsteady Wake–Turbine Blade Interaction Studies. *Journal of Turbomachinery*, 120(2):276–283, 1998. 109

[151] H. D. Li and L. He. Blade Count and Clocking Effects on Three-Blade-Row Interaction in a Transonic Turbine. *Journal of Turbomachinery*, 125(4):632–640, 2003. 109

[152] D. J. Dorney and O. P. Sharma. Turbine Performance Increases Through Airfoil Clocking. *International Journal of Turbo and Jet Engines*, 15:119–127, 1998. 109

[153] M. Arnone, A.and Marconcini, R. Pacciani, C. Schipani, and E. Spano. Numerical Investigation of Airfoil Clocking in a Three-Stage Low-Pressure Turbine. *Journal of Turbomachinery*, 124(1):61–68, 2002. 109

[154] O. Schennach, J. Woisetschlger, A. Fuchs, E. Gttlich, A. Marn, and R. Pecnik. Experimental Investigation of Clocking in a One-and-a-Half Stage Transonic Turbine Using Laser Doppler Velocimetry and a Fast Response Aerodynamic Pressure Probe. *Journal of Turbomachinery*, 129(2):373–381, 2007. 109

[155] T. Arts, J. M. Duboue, and G. Rollin. Aero-Thermal Performance Measurements and Analysis of a Two-Dimensional High Turning Rotor Blade. *Journal of Turbomachinery*, 120(3):494–499, 1998. 119

[156] D. R. Buttsworth and T. V. Jones. Radial Conduction Effects in Transient Heat Transfer Experiments. *Aeronautical Journal*, 101(1005):209–212, 1997. 120

[157] S. S. Rao. *The Finite Element Method in Engineering.* Pergamon Press, second edition edition, 1989. 120

[158] J. E. Doorly and M. L. G. Oldfield. The Theory of Advanced Multi-Layer Thin Film Heat Transfer Gauges. *International Journal of Heat and Mass Transfer*, 30(6):1159–1168, 1987. 120

[159] V. Iliopoulou, R. Dénos, N. Billiard, and T. Arts. Time-Averaged and Time-Resolved Heat Flux Measurements on a Turbine Stator Blade Using Two-Layered Thin-Film Gauges. *Journal of Turbomachinery*, 126(3):570–577, 2004. 120

[160] S. W. Churchill and H. Ozoe. Correlations for Laminar Forced Convection with Uniform Heating in Flow Over a Plate and in Developing and Fully Developed Flow in a Tube. *Journal of Heat Transfer*, 95:78–84, 1973. 123

[161] M. S. Bhatti and R. K. Shah. *Turbulent and Transition Flow Convective Heat Transfer in Ducts.* New York, John Wiley & Sons, 1987. 125

[162] W. Traupel. *Termische Turbomaschinen Zweiter Band Gelnderte Betriebsbedingungen, Regelung, Mechanische Probleme, Temperaturprobleme.* Springer-Verlag, New York, 1977. 141